Department of Applied Geology
Western Australian School of Mines

Mapping the Regolith and its Mineralogy of the Tick Hill Region, Mount Isa, Queensland, using HyMap and ASTER Remote Sensing Data

Fitriani Agustin

This thesis is presented for the Degree of
Master of Science (Geology)
Curtin University of Technology

March 2011

Certificate of Originality

I hereby declare that this submission is of my own work and that, to the best of my knowledge and belief, contains no material previously published or written by another person, unless it has been acknowledged accordingly. I have endeavored to perform the research encapsulated in this document from any my own ideas. I give consent for this thesis to be loaned or photocopied. However, I request acknowledgment when the original ideas, data, or figures contained within this thesis are used.

Fitriani AGUSTIN, June 2010

Abstract

The study involved investigating the use of ASTER and HyMap datasets from the Tick Hill area, Mount Isa region in Queensland, to make mineral maps and validate them, and subsequently to use the mineral maps to map and study the regolith-landforms. The processing techniques used on the multispectral and hyperspectral data were relative band depth (RBD) and Spectral Indices, and a sequence of masking procedures to minimize spectral overlap effects from other materials such as vegetation, atmospheric particles and minerals. The ASTER datasets allowed mapping of mineral groups such as Al-OH, Mg-OH and iron oxides rather than individual mineral maps. HyMap data, due to its better spectral resolution was able to map kaolinite, kaolinite crystallinity, iron oxides (hematite and goethite), white mica, Mg-OH + carbonate minerals, and to an extent silica and Al-smectite.

The application of the mineral maps applied to map regolith-landforms allowed better characterization of regolith materials as compared to traditional band combination methods. Surface mineralogy could be linked to specific surface regolith materials such as kaolinite and iron oxides representing ferruginous materials (duricrusts, soils or mottled zones), abundance of well crystalline kaolinite equated to saprolite and mottled saprolite and high Mg-OH equated to slightly weathered (saprock) exposures of Pre-Mesozoic basement rocks. Spatial variation in mineralogy permitted interpreting changes in surface regolith and refining regolith-landform units as mapped from simple Red-Green-Blue band combinations. Kaolinite crystallinity maps were effective in highlighting *in situ* regolith from transported regolith, and allowing interpretation of the presence of deep weathering profiles being capped by ferruginous materials (duricrusts) or saprolite exposures on the hills, rises and erosional plain landforms of the regions.

Acknowledgments

I would like to thank to the following people and organization:

- Australian Development Scholarship for sponsoring me to study my Masters degree at Curtin University of Technology Australia. Special thanks to Julie, Kristen, Caroline; the AusAid sponsor officers at Curtin for guiding me through my study and all other administrative work.
- The head of Department Applied Geology, A/Prof Ian Fitzsimons.
- My supervisor Dr. Mehrooz F. Aspandiar, for the great help, assistance and patience to supervise me.
- My co-supervisor Dr. Thomas Cudahy, from CSIRO Exploration & Mining for the excellent assistantship and help in understanding the hyperspectral work and processing.
- CSIRO Exploration and Mining colleagues; Ian lau for sharing his regolith and hyperspectral experience; Rob Hewson for ASTER guide and private lectureship, Mike Verrall for assisting me do some work on XRD analisis, Andrew Hacket for helping me out with ASD spectral and TSG software, Andrew, Cindy Ong, Cheryl, Mike, and Karnsten.
- My research colleagues Erin Gray from Australia, Ivor Kahimise from Namibia, Ivan Vitin from Switzerland and Muhammad from Oman. Thanks for sharing research experiences so far.
- My office colleagues at Geological Survey of Indonesia; Dr. .Jajang Sukarna and others.
- My dearest friends, thanks for your wonderful support: Hajir, Fathyah, Adilla, Clinton, Iwan, Ira and Yosfi.
- And finally, my family; Mom and Dad, my sister Nita and my Brother Dudi; thanks for always encouraging me every time and for never ending praying for my study.

Table of Content

List of Figures

Chapter 4

List of Tables

List of Terms and Acronyms

ASTER : Advance Space-borne Thermal Emission and Reflection Radiometer
ASD : Analytical Spectral Device
BOCO : Base of the Complete Oxidation
CERES : Clouds And The Earth's Radiant Energy System
CRC LEME : Cooperative Research Center for Landscape and Mineral Exploration
CSIRO : Commonwealth Scientific and Research Organization
DEM : Digital Elevation Model
DN : Digital Number
EFFORT : Empirical Flat Field Optimal Reflectance Transformation
GA : Geoscience Australia
HyCore : Hyperspectral Correction
HyMap : Hyperspectral Mapper
LANDSAT TM : LANDSAT Thematic Mapper
METI Japan : Ministry of Economy, Trade and Industry Japan
MISR : Multi-angle Imaging SpectroRadiometer
MNF : Minimum Noise Fraction
MODIS : The Moderate Resolution Imaging Spectroradiometer
MOPIT : Measurements of Pollution in the Troposphere
MTMF : Mixture Tune Match Filtering
NASA : National Aeronautics and Space Administration
NDVI : Normalised Difference Vegetation Index
RBD : Ratio Band Depth
RED : Residual Erosional Depositional
RGB : Red Green Blue
RLU : Regolith Landform Unit
SAM : Spectral Angle Mapper
SFF : Spectral Feature Fitting
SRTM : Shuttle Radar Topography Mission
SWIR : Short Wave Infra Red
TIR : Thermal Infra Red
USGS : United States of Geological Survey
VNIR : Very Near Infra Red
XRD : X-Ray Diffraction

List of Appendices

Chapter 1

Introduction

1.1 Aims and Objectives

1.1.1 Aims of Research

In view of the need to use multispectral and hyperspectral remote sensing to make mineral maps and validate the maps for specific surface materials and conditions, the research conducted in this thesis attempts to address the effectiveness of mineral mapping using multispectral and hyperspectral sensors in the North Queensland locality of Tick Hill, and use the produced mineral maps to then make regolith-landform maps and interpret regolith processes.

The specific aims are:

- Make mineral maps of study area using multispectral and hyperspectral sensing (ASTER and HyMap) and compare maps from both methods.. The minerals or mineral groups selected to be mapped are those that show spectral response in the VNIR-SWIR range and whose spectral response characteristics can be distinguished by the ASTER and HyMap band width.
- Assess the validity of remotely sensed mineral maps with ground truth spectral measurement data.
- Demonstrate the ability of spectral responses and mineral maps derived from multispectral and hyperspectral data to map regolith material and to produce remotely sensed RLU (Regolith Landform Unit) in order to aid interpretation of regolith materials and genesis.

1.1.2 Thesis Outline

Chapter I provides background information regarding remote sensing systems (ASTER and HyMap) and their use in making mineral maps as well as regolith mapping. Chapter 2 describes regional geology of the Mount Isa region, local geology of the Tick Hill region and regolith geology in general in the Mt. Isa region. Chapter 3 describes the remote sensing techniques used in detail including pre-processing, methods used to process ASTER and HyMap data including proximal sensing data acquired via ASD and XRD (ground truth), and the application of this

data to identify minerals. Chapter 4 presents the results and the interpretation of mineral products derived from HyMap and ASTER, the technical procedures and steps employed to produce mineral maps and the validation of the product by ground truth ASD and XRD analysis. Chapter 5 applies the mineral map products produced together with additional data (DEM, Radiometric imagery, regional published geology) to identify regolith materials and classify the remotely sensed RLU (Regolith Landform Unit). Chapter 6 is a summary with recommendations for the application of mineral mapping for future research in the project area.

1.1.3 Research Location

This research project is a part of The Smart Exploration Project program announced by CSIRO Exploration and Mining and Geological Survey of Queensland cooperation through Hyperspectral Technology (*http://www.dme.qld.gov.au/mines/hyperspectral.cfm*). This technology has been used to derive smart mineral mapping to guide mineral exploration (Cudahy, 2005; Vaughan, 2005).

Geographically, the research area (Block G TickHill) is located in 21° 14’ 1’’ and 21° 43’ 24.24’’ South and 139° 47’ 47.04’’ - 140° 1’ 19.20’’ East. As part of North-central Queensland within location Block G TickHill, it is an ideal location to test the effectiveness of multi and hyperspectral remote sensing for Australian conditions, as it hosts a wide variety of lithology and is covered by regolith, such as variably preserved deep weathering profiles typical to the Australian landscape. Besides a large scale regolith map (Anand *et al.*, 2002) no other information regarding regolith-landform mapping and regolith interpretation exists for this important region. Further, a recent Queensland Geological Survey project to HyMap data provided access to hyperspectral data including field based data. The figure 1.1 below represents the location of TickHill mine area around Mt Isa.

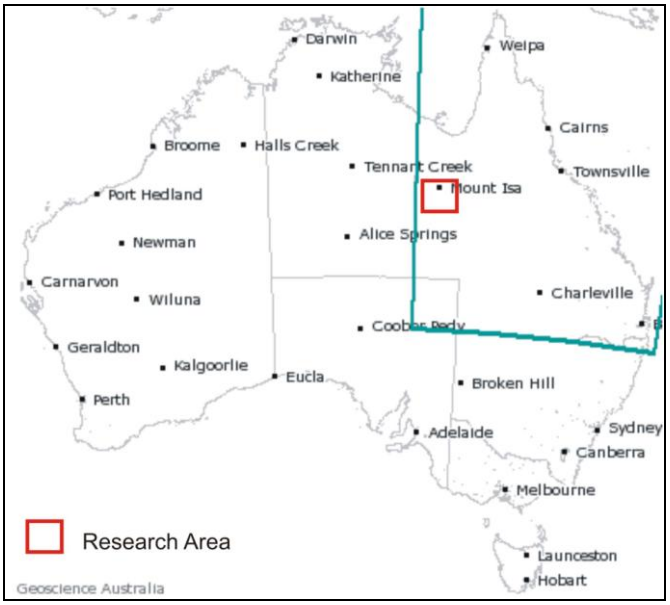

Figure 1.1: The location of research area in Tick Hill Mt.Isa Inlier, NW Queensland

1.2 Background

1.2.1 Limitation of present geological maps

A geological map represent spatial distribution of lithology and structural information. In the geological maps, spatial mineralogical information is absent or has to be interpreted inspite of spatial mineralogical information being critical to the geological understanding of the area. For example, spatial distribution of metamorphism indicator minerals can provide valuable information regarding scale and extent of metamorphic facies changes. The presence and distribution of hydrothermal minerals can provide critical information regarding alteration systems and location of ore deposits. Mineralogical information is also critical to the understanding of geological processes and pre-competitive mineral exploration. In Australia, where regolith covers much of the continent, mapping regolith material distribution is vital to many applied disciplines such as selection of appropriate sample media for geochemical exploration (Anand and Paine, 2002; Butt, 2005) and environmental management. Therefore, any technique which rapidly and effectively maps the surface minerals can aid the interpretation of geological and regolith evolution of an area as well as optimize mineral exploration and environmental management.

1.2.2 ASTER and HYMAP remote sensing and mineral mapping

Multispectral remote sensing in the form of sensors on board the Landsat series satellites (MSS, TM) has been fulfilling the need of the earth science community to remotely map the Earth's surface (Sabins, 1987; Drury and Hunt, 1988). However, the poor spatial and spectral resolution of the Landsat TM sensor restricts its application to broad scale mapping with limited mineralogical information. Newer multispectral and hyperspectral sensors address the Landsat TM limitations by improving spectral and spatial resolution in the VNIR and thermal range. In the past decade several new sensors, ranging from spaceborne to proximal and from multispectral to hyperspectral, have become available for geoscience studies (Mauger, 2003). The two sensors that have contributed substantially to the Australian earth science mapping programs have been the multispectral ASTER and the hyperspectral HyMap. These sensors have allowed the mapping of spectrally sensitive minerals in the VNIR and thermal range, namely Al-OH, Mg-OH, Fe-OH bearing minerals, iron oxides and carbonates. Many of the minerals identified and mapped are important, as their presence and distribution is linked to hydrothermal alteration such as Al-OH bearing phyllosilicates (muscovite, illite, kaolinite), Mg-OH bearing phyllosilicates (chlorite) and carbonates, and also to regolith materials such as kaolinite, iron oxides and carbonates. Accordingly, the sensors are increasingly employed to map the spatial distribution of spectrally responsive minerals.

The ASTER sensor has been employed to make mineral maps in Australia (Hewson *et al* 2005; Oliver and van der Wielen, 2006) and other parts of the world (Rowan and Mars, 2003; Mars and Rowan, 2006). Although an improvement on the Landsat TM sensor, ASTER is limited by its spatial and spectral resolution. This limitation is addressed by HyMap which collects spectral information in 128 bands with a 5 m spatial resolution. HyMap data has been used to map individual minerals successfully and has been applied to map rocks and minerals (Rowan *et al.*, 2004) metamorphism and hydrothermal alteration mapping (Bierwerth *et al.* 2002; Brown *et al.*, 2006).

There are several processing methods available to make mineral maps and the validity and effectiveness of each, needs to be established for specific surface materials. For example, for the multispectral ASTER sensor, band ratio or relative

band depth has been employed to distinguish specific minerals or mineral assemblages (Hewson *et al.*, 2006; Mars and Rowan, 2006). For hyperspectral analysis, several processing methods have been advanced and employed such as Spectral Feature Fitting (SFF), Spectral Angle Mapper (SAM), Unmixing and Minimum Noise Function (MNF) and Spectral Indices (Swaze *et al.*, 2000; Bierwirth *et al.*, 2002; Rowan *et al.*, 2004; Cudahy *et al.*, 2008), although besides MNF function (Deehan and Taylor, 2004), no other methods have been used to map and study the regolith. There is a need to use the most effective processing method to map minerals for the specific surface materials being investigated and validate the results.

Making mineral maps is central to geoscience remote sensing and is also the main aim of this research. Therefore, an introduction to mineral mapping and mineral spectroscopy is provided. Cudahy *et al.*, (2008) define mineral mapping as particular interaction of geological materials with electromagnetic radiation anywhere across the wavelength range between 400nm to 14000nm.

Mineral mapping relies on spectral characteristics of minerals which are in turn dependant on mineral composition (Hunt, 1977; Clark 1999). The typical measured reflectance spectra of minerals contain spectra features which are indicative of the mineral composition. In the wavelength range detected by available VNIR-SWIR and Thermal sensors, the minerals that bear diagnostic spectral features and therefore are capable of being recognized and mapped, fall into a select composition.

The minerals that have spectral absorption features in the Visible Near Infrared (NIR) region are ferric iron bearing minerals hematite, goethite, ferrihydrite and other iron oxides and hydroxides. Also, vegetation can be easily detected because of absorption due to their chlorophyll and leaf water content.

The minerals that are detected in the Short-Wave Infrared range (SWIR) are dependant on presence of cation-OH bonds and CO_3 ion, both of which are vibrationally sensitive in the specified range. The minerals are

- AlOH bearing minerals (white mica, paragonite, muscovite, illite, phengite, and pyrophyllite), kaolin (kaolinite, halloysite, dickite and nacrite) and smectite (montmorillonite, beidellite).

- Sulphate : alunite, jarosite, gypsum
- Si(OH) : opaline silica
- Fe(OH) bearing minerals : nontronite, Fe-Chlorite
- MgOH bearing minerals: saponite, epidote, hornblende, actonolite, antogorite, tremolite, chlorite (Mg/Fe), biotite.
- Carbonates: calcite, dolomite, magnesite, ankerite and siderite.
- Vegetation component: cellulose, lignin, waxes, oils, protein and leaf water.

Minerals detected in the Thermal Infrared (TIR) range are

- Silica : quartz and opaline silica
- Feldspar : microcline, albite, anorthite
- Pyroxene : orthopyroxene, clinophyroxene
- Garnet : almandine, spessartine, pyrope, andradite, grossular
- Olivines : forsterite, fayalite
- Carbonates: calcite, aragonite, dolomite, magnesite, ankerite, siderite, and cerrusite.
- Sulphates : jarosite, alunite and gypsum
- Vegetation: including composition and structure

The multispectral ASTER and hyperspectral HyMap permit the recognition of minerals or mineral groups in the VNIR – SWIR – TIR range, and their data on processing allows potential mapping of minerals.

1.2.3 Regolith Mapping

Although remote sensing has long been used to map and identify regolith (Tapley and Gozzard, 1992), the full potential of employing individual minerals and mineral assemblage maps to map the regolith and subsequently interpret the regolith processes and landform evolution of selected areas has not been explored. The value of using mineral maps to map regolith is essential to a continent like Australia whose surface is largely covered with regolith materials which vary from the slightly weathered rock to highly weathered profiles to fresh or weathered transported cover (surficial sediments) (Taylor and Eggleton, 2001, Anand and Paine 2002). A

mineralogical map that encompasses regolith minerals such as kaolinite, iron oxides and illite, would allow rapid characterization of regolith materials within a landscape. An effective remotely sensed method to map regolith and interpret its origins would be valuable to basic and applied research. In this respect, some recent progress has been made to interpret hysperspectral derived mineral maps to make regolith material maps (Dehaan and Taylor, 2006; Cudahy *et al.*, 2006), although much more needs to be done.

Chapter 2

Regional and Local Setting

2.1 Regional Physiography, climate and vegetation

Physiographic of study area

The landsurface of Mount Isa region is represented by an immature, dissected plateau that forms part of the larger Western Plateau Division. The elevation of the plateau varies from a maximum of 500m to a low of approximately 60m with an average local relief of less than 100m above sea level (Jenning and Mabbout, 1977 in Anand *et.al* 2002). The overall relief of Mount Isa region mostly reflects the underlying structure and lithology (Birot, 1985; Twidale 1966 in Anand *et al.*, 2002).

Topography consists of a series of hills, isolated mesas and undulating flat plains. These geomorphic features are divided into small scale provinces; Hills into Hill Belts, mesas into mesas with underlying Proterozoic bedrocks and mesas and plains with underlying Mesozoic sediments, and plains into three - gently sloping plains, undulating to rolling plains and flat plains (Anand *et al.*, 2002).

Climate and Vegetation

The climate in the Tick Hill region is semi-arid with much of the precipitation falling during summer months as storms (Ryburn, 1988). Vegetation type varies across the landforms with dominant species being native grasses, sparse stands of *Eucalyptus* and only rare gidgee (*Casuarina sp.*). There is a suggested relationship between soil and lithology types and vegetation in regolith landform. The clay-rich and calcareous soils are more abundant of grasses and gidgees which develop in flatter areas such as floodplains and other shallow drainage depressions. The iron-rich soils and weathered bedrock outcrops are mostly covered by abundant *spinifex,* with sparse *Eucalypt, Acacia and Grevillea (*Figure 2.1*).*

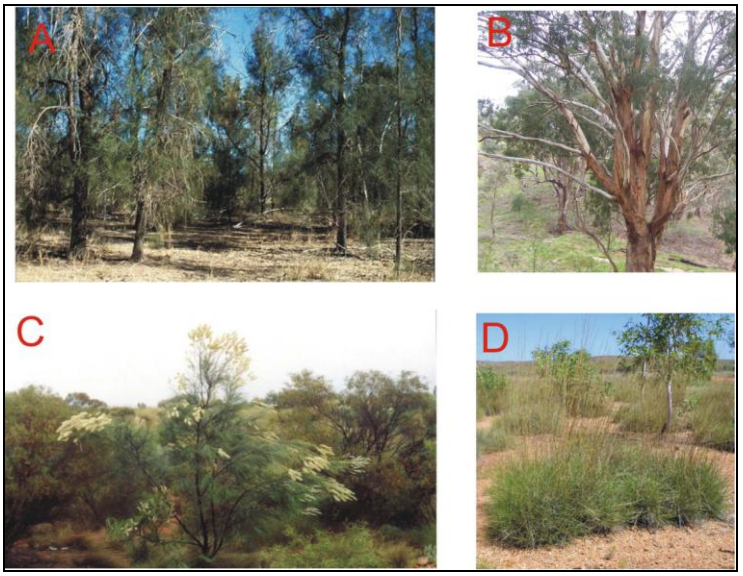

Figure 2.1 : The various semi-arid vegetation in Mt.Isa Inlier and surroundings; A (*Casuarina sp.)*, B (*eucalyptus*), C (*grevillea)* and D (*spinifex).*

2.2 Regional Geology and Regolith Framework

2.2.1 Regional Geology

Tick Hill region is part of Mount Isa Inlier which comprises of rocks from early to middle Proterozoic to Quaternary sediments. Mount Isa Inlier is bounded to the northwest by Proterozoic south Nicholson Basin, to the west and south by Paleozoic Georgiana Basin and to the south by Eromonga Basin and to the northeast by Mesozoic Carpentaria Basin.

Tick Hill is part of the Proterozoic Eastern and Western Fold Belt Province and some parts of it are covered by Mesozoic and Paleozoic lithology (Figure 2.1). The area is mostly dominated by Wonga Sub-province which consists of Wonga Batholith (medium to coarse hornblende-biotite granite) and gneiss; both of which intruded during 1760 – 1720Ma (Geology of The Dutchess- Urandagi Region, 1983).

Eriksson *et al.* (1991) divided Mount Isa stratigraphy into two sections; basement and cover rocks. Basement is mainly exposed in the Kalkakdoon-Leichardt Belt which comprise of quartzite, schist, migmatite and pragneiss imposed by felsic. It has been deformed and metamorphosed at approximately 1900 Ms (Blake *et al.*, 1987) which stabilized the North Australia Craton. Above the basement, there are three cover sequences (figure 2.3). Cover 1 sequence is the Leichhardt Volcanics dated at 1870 Ma and consisting of dacitic and rhyolitic which are intruded by cogenetic granitoid batholiths, comprising of kalkadoon Granite (tonalities to

granites in composition, dated 1860 Ma). Cover II consists of Mount Guide Quartzite, Eastern Creek Volcanics, Myally Subgroup and Quillar Formation. Cover III sequence consistes of Granite and Rhyolite dated 1670 – 1740 Ma (Eriksson *et. al.*,1991).

The broad subdivision of Mount Isa Block including major faults, mines and granitoids have been carried out by Rubenach and Foster, 1996 in Oliver *et al.* (2008) subdivided the Mount Isa Block into several belts. The belts are:

Sybella-Yaringa Zone, west of the Mount Isa Fault: ECV-Isa Zone, eastpart of the Mount Isa Fault, incorporating the Mount Isa host sequences (Pb-Zn-Cu) as well as the main body of (low metamorphic grade).

Eastern Creek Volcanics: Kalkadoon-Leichardt Block is the central basement block of Inlier.

Mary Kathleen Fold Belt (MKFB) marks the western edge of the Eastern succession which is highly deformed.

Tommy Creek Block straddles the MKFB and the northern extension of the Mitakoodi Block.

Mutakoodi Block is located to the east of the MKFB and in the south of the Tommy Creek Block which is dominated by the rock of Duck Creek Anticline-Argylla and Marabba Volcanics, Mitakoodi Quartzite and Overhang Jaspillte.

Cloncurry Fold Belt consists of the mineralized black slate, schist, and ironstone sequences in the west, extending through brecciated Corella Formation rocks (which host the Ernest Henry Cu-Au deposit), and across the Cloncurry Fault. This belt is dominated by pelitic rocks of the Soldiers Cap Groups and including Cannington (Ag-Pb-Zn) deposit.

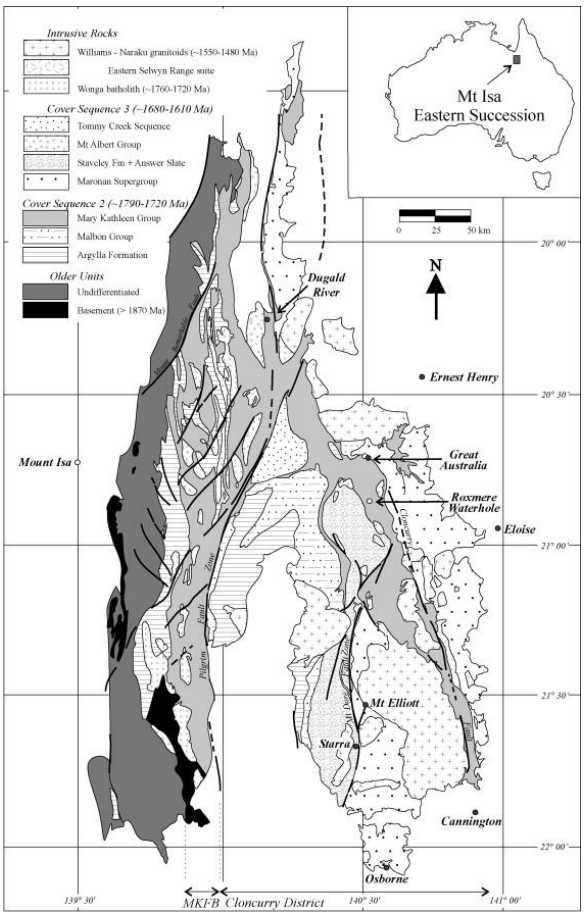

Figure 2.2: Simplified regional geology of Mt. Isa Inlier (in Marshall, 2008, modified after William 1998).

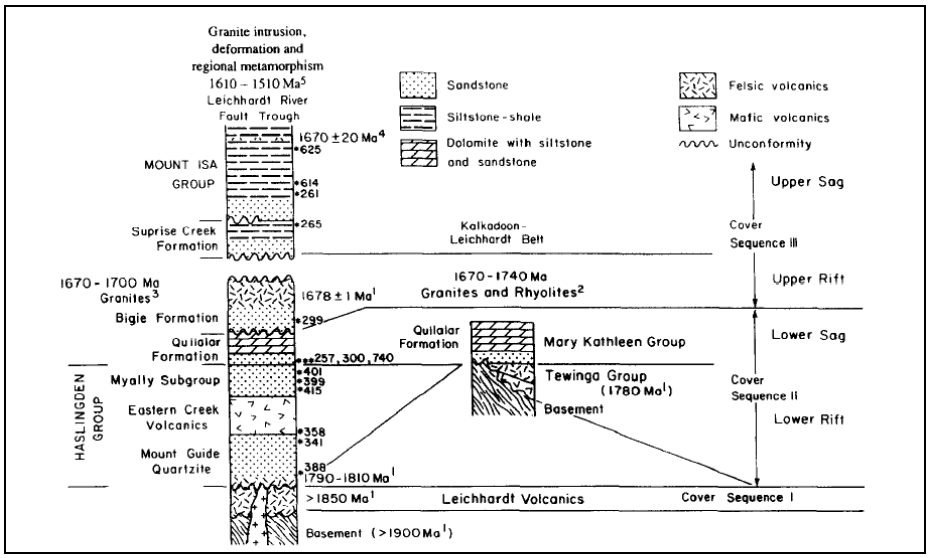

Figure 2.3 : Lithostratigraphic column for cover rocks in the Leichardt River Fault and Kalkadoon-Leichardt Belt, Mount Isa (K.A. Eriksson, 1991 as adapted from Derrick *et al*.,1980;Blake,1987)

2.2.2 Regional Regolith Framework

Regolith was first defined by Merrill (1897) and is a word derived from Greek word *regos* which means blanket or cover, and *lithos* which means rocks or stones. There are many definitions of regolith (Pain *et.al.*, 1991; Ollier & Pain, 1996; Jackson, 1997) and Taylor and Eggleton (2001) defined regolith as "The layer at the Earth's surface that is the result of weathering, erosion and deposition. It includes weathered rocks, soils and sediments (sand, silt, clay and gravel)".

Anand *et.al.*, (2002a) conducted regolith research in some parts of Mt. Isa region and they concluded that regolith distribution and genesis in Mt Isa region was complex due to multiple weathering, erosion and depositional episodes during the Mesozoic and Cenozoic era.

2.2.2.1 Regional Regolith-Landform Morphology

Anand *et al.* (2002) have divided regolith-landforms in Mt.Isa region into three basic provinces, namely hill belts, undulating terrain and plain, each being characterized by their particular degree of weathering, erosion and depositions.

The Hill Belts are present in the middle of the region (17°30'S-22°00'S; 137°30'E-141°00'E) and form north trending the ridges and hills. The various weathering profiles developed underlying these landforms were influenced by lithology. The Mesozoic sediments have experienced weathering followed by erosion and the deep weathering profiles are currently present underlying mesas. The weathering profiles are dominated by kaolinite, smectite, and pedogenic carbonates with some secondary silicification (Anand *et al.* 2002). Part of the landform is covered by colluvium which varies in thickness from less than 1 meter to up to 12 metres in certain places.

The undulating terrain landform consists of a complex mesas and plains underlain by lateritic weathering profiles. This terrain landform is present in the Tick Hill Region which part of the western Mt. Isa region and extends out into the eastern succession. The weathering degree and depth varies across the landforms. Some landforms such as mesas have deeply weathered profiles and while pediments and erosional plains have shallow weathering profile. Shallow alluvium, 1 – 5 m deep and variably cemented (ferruginous and siliceous), fills the depositional plains.

The Plains are low relief and are underlain by weathered to fresh, eroded Cenozoic, Tertiary and Mesozoic sediments.

2.2.2.2 Regolith Materials and Weathering Profile

The deep weathering profiles observed in the region are similar to those of an ideal lateritic profile described by Nahon and Tardy (1992), Taylor and Eggleton and (2001) and Anand and Paine (2002) where uppermost soil is underlain by duricrust, then by mottled zone followed by saprolite and then saprock. Anand *et al.* (2002) found the weathering profile in Proterozoic and Mesozoic rocks to be controlled by bedrock composition and paleo-topography. The typical highly weathered profile in the Mt. Isa region is represented from the top to the base by lateritic nodules and pisoliths, pockets of duricrust, indurated ferruginous saprolite, a clay zone, saprolite (silicified in part), saprock and bedrock (figure 2.4). In some Mesozoic sediments, lateritic duricrust and silcrete developed widely while in Tertiary sediments mottled zones are common.

Other factors that influence the regolith profile are proximity to the fault zone and mineralization, as well as alteration and landscape position (Conaghan *et al.*, 2003). In the mine site, the base of the saprolite (Base Of the Complete Oxidation-BOCO) is about 40-100 m deep, compared to the pre-mining water table at 50m beneath the surface. In major fault zones, development of very deep saprolite zons (500 m deep) are possible due to migration of meteoric water along these conduits (Hewett, 1968 in Conaghan *et al.*, 2003, see the regolith landform and mineralization for detail).

The weathering profiles in the region are considered to have formed under the influence of multiple climates. Materials such as ferricretes ("laterites") and silcretes are probably related to past wetter climates, while calcretes and smectite in weathering profiles that develop under the Hill Belts and on the erosion plains which are a product of present climate (Anand *et al.*, 2002).

Regolith materials in the region vary from massive, fragmental and nodular duricrusts[1] and Fe-rich weathered rocks, with most of the duricrusts being residual. In lower slopes and at plateau or mesa boundaries, slabby duricrust are often found

[1] A duricrust that has a fragmental or blocky fabric in outcrop and/or hand specimen. The interstices between fragments are commonly occupied by a clayey, ferruginous or sandy matrix.

and can be distinguished by their goethite-rich and Mn-rich mineralogy (Anand, 2002). In addition, silcrete[2] has also developed in weathering profiles over sediments and is found as a siliceous cement of alluvial sands present on higher topography areas.

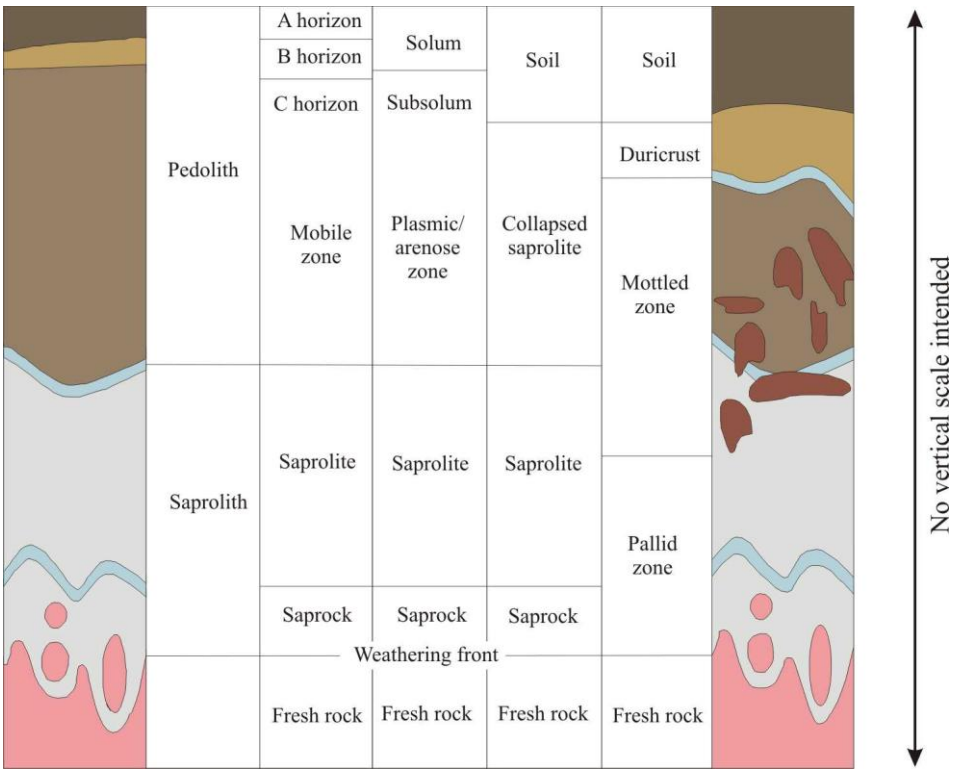

Figure 2.4: The schematic diagram of variety terms and regolith profile. The difference might reflect the variety in nature and author preference (modified from Taylor and Eggleton, 2001).

2.2.2.3 Regolith Mineralization and Mineral Exploration

Understanding of regolith material distribution in landforms and regolith evolution has been critical to the judicious selection of sample media for mineral exploration as showcased for the Yilgarn Craton (Anand and Paine 2002). Several deposits such as bauxite, supergene gold, nickel and copper, are hosted within the regolith because of intense weathering of specific primary rocks.

The Mt Isa region has been reported to has supergene enrichment of base metals. Conaghan *et al.*(2003) investigated the relationship between the regolith profile and the mineralization surrounding Mount Isa Northwest Queensland area.

[2] Strongly silicified, indurated regolith, low permeability, have a conchoidal fracture with a vitreous lustre. Silcrete appears to represent the complete/near-complete silicification of precursor regolith by the infilling of available voids and fractures. Most are dense and massive, some may be cellular, with boxwork fabrics.

There is interaction between meteoric water and bedrock at the Base Of Complete Oxidation (BOCO) zone which resulted in the formation of supergene ore just above BOCO zone (transition zone). The supergene accumulation is dominated by Zn-Ag and Cu oxide-carbonate assemblage. In contrast, the secondary Cu-sulphide, particularly chalcosite, accumulated in the transition zone (Smith 1966 in Conaghan *et al.* 2003).

Vasconselos (1998) in his study weathering history and the age of regolith dated Mount Isa gossan between 15-21 Ma based on the K-Ar ages acquired from manganese oxides. However, the supergene enrichment and leaching which contributed to the Mt.Isa gossan deposit could have been occurring in the wet periods since Miocene, when the silcrete and calcretes capping mesas are suggested to have formed. In addition, the evidence showed that Phanerozoic sediments had already eroded allowing the amount of meteoric water to interact with the regolith material to form an ore sequence during the early Tertiary.

2.3 Local Setting of Study Area

2.3.2 Geology of the Block G Tick Hill Region

The Tick Hill region consists of rocks ranging in age from the Precambrian to Cambrian to Mesozoic to the Quaternary.

2.3.2.1 Precambrian Sequence

Precambrian sequence represents the dominant rocks in Block G Tick Hill and forms the basement rock of this area. The sequence consists of metasediments of the Corella Formation, Birds Well Granite, Mungo Granite and the Plum Mountain Gneiss.

- **Corella Formation (PLkc)**

The Corella Formation consists of calcareous siltstone, limestone, calcareous scapolitic granofels, quartzite, amphibolite, shale, feldspathic granofels, meta-arkose, feldspar porphyry (PLKca) and it also comprises of schistose quartzite (PLkq).

The basement rocks have been structurally deformed and are considered to have controlled the fluid flow for some the ore deposits developed surrounding the Mt.Isa Inlier complex. The formation consist of largely marbles, calc silicate rocks and

meta-siltstone to the north of Tick Hill region, and the rocks have experienced complex deformation history resulting in the development of wide spread veining and breccias. Broadly strata-bound breccia bodies are common in the Corella Formation which reflects the strong rheological process operative during its formation (Marshall & Oliver, 2008). The Corella formation is host to uranium, gold, copper formed as skarn deposits (Marshall & Oliver , 2008).

- **Birds Well Granite (PLgwz)**

This unit is located in the eastern part of Kalkadoon-Leichardt Belt and western part of Mary Kathleen Zone. This instrusive rock is part of the granitic Wonga Suite consisting of a collection of granites and volcanic rocks within Kalkadoon-Leichhardt Belt and Eastern Fold Belt (Blake, 1987) emplaced during the extensional event between 1760 Ma and 1720 Ma. The granite forms an elongated dike-pluton which is weakly foliated to gneissic and extensively recrystallised. The Bird Well Granite is pink, medium to coarse-gained, porphyritic granite, leucogranite and augen gneiss, with aplite and pegmatites present as thin veins. It is composed of K-feldspar, quartz, plagioclase, biotite with local presence of hornblende.

- **Plum Mountain Gneiss (PLap)**

This unit consists of quartzofeldspathic gneiss and augen gneiss, porphyritic granite, minor calc-silicate rocks, meta-arenite, mica schist, amphibolite; aplite and pegmatite veins. It is intruded by granites of the Wonga and Kalkadoon Batholiths (Blake *et.al.*, 1992).

- **Saint Mungo Granite (PLgwn)**

This granite intruded the Corella Formation around 1700 Ma and has experienced regional metamorphism to upper amphibolite facies (Blake, 1987). This unit consists of porphyritic hornblende-biotite granite; minor porphyritic biotite granite with medium to coarse grain aplite veins and microcline phenocrysts up to 3cm across. The mineralogy is quartz, microcline, plagioclase, biotite, and hornblende, accessory minerals such as apatite, fluorite, calcite, chlorite, scapolite, titanite and allanite. The internal structure is weakly foliated to gneissic and it forms elongated to circular bodies of no more than 30 square kilometers (GA, internal report on Burstall, Paleozoic Granite in Mount Isa Inlier). It has potential for low tonnage Au-Cu

deposit. Unaltered Saint Mungo Granite is the closest granite related to the Au-dominated deposit in Tick Hill.

2.3.2.2 Cambrian Deposits

- **Inca Shale (Emi)**

The Inca Formation is part of the Georgina Basin, which extends from the north of Australia to the centre of this continent and covers approximately 325,000 square kilometers. The Inca limestone member consists of fetid, cherty dolomitic limestone beds with some shale. The Inca shale member consists of thinly laminated siliceous shale, carbonate nodule, siltstone, and thin-bedded chert. The radiolaria fossil found in this formation indicates a Cambrian age (Won and Below, 1999).

- **Emt (Thorntonia Limestone)**

This unit is also part of Georgina Basin, and is composed of grey crystalline limestone, black and grey convoluted chert, chert nodules, and silicified beds.

The Thorntonia Limestone, a platformal carbonate unit, lies disconformably upon the Red Heart Dolostone. This formation, which seldom exceeds 100 m in thickness, is sheet-like and widespread. It consists of dark grey dolomudstone and dolowackestone with occasional packstone and grainstone intervals. Fragmentary invertebrate bioclasts are abundant. Chert nodules and other textural indications of evaporite dissolution are present at well-defined levels. Gamma-log data shows an upward decline, suggesting that it is an upward-shallowing unit and that siliciclastic material decreases upward. It was deposited in a shallow, peritidal to subtidal setting during a major transgression that spanned the Ordian and early Templetonian (early Middle Cambrian, 509–506 Ma) (Ambrose *et.al.*, 2001).

- **O'Hara Shale (Euh)**

The late Cambrian O'Hara Shale is approximately 60 m thick, consists of siltstone, minor chert, sandstone, laminated to thin bedded and commonly iron stained, and is capped by duricrust or lateritic gravel. Stratigraphically, the formation unconformably overlies Pomegranate Limestone and is underlain by Devoncourt Limestone and Roaring Siltstone.

- **Beetle Creek Formation (Eme)**

The middle Cambrian Beetle Creek Formation is part of Georgina Basin and is composed of siliceous siltstone, shale, chert, sandstone, phosphatic siltstone, phosphorite, silicified coquinite, basal conglomerate and contains trilobite fossil. This formation is host for Phosphate Hill Mine in Dueshess Area which is the largest Phosphate mining across Australia (Golden Cross Operation Pty. Ltd, Phosphate Market Update). Stratigraphically, this formation underlies Inca Formation but there is no data for the stratigraphic relation (unconformity or conformity). It has a maximum thickness is 60 meters.

- **Mount Birnie beds (Elb)**

The Mount Birnie beds are composed of massive ferruginous sandstone, cross-bedded sandstone, conglomerate, red and green shale, mudstone, dolomite. Due to deep weathering, much of this formation is capped by ferricrete and occurs underlying mesa landforms. It is overlain by Corella Formation and underlain by Beetle Creek Formation. The mesa landforms are not restricted to these beds but also form on other units such as the Proterozoic and Mesozoic rocks and within the basinal sedimentary assemblages present within the Eromanga and Georgina basins (Anand *et.al.*, 2002).

- **Devoncourt Limestone (Emd)**

This Middle Cambrian formation consists of limestone which is hard to flaggy, medium-bedded to laminated and essentially detrital. Trilobite fossils are locally present. Some of them are pure limestone, calcilutite, bituminous limestone and marl. The formation is overlying Inca Formation (unconformity) and underlying O'Hara Shale.

- **Roaring Siltstone (Emr)**

The middle Cambrian Roaring Siltstone consists of finely laminated siltstone, silicieous shale, and fine-grained sandstone with some parts being minor chert and silicified shale. It is upper laying Mount Birnie Beds and Thorntonia Limestone. The maximum thickness is about 75 meters.

2.3.2.3 Mesozoic Deposit

- **M (M-6854);**

It comprises of conglomerate, siltstone, mudstone, sandstone, grit.

2.3.2.4 Tertiary Deposits

Tertiary deposits in the Tick Hill region consist mainly of weathering products such as laterite and its associated weathering profile materials such as saprolite. Lateritic rubble (gravel) is also present as unconsolidated surface sediment.

2.3.2.5 Recent Deposit (Cainozoic Deposit, unconsolidated sediments)

- **Recent deposit (Cz);**

The recent deposits consist of unconsolidated to consolidated and cemented surficial sediments of colluvium and alluvium. The sediments are siltstone and sandstone and their weathering products.

2.3.3 Tectonic Setting of the Block G Tick Hill and Mineral Deposit Information

The structural deformation and regional metamorphism activity in the Tick Hill region occurred between 1610 – 1510Ma. The deformation activity led to the creation of several north-south trending structural elements; The Kalkadoon-Leichhardt Belt, Leichhardt River Fault, Eastern Fold Belt, and Lawn Hill Platform (Eriksson *et al.,* (1991). The region is folded and faulted with a dominant north-south trending anticline. (Blake, 1987).

The basement of Mt.Isa consists of Paleoproterozoic metamorphic rocks that were deformed and metamorphosed in Barramundi Orogeny in the interval 1880-1870 Ma (Oliver *et al*, 2008). This event was followed by the deposition of volcanic and sedimentary rocks which are divided into three sequences. The first sequence (1870-1850Ma) is dominated by felsic volcanics and comagnetic granites and formed a basement high separating two basins. The second sequence composed of Eastern and Western Succession (1790-1720Ma) and refers to all of the rocks exposed and under shallow cover to the east of the central Kalkadoon-Leichhardt Block, while the third sequence was deposited during 1680-1625Ma (Oliver *et.al.*, 2008).

Copper, lead and zinc deposits were discovered in 1923 in Mount Isa block By 1994, Mount Isa became the largest copper producer worldwide. Chalcopyrite is

the main mineral in the ore deposit and it occurs together with pyrite, and the width of ore body is up to 700 meters.

Chapter 3

Research Methodology

This chapter describes the different remotely sensed data used the processing methods employed to construct mineral maps, the results of which are reported in chapters 4 and 5. The chapter also describes other instrument techniques used for validation such as XRD and ASD.

3.1 Mapping data

Several remotely sensed data sets (spaceborne, airborne and proximal) were used in the making of mineral maps of the Tick Hill region. Further, other techniques to validate remotely sensed data were also used. The sensors and other validation techniques used were:

1. Multispectral satellite ASTER sensor data.
2. A 30 m pixel Digital Elevation Model (DEM) extracted from ASTER.
3. Airborne Hyperspectral HyMap sensor data.
4. Proximal sensor data from the ASD of seventy-five field samples.
5. XRD for clay mineral analysis.
6. Digital published geology Tick Hill scale 1:250,000.
7. Digital published surface regolith and terrain scale 1:250,000.

For some of the above data sets, the characteristics of the sensors, the preprocessing and image processing techniques employed are described below.

3.2 ASTER Multispectral Image and Processing

The Advance Spaceborne Thermal Emission and Reflection Radiometer (ASTER) is the joint science project between METI of Japan and NASA, with the sensor being part of the TERRA satellite, which is NASA's Earth Observed system satellite. Besides the ASTER sensor, the satellite has other sensors - MODIS, CERES, MOPIT and MISR. The maintainance of sensor and correction of the data received from it are conducted in Japan and in the USA. ASTER records reflected and emitted solar radiation in 14 wavelength ranges or spectral bands. The reflected radiation (VNIR) is recorded in three bands with a 15 m spatial resolution. The shortwave infrared (SWIR) reflected wavelength is recorded in 6 bands with a spatial

resolution of 30 m and the thermal infrared (TIR) radiation is recorded in 5 bands with a spatial resolution of 90 m. The band numbers, widths and spatial resolutions are listed in table 3.1. Each ASTER scene covers an area of 60 x 60 km and can be extended with the total cross-talk view up to 232 km (Fujisada in Rowan, Mars, et al., 2004).

Table 3.1 ASTER bands wavelength (Iwasaki and Fujisada, 2005)

Band number	Wavelength (micrometer)	Wavelength name	Resolution (m)
Band 1	0.25 to 0.60	visible green	15
Band 2	0.63 to 0.69	visible red	15
Band 3	0.76 to 0.86	near infra red	15
Band 4	1.60 to 1.70	shortwave infra red	30
Band 5	2.145 to 2.185	shortwave infra red	30
Band 6	2.185 to 2.235	shortwave infra red	30
Band 7	2.235 to 2.295	shortwave infra red	30
Band 8	2.295 to 2.365	shortwave infra red	30
Band 9	2.360 to 2.430	shortwave infra red	30
Band 10	8.125 to 8.475	thermal infra red	90
Band 11	8.475 to 8.825	thermal infra red	90
Band 12	8.925 to 9.275	thermal infra red	90
Band 13	10.25 to 10.95	thermal infra red	90
Band 14	10.95 to 11.65	thermal infra red	90

3.2.1 ASTER Data

The ASTER datasets used for this project were level 1B, which have had radiometric and geometric calibration done on them. Other data sets such as Level 1A ASTER data, requires further processing for correction by using software such as Real ASTER User System (RASTUS) written by Dr.Neil Pendock, University of Witwatersrand, Johanesburg, South Africa (Gozzard, 2006).

3.2.2 Image Processing

Some pre-processing of ASTER level 1B is required in order to obtain 14 single bands. The pre-processing employed also removes the atmospheric effects as much as possible and registers the imagery to an accurate topographic base. The pre-processing steps used followed those documented in the ASTER Mineral Index

Processing Manual (Kalinowski and Oliver, 2004) and Image Processing of ASTER Multispectral Data, (Gozzard, 2006).

Crosstalk Correction

Crosstalk is an effect in ASTER imagery caused by a leakage of photons from the band 4 detector element to other detector elements in the SWIR subsystem producing an increase in photons for these other detector elements (Earth Remote Sensing Data Analysis Centre, 2005). The cross-detector leakage is most pronounced in band 5 and 9, but it affects all SWIR bands. This can result in the creation of false "anomalies" in processed ASTER imagery (Gozzard, 2006). Crosstalk correction was done via the free software ERSDAC Crosstalk 3 provided by http://www.grds.aster.ersdac.or.jp/gds_www2002/service_e/u.tools_e/set_u.tool_ecross.html.

Calibration to radiance at sensor

The level 1B ASTER data has radiometrically calibrated and geometrically co-registered data for all the channels acquired previously by applying the radiometric calibration and geometric correction coefficients to the Level 1A data. Radiance is defined as the total emitted light which is passed through the horizontal surface in unit area per unit time (watts/m^2/stereoradian/micrometer), recorded at a sensor. A conversion from radiance to reflectance is necessary to eliminate effects of scattering and absorption and this conversion is done on the Level 1B data. Reflectance represents the ratio of exitace to irradiance, and thus provides a standardized measure which is directly comparable between images (Drury, 2001). The procedure followed to convert DN values to radiance and then radiance to reflectance, was that documented by Smith AMS (http://www.cnrhome.uidaho.edu/default.aspx?pid=85984).

Resampling

Resampling of the ASTER data is required because the band data are acquired at three different spatial resolutions (table 3.1). Standardizing spatial resolutions for all bands is essential for creating RGB band combination images of different wavelength regions. Therefore, VNIR and SWIR ASTER bands were integrated by resampling into 30 meter resolution, rather than the 15 m resolution for VNIR. The 90m resolution of TIR images is processed separately because it has

different wavelength region. The re-sampling was conducted in ENVI Layer Stacking process (ENVI Online Tutorial).

Mosaicing the image

The Block G Tick Hill region is covered by two scenes (or granules) of ASTER image which cover 60km x 60km each with some overlap. Cloud masking was not required because the chosen scenes were clear of clouds. It was necessary to make a seamless image from the two scenes so image processing for making mineral maps could be done with one combined scene. The different times at which the scenes were acquired influenced the image quality due to the different solar illumination conditions. Further, the quantity of seamless mosaicing is influenced by data acquisition times and variability in atmospheric water vapors especially in the bands whose wavelengths are greater than 2.5 µm, particularly band 9.

During processing for mosaicing, it is also important to choose the correct color balancing on the overlapped images. The Map Based Mosaic tool in ENVI provides the menu for mosaic parameter and adjusts the color from the overlapping regions by choosing the base image for the color balancing and the other images are adjusted to the base images color. Offset and gains are calculated from the fixed image and applied to the other image to achieve the same statistical range for the data (Gozzard, 2006).

The fundamental digital image processing methods such as histogram parameters, manipulating digital numbers (DN), enhancing and contrasting the image are included in this processing.

3.2.3 ASTER Image Interpretation Method

The common image construction and interpretation methods are published in several scientific journals. The three main image processing techniques and methods used to make mineral maps are described below.

RGB Combination

The RGB model is based on assigning single bands or band ratio's to the primary colours (red, green, blue) to enhance specific surface spectral characteristics for easy visual interpretation. Several factors such as screening and selecting the appropriate bands which including the atmospheric effects, knowledge of ground material spectra and the object of interests such as vegetation, rock outcrops,

morphology, plain terrain, man made buildings need to be considered before should be considered before trying to select bands for RGB combination (Gupta, 2003). The RGB combination for each multispectral bands are different. For the ASTER sensor, workers have developed several RGB combinations which highlight geological features. Abrams and Hook (2002), Rowan and Mars (2003), Hewson *et al*. (2005), Bierwith (2002) and Ninomiya (2002) all advanced ASTER RGB combinations for making individual or mineral group maps. Table 3.2 lists a compilation of RGB combinations used for the ASTER sensor (taken from Gozzard 2004).

Table 3.2 : Compiled common RGB combinations for ASTER sensor to highlight surface mineral groups (Gozzard, 2004)

No	Feature	Red	Green	Blue	Reference
1	Vegetation and visible band	3,3/2/NDVI	2	1	-
2	AlOH minerals-advanced argilic alteration	5/6(phengite)	7/6 (muscovite)	7/5 (kaolinite)	Hewson,*et al* 2001, 2004
3	Clay,amphibole, host rock	(5x7)/6 (clay)	6/8 (amphibole)	4/5laterite	Bierwith 2002
4	Gossan, alteration, host rock	4/2 gossan	4/5 (alteration)	5/6 (host rock)	Volesky *et al* 2003
5	Gossan, alteration, host rock	6(gossan)	2 (alteration)	1(host rock)	-
6	Decorrelation stretch	13	12	10	Bierwith 2002
7	Silica, carbonate, basic degree index	10/12 silica	13/14 (carbonates)	12/13 basic rocks	Bierwith 2002
8	Silica, carbonate	(11x11)/(10x12)	13/14	12/13	Ninomiya 2002
9	Silica	11/10	11/12	13/10	Hewson *et al* 2001; 2004
10	Discrimination for mapping	4/1	3/1	12/14	-
11	Discrimination in sulfide-rich areas	12	5	3	-
12	Discrimination	4/7	4/1	(2/3)x(4/3)	-
13	Discrimination	4/7	4/3	2/1	Abrams&Hook 1995
14	Silica Fe3+	14/12	(1/2)+(5/3)	MNF band 1	Rowan & Mars 2003
15	Enhance structural features	7	4	2	Rowan & Mars 2003
16	True Color	3	2	1	Rowan & Mars 2003
17	Regolith and lithology	6	4	3	Rowan & Mars 2003
18	Silicate minerals mapping	12	13	10	Rowan & Mars 2003

The RGB combinations 3:2:1 give the true color of image, RGB 6:4:3 shows the regolith landform units and highlight the lithology and geology outcrops and

RGB 12;13;10, from the TIR image is capable to map the silicate content minerals. Those are explained detail in the next chapter.

Band Ratio

Band ratio is simple method of dividing the DN (digital number) of each pixel in one band by the DN for equivalent pixels in another band. The bands chosen should have a contrast in their absorption for the specific mineral(s) or surface material under consideration. The process results in reducing topographic features of the image (Drury, 2001). Band ratio have been successfully used to map lithological variations based on mineral composition (Hewson *et al.* 2001; Watts et al., 2005; van Ruitenbeek, *et al*. 2006; Gad and Kusky 2007). The main band ratios used to identify specific minerals are listed in table 3.2.

Relative Band Depth (RBD)

This method is an extension of the band ratio method, where simple addition and division is conducted on several bands to enhance a specific spectral feature of interest. Relative Band Depth (RBD) method was designed to enhance the presence of an absorption feature diagnostic to a mineral by taking into account sum of two or more bands from absorption shoulders and dividing by the absorption band minimum (Crowley *et al.*, 1989, figure 3.1). Similar to the ratio images, images produced from RBD, minimize reflectance related to topographic and albedo effects. A simple RBD index could take the form of (b1+b2)/b3 so a diagnostic absorption feature at specific wavelength is detected and enhanced. To use RBD method, it is important to know the specific mineral(s) spectral characteristics and the ASTER (or another sensors) bands that correspond to the spectral feature. Accordingly, the band combination can be designed to choose the diagnostic absorption feature. However, for the ASTER sensor (unlike the hyperspectral sensors), the band widths are broad and therefore the diagnostic features are not strictly related to individual mineral absorption features, but rather the dominant ionic groups of minerals (for example, Al-OH, Mg-OH). Details about RBD processing for individual minerals and mineral groups are described in chapter 4. Figure 3.2 shows the flow chart of the step by step procedure followed to process ASTER data.

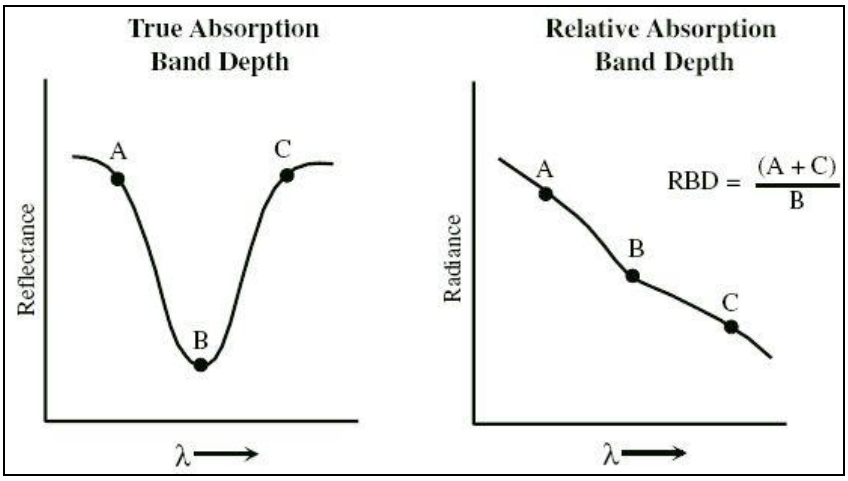

Figure 3.1. The Relative Band Depth (RBD) schematic concept
(from Mars and Rowan, 2006, after Crowley *et al*, 1989).

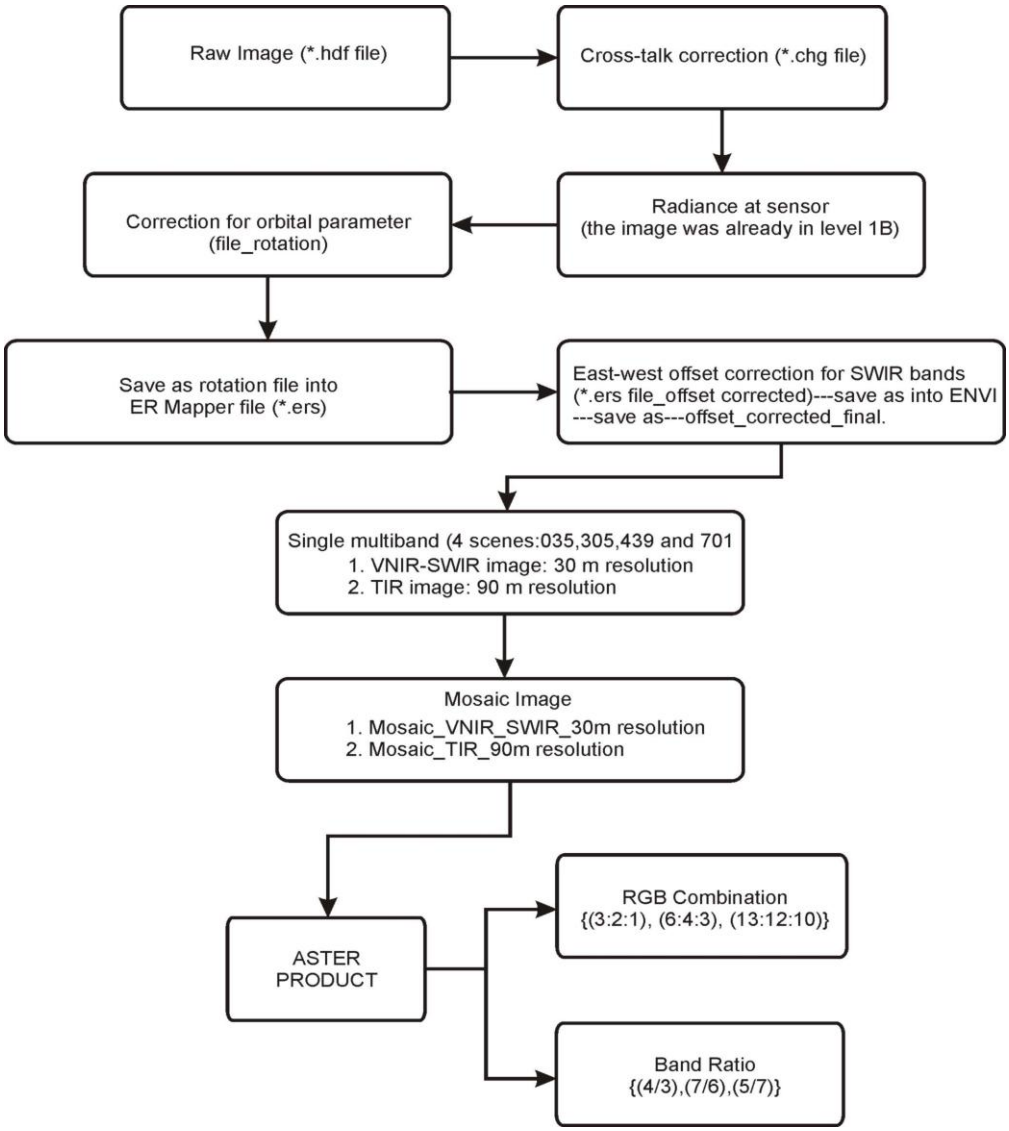

Figure 3.2: ASTER Image Interpretation flow chart (Oliver & van der Wielen, 2006;Kalinowski, 2004)

3.3 HyMap Hyperspectral Image and Processing

Hyperspectral sensing is often referred to as imaging spectrometry. Hyperspectral sensors detect energy in multiple, very narrow, contiguous bands and have over 100 bands thereby providing a continuous spectrum of the surface. Availability of continuous spectrum enables a more accurate interpretation of the surface mineralogy as compared to multisepectral sensors.

The analysis and interpretation of hyperspectral data are extensively based on the use of spectral libraries covering a wide range of inorganic and organic natural materials and comparison of data between different areas and sensor systems.

3.3.1 HyMap data specifications

The hyperspectral data for the project was collected by the HyMap sensor. The HyMap™ sensor (Hyperspectral Mapper) is a hyperspectral sensor designed and manufactured by Integrated Spectronics Proprietary Limited (ISPL) and operated by HyVista Corporation based in Sydney Australia. The HyMap sensor has128 bands in VNIR-SWIR spectra coverage (0.45 – 2.5 micrometer) with bandwidths between 15 – 20 nm. The spatial resolution of HyMap is approximately 4.5 meters. The spatial configuration of the HyMap sensor includes (www.hyvista.com):

- Whiskbroom imaging with 512 pixel swath and 61.3 degrees swath width;
- 450-2500 nm spectral range with 126 spectral bands in three wavelength regions (VNIR, SWIR-1 and SWIR-2), with a spectral bandwidth of 10-20 nm;
- Spatial resolution of 3-10 m depending on flying height; and
- On-board radiometric calibration.

3.3.2 HyMap Pre-Processing

Geometric Correction

Most of the preprocessing of the HyMap data was conducted by the sensor data provider (HyVista Corp) using their proprietary algorithms and software. The preprocessing done by HyVista Corp included conversion of raw radiance to at-sensor radiance, geometric, radiometric and spectral calibration. Geometric

calibration is related with the aircraft instability due to terrain roughness while acquiring the data.

Atmospheric Correction

HyMap atmospheric correction was done by Spectral Sensing Technology Group in CSIRO using HyCorr. HyCorr is the software developed by CSIRO Exploration and Mining Divison Mineral Mapping Technology for HyMap atmospheric correction. It is modified from ATCOR (Atmospheric Removal) which uses the spectral feature of water vapor absorption at band 0.94 micrometer and 1.14 micrometer to form the atmosphere at the time of light. HyCorr uses three band ratioing technique which covers water absorption features to calculate the parameter of atmospheric gases (O_2, O_3, H_2O, CH_4, CO, CO_2, N_2O). These gases often create noise in HyMap signals due to an aerosol scattering (Berk *et al*, 1989 in Lau, 2004).

Spectral Smoothing and Noise Reducing

EFFORT (Empirical Flat Field Optimized Reflectance Transformation) is the hyperspectral processing method used to remove residual products of hyperspectral data collection such as noise and atmospheric effects. This calibration has a function for improving the quality of the spectra and providing the best reflectance from the image (Broadman, 1988).

Technically, the EFFORT method finds a featureless spectra ("flat spectra") in the HyMap scene, then calculates the least squares fit between this featureless spectral and a low order polynomial that is derived from the spectra. It then uses a gain factor to remove both the systematic and coherent noise from every spectrum.

In addition, the adjustment for noise is essential to reduce the unused signal measured by the sensor. Signal-to-noise ratio plays the important role in sensor performance. The high ratio of S/N for a sensor is better to distinguish minerals. Minimum Noise Fraction (MNF) transform is one method to reduce the noise in a hyperspectral image (Green *et. al*, 1988). This is a modification of Principal component Analysis (PCA). The end result is that the noise is separated from the data thereby improving the spectral processing. The process of MNF transformations are detailed in appendix and was conducted using the MNF tool provided in ENVI.

3.3.3 Hyperspectral Mineral Mapping Methods

There are several methods available to process hyperspectral data (van de Meer, 2001). The basics of the common methods are described below and the relevant ones to mineral mapping are discussed in detail.

Spectral Angle Mapper (SAM)

This method assumes that the data have been reduced to apparent reflectance (true reflectance multiplied by some unknown gain factor, controlled by topography and shadows). The method is based on the assumption that the reflectance spectra can be considered as a vector in multidimensional space. For explanation purposes, only two band scatter plots are considered rather than all bands. In the scatter plot of the two bands, and the pixel spectra (unknown) and the target spectra (known) will plot as points. Vector drawn to both the points will then provide an angle between the two and the value of this angle is linked to the similarity between the spectra. Tolerance levels can be set for the angle and if the angle between the pixel and known is smaller than the tolerance level, the two features are considered to match. The algorithm considers all the bands in the image rather than only two.

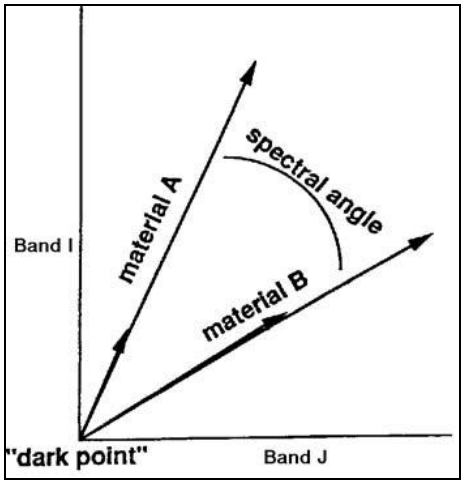

Figure 3.3: Spectral Angle Mapper principle (ENVI Manual Tutorial)

Because SAM uses only the direction of the spectra and not the length of spectra, SAM is insensitive to the unknown gain factor. All possible illuminations are treated equally. Poorly illuminated pixels fall closer to the origin of the scatter plot. The color of a material is defined by the direction of its unit vector. The angle between the vectors is the same, regardless of the length. The length of the vectors relates only to how fully the pixel is illuminated. The SAM algorithm generalizes this geometric interpretation to n-D space.

Spectral Feature Fitting (SFF)

The algorithm used is based on matching the absorption feature in an image to reference mineral spectra (Clark *et al* 1990; Clark, *et al.* 1991; Crowley and Swayze, 1995). The continuum removed spectra from images are used to compare the width and absorption wavelength of the spectra (shape) from a chosen spectral library such as USGS spectral library or spectra from a field sample (figure 3.4). Another option is to compare only a specific wavelength between the image and known spectra, especially when a specific absorption feature is being targeted and its wavelength range known. A least-squares fit is calculated on band by band between each reference end member and unknown pixel spectra. The total RMS (root mean square) error provides a guide to the goodness of fit of the two spectra.

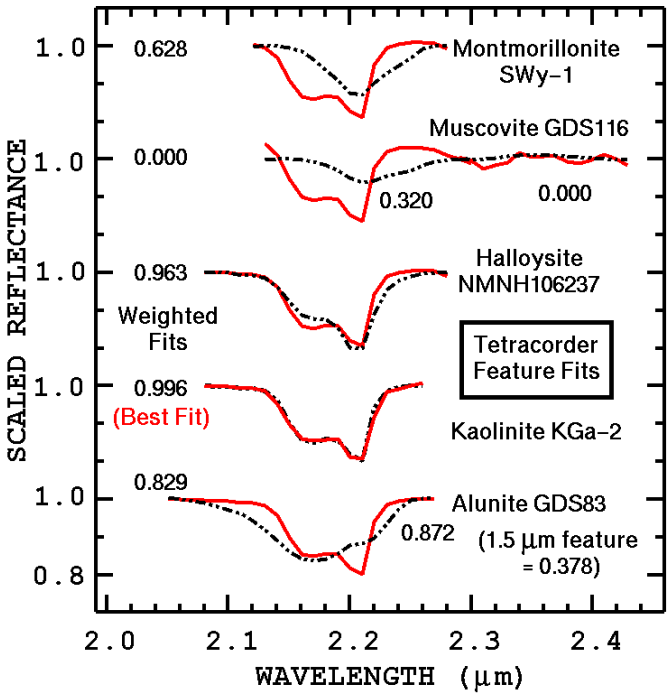

Figure 3.4: The principle of spectral feature fitting method applied to clay minerals. Laboratory mineral spectra (red) are fitted to the pixel absorption feature (black) and shows that kaolinite has the best fit compared to others (Clark *et al.*, 2003).

Spectral Un-mixing

The method assumes that the reflectance spectra from each pixel are a product of linear combinations of the spectra of all its endmember inside that pixel. Therefore, if all the endmembers in a scene are known, then their contribution to

each pixel can be calculated based on the pixel's spectrum. The method achieves this by solving a set of *n* linear equations for each pixel, where *n* is the number of bands in the image. The results of the calculation are displayed as one abundance image for each endmember with the value in the pixels indicating the contribution of the endmember to that pixel. For example, in an abundance image for kaolinite, a pixel value of 0.5 would indicate 50% of the pixel contains kaolinite. Van der Meer (2001) stated that this method requires the pure spectra endmembers to minimize the noise or error in model.

Relative Band Depth and Associated Filters (masking)

The identification of a mineral or mineral group from wavelengths of diagnostic absorption features is still one of the most powerful methods, and hyperspectral data provides sufficient spectral resolution to achieve diagnostic absorption feature separation between minerals that have spectral absorption features in the detected wavelength. To enhance the diagnostic features, band depth absorption is a powerful tool to determine the mineral surface composition. Van der Meer (2001) argued that even though the method is considered "conventional", it provides straight forward mineral identification which is close to field sample spectra and mineral samples from spectral library. The interpreter has greater control and is able to choose and manipulate the spectral features from the image, and is also able to match the feature with the spectra library absorption feature of targeted minerals. The method is also better suited to minerals that vary in composition as the wavelengths of their main absorption feature change with composition (e.g white mica, chlorite). This method will be mainly used to map the minerals in this project.

The method works by measuring the depth, wavelength and sometimes the geometries (symmetry) of the diagnostic absorption features of minerals and is same as the relative band depth (RBD) described for the ASTER data processing (Crowley et al., 1989). This is a simple method, robust and easily reproducible without any additional or proprietary software needs. The method also assumes that the band depth is proportional to the mineral abundance and therefore spectral indices created from band combinations represent mineral abundance maps. Absence of a diagnostic absorption feature is interpreted as absence of mineral in the pixel. An example of the RBD method used with HyMap is shown for kaolinite where different spectral absorption features can be enhanced via band combinations (figure 3.5). Because

kaolinite has a symmetric Al-OH absorption feature, the two absorption depths can be used to distinguish kaolinite and the resulting values calculated for each pixel of the image are assumed as abundance of the mineral based on RBD. Most of the mineral maps produced in chapter 4 are based on the RBD method.

Some of the minerals diagnostic absorption features either overlap or interfere with each other and so does vegetation absorption. For example, organic-compound features (depending on organic structure) have absorption features centered range 2100-2300 nm, which can interfere with Al-OH absorption of kaolinite and micas. To minimize these spectral absorption overlap effects, a series of digital masks were created. To create a mask, first the RBD for the specific material or mineral diagnostic absorption is made and then a mask is created using a threshold value. The threshold value is estimated by viewing the spectrum for particular pixels. The creation of the mask results in true or false (0 or 1) for pixels whose DN values fall below or above the chosen threshold.

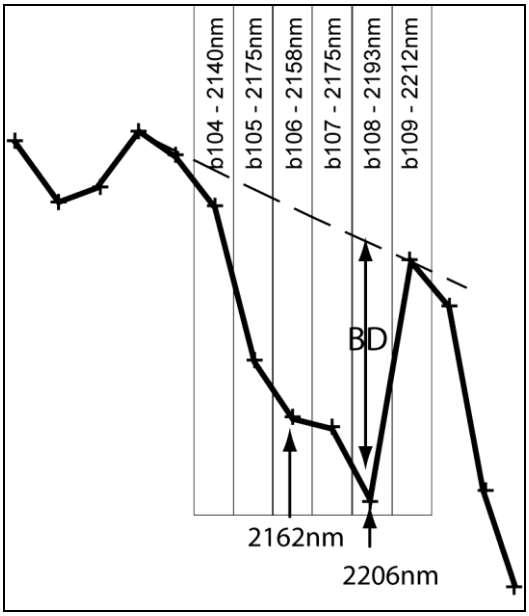

Figure 3.5: A typical HyMap reflectance spectra of kaolinite from a pixel with HyMap band numbers and wavelengths. The band center positions are shown as +. The dashed line represents the continuum. BD is the band depth. The two main absorption depths of kaolinite are labeled and relative band depth combinations enhance these two spectral features.

Most mineral maps created had composite mask applied to them. The composite mask consists of green vegetation, dry vegetation and albedo effects. For example, to mask out green vegetation contribution to the pixel spectra, the green vegetation contents are measured via the band ratio b26/b18, and a mask is created

with a threshold value of less than 2 (estimated by viewing spectra for pixels of known green vegetation). Such masks created for dry vegetation and albedo effects are summed to make the composite mask (figure 3.6). An example of the process followed to create the kaolinite mineral map is also shown in figure 3.6. Mars and Rowan (2006) conducted a similar process of RBD followed by masking on particular threshold values for ASTER scenes, and referred to the process as logical operators.

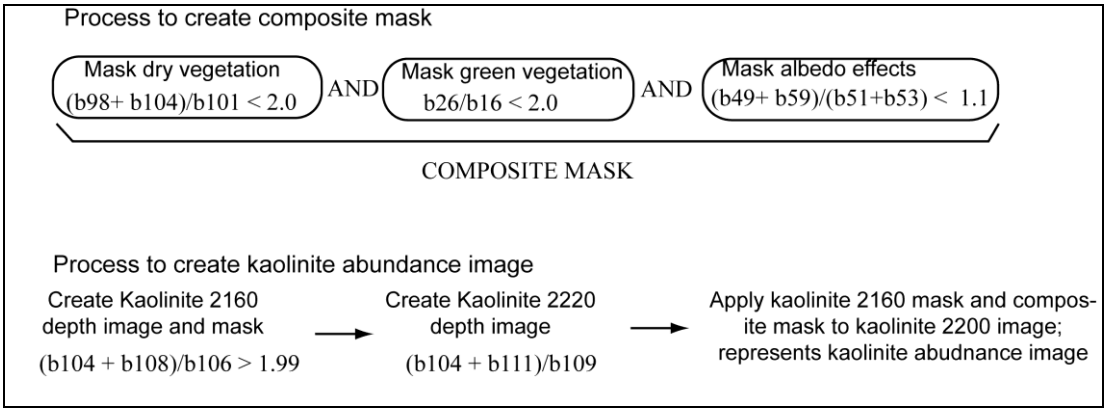

Figure 3.6. Process involved in creating the composite mask which is applied to most spectral indices chosen for most mineral maps. Example shown is of the process followed to create kaolinite abundance image.

Spectral Indices (Polynomial fitting)

Spectral Indices is method that is focused on extracting absorption features by curve matching (MMTG software, CSIRO Exploration and Mining), and therefore falls in between spectral feature fitting method and curve matching. The basic concept is to fit a polynomial to an identified absorption feature or features within a specific wavelength, and use the depth and geometry information from the fitted polynomial to identify the mineral and subsequently create an abundance map. Currently, spectral indices procedure is conducted via proprietary software MMTG-A List produced by CSIRO Spectral Group.

Example of using spectral indices via polynomial fitting is provided by Cudahy *et al.*, (2008) and their example is explained here. Figure 3.7 shows a HyMap spectrum of white mica with the main absorption at 2200 nm and 4^{th} order polynomial curve has been fitted to the peak between specified wavelength ranges. The depth of the curve normalized to the continuum between its endpoints is then

assumed to be linearly proportional to the abundance of white mica. The advantage of fitting curves is that subtle changes in mineral chemistry can also be tracked by finding the maximum absorption position of the fitted curve. To make a map of white mica, however, contribution to the Al-OH peak need to be minimized from two contributing minerals – kaolin and Al-smectite. This is achieved via the masking procedure outlined above. Al-clay abundance is masked by using a RBD for kaolinite 2162 nm peak below a threshold value.

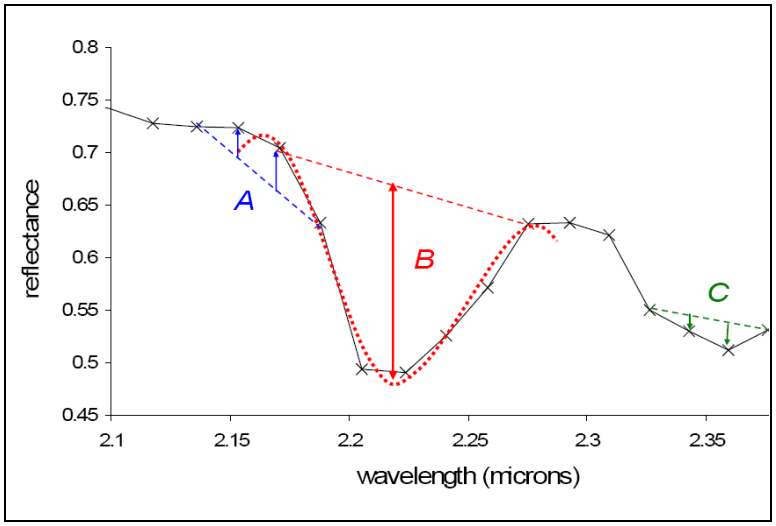

Figure 3.7: The schematic of extracting the mineral abundances from hyperspectral imagery bands (Cudahy *et al*., 2008). The main Al-OH peak is fitted with a curve (red) and the depth of curve assumed to be proportional to the abundance of Al-OH minerals. Red, blue and green dash lines are the continuum removed features while the arrows from those colors represent the absorption reflectance values.

3.4 ASD (Analytical Spectra Device) and Field Validation

Field sample spectra measurements was conducted first by CSIRO team for Queensland mineral project using ASD fieldspec Pro I and selected group were measured in duplicate by the author. The ASD has the spectral range between 350 – 2500 nm. Approximately 250 samples are taken from three different earth materials; weathered rocks, fresh rocks and soil. The samples then were labeled by "F" for freshrock, "W" for weathered and "S" for soil, to simplify the identification. The detail description of minerals based on spectra pattern absorption is listed in appendix X. The ASD collected spectra were viewed and analyzed via the The Spectral Geologist (TSG) (http://www.thespectralgeologist.com/).

The ASD acquired spectra were used to validate the ASTER and HyMap mineral maps. The ASD spectra were first resampled to the respective sensors band

widths and then the same RBD used to make individual mineral maps with ASTER and HyMap were employed on the resampled ASD spectra. The measured values from ASD RBD were then plotted against band depth values estimated from ASTER and HyMap spectra for pixels representing corresponding field sample.

3.5 X-Ray Diffraction Analysis

X-ray powder diffraction (XRD) is arguably the best method to identify the structure of minerals as well as other crystalline materials (Dulong and Jackson, 1997) and is possibly the best method to identify the fine grained clay minerals. XRD identification of a mineral (if present in > 1-2%) is therefore a good validation tool for minerals identified via spectral characteristics. For the current research, XRD was used to identify clay minerals, carbonates and silica related minerals. The data was used to validate the presence of minerals as indicated by ASD, ASTER and HyMap processing.

Bulk samples were crushed and ground to a fine powder in mortar and pestle. Random powder mounts were made and the samples were X-rayed with a Phillips PW1050 Diffractometer using CuK α radiation from 2 and 65° (2Θ angle) with a 0.02° step size over 30 minutes. Mineral identification was done with search-match software (X-Plot) and all major peaks were accounted for and labelled.

Five samples were analysed as clay separates to properly identify clay minerals. The samples were ultrasonically dispersed in de-ionized water and < 2 μm fraction was separated and passed through a porous ceramic plate so the clay particles were oriented along their 001 planes. Samples were X-rayed as air dried sate (AD), Mg saturated and glycolated and K-saturated and heated to 300 ^{0}C. These treatments are necessary to correctly identify the clay minerals (Moore and Reynold, 1989).

Chapter 4
ASTER and HyMap Mineral Maps - Comparative Approaches

In this chapter, the results of mineral abundance maps from the Tick Hill area produced from multispectral ASTER data and hyperspectral HyMap data are shown and their validity discussed. In the next chapter, the mineral maps produced are used to map regolith-landforms and interpret associated processes. The hyperspectral algorithms used to produce the mineral maps were Ratio Band Depth (RBD), SFF and spectral indices using MMTG A-List software (Mason, 2002) combined with associated filters (masking) (the summary of the techniques is described in chapter 3). Other hyperspectral methods - spectral un-mixing, MTMF, and SAM – were also applied to map the minerals, but the results of these methods when validated to ground spectral data were found to either be of poor validity or not as effective in comparison with RBD, spectral indices and SFF methods. Therefore, the results from spectral un-mixing, MTMF and SAM methods are not shown or discussed further, and only RBD, SFF and spectral indices methods are described. Also, as RBD method is the simplest and easily reproducible irrespective of software requirements (is not bound to special software such as spectral indices), it is the method of choice, and spectral indices are only used where RBD method results were not effective due to absorption overlaps between minerals (explained for individual minerals below).

In addition, the step by step procedures of the methods used such as algorithms, basic formulas, and masking are documented for individual minerals. The effectiveness of minerals maps produced is assessed by comparison of the mineral map products with the ground sample spectra (ASD) and mineralogy determination by XRD.

The minerals selected to be mapped via the two sensors were based on two criteria; they should have absorption features in the VNIR-SWIR range and they had to be detected in samples via XRD. The minerals detected with XRD and those which are identifiable via spectral resolution of ASTER and HyMap are kaolinite, smectite, iron oxides and hydroxides (hematite and goethite), illite/white mica, Mg-OH minerals (hornblende, chlorite), carbonates and opal silica. Because the spectral resolution of ASTER and HyMap are different, the measure of validity of the mineral map is arranged and compared based on the main compositional feature (such as Al-OH, Mg-OH)

causing absorption. For example, kaolinite is mapped via HyMap, but via ASTER, only Al-OH bearing minerals can be mapped which includes micas and smectites in addition to kaolinite. The mineral maps produced from ASTER and HyMap enable the comparison of the efficiency of the two sensors.

The validation of the HyMap and ASTER sensor produced mineral maps was done by resampling the ASD field spectra measurement of field samples to the ASTER and HyMap bandwidth, and then comparing the diagnostic absorption features of pixel and ground spectra by regression analysis to estimate their correlation.

4.1 Field Sampling

Field samples were taken from sixteen field sites located within Block G area in Tick Hill region (Figure 4.1). Seventy-eight reflectance spectra were acquired from samples collected from the 16 locations. For most locations, several samples were collected and analyzed via the ASD in the field and again in the laboratory. Many locations had more than one variety of sample depending on the sample type and degree of weathering. The types of sample fell into three categories: fresh rocks, weathered rocks (saprock and saprolite) and soil sample. Most of the field samples were located in the regolith covered areas (weathered rocks and surficial deposits) because part of the aim of this research was to map regolith mineralogy and materials. Whole sample mineralogy was determined by XRD (Appendix 3).

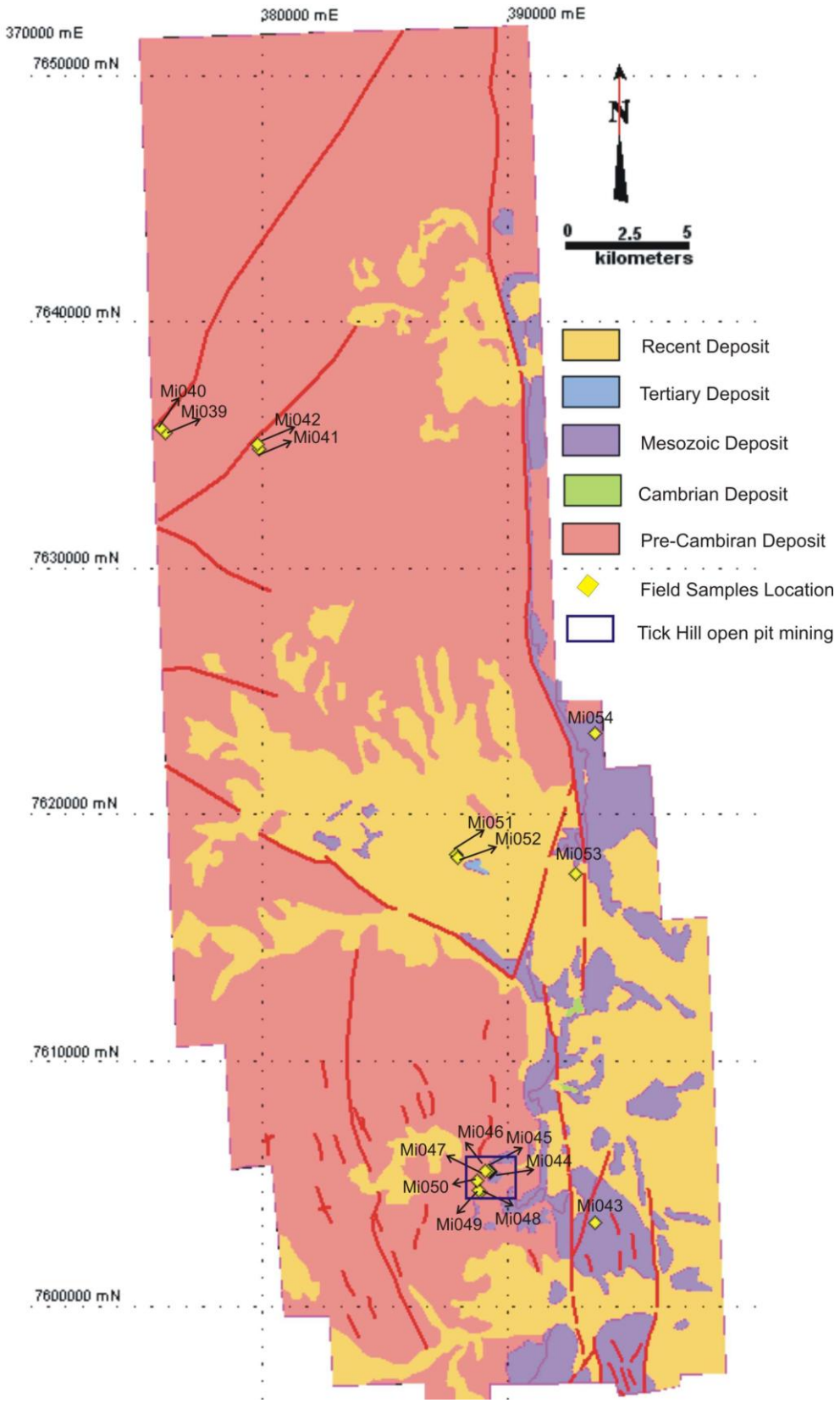

Figure 4.1: Field sample locations on the simplified geological map of Block G TickHill and surrounding areas, Mt.Isa, Northwest Queensland (Blake, 1982).

4.2 Al-OH Group Mapping

The similarity of the main absorption feature at approximately 2200 nm for Al-OH bearing clay minerals (kaolinite, illite, smectite, and muscovite) is the main problem in separating individual clay minerals via remote sensing, especially via broad band multispectral sensors such as the ASTER. However, by developing the spectral RBD and logical operator for ASTER and HyMap (Mars et al., 2006), it is possible to match the targeted individual Al-OH bearing clay mineral absorption based on its diagnostic feature depth. The process was aided by first configuring the spectral end member from the ASD spectra of the field samples or spectra from the USGS spectral library for the specific mineral, and then selecting ASTER or HyMap bands suitable for highlighting the clay minerals. The RBD technique is described and discussed below for Al-OH group (kaolinite, Al-smectite, illite-muscovite).

4.2.1 Kaolinite Spectral Characteristics and Mapping

Kaolinite ($Al_2Si_2OH_5$) is a clay layer silicate mineral which is common in the regolith as a product of weathering of primary minerals and also occurs in specific hydrothermal alteration zones (Ollier and Pain, 1996; Taylor and Eggleton, 2001; Wilson, 2004). The kaolinite spectral feature in the SWIR range is characterized by an intense Al-OH absorption at 2200 nm similar to other Al bearing layer silicates namely micas. Unlike the micas, however, the kaolinite Al-OH absorption feature shows a characteristic doublet absorption at 2160 nm in addition to the more intense peak at 2200 nm. The 2160 nm absorption distinguishes kaolinite from the micas (Hunt, 1977; Pontual and Merry, 1996; Phang and Anand, 2000) (figure 4.2). On the basis of its doublet absorption feature, kaolinite is potentially mappable from Al micas via HyMap, but not via the ASTER sensor whose spectral band width does not allow the doublet separation to be resolved.

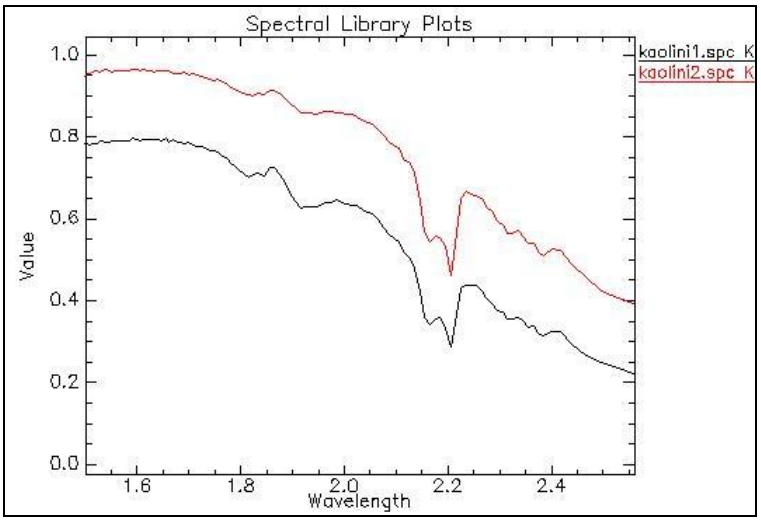

Figure 4.2: Kaolinite spectra profile from USGS spectral Library shows the doublet on its main absorption feature at 2160nm and 2200nm (Clark *et.al*, 2007).

4.2.1.1 Kaolinite mapping using ASTER Image

The kaolinite map produced from ASTER takes into account a map of kaolin group minerals such as halloysite, dickite and kaolinite. Extracting the spectral pattern of kaolinite in ASTER is done by resampling USGS library spectra of kaolinite to fit the ASTER band positions (figure 4.3). Band ratio b7/b5 was used, where band 7 (2.23 µm - 2.28µm) has the maximum reflectance of kaolinite (2200nm) and band 5 (2.145 µm - 2.185 µm) has relatively minimum absorption at 2160nm (figure 4.3). These two bands are suitable for ASTER data to obtain kaolin group abundance (Rowan & Mars, 2003; Hewson et al., 2005**).**

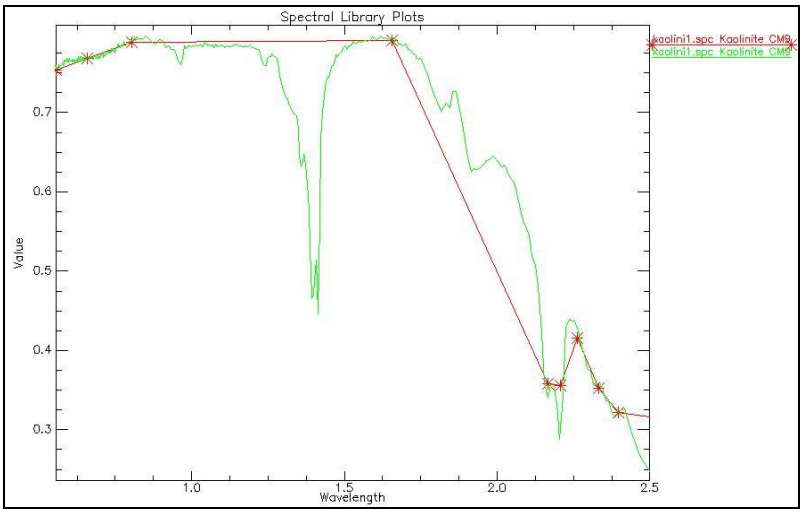

Figure 4.3: Kaolinite spectral (green) from USGS Spctral Library is used to resample ASTER bands. The resampled spectral is shown in red with band positions as red stars (Clark *et.al*, 2007).

As other Al-OH bearing minerals might interfere with the kaolin group at 2200nm, the RBD for Al-OH absorption (b5+b7)/b6 and band ratio index b5/b6 for white mica composition were created to mask kaolinite. It is assumed that all Al-OH absorption features centered at 2200nm such as Al mica and possibly illite and smectite have been removed and only kaolin group minerals are highlighted. However, the result is not likely to accurately distinguish kaolin minerals from micas.

Figure 4.4A shows the kaolin group abundance derived from band ratio 7/5, after masking out the Al-OH at 2200nm and Al-mica on band ratio (b5/b6). The false color scaled image shows kaolin group high abundance occurrence as red, and low occurrence as blue, with absence of kaolin indicated as black.

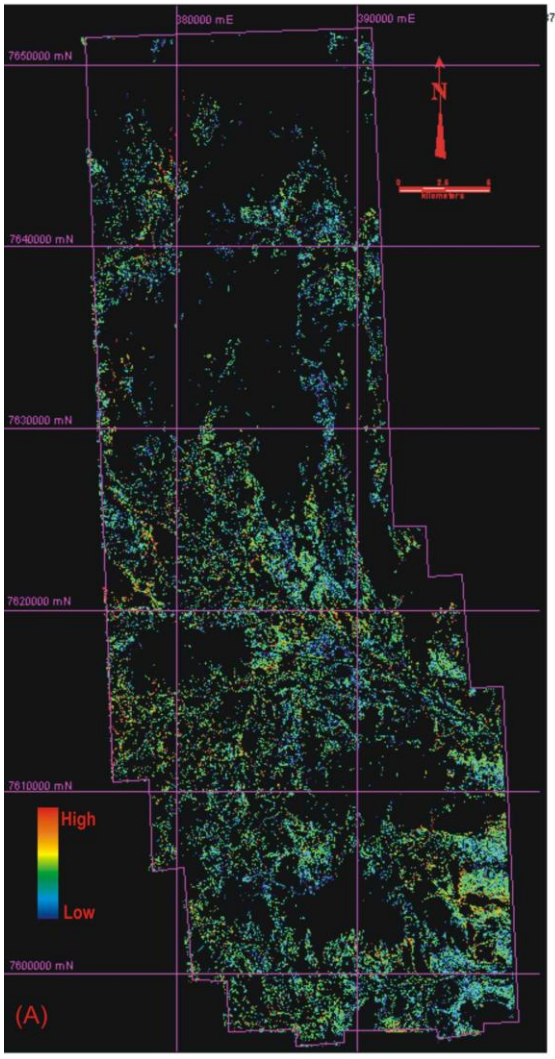

Figure 4.4A: Kaolin group abundance map produced from ASTER band ratio (band 7/5).

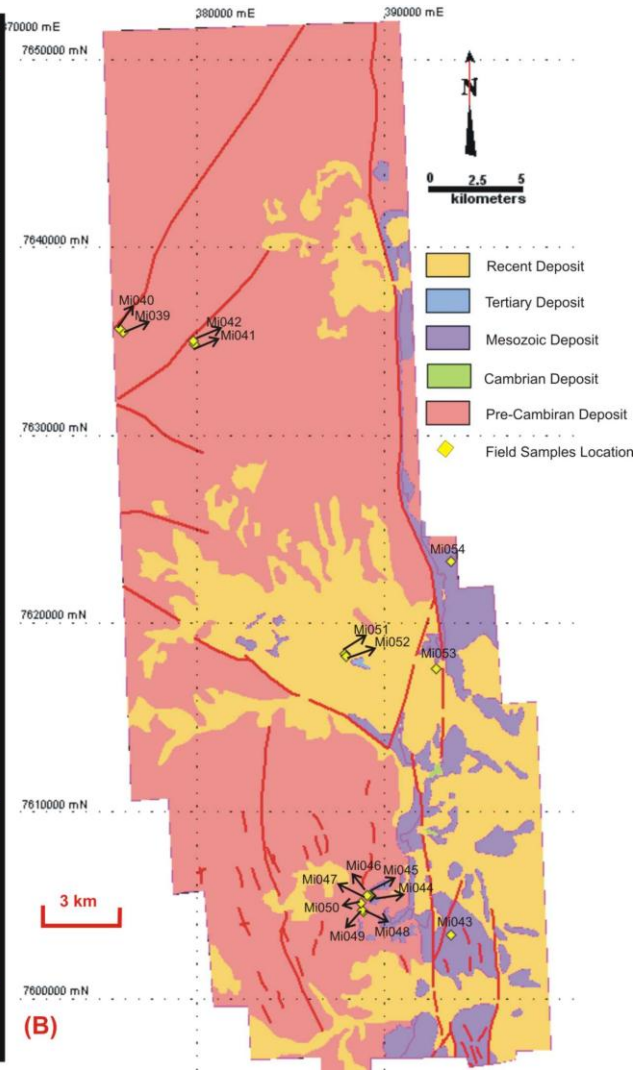

Figure 4.4B: Lithology map taken from published regional geology map (Blake, 1982 Geoscience Australia scale 1:250 000).

Figure 4.4B represents the regional geology of the same area. Comparison of the spatial distribution of kaolin minerals with mapped lithology suggests that kaolin is dominantly present on the surface of the lithology mapped as recent deposits and comparatively lesser on the Precambrian rocks. The distribution of kaolin is linked to regolith material distribution and the regolith is not clearly expressed in the geology map. For example, kaolin is dominantly an alteration product of feldspars, muscovite and biotite minerals (Taylor and Eggleton, 2001) and rocks containing these mineral on weathering are likely to host kaolinite. Therefore, the relationship between kaolinite occurrence and recent deposits and other older weathered rocks will be discussed further in the next chapter on regolith mapping and products.

4.2.1.2 Kaolinite mapping using HyMap Image

The HyMap data used to derive kaolinite abundance map was first corrected for reflectance, and then masked for green and dry vegetation and water (collectively called composite mask). The kaolinite abundance was generated by using RBD algorithm to highlight the main absorption doublets in kaolinite; 2160nm and 2200nm (Hunt, 1977). The ratio band depth used was $\mathbf{(b_{104}+b_{108})/(b_{106})}$ or $\mathbf{(R_{2122}+R_{2193})/(R_{2158})}$ for 2160nm depth and $\mathbf{(b_{104}+b_{111})/(b_{109})}$ **or** $\mathbf{(R_{2122}+R_{2247})/(R_{2212})}$ for the major feature at 2200nm (Table 4.1). Therefore, the white mica absorption peaks occurring beyond 2200 nm are avoided.

Kaolinite abundance is assumed to have the main feature absorption at 2200nm. The image produced from 2200nm absorption was then masked by kaolinite image from 2160nm which is related to kaolinite crystallinity (Cudahy et al., 2005). The sequence of operations to make the kaolinite map is listed in table 4.1.

Table 4.1: The products and steps of RBD method used to produce kaolinite abundance and kaolinite crystallinity map.

Map Product	Base Algorithm (RBD)	Mask (Filter)	Linear Stretch	Color Chart	Accuracy
Kaolinite abundance	Kaolinite_2200D $(R_{2122}+R_{2247})/(R_{2212})$ Including validation	Kaolinite 2160D $(R_{2122}+R_{21931})/(R_{2158})$ Composite mask	Min 0.001 Or 0-255 In RGB	Rainbow Red: high Blue: low	Moderate; highlighted kaolinite major depth at 2200D
Kaolinite crystallinity	Kaolinite 2160D $(R_{2122}+R_{2193})/(R_{2158})$	HyMap kaolinite abundance; mask min.1.96		Rainbow Red: high Blue: low	Moderate; highlight kaolinite 2160D

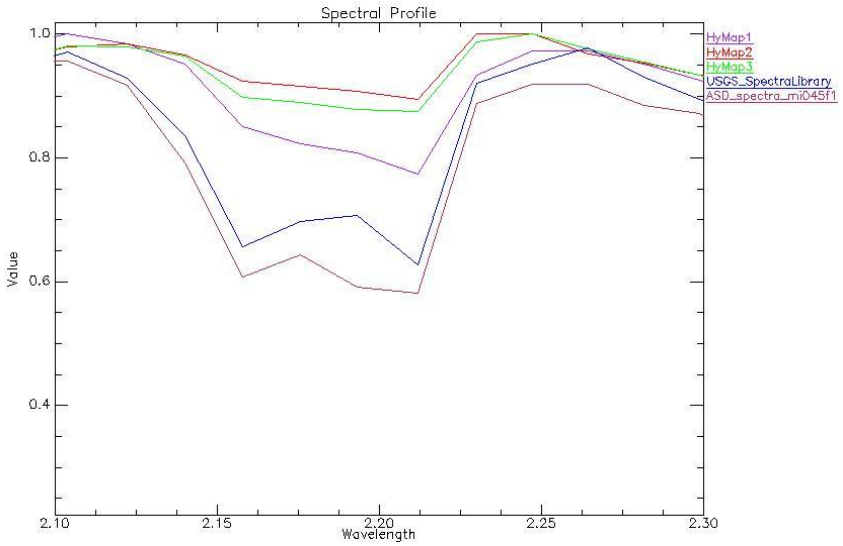

Figure 4.5A: Comparison between USGS spectra, ASD spectra library for kaolinite and HyMap spectra profile for kaolinite abundance.(Clark *et.al*, 2007).

Figure 4.5A is comparison between kaolinite main doublet in ASD field spectra measurement and USGS spectra library and spectra of kaolinite from HyMap pixels in areas dominated by kaolinite such as those shown in figure 4.4B.

Figure 4.5B represents the kaolinite abundance image as produced from the sequence listed in table 4.1. The inset image is that of a smaller area from the main map and shows high kaolinite abundance along a mesa. Kaolinite abundance appears high along exposures of regolith materials on the slopes of mesa

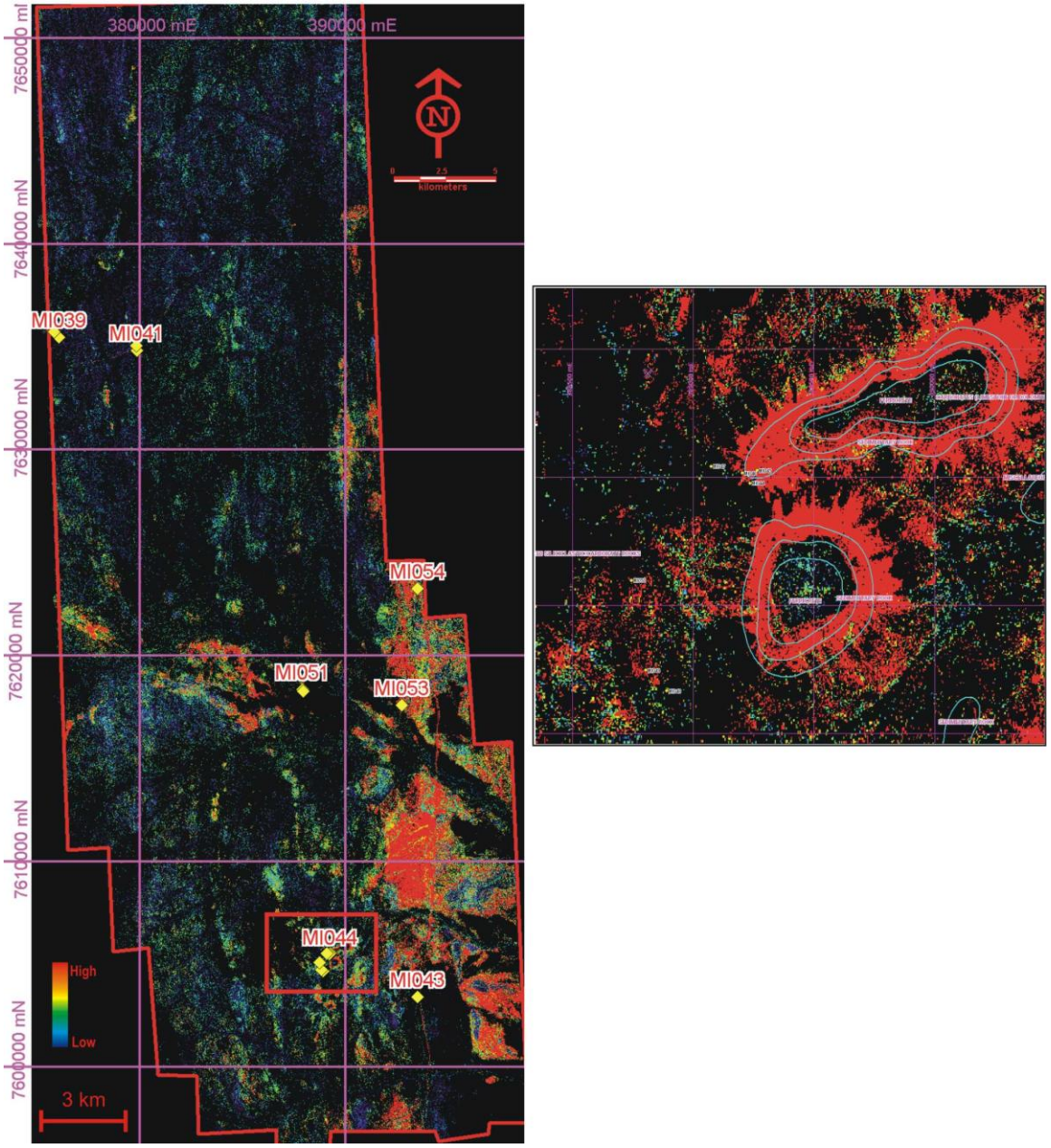

Figure 4.5b: Map of kaolinite abundance constructed using HyMap data with processing sequence listed in table 4.1. (red: high abundance; blue: low abundance). Right image: High kaolinite abundance along the slopes of mesas close to Tick Hill open pit gold mine. The slopes of mesas were identified as saprolite which has a high abundance of kaolinite.

Cudahy (2005) proposed that kaolinite disorder or "crystallinity" can be identified by using the minerals spectral feature at 2160nm. Kaolinite "crystallinity" or disorder map can be produced by applying mask of kaolinite abundance (capturing 2200nm depth) to kaolinite 2160nm depth (Figure 4.5C). The processing sequence followed to produce kaolinite crystallinity (disorder) map are listed in table 4.1 and briefly are; produce kaolinite map using 2160 nm → create mask from kaolinite

abundance at threshold min 1.96 → apply mask to kaolinite 2160D → kaolinite crystallinity map → the map is then enhanced using linear stretch with the histogram range 2 – 2.1 on average for all 11 HyMap image strips of Block G Tick Hill. The kaolinite crystallinity or kaolinite disorder produced here will be used later in next chapter for map the regolith transported and *in situ* materials.

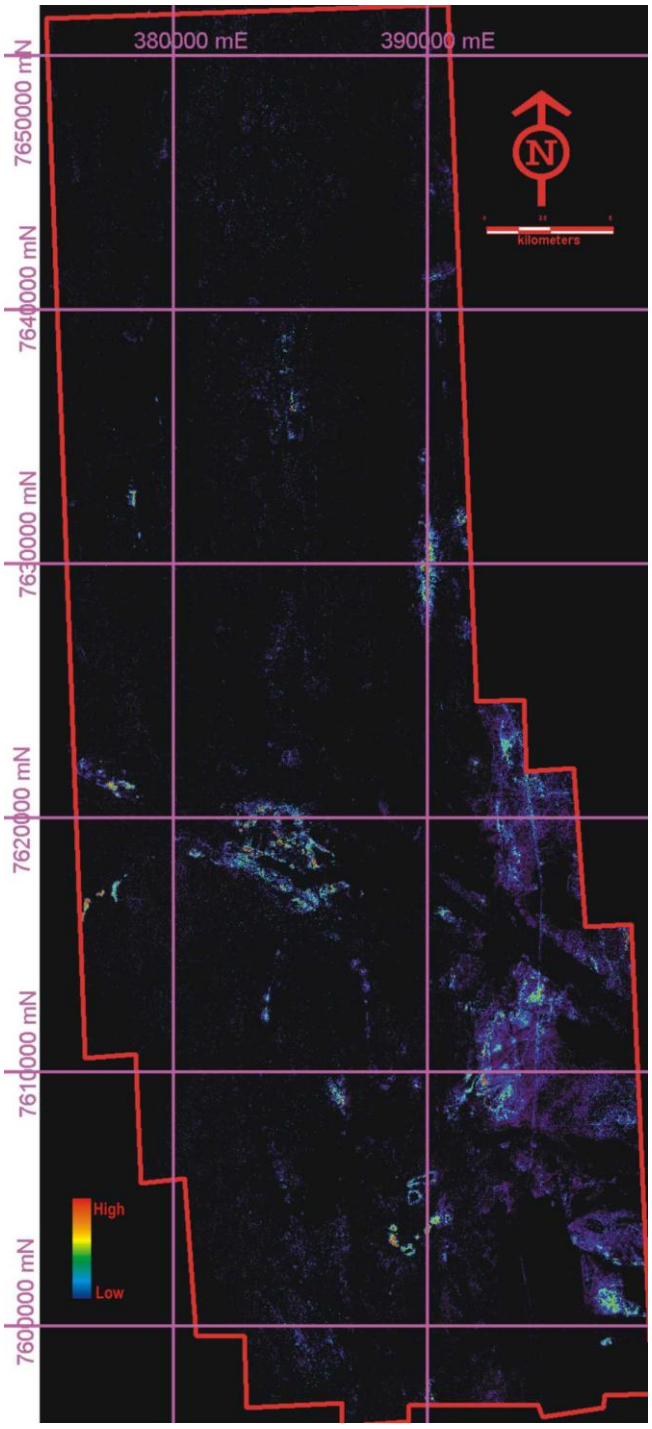

Figure 4.5C: HyMap processed map of kaolinite crystallinity over Block G TickHill red (high crystallinity), dark blue (low crystallinity).

4.2.1.3 Validate the ASTER and HyMap Kaolinite Map with the ground truth Data (ASD, X-ray Diffraction)

Validating the remotely sensed mineral map by field sample measurement is important in order to assess the effectiveness of the mineral maps. Field spectra measurements acquired by ASD were compared with XRD analysis of the same samples. In order to compare ASD with the HyMap produced map, the depth of absorption feature in kaolinite spectra from ground location (ASD) were compared with the depth of absorption feature of the same location pixel spectra of HyMap or ASTER band ratio. In this comparison, there will be some loss of spatial precision because each sensors spectral resolution (bandwidth) is different.

Kaolinite was identified via ASD and XRD in twelve samples (mi045f1, mi045f2, mi045w1, mi045w2, mi045w3, mi54f1, mi054f2, mi054f3, mi054s1, mi054w1, mi054w2, mi054w3). Those samples in which kaolinite were present are mostly weathered rocks (saprock or saprolite) and soils. In the XRD patterns, kaolinite shows diagnostic peaks at 0.715 nm and 0.357 nm which correspond to d_{001} and d_{002} reflections respectively (appendix 3: XRD measurement of Tick Hill Samples).

In most samples, iron oxide is present with kaolinite particularly in weathered rock (saprock, saprolite) and soil samples. Kaolinite appears both in fresh rock sample and weathered samples. Kaolinite present in fresh rocks is likely to be of hydrothermal origin and where present in weathered samples is dominantly a product of weathering (Taylor and Eggleton, 2001). The detail description of ASD spectral analysis, including the associated minerals will be explained further in appendix 4.

1. Validating ASTER Kaolinite Map

Values calculated from ASTER kaolinite map with band ratio method for specific pixels were compared with the kaolinite content calculated from ASD spectra of the corresponding ground sample. The values were plotted against each other which provided a visual estimate of correlation between the samples (figure 4.6) and a correlation coefficient (R^2) was calculated. The high correlation coefficient of 0.90 between the ground samples and that estimated from ASTER data indicates that ASTER kaolinite band ratio is effective in mapping the kaolin group of minerals.

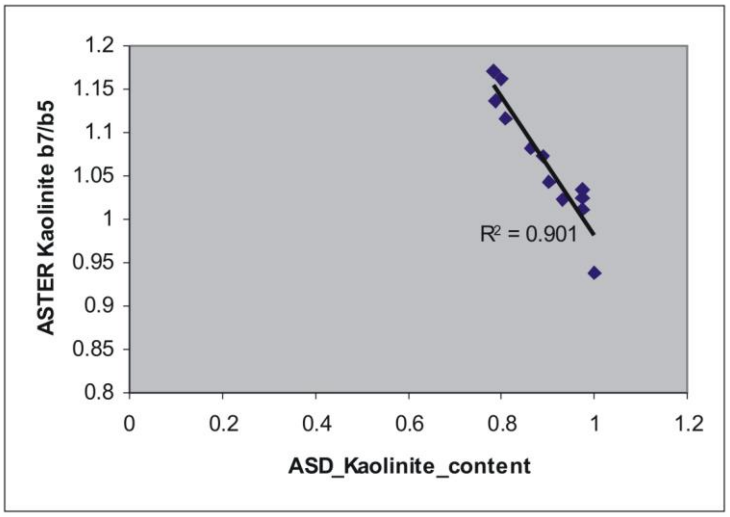

Figure 4.6: Scatter plot of kaolinite values estimated from ASD spectra of field samples against calculated ASTER kaolinite content for same pixel location as that for ground sample.

2. Validate HyMap kaolinite map

Kaolinite abundance estimated from HyMap spectral indices was compared with kaolinite abundance extracted from field sample spectra for similar locations (figure 4.7). The very strong positive correlation (0.965) between the two datasets indicates that the HyMap RBD $(R_{21222}+R_{21931})/(R_{21580})$ is very effective in mapping kaolinite.

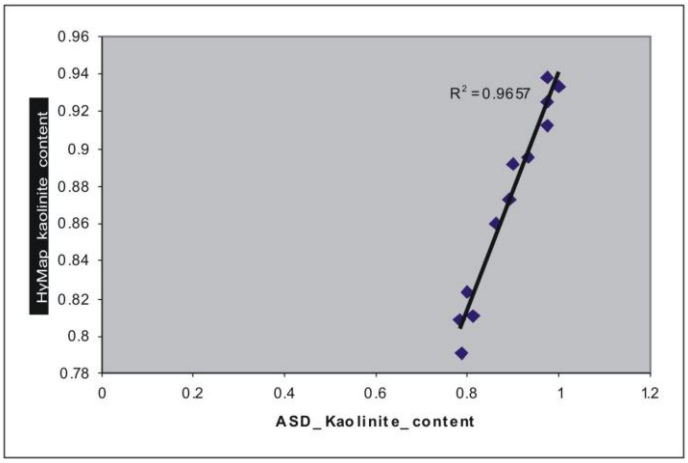

Figure 4.7: Scatter plot of kaolinite content estimated from ASD spectra of field samples against calculated HyMap kaolinite content for same pixel location as that for ground sample.

4.2.2 Al-smectite, illite-muscovite Mapping

Illite and smectite are the other common Al-OH minerals. Illite occurs as an individual or pure mineral in regolith materials, mudrocks and in hydrothermal alteration zones, but it also commonly occurs interstratified with smectite (Moore and Reynolds 1989). Although illite can be identified via the Al-OH spectral absorption feature at 2200 nm, its confirmation in a sample is best achieved via XRD where the 1nm d_{001} peak does not shift on glycol treatment (Moore and Reynolds, 1989). Smectite is the name given to a family of clay layer silicate minerals whose composition varies between Mg-Al-Fe end members and has a layer charge between 0.4-0.6 and typically swells in water or organic solvents. It occurs individually and as interstratified with illite or kaolinite (Moore and Reynolds, 1989). It is a common product of weathering of mafic primary minerals (Taylor and Eggleton, 2001) and is also common in mudrocks and hydrothermal zones.

Illite and smectite, if occurring individually, can be identified via their SWIR spectral features, although if both minerals are present as interstratified varieties, it is more difficult to do so via reflectance spectra and only XRD can confirm their occurrence.

Figure 4.8 shows the spectra characteristic of montmorillonite which is part of smectite group.

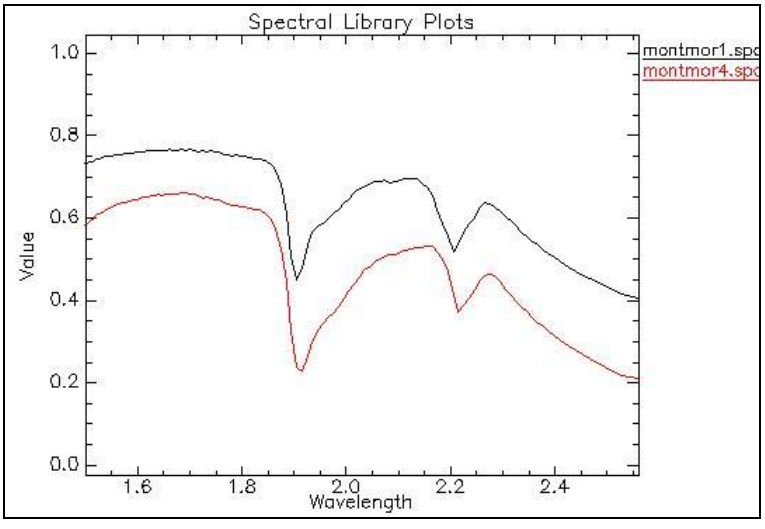

Figure 4.8: Al-smectite (montmorillonite) from the USGS spectral library showing the strong absorption at 2200nm. The large absorption at 1900 nm is related to the water in smectites .(Clark *et.al*, 2007).

The main Al-OH absorption feature at 2200nm appears in illite and muscovite but both minerals cannot be separated easily due to the similar absorption features at 2200nm and 2350nm (Hunt, 1977). Water absorption difference between illite and muscovite is a good indicator to differentiate from the spectral library (Clark, 1999). The spectra pattern in figure 4.9 obviously shows that illite has greater water absorption detected at 1900nm compared to muscovite.

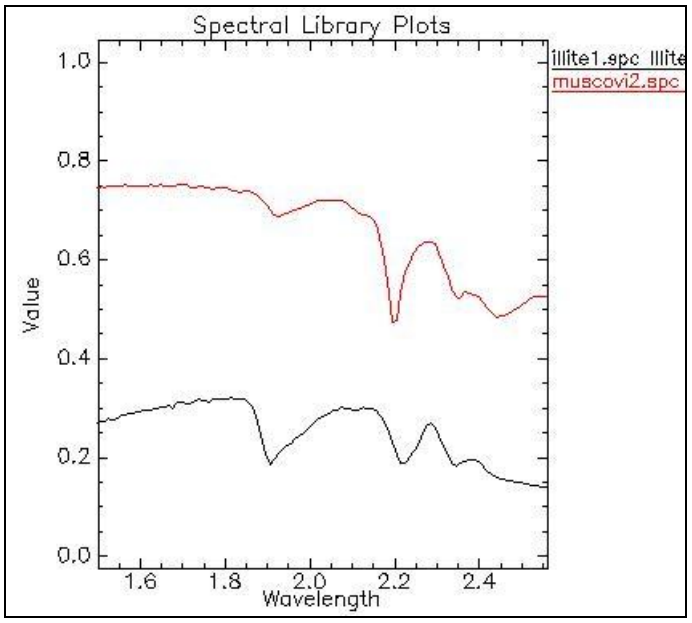

Figure 4.9: Reflectance spectra of illite and muscovite from USGS spectral library showing the main absorption features in the 2.0 – 2.3 µm range. Illite has a greater water related absorption feature depth.(Clark *et.al*, 2007).

4.2.2.1 Mapping white micas and Al-smectite using ASTER Image

The term white mica includes the group sericite-muscovite-illite. To identify white micas and Al-smectite as individual minerals with ASTER is difficult, because of the broad bandwidth of SWIR bands of the ASTER sensor (approximately 40 nm bandwidth) (Fujisada, 1994). Therefore, only Al-OH mineral group as a whole can be distinguished rather than individual Al-OH bearing minerals. Several researchers have employed the RBD of (band5+band7)/band6 to discriminate Al-OH minerals such as sericite-muscovite-illite-smectite from other non Al-OH bearing minerals (Rowan& Mars, 2003; Hewson, et al. 2005; Rowan, et al. 2005; Rowan, et al., 2006)**.** The RBD highlights the Al-OH bearing minerals occurring in the 2.14 µm - 2.28 µm and have been used to produce white mica-Al-smectite maps from the ASTER data.

As shown in figure 4.10, the distribution of white mica and Al-smectite minerals as mapped via ASTER data shows a higher occurrence in Precambrian rocks which are located in the north and the southwest of the mapped area. There appears to be variation in the abundance of Al-OH group minerals within the Precambrian rocks and this could be due to variation in white mica in the rocks itself, or due to weathering of the rocks. Changes in mineralogy based on lithology and weathering are described in chapter 5.

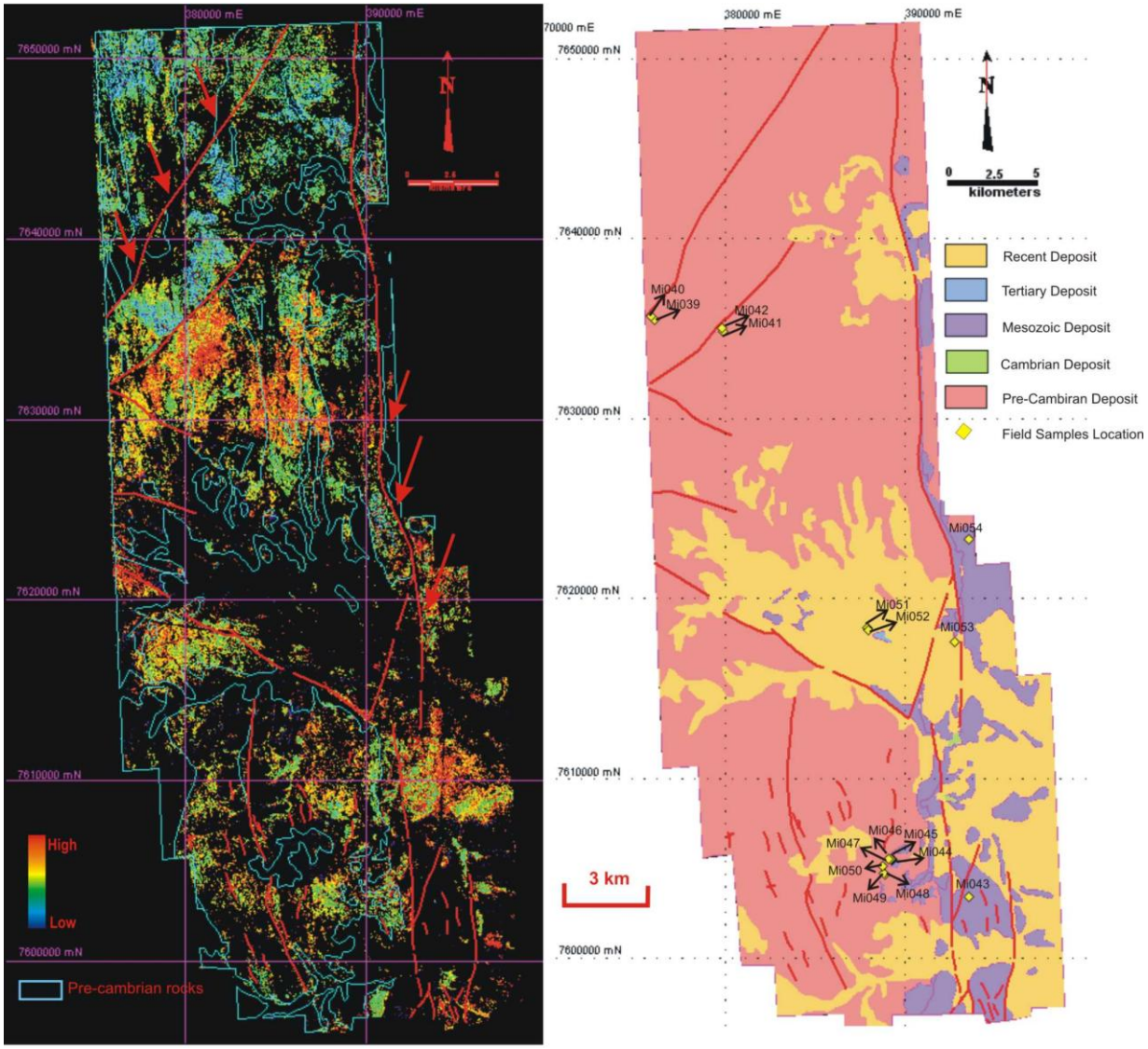

Figure 4.10: Muscovite-illite-smectite image processed from ASTER data using band combination ratio (5+7)/6 after masking out the vegetation content. Regional geology map (right image) (from Blake, 1982).

4.2.2.2 Al-Smectite content mapping using HyMap Image

The better spectral resolution of the HyMap sensor allows possible discrimination of illite, muscovite and smectite from other Al-OH bearing minerals (kaolinite) which was not possible with ASTER. To make an Al-smectite map, the spectral absorption features of the mineral need to be assessed.

Based on the spectral features of Al-smectite concentrate at 2200nm (figure 4.8), spectral indices method was employed using MMTG A-list software. The software was used to fit the 4^{th} order polynomial between the wavelengths 2120 – 2245 nm of the HyMap data and the depth of fitted polynomial at 2200 nm was extracted. Subsequently, the 2^{nd} order polynomial 2350 nm depth of white mica absorption was used to create a mask with threshold < 1.035. Composite mask content of dry vegetation, green vegetation and albedo are masked out from the 2160nm depth kaolinite (table 4.2).

Table 4.2: The steps used in spectral feature fitting (spectral indices method) to produce the Al-smectite abundance map.

Map Product	Base Algorithm (spectral indices)	Mask (Filter)	Linear Stretch	Color Chart	Accuracy
HyMap Al smectite Content	Normalized depth 4^{th} order polynomial between 2120 to 2245 nm (MMTG A-List) OR $(b_{106}+b_{112})/(b_{109}+b_{106})$ $(R_{2158}+R_{2264})/(R_{2212}+R_{2158})$ For validation	white mica 2350D mask max. 1.035 kaolinite 2160D mask max 1.98 composite mask	Min 0.001 Or 0-255 In RGB	Rainbow Red: high Blue: low	Low; mix with kaolinite 2200D and in red(high) complicated with mica 2350D

Figure 4.11 is the mineral abundance map for Al-smectite, the distribution of which appears to be associated with the distribution of kaolinite (refer to figure 4.5b). The Al-smectite does not appear to be related to any specific mapped lithology and occurs over various lithologies including Precambrian, Mesozoic, Cenozoic and recent deposits. Since smectite is dominantly a weathering product, its occurrence is likely to relate to the composition of bedrock and the development of weathering profiles. However, it is likely that the presence of kaolinite and to an extent illite (both containing Al-OH), interfere in the process of making the Al-smectite map.

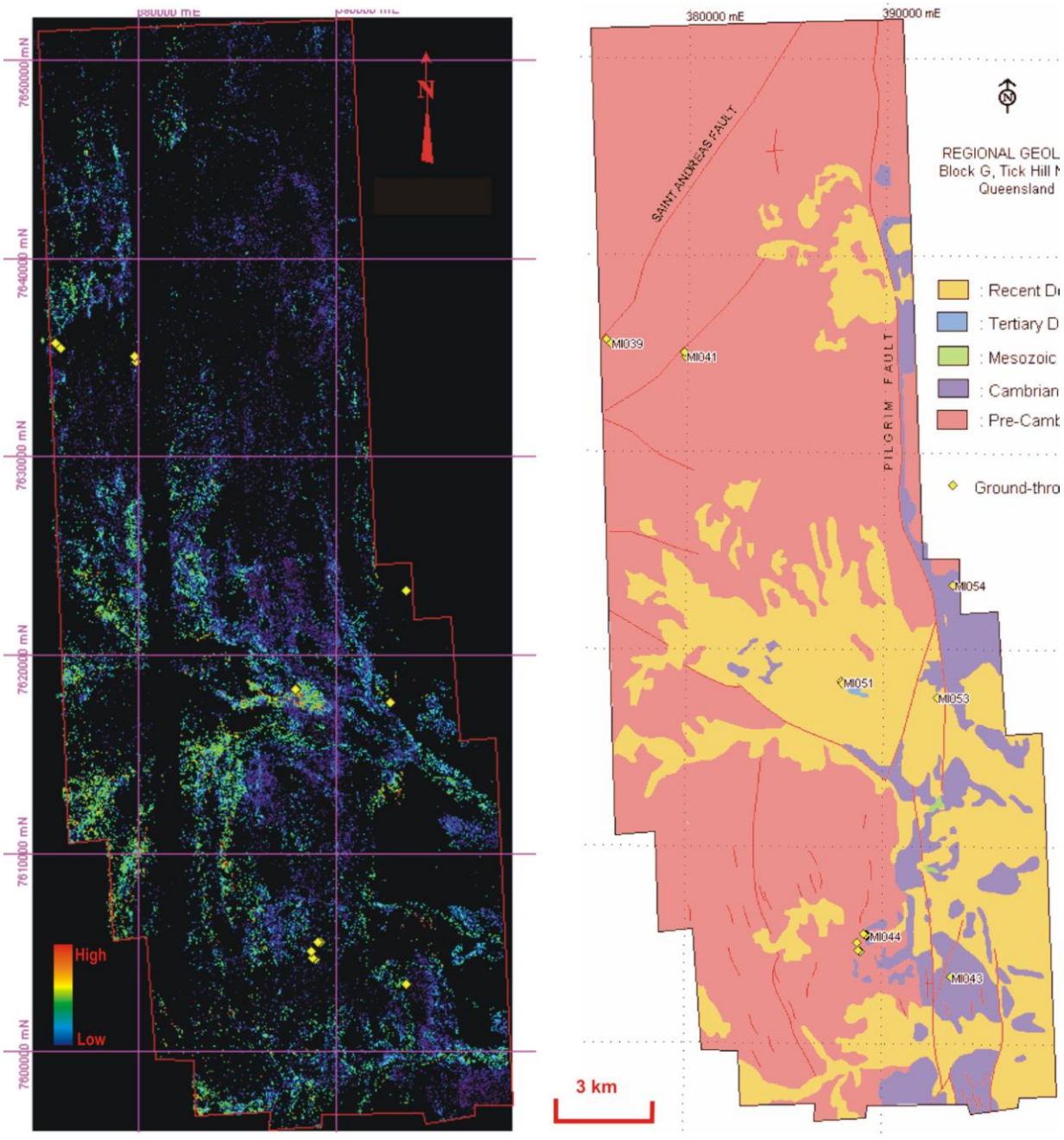

Figure 4.11: Al-smectite distribution map produced from HyMap RBD method (left image) with published regional geology map (right image) (Geology map from Blake, 1982).

4.2.2.3 Illite-muscovite mapping using HyMap

The RBD and spectral feature fitting method for white mica mapping has been used by others to highlight the white mica (muscovite) absorption at 2200nm and 2350nm (Duke, 1994; Clark, 1999).

Van Ruitenbeek, et al. (2006) developed RBD method to differentiate and map white mica (muscovite) via hyperspectral data rather than by using conventional statistical default methods such as spectral un-mixing and SAM. Based on their argument that the endmember for white mica does not have any correlation with the general shape of white mica reflectance absorption, the following two band ratios for white mica were proposed; 2220nm/2202nm and 2237nm/2220nm.

Base algorithm for white mica composition was created using advance feature fitting called Spectral Indices method from MMTG A-list software by highlighting the spectral absorption depth between 2120nm and 2245nm. Several filters have been used on the white mica base algorithm. First is a mask of white mica absorption 2350D from RBD of $(R_{2318}+R_{2295}+R_{2369})/(R_{2333}+R_{2350}+R_{2366})$ and using a threshold for the image is min 1.035 (> 1.035). Thus, anything below 1.035 will be masked out. Second is to create white mica image for absorption depth at 2200nm by applying RBD of $(R_{2138}+R_{2190})/ (R_{2156}+R_{2179})$ and apply threshold max. 1.005 (< 1.005). The composite mask was also applied (dry vegetation; green vegetation and albedo). The detail steps and description of how to produce white mica image can be seen in table 4.3.

Table 4.3: Processing steps involved in making illite/white mica map (after Cudahy et al., 2008).

Product	**Basic algorithm**	**Filter Masking**	**Linear Stretch**	**Color chart**	**Accuracy**
HyMap, white mica content (muscovite, illite, possibly smectite, kaolinite)	Normalised depth of a fitted 4^{th} order polynomial between 2120 and 2245nm (MMTG A-List) **OR** $(b_{106}+b_{113})/(b_{108}+b_{109})$ $(R_{2158}+R_{2281})/(R_{2193}+R_{2212})$ for validation	CM(green veg, dry veg, albedo) $(R_{2318}+R_{2295}+R_{2369})/$ $(R_{2333}+R_{2350}+R_{2366})$ For 2350D threshold >1.035 $(R_{2138}+R_{2190})/$ $(R_{2156}+R_{2179})$ For 2200D threshold <1.005	Min 0.001 Or 0-255 In RGB	Rainbow Red: high Blue: low	Moderate : highlighted the white mica absorption at 2200D and 2350D

* CM= composite mask

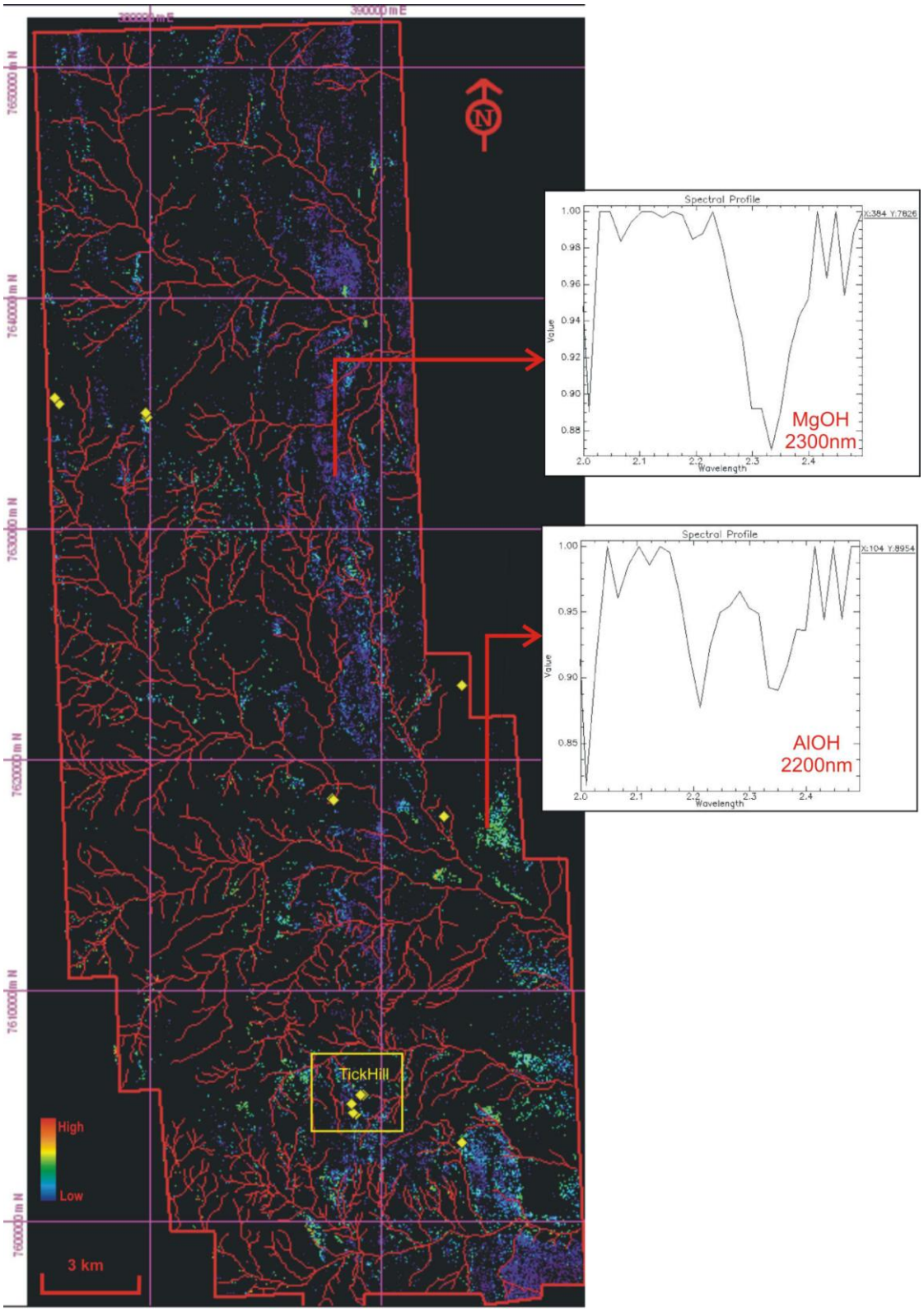

Figure 4.12: HyMap Illite/muscovite map derived from RBD method. High-moderate abundance of illite-muscovite (yellow-green) is mixed with smectite/AlOH at 2200nm and low abundance of illite-muscovite (dark blue-blue) associated with Mg-OH absorption depth at 2330nm.

Figure 4.12 shows the illite and muscovite mineral map produced from sequence of operations listed in table 4.3. The map is likely to show mixture of minerals with illite mixed with smectite and kaolinite in areas showing high abundance of micas. Illite is likely to be mixed with Mg-OH absorption in areas with low abundance of white micas. Cudahy et al. (2008) also noted that the spectral indices and thresholds applied in masking to produce illite-muscovite map allow mixing with kaolinite and smectite to a minor extent.

4.2.2.4 Validate ASTER and HyMap mapping of Al-smectite, illite-muscovite with the ground truth Data (ASD, X-ray Diffraction)

In thirteen field samples smectite was identified based on the diagnostic Al-OH 2200nm absorption feature spectra feature and high water absorption (mi040s1, mi043w2, mi044f1, mi044f3, mi047s1, mi047w2, mi049s1, mi049w1, mi051s1, mi053f1, mi053w1) (Figure 4.13).

Reflectance spectra of smectite (montmorrilonite, nontronite, beidellite end members) has a deep water absorption at 1900nm that is typical of swelling clays (Taylor and Eggleton, 2001). Smectites are present in the lower parts of weathering profiles and are one of the first products of ferro-magnesian silicate minerals (Taylor and Eggleton, 2001). XRD of field samples identified smectite in samples mi047f1 and mi047f2. XRD of clay separates from the two samples showed d_{001} peak at 1.25 nm in air dried state which expanded to 1.8 nm on glycol treatment, followed by collapse to 1 nm on heating. This expansion and collapse on treatments is indicative of smectite (Moore and Reynolds, 1989).

Six field spectra samples indicate illite or muscovite (mi042w5, mi044w1, mi044w3, mi046f2, mi047f1, mi047f2). The typical absorption features of the minerals occur at 2200nm and 2350nm in the ASD spectra (figure 4.14). Pure illite-muscovite (or illite only) was identified in sample number mi047f1 and mi053f1 via the clay separate XRD pattern. In the oriented clay XRD pattern, the 1.0 nm d_{001} peak did not shift on glycol treatment or on heating (appendix:2), indicating presence of mica.

Illite and muscovite were found in fresh-rock (mi047f1 and mi047f2), but the weathering variety of the same rocks showed the presence of smectite (mi047w2) and smectite also appears in soil (mi047s1). It is assumed that muscovite is likely to be associated with the hydrothermal activity considering the samples location close to

active open-pit mining in Tick Hill (see figure 4.1, sample location) Also, illite is a product of hydrothermal alteration (Brown et al. 2006).

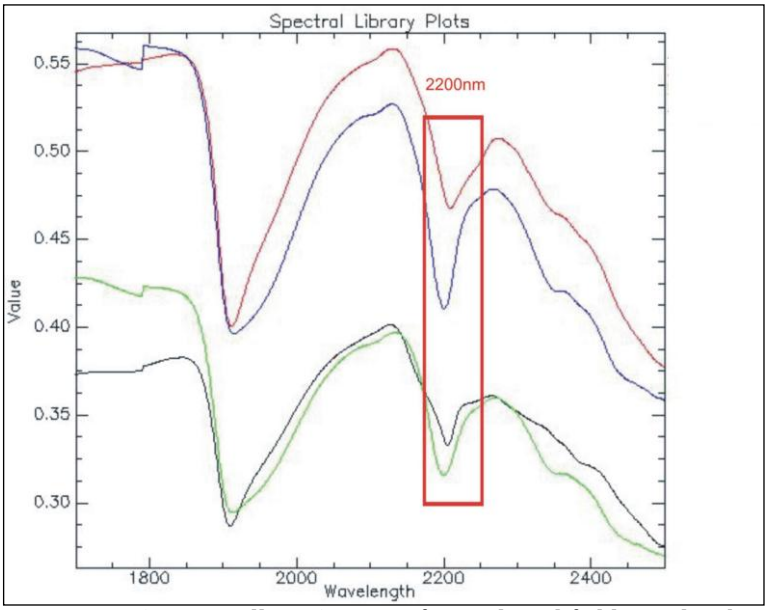

Figure 4.13: Smectite (montmorillonite) spectra from selected field samples showing main absorption at 2200nm and a deep water absorption peak at 1900nm ; s (soil samples), w (weathered samples), f (fresh rock samples).

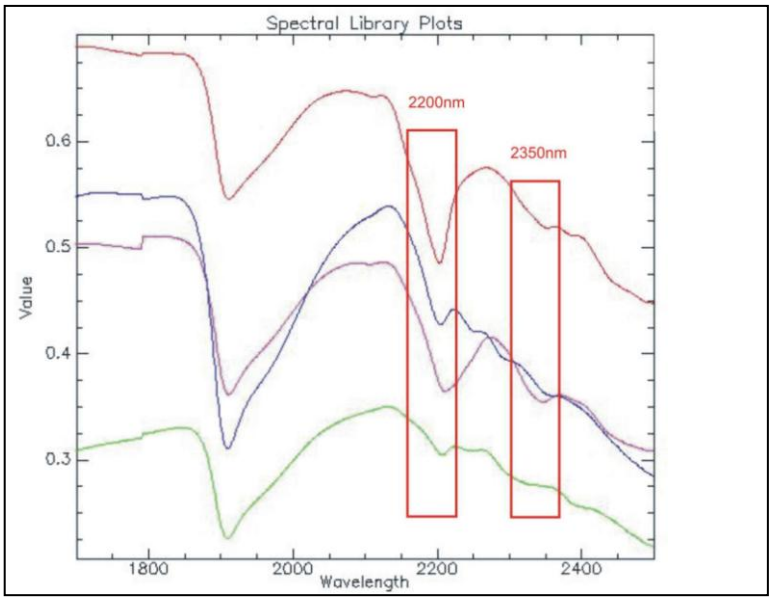

Figure 4.14: Illite-muscovite spectra from field samples showing typical absorption at 2200nm & minor 2350nm feature; w (weathered samples), f (fresh rock samples).

1. Validation of ASTER muscovite-illite-smectite map

Validation of Al-OH bearing minerals (besides kaolinite) - muscovite-illite-smectite- was conducted for ASTER band ratio (5+7/6) against laboratory spectra (ASD) for specific field samples. The ASD spectra for the (illite-smectite) content samples were resampled to ASTER SWIR band wavelengths. ASTER Al-OH values were calculated from band ratio (5+7/6). The ASTER band ratio values were plotted against the ASD ratio band depth values for 2200nm which show a good correlation (R^2 = 0.8954 for smectite, R^2=0.8877 for illite-muscovite)

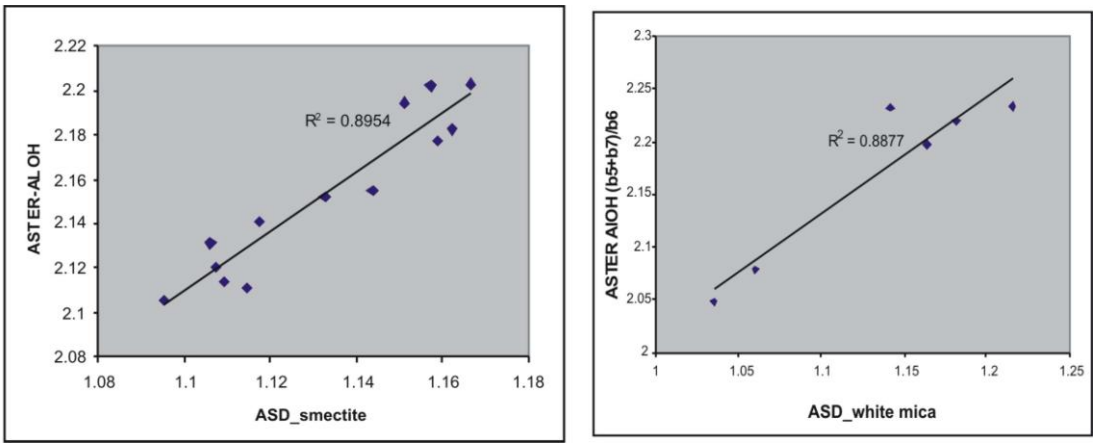

Figure 4.15: Scatter plot of Al-OH values estimated from ASD spectra of field samples resampled to ASTER band width against calculated ASTER Al-OH content (b5+b7/b6) for same pixel location as that for ground sample.

2. Validation of HyMap smectite map

The ASD spectra of 13 field samples potentially containing smectite were resampled to HyMap bands and values calculated from band ratio $(R_{2158}+R_{2281})/(R_{2193}+R_{2212})$ were plotted against the smectite band ratio of ASD $(R_{2165}+R_{2275})/(R_{2195}+R_{2205})$. The result of R^2 = 0.877 indicates that the HyMap bands used to produce smectite map correlates moderately with the on ground spectra for smectite, with the correlation below 0.9 (figure 4.16).

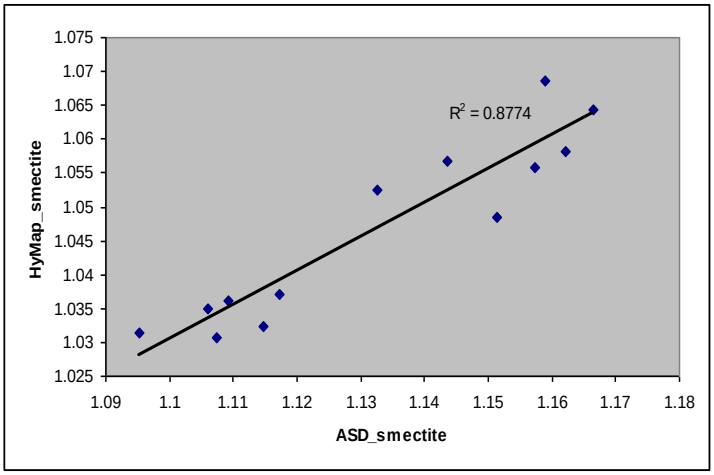

Figure 4.16: Scatter plot of Al-smectite estimated from ASD spectra of field samples resampled to HyMap band width against calculated HyMap values for same pixel location as that for ground sample.

3. Validation of HyMap illite-muscovite map

The spectral features used to validate white mica assumed that they had a specific strong symmetric absorption feature at 2200nm corresponding to Al-OH and also a minor absorption feature at 2350nm. The ratio band depth used to identify white mica for this validation is $(R_{2158}+R_{2281})/(R_{2193}+R_{2212})$. Compared to Al-smectite, illite-muscovite (white mica) HyMap processed data with ground spectra shows better validation results having a correlation of $R^2= 0.9784$ (figure 4.17). Therefore, compared to Al-smectite, mapping of white mica is more effective via HyMap.

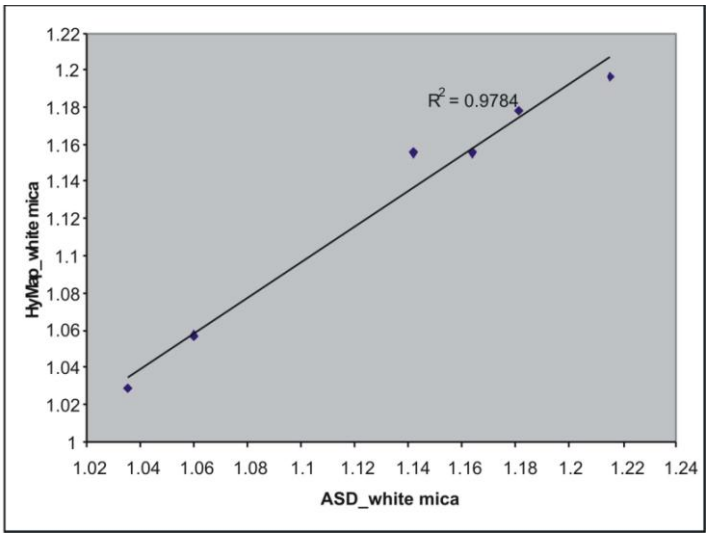

Figure 4.17: Scatter plot of white mica values estimated from ASD spectra of field against calculated HyMap white mica content for same pixel location as that for ground sample.

4.3 Iron Oxide Mapping

Iron oxides and hydroxide minerals (here in referred to as iron oxides) are common in the Australian regolith. The main iron oxides are hematite and goethite with minor magnetite and maghemite (Anand and Paine, 2002). Hematite and goethite are identified from their VNIR spectral features arising due to charge transfer and crystal field absorption of the Fe^{3+} ion which octahedrally bonded to ligands of oxygen (hematite, Fe_2O_3) or oxygen and hydroxyl (goethite, FeOOH) (Cudahy and Ramanaidou, 1997). The band depth for iron oxide concentrates at wavelength 880nm to 900nm (Hunt, 1977; Cudahy and Ramanaidou, 1997; Clark 1999; Ong et al., 2001). The difference between hematite and goethite can be found in the absorption maxima for the crystal field absorption for hematite at 870 nm as compared to that of goethite that occurs at 938 nm (Crowley et al, 2003) (Figure 4.18).

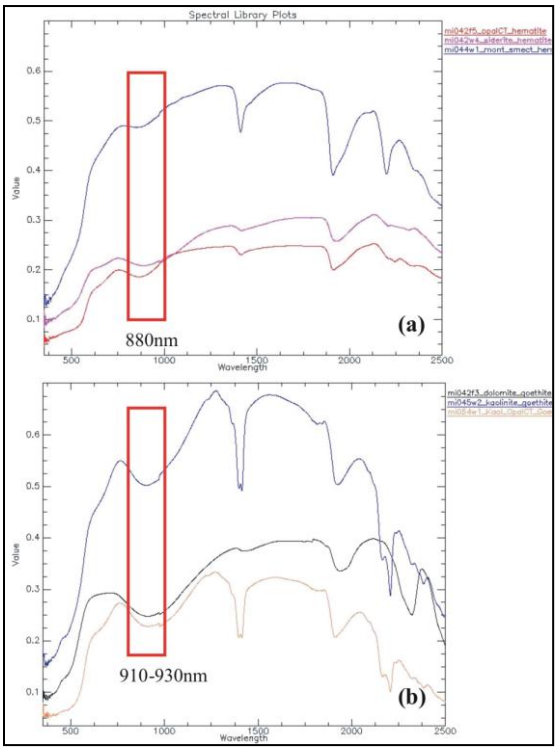

Figure 4.18: Two main iron oxide mineral spectra. A) hematite and b) goethite. The boxes show the main Fe-O related broad absorption features.

Hematite and goethite VNIR spectral features are often difficult to separate in sensors having poor spectral resolution due to the close absorption features of the two minerals occurring between 870 – 930nm. They are often occur mixed and their Fe-O

absorption features overlap (Cudahy and Ramanaidou, 1997). The peak absorption from goethite occurs at 939 nm while that for hematite occurs as 870 nm although Al substitution in the structure of both minerals can shift the peaks slightly (Crowley et al., 2003).

4.3.1 Iron-Oxide mapping using ASTER Image

Using the ASTER data, the iron oxide (total hematite and goethite) surface map is best constructed using the band ratio (2/1) as this band wavelength ratio highlights ferric iron (hematite and goethite) (Rowan and Mars 2003; Hewson, et al. 2005; Gozzard, 2006), although there are other recommendations such as the ratio (4/3) (Gozzard, 2006). The iron oxide map produced by two band ratio combination (2/1 and 4/3) is shown in figure 4.19.

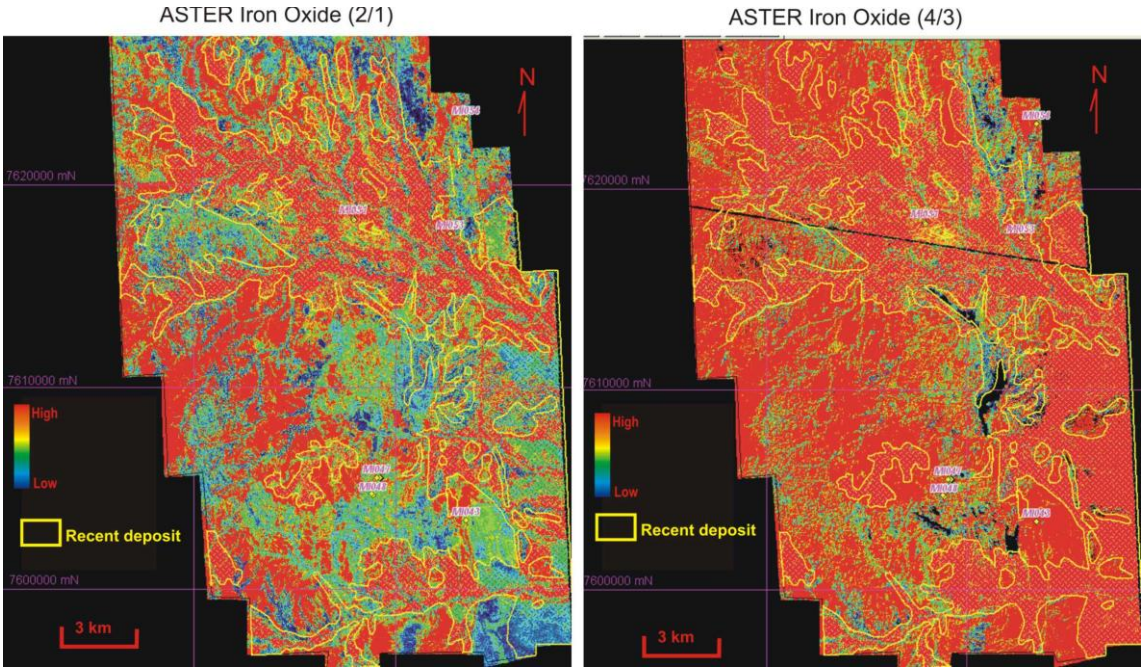

Figure 4.19: Iron-oxide maps produced using two different band ratios of ASTER: 2/1 (left) and 4/3.

The occurrence of high abundance of iron oxides on the ASTER data maps appears associated with recent Quaternary alluvial and colluvial deposits that dominate the middle of Block G Tick Hill area (figure 4.19). However, the iron oxide distribution also appears to correlate with vegetation distribution, namely along the drainages. This could be due to the absorption features of iron oxides as seen in the broad bands of ASTER, are close to the vegetation absorption peaks (Lewis, 2002). The vegetation absorption peaks are also concentrated in bands 1 and 2 of ASTER. Therefore, for

further analysis of iron oxides using ASTER, vegetation effects need to be considered. The difference between 2/1 and 4/3 images appears to show that the former ratio shows iron oxides to be spatially confined as compared to 4/3 which shows iron oxides to be more widespread.

4.3.2 Iron Oxide mapping using HyMap Image

Iron oxide abundance maps were produced from the HyMap data using the basic algorithm derived from the spectra indices tool in MMTG A-list software which used the normalized depth of the 900nm absorption feature calculated using a fitted 2nd order polynomial between 776 and 1074nm (Cudahy et al., 2008). Composite masks, which comprise of dry vegetation, green vegetation and albedo at 1650 nm have been applied to the depth of the ferric iron feature.

The resulting scaled iron oxide surface map is shown in figure 4.20. The high abundance of iron oxides is mainly confined to Quaternary recent deposits and erosional areas (Cz) in Block G Tick Hill. Besides shales or ferruginous sandstones, iron oxides are unlikely to be associated with fresh rocks, and therefore this mineral group distribution is most likely linked to regolith materials on the surface, and regolith variation will be described and discussed in chapter 5.

Table 4.4: Processing sequence used to map iron oxides (after Cudahy et al., 2008)

Map Product	**Base Algorithm (spectral indices)**	**Mask (Filter)**	**Linear Stretch**	**Color Chart**	**Accuracy**
HyMap Iron oxide	Normalized depth fitted 2nd order polynomial between 776 and 1074nm -900nm (MMTG A-List) **OR** $(b_{23}+b_{43})/(b_{29}+b_{35})$ $(R_{774}+R_{1058})/(R_{859}+R_{937})$ for validation	Composite mask (dry veg, green veg, albedo)	Min 0.001 Or 0-255 In RGB	Rainbow Red: high Blue: low	Moderate ; mix with vegetation a bit

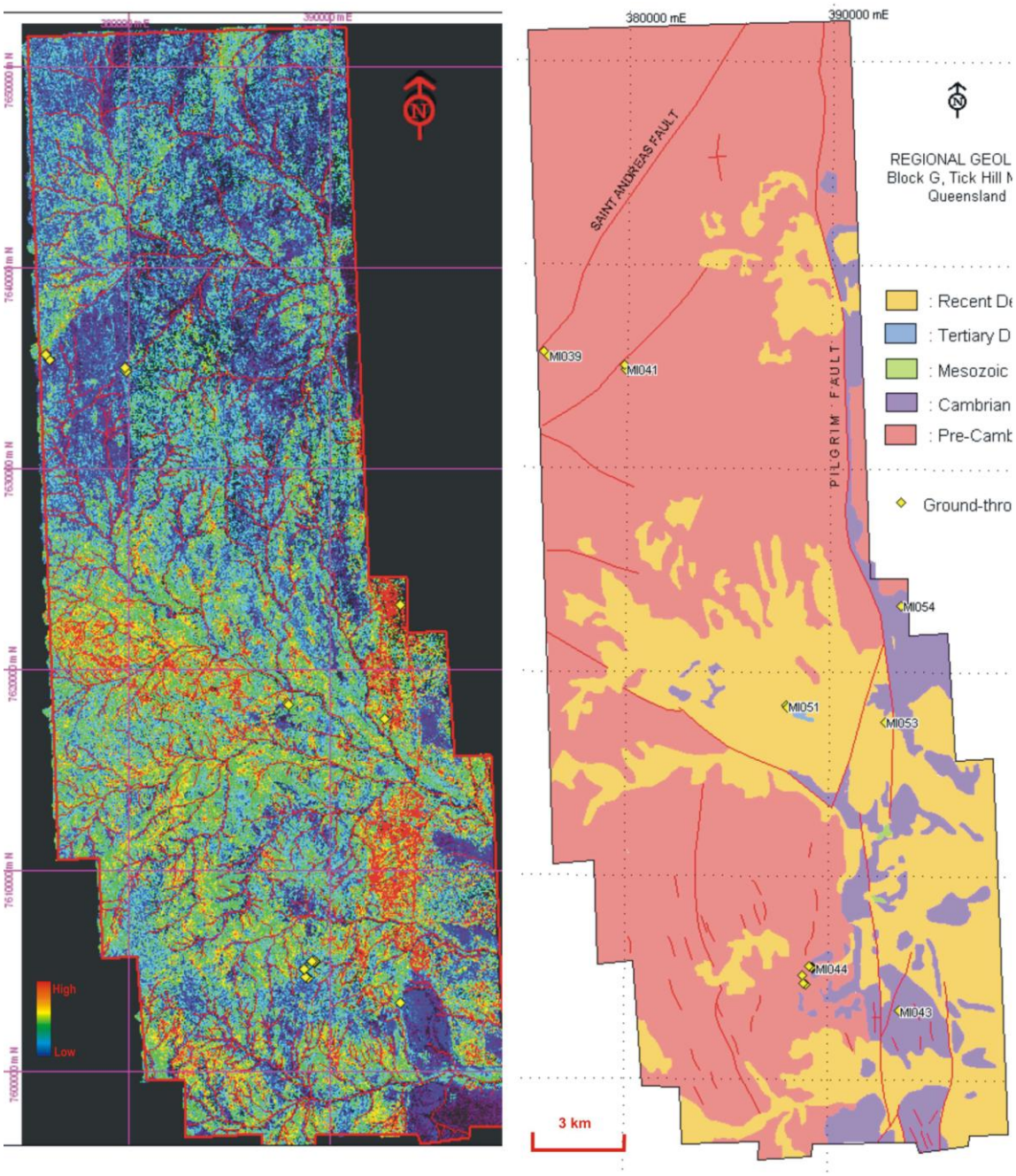

Figure 4.20: HyMap ferric iron content (goethite, hematite possibly jarosite) in Block G Tick Hill (left image). The iron oxide abundance is related to recent deposits (right image, regional geology map). Iron oxide distribution is likely related to weathering and regolith, which are covered in chapter 5.

4.3.3 Validation of Iron Oxide Mapping using ASD field spectra

Based on XRD and ASD spectra, hematite and/or goethite were identified in 14 ground samples (mi042f3, mi042f5, mi042w4, mi042w7, mi044w1, mi045f3, mi045w2, mi052w1, mi054f1, mi054f2, mi054f3, mi054s1, mi054w1, mi054w2). Most of them are associated with kaolinite.

1. Validate ASTER Iron Oxide map

Figure 4.21 and figure 4.22 represent the correlation between the two ASTER band ratio methods used to map iron oxide abundance with the iron oxide (mainly goethite and hematite) content identified from ASD spectra of field samples. The ASD spectra were resampled to ASTER band width and plotted against the iron oxide band depth identified from ASD. The correlation between the two allows an assessment as to which method is better to map iron oxides. The correlation for both methods is moderate at best with the band ratio 4/3 being slightly better (R^2= 0.519) than band ratio 2/1 (R^2=0.4006). This result confirms the visual image interpretation that ASTER band ratios are not very effective in mapping iron oxides. One reason for this poor result could be the influence of vegetation within the bands chosen.

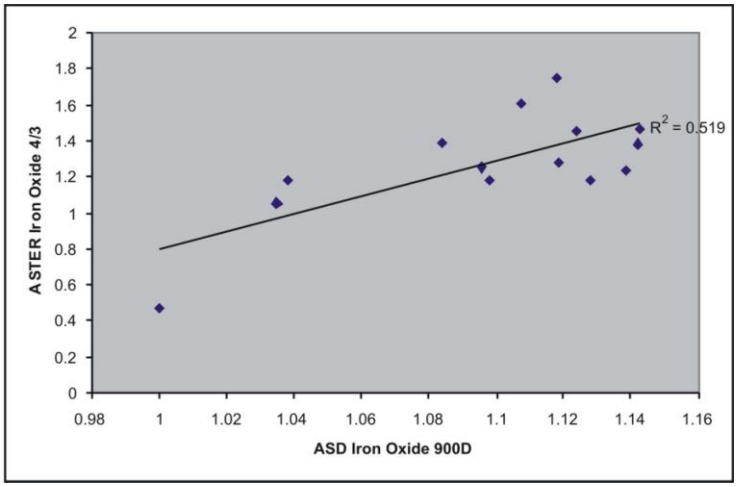

Figure 4.21: Scatter plot of ASTER band ratio 4/3 values against calculated ASD spectral of field samples resampled to ASTER band widths.

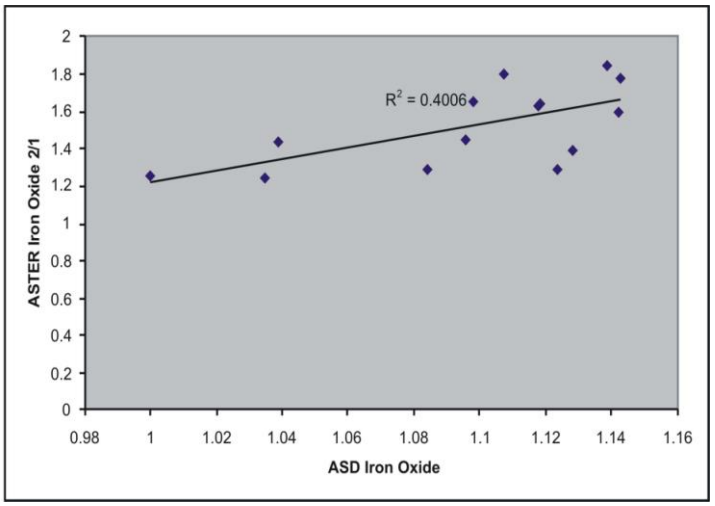

Figure 4.22: Scatter plot of ASTER band ratio 2/1 values against calculated ASD spectral of field samples resampled to ASTER band widths.

2. Validating HyMap Iron Oxide map

Figure 4.23 represent the correlation plot of band depth of ferric iron estimated from RBD $(b_{23}+b_{43})/(b_{29}+b_{35})$ of the HyMap pixel and the band depth of ferric iron extracted from field samples acquired from same pixel (n = 14 samples). The high correlation between the two suggests that unlike the result for ASTER, HyMap is effective at mapping the abundance of iron oxides.

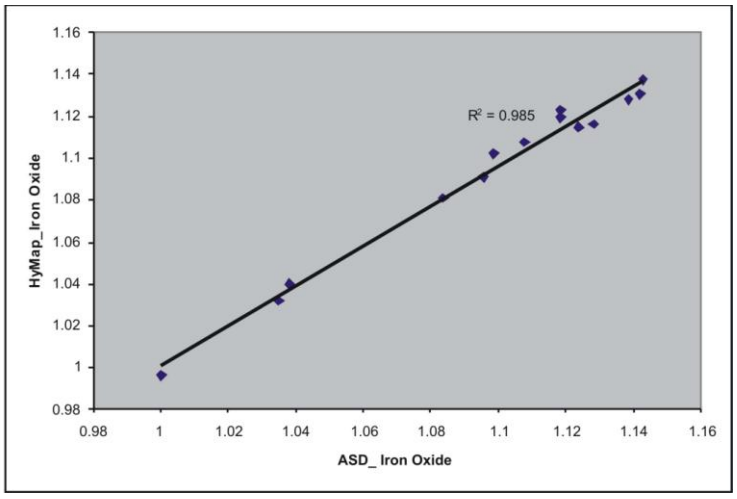

Figure 4.23: Scatter plot of HyMap RBD $(b_{23}+b_{43})/(b_{29}+b_{35})$ values against calculated ASD spectral of field samples re-sampled to HyMap band widths.

4.4 Mg-OH mineral group and Carbonates group Mapping

Carbonate minerals on the surface in Tick Hill region mostly appear in the form of the regolith material calcrete, as reported for the Mt. Isa region (Anand et al., 2002). The composition of the carbonates is varied ranging from Mg rich (dolomite) and Ca rich (calcite).

Carbonate minerals and Mg-OH bearing minerals such as Mg-chlorites, epidotes and hornblende can be identified and mapped via remote sensing methods (Cudahy et al., 2005; Gozzard, 2006). The carbonates are mapped on the CO_3 absorption at 2350 nm, but this is very close to the main Mg-OH absorption (Clark, 1999). However, subtle differences in wavelength for individual carbonate minerals and chlorite minerals exist, which has the potential to distinguish one from the other. The presence of carbonate has significant impact for investigation of resources of an area. Hewson et al. (2006) examined the carbonate abundance including Mg-OH and chlorite using spectral mapping method to highlight manganese mineralization in Woodie Woodie Western Australia.

Figure 4.24 show the similarity of both carbonates minerals and Mg-OH bearing minerals in USGS spectra library.

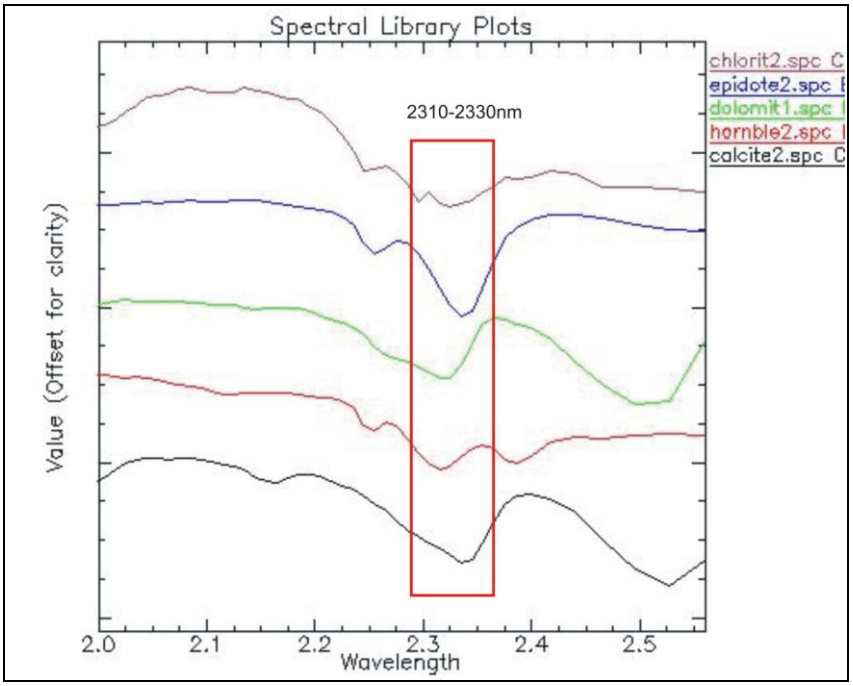

Figure 4.24: Spectra of carbonates (dolomite and calcite) and Mg-OH bearing minerals (epidote, hornblende, chlorite) from USGS spectra library, showing the similarity in absorption of the main 2350 nm peaks. (Clark *et.al*, 2007).

4.4.1 Mapping of carbonates using ASTER

Several studies have reported the success of using ASTER SWIR band ratios to map carbonates and Mg-OH minerals. RBD of (6+8)/7 have been employed to highlight carbonates, chlorite and epidote (Rowan and Mars, 2003; Hewson et. al, 2004). In addition, RBD of (6+9)/8 also can delineate Mg-OH mineral group and carbonates. For this study, the ASTER band combination of (6+8)/7 was used to produce carbonate and Mg-OH mineral map of the area and the results are shown in figure 4.25

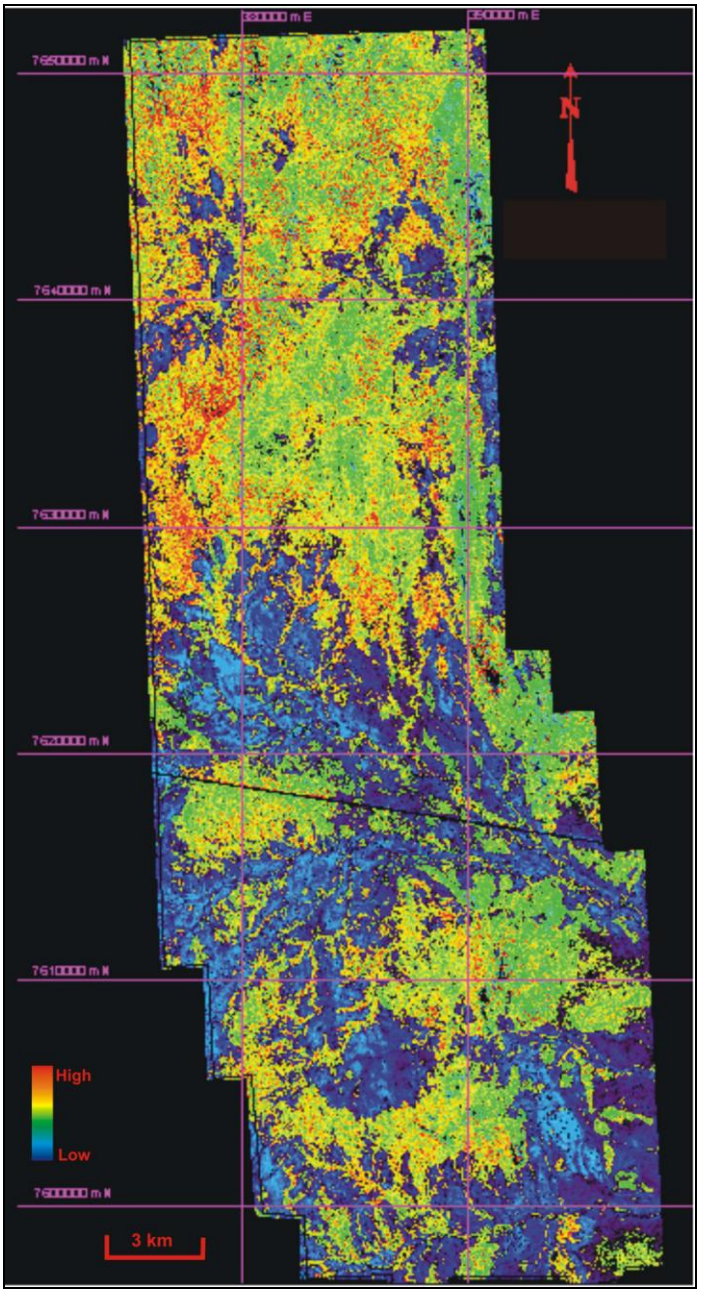

Figure 4.25: ASTER MgOH-carbonates mineral map produced using RBD (6+8/7), Red indicates high abundance and blue indicates low abundance.

The image shows carbonates and Mg-OH group minerals are concentrated in the northern part of Tick Hill region which is occupied by Precambrian rocks composed mainly of meta-volcanic, foliated granite, pegmatite and gneiss. The Mg-OH minerals mapped seem to be present over fresh to weathered Precambrian rocks and are likely to be either primary minerals (amphiboles) or alteration minerals (mainly chlorites and carbonates). It is important to note that the broad band nature of ASTER sensor precludes identifying individual CO_3 and Mg-OH bearing minerals from their main absorption features that subtly vary in wavelength in the 2300nnm range. Therefore, pure carbonate and Mg-OH spectra are difficult to separate in the image. Furthermore, the carbonate signal is affected by residual crosstalk errors which are most noticeable in low albedo areas (Hewson et al., 2004).

4.4.2 Carbonates and Mg-OH mineral group Mapping using HyMap

Similar to ASTER bands, HyMap spectral resolution may not be able to individually distinguish and map carbonates as a single mineral such as dolomite and calcite, and may include mixtures of Mg-OH bearing minerals, mainly hornblende, Mg-chlorite and epidote due to their similar absorption depth range at 2310 - 2330nm.

The two methods used to map Mg-OH bearing minerals via HyMap were RBD (Ratio Band Depth) and Spectral Feature Fitting (SFF). To test the methods, a case study of line 63 in Block G which has the open cut gold mine within it was conducted. (figure 4.1).

4.4.2.1 SFF method for Carbonates and Mg-OH mineral group mapping

Carbonates and Mg-OH mapping was created using Spectral Feature Fitting method (SFF) with end member spectra taken from ground truth spectra measurement of sample mi039f1 which shows carbonates (dolomite) spectra absorption at 2316 nm (corresponding to band 115 in HyMap). This end member was taken to map the carbonates separating them from MgOH. The resulted image shows a poor relationship between the occurrences of high to moderate carbonate as shown in the pixel (yellow to green) which corresponds to the field sample mi48f1. The pixel spectra show a broad absorption feature between 2310-2340 nm. The field spectra for mi48f1 is closer to hornblende showing sharp 2310-2315 nm absorption feature as opposed to carbonate 2325-2330 nm (in this case is dolomite)(see figure 4.26). Therefore, for SFF, dolomite and hornblende spectral feature overlaps are not resolved from HyMap data. The SFF

HyMap dolomite mineral maps show that HyMap band width cannot separate between hornblende and dolomite.

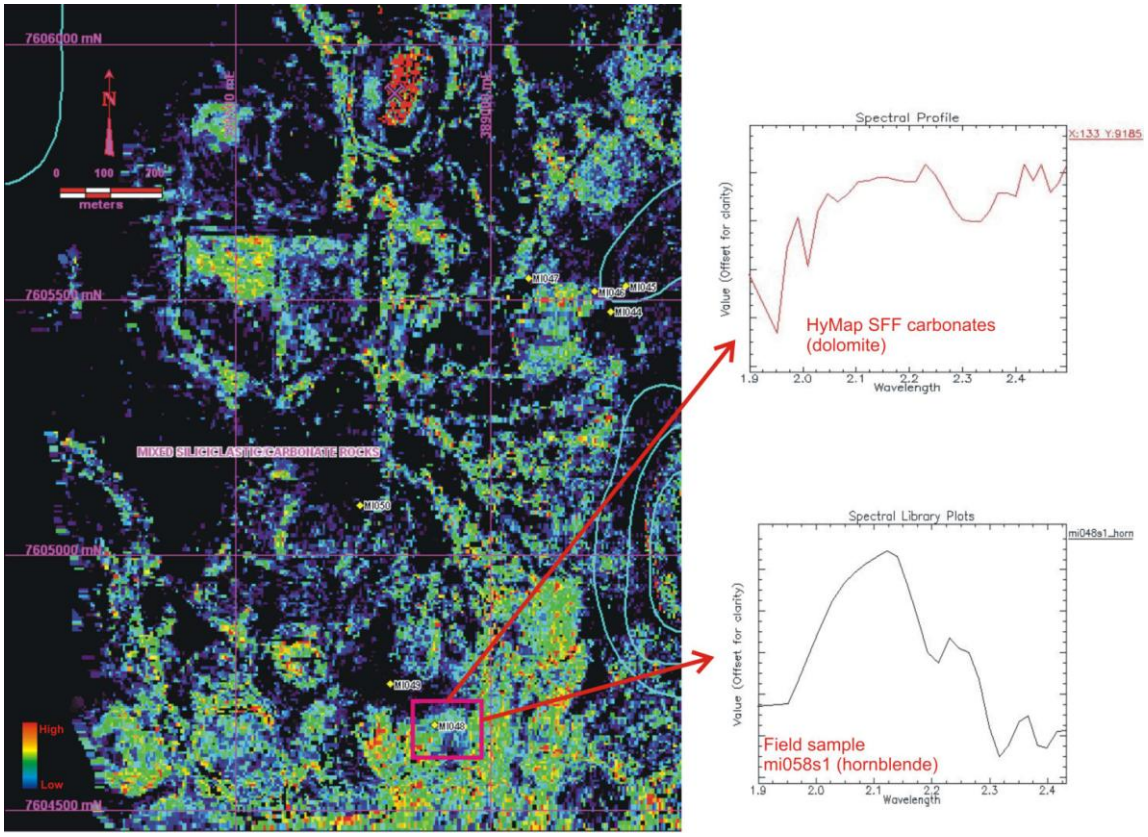

Figure 4.26: Carbonates and MgOH minerals created using SFF method and ASD end-member (mi039f1). Field sample mi058 spectra from a location shows presence of MgOH minerals (hornblende) as sharp 2.30-2.32 μm feature. Also shown is pixel spectra for the same location which shows a broad absorption feature between 2.30-2.34.μm.

4.4.2.2 RBD method for Carbonates and Mg-OH mineral group mapping

The RBD method has been used to map carbonates and Mg-OH mineral groups (calcite, dolomite, chlorite, epidote, amphibole, talc and serpentine). From the reference spectra, an absorption feature related combination algorithm was constructed using RBD $(R_{2265}+R_{2349})/(R_{2316}+R_{2333})$ or in terms of HyMap bands or the band formula of $(b_{112}+b_{117})/(b_{115}+b_{116})$. This formula highlights minerals with absorption peaks around 2320 – 2330nm. The composite mask of dry vegetation, green vegetation and albedo has been applied to the basic algorithm to mask out those three materials. Subsequently, another mask of kaolinite abundance at 2200nm with threshold < 1.005 was applied (Table 4.5). The resultant image is referred to as showing "carbonates and Mg-OH content" which represents group of minerals rather than individual mineral.

Table 4.5: Processing steps used to make carbonate and MgOH map (Cudahy et al., 2008).

Map Product	**Base Algorithm (spectral indices)**	**Mask (Filter)**	**Linear Stretch**	**Color Chart**	**Accuracy**
HyMap Carbonates and MgOH content	$(b_{112}+b_{117})/(b_{115}+b_{116})$ $(R_{2265}+R_{2349})/(R_{2316}+R_{2333})$ Including validation	Composite mask HyMap kaolinite abundance; Threshold <1.005	Min 0.001 Or 0-255 In RGB	Rainbow Red: high Blue: low	Moderate-Low Blue (low); mix with 2200D and 2350D white mica Red (high); typical carbonates at 2300-2400nm

Figure 4.27 represents the image of Mg-OH and carbonates of the selected area. High abundance of the mapped minerals (calcite, siderite, amphibole and chlorite) is represented by red and low abundances in blue. Field spectra sample at specific location mi048 (see figure 4.26) shows presence of dolomite and hornblende, but the same location in the Mg-OH + carbonates image appears green, which corresponds to moderate abundance. The issue regarding presence of mineral mixtures within the map is still likely to be a contributing factor. For example, the image shows a mix of kaolinite and white micas which have a minor spectral feature at 2350nm, and can be incorporated with the Mg-OH minerals spectral peak.

The occurrence of carbonates and Mg-OH bearing minerals is related to the bedrock. High abundance of carbonates and Mg-OH is associated with the Corella Formation, which consists of carbonate rocks mixed with silisiclastic rocks, which are composed of calcareous siltstone, limestone, calcareous scapolitic granofels, quartzite, amphibolite and shale (Blake et al., 1982).

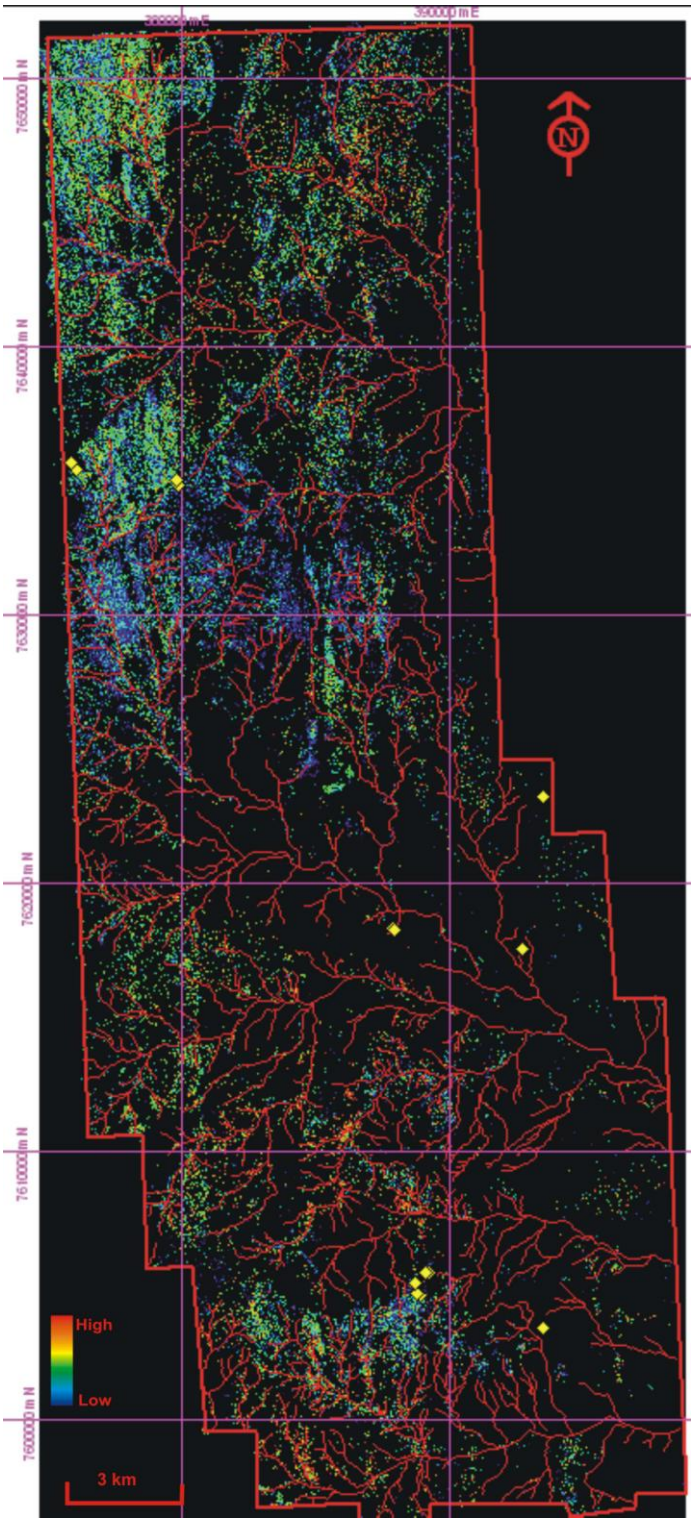

Figure 4.27: HyMap image of carbonates and Mg-OH of Block G using RBD method. The presence of these minerals is likely related to bedrocks exposures.

4.4.3 Validation of Carbonates and Mg-OH mineral group

Approximately 15 samples taken from 6 locations showed absorption features indicative of carbonates (mi039f1, mi039f3, mi039f4, mi039w1, mi039w2, mi039w3, mi039w4, mi042f3, mi043f1, mi043f2, mi046f1, mi046w1, mi046w2, mi048s1 and mi050w1) (figure 4.28). The strong absorption peaks between 2310-2350 nm were used but these could also relate to Mg-OH minerals such as hornblende. Some samples - mi039f1, mi039f2, mi039w2, mi042f3 and mi050w1 – suggested presence of dolomite with peaks at 2325 nm. Carbonates occur in fresh and weathered rocks and are often associated with clay minerals and iron oxides.

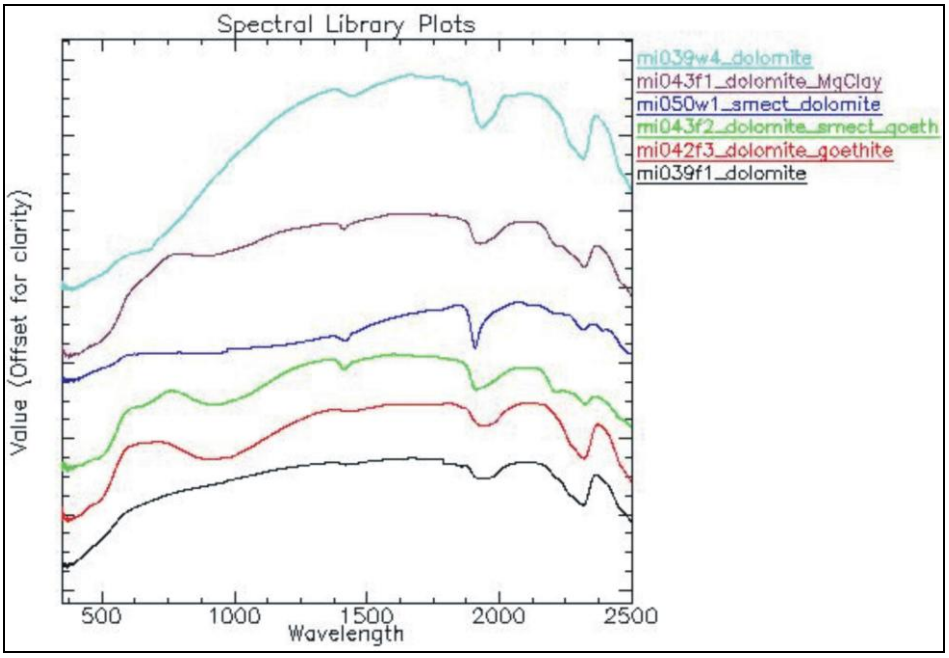

Figure 4.28: Spectra pattern derived from Tick Hill samples containing dolomite.

In addition, due to the similar absorption for carbonates (dolomite) and chlorites, it is often difficult to identify pure dolomite (class of carbonates) or pure chlorite (class of MgOH), unless the spectra has iron related absorption features between 700 to 900nm. However, the presence of iron oxides in weathered samples precluded identifying chlorite from other carbonates. X-Ray Diffraction of the field samples mi047f1 and mi047f2 identified some chlorite in the samples (see the appendix 3: XRD result analysis). Thus, many carbonate samples identified as such from ASD spectra, are or could be a combination of carbonates and Mg-OH minerals.

1. Validation of carbonates and Mg-OH mineral groups from ASTER

Regression analysis has been used to validate the ASTER RBD (b6+b8)/(b7) which capture carbonates and Mg-OH bearing mineral group by resampling 15 field spectra containing mixture of carbonates and Mg-OH minerals into ASTER bandwidth. The resulting correlation coefficient was $R^2 = 0.9013$ (n = 15). This high coorelation suggest the ASTER RBD method was reasonably effective in mapping carbonates and Mg-OH bearing minerals together.

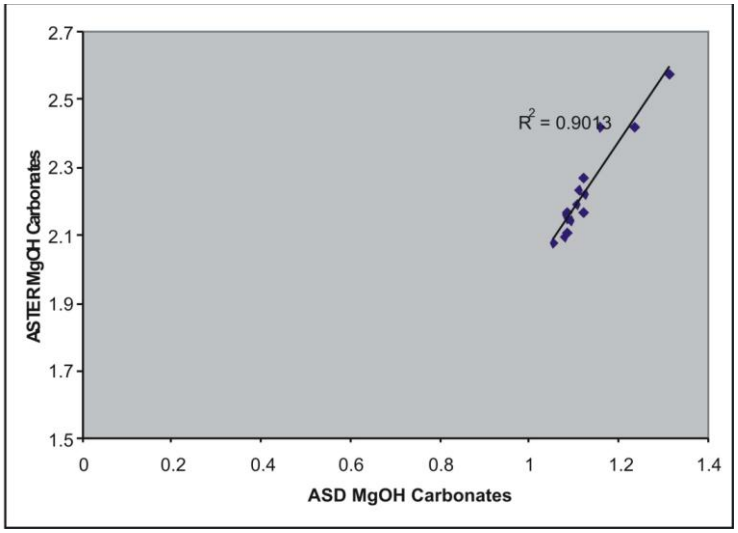

Figure 4.29: Scatter plot of ASTER {(b6+b8)/(b7)} RBD values from pixels and corresponding ASD field sample spectra values using same RBD.

2. Validation of HyMap Carbonates and Mg-OH mineral groups

Comparison of values estimated for carbonates and Mg-OH mineral group calculated from HyMap RBD of $(R_{2265}+R_{2349})/(R_{2316}+R_{2333})$ and those calculated from ASD spectra for ground samples from the same pixels showed a very high correlation of .99 (figure 4.30). This very strong correlation indicates that the HyMap based RBD method is effective in mapping carbonates + Mg-OH mineral groups.

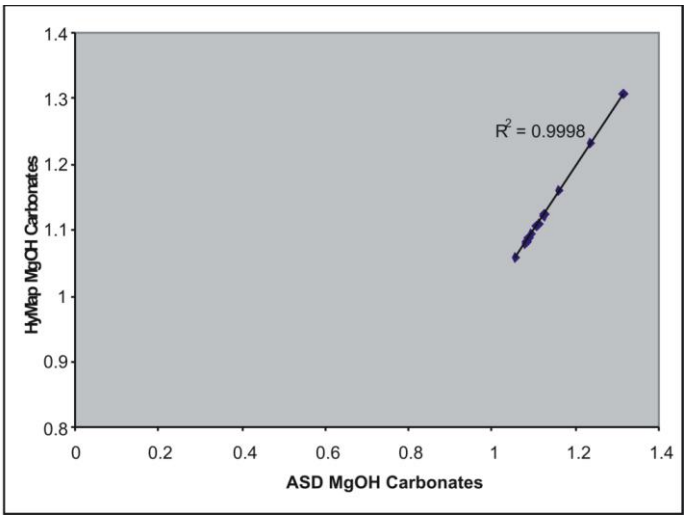

Figure 4.30: Scatter plot of HyMap RBD method for Mg-OH and carbonates against similar RBD for ASD field spectra for same pixels.

4.5 Opal Silica Mapping

Opal silica, which includes opal-CT (Smith, D.K., 1992) and opaline silica, is common in the regolith, especially silcretes (Taylor and Eggleton, 2001). It is also part of hydrothermal alteration and therefore its detection is important to earth surface mapping and exploration (Brown et al., 2006). Field observations showed the presence of siliceous material outcrops resembling silcretes, which were confirmed to be composed of opal silica or opal-CT. Therefore, an attempt was made to test whether opal silica (opal-CT and opal-A), could be mapped using remote sensing.

The SWIR spectral features of opal silica are broad features. The Si-OH absorption feature for opal silica from reference spectra shows the broad feature at around 2240nm (Hunt 1977; Clark 1999) (Figure 4.31).

In the thermal wavelength range, silica bearing minerals are more easily detected. The thermal band ratio of ASTER has been employed to map silica group in general (including quartz) using band 12/10 (Ninomiya et al., 2005; Mars&Rowan, 2006). The broad bands of ASTER preclude the identification of opal silica. Therefore, the procedure to make opal silica maps will only use HyMap data.

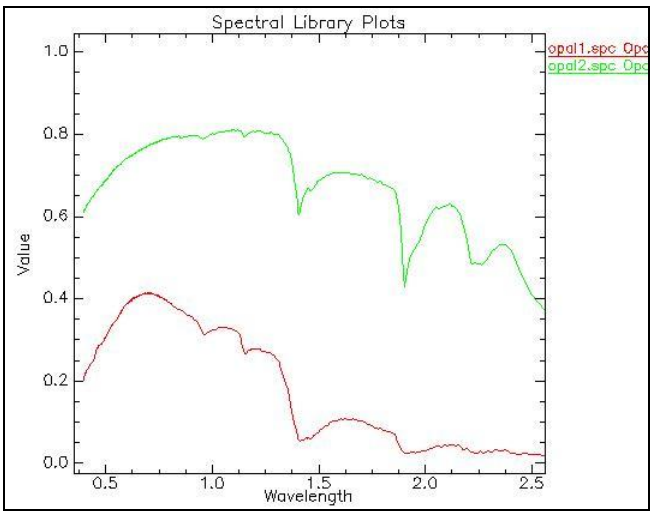

Figure 4.31: Opal silica spectra showing diagnostic broad absorption feature around 2240nm (USGS Spectral Library). (Clark *et.al*, 2007).

For HyMap data, two methods were employed to test the potential to highlight opal silica. The first is Spectral Feature Fitting (SFF) method where the Si-OH feature is fitted to the HyMap data, and the second is spectral indices method which has been used for other minerals.

4.5.1 HyMap Opal Silica Mapping with SFF method

The SFF method has been applied to opal silica mapping using pure endmember opal silica spectra from field samples. The ASD field sample spectra (sample mi052f1) shows a broad spectral feature at 2200 - 2240nm which conforms to opal silica and has been confirmed via XRD (appendix 3: XRD result of Tick Hill samples). Data used for silica mineral extraction was first masked for dry and green vegetation.

The results for opal silica map produced via the SFF method are shown in figure 4.32. The accuracy of silica distribution is difficult to judge. High occurrence of opal silica is shown in the mine site by the red colors. The spectra from the mine site showed a lot of noise in the band absorption and it is not clear as to whether opal silica is present. Furthermore, the pixel represented as high to moderate opal silica on the SFF produced image (red to yellow pixels) when compared to ground samples, show field spectra for those points to be dominated by Al-OH absorption at 2200nm (sample mi044, see figure 4.32). Therefore, the SFF method used appears to have spectral overlap problems with Al-OH minerals and is not effective in mapping opal silica.

.

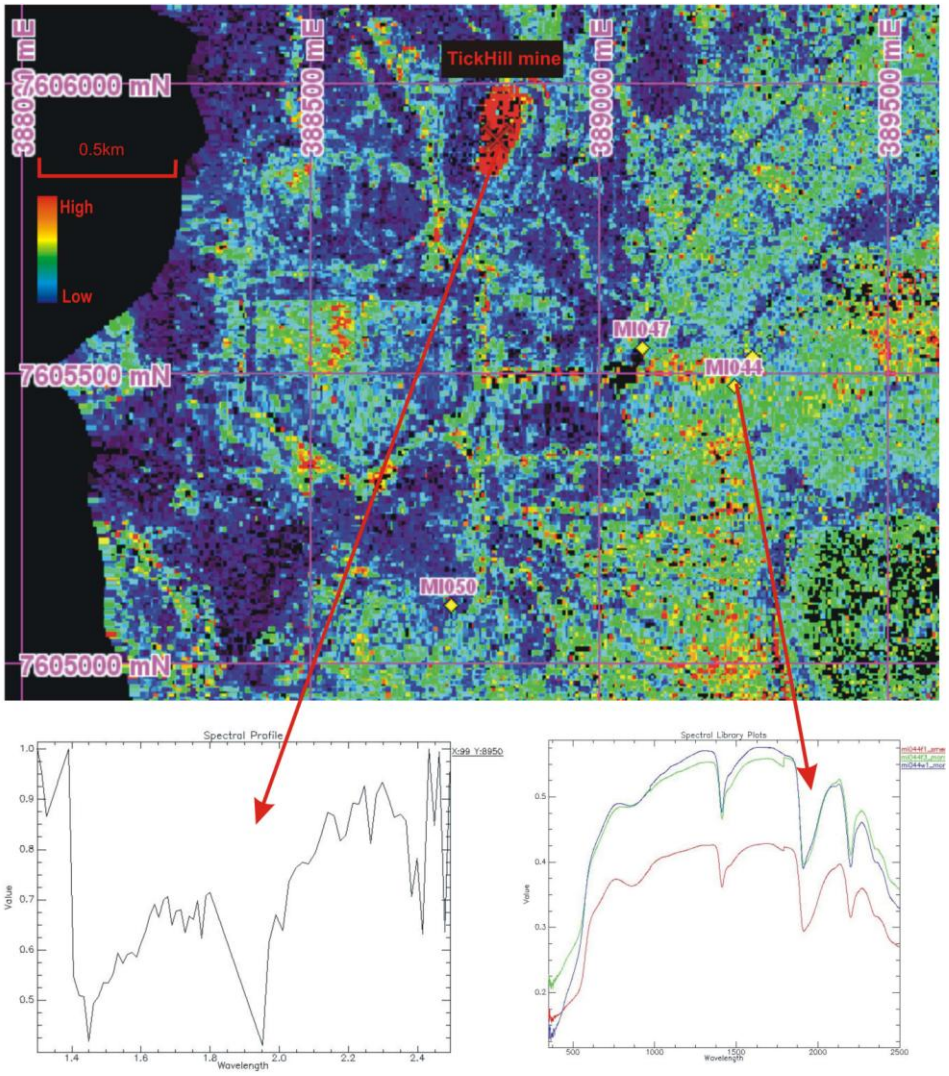

Figure 4.32: SFFmethod produced opal silica map from line_63 TickHill mine. HyMap derived spectra from the Tick Hill mine is dominated by noise (left spectra) and ASD spectra of field sample containing opal silica (mi044 mix) showing broad Al-OH absorption at 2200nm (right spectra).

4.5.2 HyMap Opal Silica Mapping with RBD Method

An attempt to map opal silica was made using the RBD method. The broad absorption feature of opal silica makes it difficult to constrain the band combinations for opal silica, but based on the reference opal silica spectra, couple of band combinations were constructed and tested. The two spectral indices combinations are described below.

1. Opal Silica map with RBD 1

The first RBD considered was $(b_{105}+b_{116})/(b_{110}+b_{111})$ or $(R_{2140}+R_{2333})/(R_{2229}+R_{2247})$ to highlight the absorption depth around 2240nm. The resulting image shows high abundance of opal silica along the mesa sides or slopes (there are two mesas in the Tick Hill test site; Line_65_BlockG_TickHill) and the slope

of open pit mining site. The spectra from pixel location potentially showing high opal silica (red in image of figure 4.33), shows a spectra in the range 2100-2400 nm to be similar to kaolinite (figure 4.33). The pixel spectra has characteristic doublet around 2260 nm which is typical of kaolinite. Further, mesa slopes are dominated by kaolinite as indicated by the kaolinite mineral map. Thus, the mineral map of opal silica produced from the RBD combination matches that of kaolinite abundance and therefore the selected RBD combinations cannot be reliably applied for opal silica mapping (see Figure 4.33).

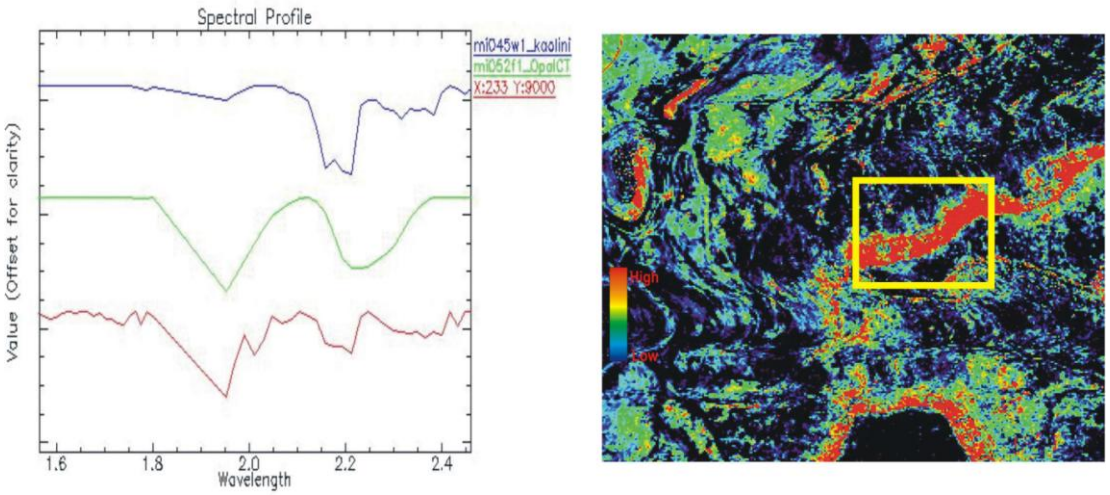

Figure 4.33: The right image is an RBD image generated using $(b_{105}+b_{116})/(b_{110}+b_{111})$ to map opal silica and shows possible high abundance along mesa slopes. The left image is spectra taken from boxed area. The red spectral is from the boxed area on image, while green and blue are opal CT and kaolinite respectively taken from the ASD field spectra measurement at the same areas.

2. Opal Silica map with RBD 2

The second RBD has been simulated based on wider absorption of opal silica in 2200- 2240nm. RBD $(b_{104}+b_{119})/(b_{110})$ or $(R_{2122}+R_{2382})/(R_{2229})$ is applied to continuum removed reflectance to get less noise of overlapping spectra. The resulting mineral map image is shown in figure 4.34. High abundance of the targeted mineral (opal silica) is shown in red but its distribution again matches that of kaolinite and white mica distribution with the sharp spectra absorption centered at band 109 (2212nm). Interestingly, in Tick Hill open pit mining location, the spectra indicate the absorption depth at 2212nm and 2349nm which correponds to the white mica/illite spectra absorption features. White micas minerals are part of the hydrothermal alteration

(Brown et al., 2006). The RBD combination used does not adequately appear to map opal silica.

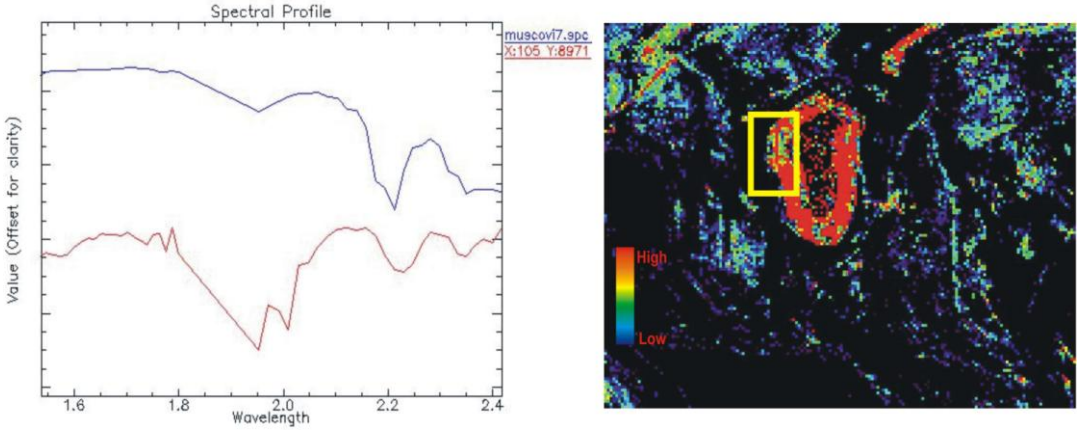

Figure 4.34: The right image is a opal silica map produced using HyMap band combination $(b_{104}+b_{119})/(b_{110})$, the yellow box is Tick Hill open pit mining location. Left image shows two spectra; one from pixel within the red area on image and the upper spectra is white mica.

4.5.3 Spectral Indices Method using MMTG A-List software to map opal silica on HyMap

Cudahy et al. (2008) used this method to extract the expected pure opal silica absorption feature corresponding to the broad Si-OH absorption at 2240 - 2250nm. The area for testing this method is around Mayfield station where the two field samples contents of opal silica were taken. The spectral feature of interest was fitted with a 4^{th} polynomial order for relative feature depth between 2140nm and 2365nm. Three masks were applied:

1. Mask Al-OH absorption at 2200nm
2. Mask Mg-OH at 2330nm
3. Mask white mica interruption at 2200nm and 2350nm

The sequence of operations is listed in table 4.6.

Table 4.6. Procedures used to make opal silica map (after Cudahy et al., 2008).

Map Product	Base Algorithm (spectral indices)	Mask (Filter)	Linier Stretch	Color Chart	Accuracy
HyMap Opal silica	Normalized depth 4^{th} order polynomial between 2140nm and 2365nm **OR** $(b_{104}+b_{117})/(b_{110}+b_{111})$ $(R_{2122}+R_{2349})/(R_{2229}+R_{2247})$ for validation	Al-OH absorption;mask >1 Mg-OH $(b_{112}+b_{117})/(b_{115}+b_{116})$ mask < 1.1035 HyMap white mica content; mask < 0.015	Min 0.001 Or 0-255 In RGB	Rainbow Red: high Blue: low	Moderate: opal silica mix with Al-OH absorption at 2200D.

The mineral map image produced by applying the procedure in table 4.6 shows opal silica occurring in selected locations (figure 4.34). These locations correspond directly to samples bearing opal silica as identified from field and lab spectra of those samples. Field spectra of those particular samples show broad 2200-2240 nm absorption typical of opal silica and the presence of opal silica was confirmed by XRD. In previous RBD methods to map opal silica, the Tick Hill mine was shown to have high opal silica content (figure 4.34). In the map produced from spectral indices, the same mine shows little opal silica presence (figure 4.35). Therefore, the spectral indices method after applying a sequence of masks to eliminate overlap from Al-OH and Mg-OH absorption appears to map silica.

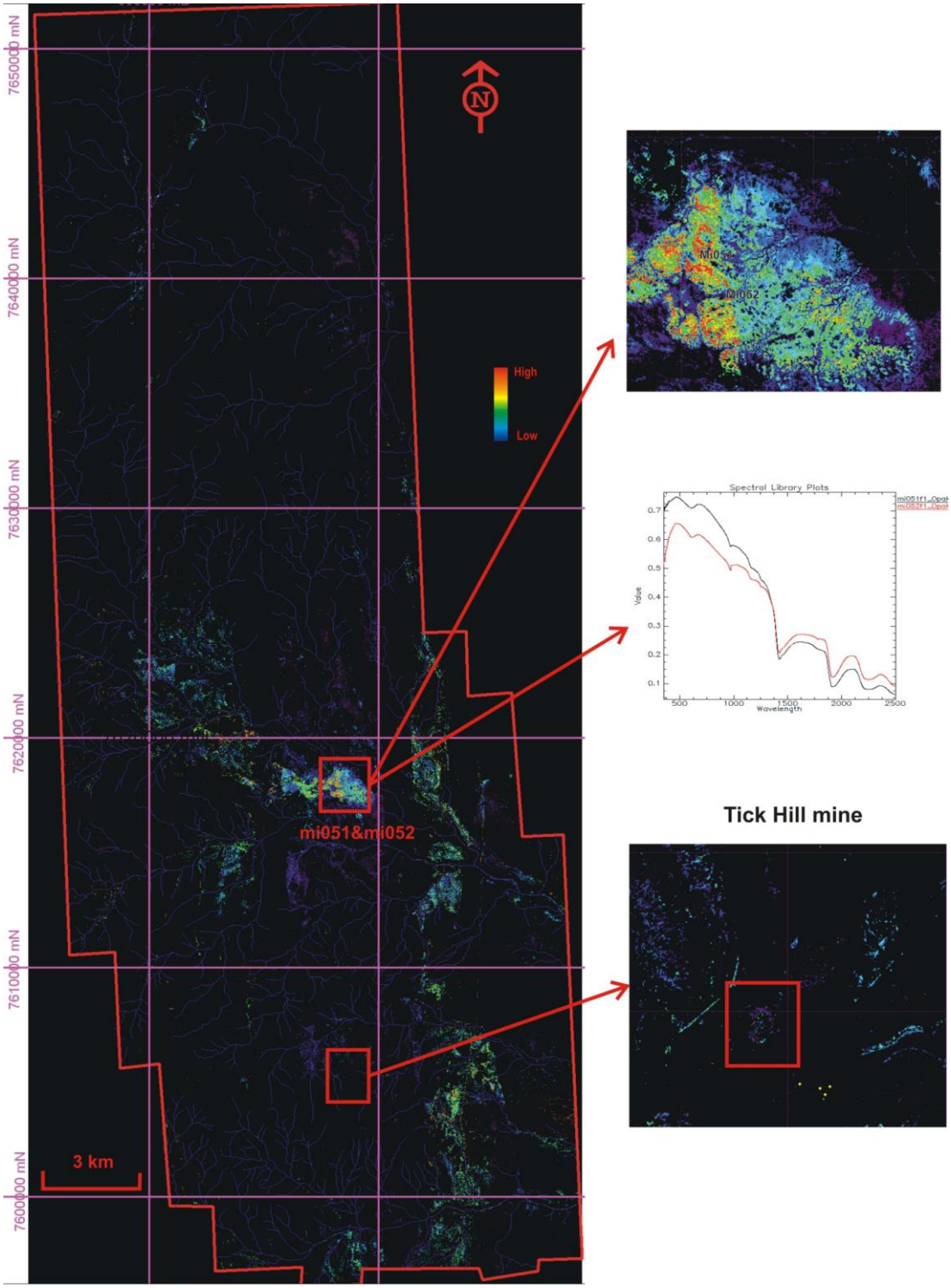

Figure 4.35: Map of opal silica (block G line_63) produced using spectral indices method and masked for Al-OH, Mg-OH and white mica content. The top inset image shows high opal silica which matches with ground spectra of the area showing broad Si-OH absorption features. Lower inset image shows the Tick Hill mine which has low or negligible opal silica.

4.6 Discussion and Conclusions

Mineral maps derived from relative band depth ratios of ASTER and HyMap data and spectral indices methods, and subsequently validated by ground sample spectral measurements including XRD analysis, showed the sensors to be effective in mapping the minerals. However, some spectral overlap related difficulties were encountered for specific minerals. Mapping of most minerals via both multispectral and hyperspectral datasets, required a sequence of masks to be applied in order to minimize spectral contribution of one material or mineral to the mineral being mapped. The main mask was a composite mask of green + dry vegetation + albedo.

Kaolinite, white mica and iron oxides were easily mapped and validated for HyMap data. Kaolinite maps could be further separated based on their crystallinity or disorder according to the value of the asymmetry in the main Al-OH peak and depth of the 2162 nm peak. White mica and smectite minerals (especially if Al rich smectite) were difficult to resolve with RBD method due to the overlaps of absorption features of the two minerals. Carbonates and Mg-OH bearing minerals (hornblende, chlorite, epidote) also showed spectral overlap difficulties and the maps produced by RBD were better classified as combination of carbonates and Mg-OH minerals rather than separate maps. Opal silica mapping was attempted with experimental RBD combinations, although spectral overlap between broad opal silica related Si-OH spectral feature and Al-OH and Mg-OH features made it ineffective. The spectral indices method to fit the broad absorption feature with masks of Al-OH and Mg-OH provided an effective result. This suggests that spectral indices method may be a powerful technique for complex overlap problems and in the future spectral indices could be employed to separate white mica from smectite, carbonates from Mg-OH minerals and goethite from hematite as proposed by Cudahy et al (2008).

The main difference between ASTER and HyMap data derived maps was the poor spectral, and to an extent spatial resolution of ASTER. Many of the validation results for ASTER showed slightly lower correlation coefficients as compared to HyMap data. Iron oxide maps produced by ASTER appeared to be poorly validated, possibly because of vegetation overlap in bands 1 and 2. Many of the validation were slightly less effective for ASTER than for HyMap.

Chapter 5

Mineral Mapping Application for Regolith-Landform Mapping and Processes

The previous chapter dealt with spectral signatures of specific minerals, comparison of processing methods available to map minerals using multispectral and hyperspectral methods, making mineral maps using RBD and spectral indices methods and the validity of the maps produced as compared to ground spectra. In this chapter, the significance and application of the mineral maps to regolith are described, interpreted and discussed. The aim is to combine individual mineral or mineral assemblage maps with simpler band combination processing methods and DEM imagery to map regolith-landforms and interpret associated regolith processes such as spatial extent and degree of weathering, erosion-sedimentation and their impact on landscape evolution of the studied area.

Considering the large size of the Australian continent, it is vital to rapidly map regolith material distribution in the landscape and differentiate the residual regolith terrains from the transported settings, and remotely sensed imagery is ideal to make these regolith-landform maps (Pain et al 2000a, Tapley and Gozzard, 1992; Dehaan and Taylor 2004). The regolith-landform mapping and the interpretation of profile characteristics and differentiation of in situ from transported regolith is important to the design, implementation and selection of sample media for geochemical exploration programs (Anand et al, 2002b), as well as for environmental purposes. Another application of spectral remote sensing is mineral alteration mapping and interpretation of associated hydrothermal processes (Bierwith et al., 2002; Di Tommaso and Rubinstein, 2005; Brown, et al. 2006; Ducart, et al. 2006; Mars and Rowan, 2006). It was not feasible to develop and apply alteration models to the Tick Hill area because of lack of fresh bedrock exposure, therefore the applications described here focused on regolith-landform mapping and associated processes.

5.1 Introduction to Regolith Landform Mapping Method

Regolith-landform maps attempt to show the spatial distribution of the mantle of regolith materials (including weathered rocks, sediments and soils, altered or formed by land surface processes) on the surface and imply 3D or even 4-D (time) information where possible. There are two contrasting methods of regolith-landform mapping (Taylor and Eggleton 2001); a factual or descriptive mapping scheme devised by Geoscience Australia (GA) and an interpretive mapping scheme devised by CSIRO Exploration and Mining and popularly known as Residual- Erosional – Depositional (RED) scheme. Both schemes use landforms as surrogates for mapping regolith. The GA Regolith-Landform Unit (RLU) scheme is used here, although when applying mineral maps to regolith processes, interpretation of regolith profiles and landscape processes are employed as envisaged by the RED scheme.

The Geoscience Australia Regolith Landform Unit (RLU) represents areas of the same regolith characteristic and similar landform for the mapable scale (Pain et al.,2000). The attributes for RLU description are; lithology, landform characteristics, mineral information, surface materials, regolith type and vegetation as combined surrogate for regolith mapping. A RLU code consists of three components; the regolith materials in capital letter, followed by landform in small letter and where applicable, a modifier number to represent the minor feature and variation in RLUs. This code is only a guide for the description and represents the general classification. For example, the regolith type of alluvial channel sediments (ah) present in the landform alluvial channel (AC) is represented on the map as ACah. If there are two contrasting ACah within the mapped area, then modifier numbers are used to differentiate the two as $ACah_1$ and $ACah_2$. The regolith landform types used are from the GA database of regolith and landform codes.

Regolith occurring within the landscape is generally divided into two main categories; *in situ* and transported. *In situ* regolith is formed by weathering of bedrock, and surface exposures of it are mainly confined to erosional landforms with the main regolith types being saprock, saprolite (different degrees of weathering are separated as slightly weathered, moderately weathered etc), residual sand or clay, mottled saprolite and residual “laterite” or duricrust(s). Transported regolith are fresh to weathered surficial deposits such as colluvium deposits (gravity), alluvium

deposits (fluvial), aeolian deposits (wind), lacustrine deposits (lakes) and beach deposits (waves) (Pain et al., 2000a; Taylor and Eggleton, 2001)

The aim for this chapter is to create regolith landform maps using the spatial mineral information derived from the mineral maps (HyMap) and simple RGB combination of HyMap and ASTER bands to interpret the regolith material, and combine it with landscape information to classify the regolith landform unit in Tick Hill region which is within the larger Mt Isa region. There are few published regolith-landform maps and associated regolith information from the Mount Isa region with the main source of information being a progress report by Anand et al., (2002) and other studies detailing regolith-landforms within the Mt Isa region (Anand, et al., 2002a; Wilford, 2003).

In addition, the multispectral and hyperspectral data are used to classify and map the regolith-landforms, and interpret the regolith nature underlying the different RLUs in the Tick Hill area. Multispectral and hyperspectral remote sensing have been used to classify and map surface regolith materials based on their surface spectral features (Tapley and Gozzard 1992; Dehaan and Taylor, 2006) although the link between regolith materials and landforms was not clearly defined.

For the study area, regolith-landform mapping is conducted via remotely sensed data; multispectral, hyperspectral and DEM, and other datasets such as geology maps and field information from previous studies for the area are utilized (Cudahy, et al., 2008). Specifically, three types of remotely processed data (spectral features and elevation) are used to make regolith-landform maps

- A broad scale regolith-landform map (~1:100,000) is constructed using specific HyMap and ASTER band combinations as RGB. This highlights surface spectral features related to regolith materials which are in turn linked to landform types.
- The broad spectral classes are combined with DEM to identify regolith-landforms. For this task, the ASTER 30m DEM was used as its resolution is better than the SRTM 90 m. Sectional profiles constructed from DEM provide information on the relative relief and 2D extent of landforms.
- Individual mineral maps constructed from hyperspectral data were used to subdivide and/or confirm regolith-landform, identify profile character underlying specific landforms and subsequently interpret landscape processes and events.

The regolith-landform maps and regolith information interpreted from these maps relies exclusively on spectral and height data and lesser on morphological characteristics of the regolith on ground, such as grain size variations and fabrics. This is a limitation of the maps produced. However, spectral information provides a valuable and at times unique tool to spatially map regolith materials and minerals, and greatly supplements, if it does not enhance field checking.

5.2 Broad scale of regolith landform unit using HyMap De-correlation Stretch and ASTER RGB combination

To map regolith on a regional scale, it is best to use a simple RGB combination to reveal different spectral classes of surface materials. An RGB combination de-correlation stretch is the simplest way to highlight the spectrally different regolith materials and vegetation as the band combinations separate classes of spectral responses based on mineral assemblages.

Much of the Australian regolith is dominated by Al-OH clays (kaolinite, illite) and iron oxides (hematite and goethite) (Taylor and Eggleton, 2001; Anand and Paine, 2002), and slightly weathered bedrock areas will be dominated by a combination of Mg-OH minerals (chlorite, amphiboles, carbonates) and Al-OH minerals (micas). Based on the reasoning of occurrence of specific minerals in the regolith that are spectrally responsive in the VNIR-SWIR region, and the corresponding HyMap and ASTER bands likely to express specific mineral assemblages, the variation in the amounts of the above minerals within individual regolith materials are likely to be expressed in an image constructed from the appropriately selected bands. One of the earliest remotely sensed methods employed to identify different regolith materials based on spectral differences was the LANDSAT band ratio in RGB (Tapley and Gozzard, 1992).

Specific HyMap and ASTER bands were used to highlight surface mineral differences based on the mineral or mineral groups being targeted. The HyMap bands; $band_{116}$ (2333nm), band $_{109}$ (2212nm) and $band_{29}$ (859nm) were used in an RGB combination because they highlight the absorption features related to the dominant composition of regolith materials. $Band_{116}$ (2333 nm) highlights Mg-OH and carbonates minerals, $band_{109}$ (2212 nm) highlights Al-OH minerals which are mostly clay layer silicates (kaolinite, illite, muscovite, smectite) and $band_{29}$ (859 nm) highlights the iron oxide and also some vegetation. For ASTER, the following band

combinations were used in RGB to highlight the regolith materials; for Red band ratio 4/3 which highlights iron oxide, for Green band combination of (b5+b7)/b6 which highlighted Al-OH bearing minerals and for Blue band combination of (b6+b7)/b8 which highlights Mg-OH bearing minerals. These band ratio combinations were also recommended by Rowan, et al. (2006) to highlight different surface mineral assemblages.

The HyMap RGB false color de-correlation stretch image of the designated bands is shown in figure 5.1. The RGB images represent the dominant materials, which are here interpreted as an iron oxide, Al-OH and Mg-OH bearing minerals. Materials rich in Mg-OH are seen as blue-green color areas, while the mix between Al-OH and iron oxide materials are represented by yellow-greenish to pink–magenta colors. Vegetation, however, does not stand out clearly in the RGB images and is better mapped via band ratios designated for it such as band26/band16 (chapter 3). From the color representation of the basic three mineral bearing ionic groups (Mg-OH, Al-OH and iron oxide), the blue-greenish hues in the image are interpreted as the weathered bedrock dominated areas (*in situ* regolith), while the area of green-yellowish represented as weathered colluvium. Pinkish-magenta areas are interpreted as high iron oxide materials, likely to be ferruginous duricrusts ("laterites") or ferruginous soils. In addition, surficial regolith materials rich in Al-bearing clays (kaolinite) appear in red to pink images. The de-correlation stretch image is useful to map the RLU characteristic in specific ways and allows a detailed analysis on a 1:25,000 scale (Lau, 2004). Together with the single mineral maps, regolith landform units can be interpreted in detail.

The ASTER band combination image is shown in figure 5.2. The false color RBG combination (R-band 4/band 3, G - band 5+band 7/band 6, and B - (band 6+band 7/band 8)) represents the degree of weathering of rocks. Blue – purple colors was interpreted as materials rich in Mg-OH and Al-OH bearing minerals. Green to yellowish colors is interpreted as materials composed of a mix of iron oxide and Al-OH, and the red colors as materials rich in iron oxide.

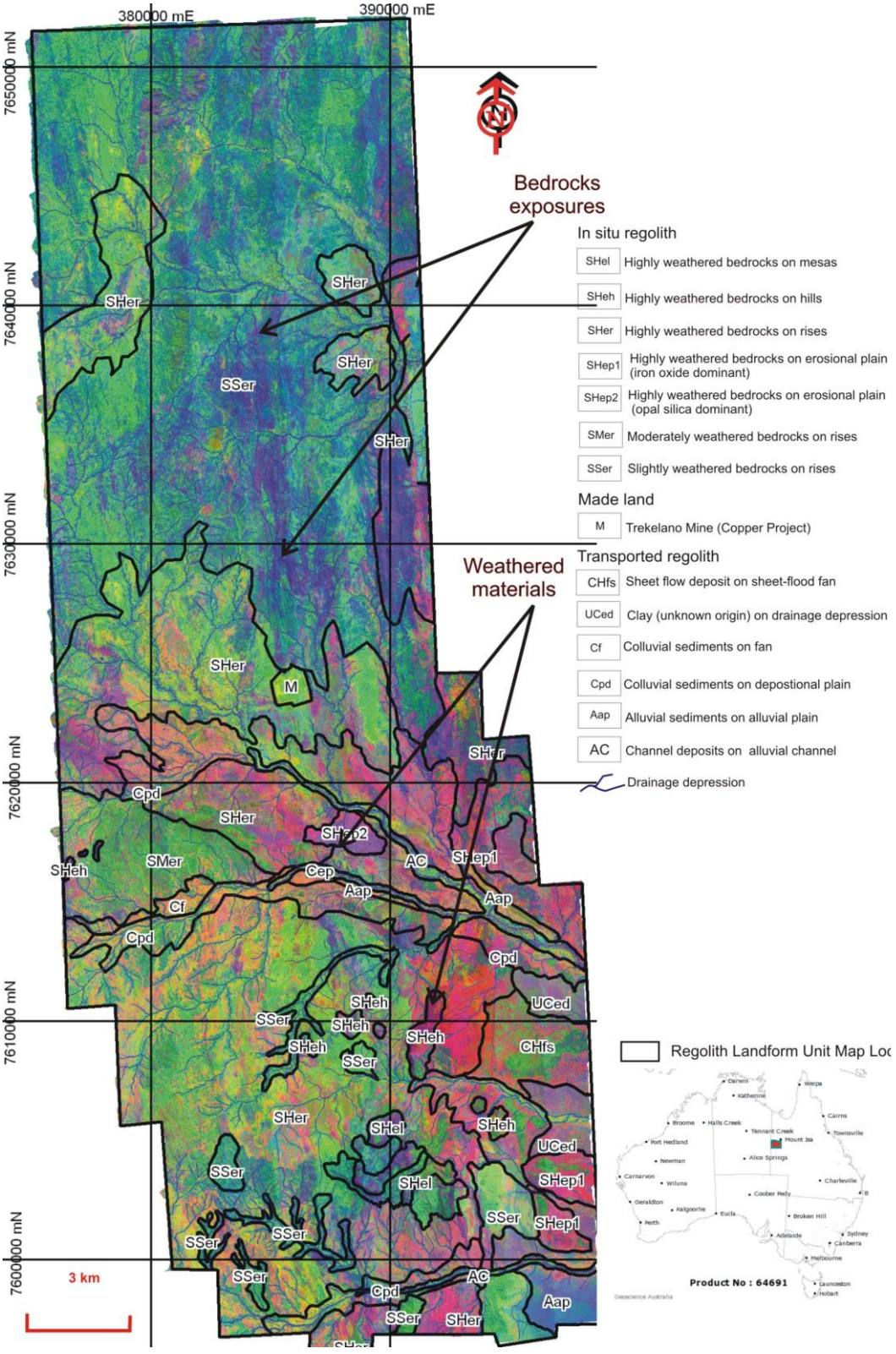

Figure 5.1: RGB de-correlation stretch of R_{2333}, G_{2212} and B_{859} created from HyMap data overlay on ASTER DEM 30m resolution. The RGB stretch highlights different regolith materials (slightly weathered, highly weathered and alluvium).

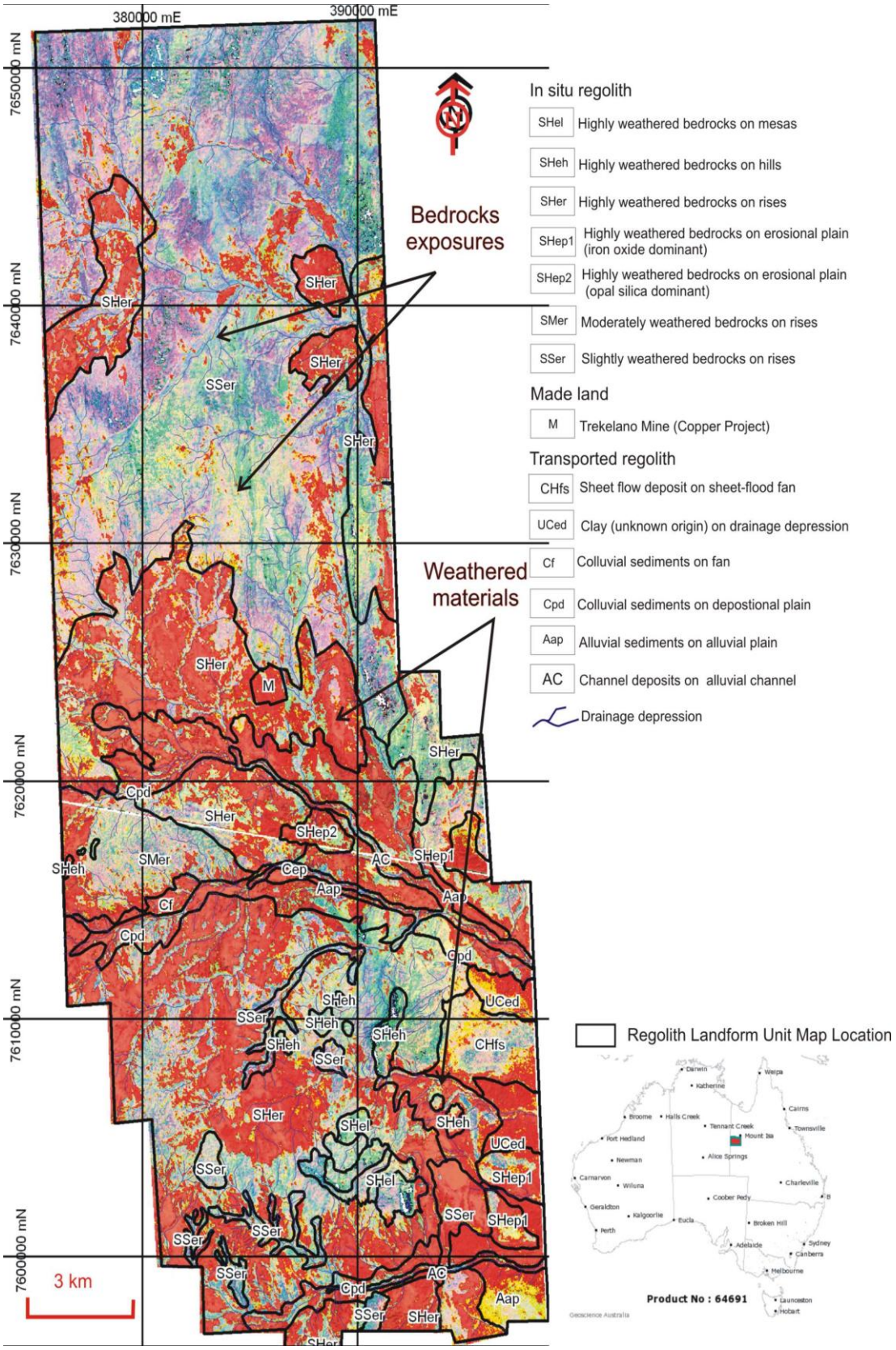

Figure 5.2: ASTER RGB combination of R (band 4/band 3), G (band 5+band 7/band 6) and B (band 6+band 7/band 8) of Block G Tick Hill, differentiate well between highly weathered materials (red-yellow) and variably weathered bedrocks exposures (purple-greenish-bluish).

The interpretation of the two RGB images (figures 5.1 and 5.2) show that bedrock related signatures of high Mg-OH content from primary Mg-OH bearing minerals such as chlorites, amphiboles and serpentines and Al-OH in micas are dominant to the north. They are mainly within the topographically higher landforms such as hills and rises and are represented by the purple-bluish-greenish colors. The highly weathered bedrock appears as red to pale yellows and the less weathered bedrock is expressed in light green to magenta and purple (Figure 5.2) and are a reflection of high Al-OH (kaolinite) and iron oxides. The ASTER image appears better in highlighting variations in the degree of weathering of the bedrock as seen from variations in the colors indicative of bedrock. Therefore, the results imply that the north of the area is dominated by slightly weathered bedrock while the south is dominated by a combination of slightly weathered bedrock and highly weathered bedrock. Transported regolith in the form of colluvium and alluvium also mantles the south-central part of the study area. The colluvium occurs as highly weathered regolith materials exposed in the lower elevation and low relief areas. The iron rich colluvium is represented as red and the iron-kaolinite (Al-OH) rich colluvium is represented as yellow to green in the image.

5.3 The Interpretation of Regolith Landform Unit (RLU) Description in TickHill region and surrounding

The simple band combination images shown in figures 5.1 and 5.2 together with 30 m DEM derived from ASTER were used as base images to map individual regolith-landform units (RLU). The broad scale initial RLU's mapped were then subdivided or modified based on other remotely sensed images. True color image (HyMap and ASTER), single mineral maps of Fe oxide abundance, and kaolinite abundance and disorder, Mg-OH and carbonate abundance and silica abundance from HyMap were used to modify the RLU's and interpret the regolith nature. Where available, field sample description, their field spectra and X-ray Diffraction analysis, were combined to validate the interpreted regolith materials. The processing of individual mineral maps together with their validation is described in chapter 4 and here they are used for smaller areas to interpret the regolith. The resulting RLUs mapped are shown in figure 5.3 and the description and interpretation of the main RLU's are described below.

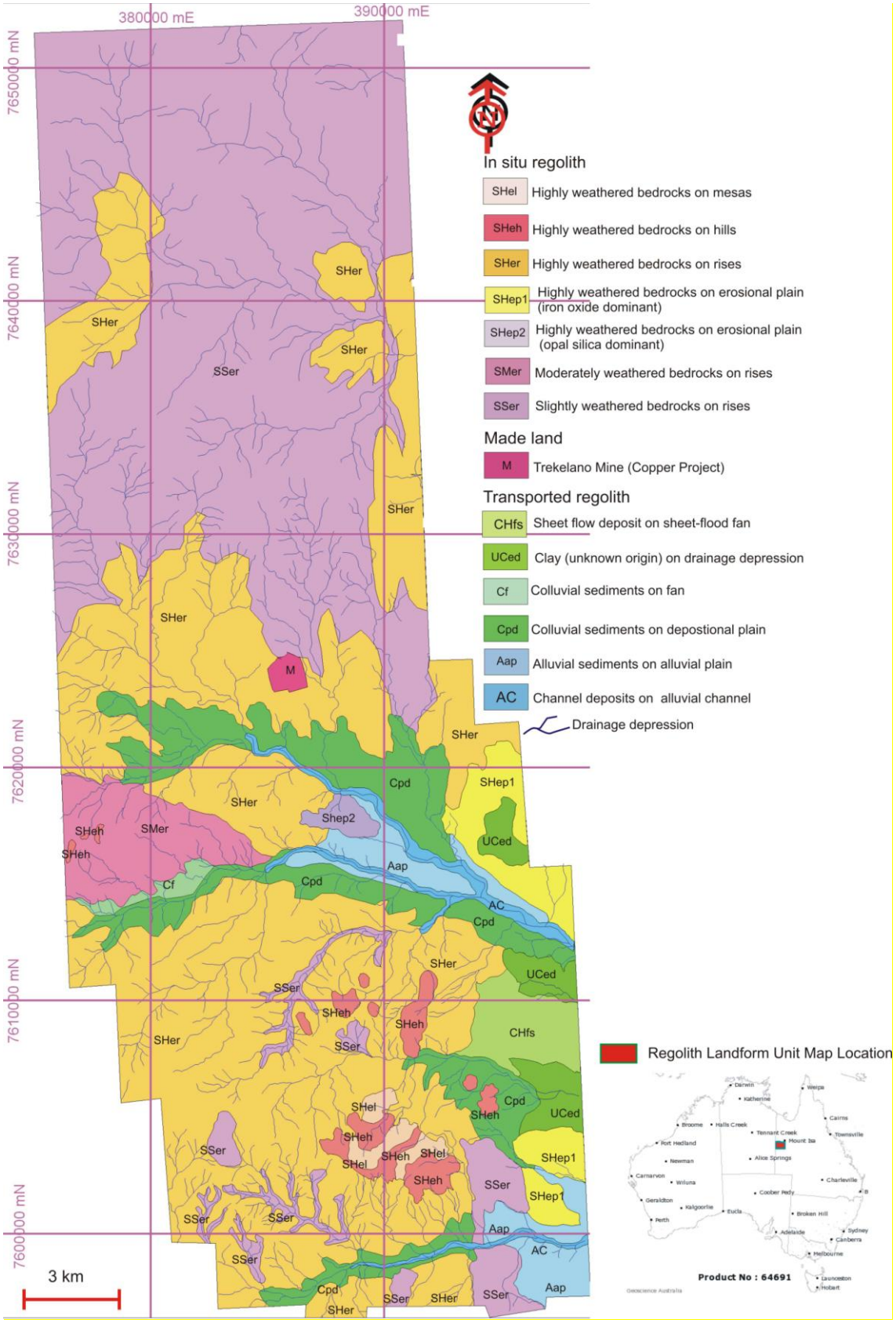

Figure 5.3: Interpreted Regolith Landform Unit of Block G Tick Hill, based on remotely sensed data (single mineral maps, simple RGB, and DEM and other integrated secondary studies).

5.3.1 *In-Situ* Regolith

In situ regolith is dominated by weathered bedrock exposures and weathering materials such as saprolite and mottled materials largely produced from weathering of underlying bedrock. For the study area, the bedrock varies in age from Pre-Cambrian to Cenozoic. The *in situ* regolith occurs mainly on erosional landforms in the study area.

5.3.1.1 SHel (Highly weathered bedrock underlying mesas and adjoining slopes)

Mesas and adjoining erosional landforms (slopes) are present in the south and southwest of study area (Figure 5.4a). The mesas and buttes are common landforms of this region (Anand et al., 2002; Wilford, 2003). On the DEM they occur as either single elevated locations or a small group of elevated areas separated by shorter lower relief exposures (Figure 5.4b, rainbow scale DEM image). A typical mesa profile has a flat top with steep sides that gradually merge with gentler slopes, and this profile is easily observed in RGB images and thereby easily mapped (Figure 5.4B).

The morphology of the mesas does not necessarily imply an underlying deep weathering profile capped by either mottled saprolite or duricrust (ferricretes, calcretes or silcretes). Mesas could develop due to erosion of flat lying sediments, basalt flows and duricrust capped profiles.

Therefore, remote sensing needs to establish the mineralogy and thereby the nature of regolith materials underlying and mantling the mesas so their formative conditions can be interpreted. Individual mineral maps help to address the question of whether the mesa is a product of weathering processes or flay lying bedrock. The information on formation conditions in turn has implications for landscape evolution of the area.

The kaolinite mineral map of the selected area shows high amounts of kaolinite mantling mesa slopes, and the kaolinite abundance comparatively decreases laterally across the topographically lower depositional areas within the entire landform (Figure 5.4A). The kaolinite “crystallinity” or disorder mineral map shows well ordered kaolinite dominant on the mesa slopes (Figure 5.5). The iron oxide mineral map shows high iron oxide content (hematite + goethite) on the upper mesa slopes and gradually decreases to the lower slopes. Interestingly, illite (white mica)

shows a lower amount on the top of mesa and its abundance is comparatively greater along the drainage depressions.

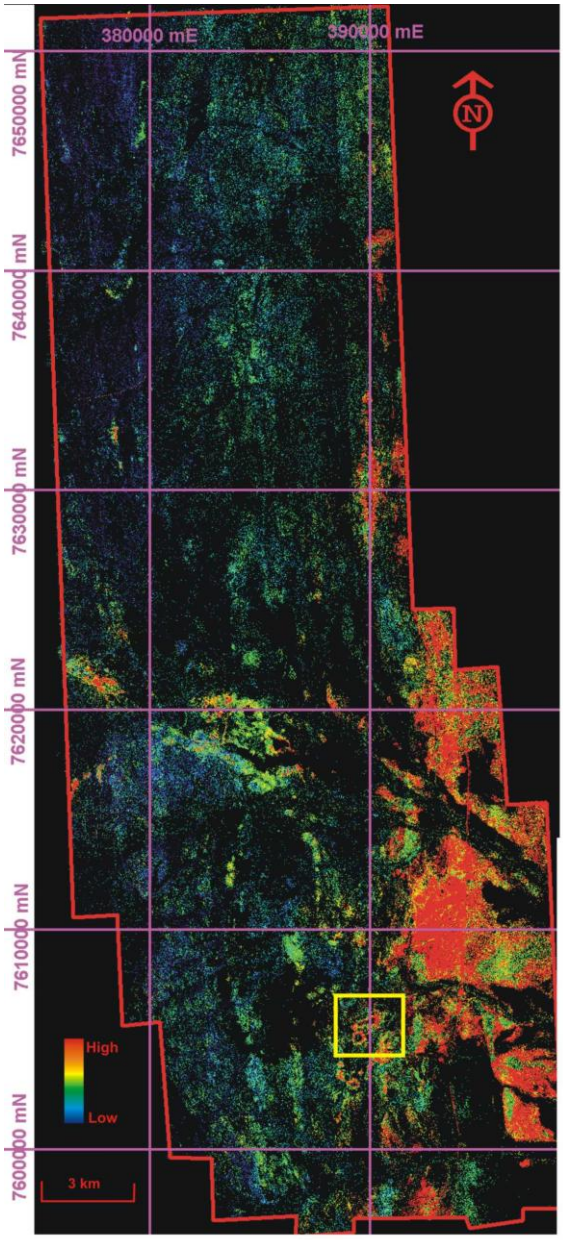

Figure 5.4A: Block G kaolinite mineral information taken from the HyMap spectral indices.

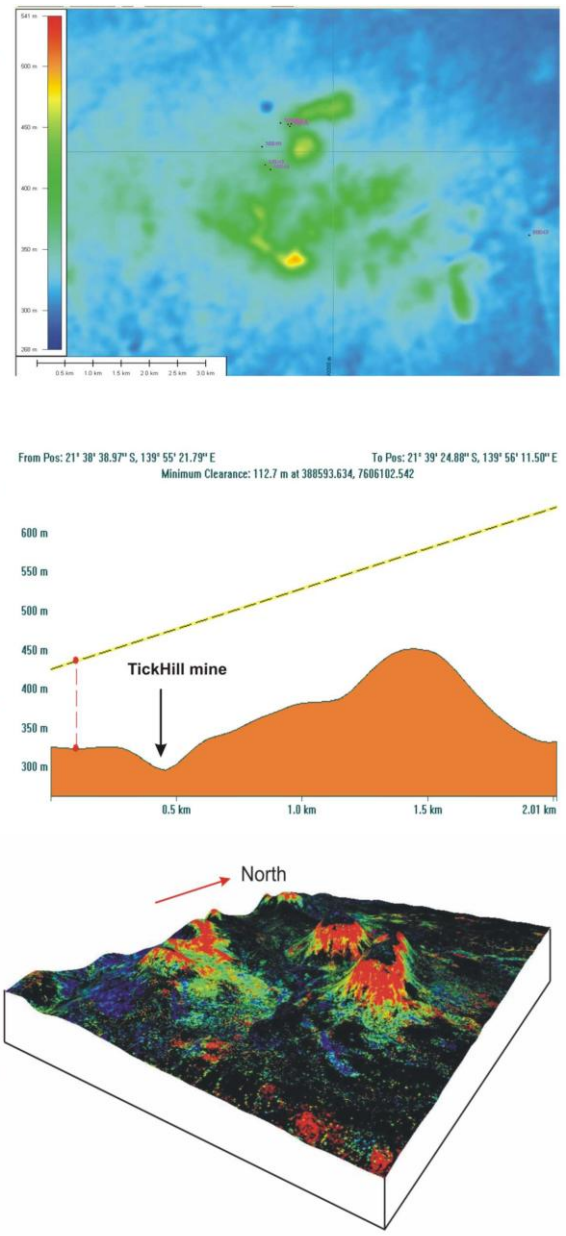

Figure 5.4B: Kaolinite abundance in Tick Hill mine test site. Lower image shows kaolinite crystallinity abundance overlaid on the 3D ASTER DEM.

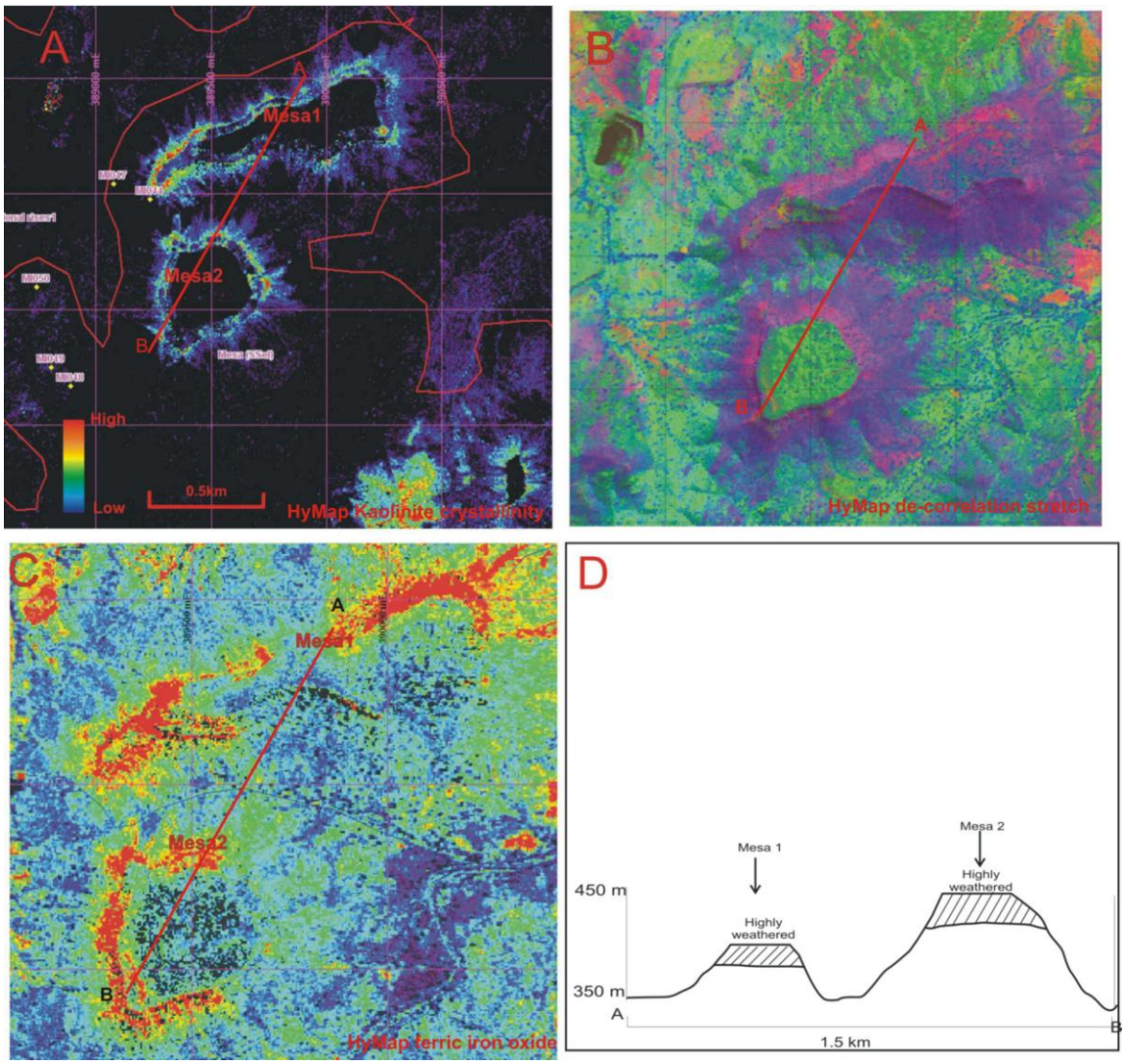

Figure 5.5: A) Kaolinite crystallinity image showing high abundance of well ordered kaolinite on the sides of the mesas, B) HyMap RGB de-correlation stretch image showing mesas. C) Ferric iron (iron oxide) abundance image showing high content on the of the upper mesa slopes. D) An interpreted cross-section of the mesas with iron oxide-kaolinite rich upper slopes and kaolinite rich lower slopes.

Interpretation

The mineral distribution patterns highlight the regolith underlying the mesa and therefore provide information on its formative processes. Based on an ideal "lateritic" profile as described by numerous workers (Nahon, 1986; Anand and Paine, 2002 for review) Cudahy (2002) developed an ideal mineralogical section through the regolith material zone which shows the changes in mineralogical composition, fabric and element substitution within clay minerals (mainly kaolinite) (figure 5.6). Kaolin disorder or "crystallinity" within the profile has been used for

classifying regolith materials, particularly, for distinguishing *in situ* regolith from transported regolith (Pontual and Merry, 1996; Phang and Anand, 2000). Well ordered kaolinite is common in saprolite and mottled saprolites of deeply weathered profiles which are often referred to as "laterite" profiles (Nahon, 1992; Anand and Paine, 2002), while the upper regolith materials which could be duricrusts and transported materials have poorly ordered kaolinite (figure 5.6).

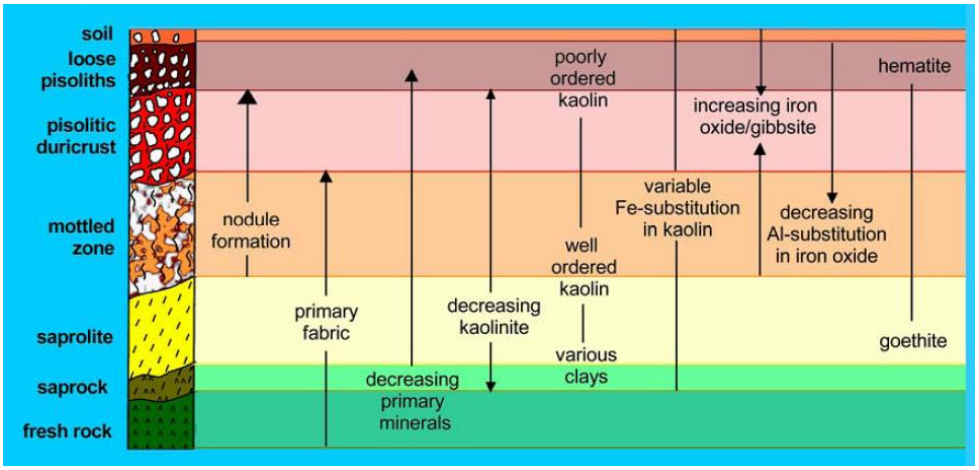

Figure 5.6: Schematic model of the mineralogy developed during lateritic weathering. Regolith cross section showing the changes in kaolinite physicochemistry, including disorder and metal substitution effects, with respect to parent rock composition and position within a truncated lateritic profile and regolith processes/materials (Cudahy MERIWA Project 2005).

Figure 5.5A and 5.5C shows abundance of well ordered kaolinite and iron oxides on the edges of the mesas with a gradual decrease towards the mantling pediments, and based on the mineralogical variation in figure 5.6, is indicative of presence of mottled zones or other kaolinite rich ferruginous materials such as lateritic residuum underlying the mesas. The distribution of well ordered kaolinite and iron oxides within the erosional mesas with gradual decrease to the drainage suggests widespread development of deep weathering profiles within the entire landform. No spectrally responsive primary minerals are identifiable surrounding the mesas which provides further support to the material being highly weathered. Therefore, the mesas are interpreted to be a product of stripping of a deeply weathered profile capped by iron duricrust rather than a product of flat lying sediments or basalt flows.

Similar conclusions of deep weathering profiles underlying mesas were arrived by Anand et al (2002), Phang et al., (2005) and Wilford (2005), in their field observation studies of the mesas in the Mt Isa region. They found mesas and buttes that had developed on Mesozoic sediments to bear signatures of deep weathering in the form of deep weathering profiles capped by ferruginous duricrusts and underlain by ferruginized and highly weathered saprolite (see chapter 2 for regolith of Mt. Isa region). From the mineral maps, it is not clear whether the upper most part of the profile is *in situ* or formed in transported regolith, but other interpretations arrived at by studying the spatial distribution of individual mineral conforms with field studies in the region (Cudahy et al, 2008).

5.3.1.2 SHeh (Highly weathered material on hills)

This regolith landform unit is underlain by regolith material similar to the mesas but is classified differently based on its topographically lower position and no flat topped-steep slope morphology. The landform is essentially an isolated hill within a larger rise or erosional plain landform. The landform was first mapped based on its topography and then regolith material, and subsequently interpreted and classified using the kaolinite abundance, kaolinite disorder and iron oxide content maps.

Figure 5.7 shows kaolinite abundance and disorder and iron oxide abundance maps of the selected RLU in the west part of Block G of the Tick Hill area. The images show three isolated hills surrounded by erosional plain landform. The three mineral parameter maps show high kaolinite abundance and high kaolinite order in the three isolated hills compared to the surrounding lower rises. The iron oxide content is not restricted to the hills and is variably spread across parts of the surrounding plains and a minor part of a hill.

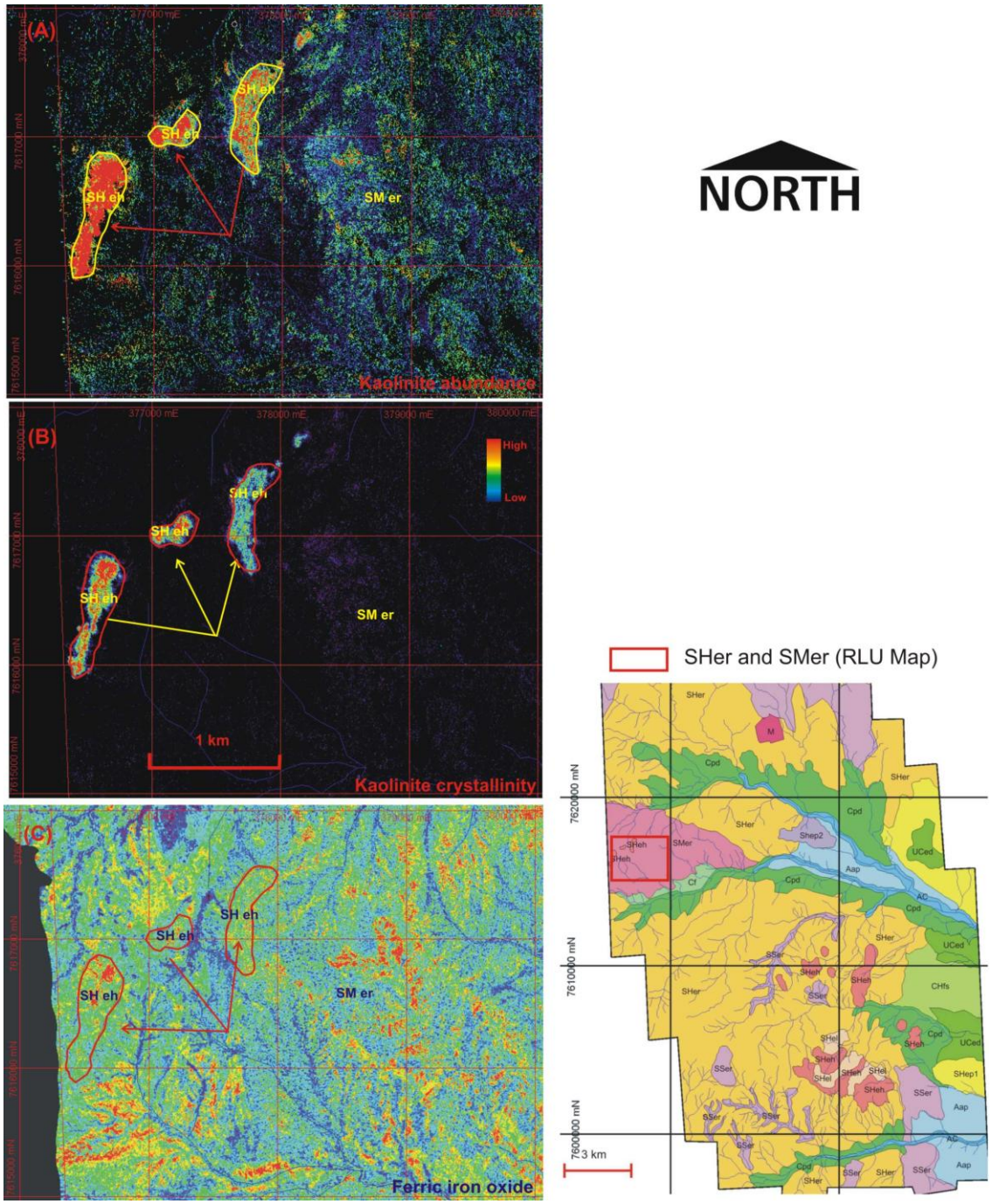

Figure 5.7: Maps showing A. Scaled abundance of kaolinite, B. kaolinite crystallinity, and C. iron oxide which is interpreted as mottle zone unit (RLU SHeh).

Interpretation

Based on the schematic deeply weathered profile shown in figure 5.6 and the occurrence of high abundance of kaolinite as well as being well ordered on the hills, the regolith is interpret as being *in situ* and of highly weathered nature. One side of a

hill shows high iron oxide content and this part could be dominated by either mottled materials or iron duricrusts. The presence of entire hill being dominated by well ordered kaolinite suggests that the hills were likely to have been once capped by ferruginous parts of the deep weathering profile as shown in figure 5.6., but erosion has stripped the upper parts of the profile leaving the saprolite exposed. The presence of some iron rich material on one hill suggests that remnants of upper parts of the profile are still present. The lithology information from published regional geology for the three small elongated SHeh units shown in figure 5.7 is mapped as laterite, although the nature of the laterite is unclear from the published maps. The difficulty is that the geology maps in general "loosely" refer to the presence of highly weathered materials as "laterite" and therefore the presence cannot be confirmed from geology maps. Field validation is required to confirm the interpretation made from remotely sensed images.

The kaolinite crystallinity shows that well ordered kaolin is comparatively less abundant on the adjoining landform. These adjoining landforms are interpreted as bearing *in situ* regolith. This comparative abundance of kaolinite disorder between landforms suggests that the kaolinite disorder maps need to be considered in relation to degree of weathering and profile development, as slightly to moderately weathered in situ regolith may not have an abundance of ordered kaolinite present.

5.3.1.3 SHer (Highly weathered material on erosional rises)

The simple RGB band combination image overlaid on DEM allows the construction of broad scale RLU's. One such RLU unit of SHer constructed from HyMap RGB image is shown in figure 5.8A and classified as highly weathered bedrock on erosional rise (SHer) or saprolite on erosional rise. However, individual mineral maps derived from spectral indices of HyMap data (with better spectral and spatial resolution) allow subdivision of the regolith on erosional rise.

The three integrated single mineral abundance maps of carbonates + Mg-OH, ferric iron oxide, and kaolinite abundance for the selected RLU of SHer are shown in figure 5.8B, C, D and the cross sectional elevation profile for section A-B is shown in figure 5.8 E. The sectional view of the landform shows two elevated regions separated by drainage. The mineral maps show a distribution strongly linked to the topography of the rises. The Mg-OH and carbonate mineral map shows the surface distribution to be restricted to the lower parts of the rises which are the drainage or

dissected areas (figure 5.8B). The kaolinite map shows its occurrence mainly on the mid and upper slopes but negligible in the drainage area (figure 5.8D). The iron oxide maps show iron oxide abundance which is restricted to the higher parts of the landform (figure 5.8 C). A cross-sectional view of the distribution of the three main mineral groups on the landform is shown in figure 5.8E and illustrates the spatial association of mineral groups to a particular part of the rises landform.

Interpretation

The summits of the rises landform appear to be rich in iron oxides and some kaolinite and grade laterally into a kaolinite rich material and finally into Mg-OH rich regolith within the more intensely dissected parts of the landform (drainage). The interpretation of spatial distribution of minerals needs to consider the regolith profile character as done previously for the mesas and which is common in these regions (Anand et al., 2002). Weathering profiles generally have ferruginous rich surface materials followed by mottled or kaolinite rich saprolites (highly to very highly weathered rock) followed by saprock (slightly weathered rock). Combining the landform, mineral distribution maps and weathering profile characteristics, the results imply that the summits are rich in ferruginous regolith materials likely to be ferruginous soils or ferruginous lag or ferruginous duricrusts. The slopes where mild erosion is proceeding have subsurface weathering profile exposed in the form of kaolinite rich saprolite. The Mg-OH bearing mineral signatures in the lower parts of the landform indicate the presence of fresh to slightly weathered primary minerals within the bedrock. Along the drainages where intense dissection is prevalent (note these are upper reaches of drainages), only Mg-OH minerals are present, while on the flanking steeper slopes, Mg-OH and kaolinite are both present (figure 8A, C). This suggests that where intense dissection is prevalent, fresh to slightly weathered rock is exposed, while in areas where milder erosion is present, moderately weathered bedrock (saprock) is present in the form of kaolinite and Mg-OH bearing primary minerals. This interpretation highlights the application of mineral maps to mapping regolith on landforms in detail.

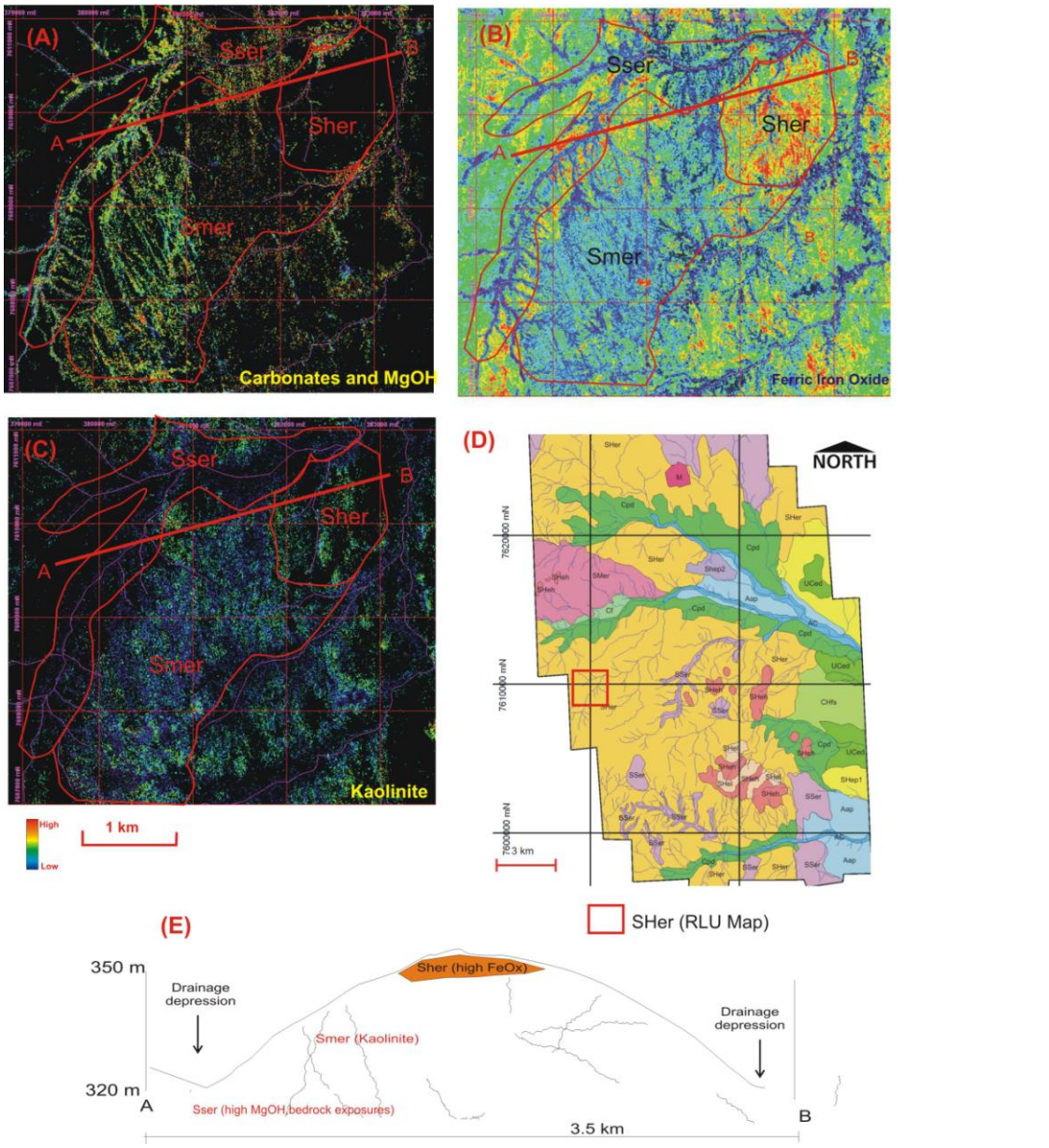

Figure 5.8. Subdivision of SHer (weathered rock on erosional rise) based on individual mineral maps. A) Mg-OH mineral map. B) Ferric iron mineral map. C) Kaolinite mineral map. D) The regolith-landform map of the entire area showing location of landform studied in detail. E). Cross-section interpretation of the landform from the mineral maps and DEM.

The above interpretation is also possible due to the presence of Mg-OH bearing minerals in bedrock, which are mainly granites and gneiss and contain Mg-OH bearing minerals (hornblende, chlorite). If the bedrock is Mg-OH poor such as silica rich sediments, this interpretation may not be feasible.

The above interpretation for this RLU is similar to that observed for the mesas and isolated hills present within the rises. However, for the mesas (SHel) and isolated hills landforms (SHeh), the boundaries between ferruginous materials and

adjacent saprolite materials are sharp, while on these landforms they appear to be relatively gradual. This may suggest that the mesa surfaces are underlain by ferruginous duricrust which buffers gradual dissection and therefore boundaries are sharp. In contrast, the SHer landform described here is likely to have ferruginous soil on the summits with erosion of ferruginous soil being gradual. The cementing differences between soil and underlying saprolite are not significantly different and therefore the erosion is gradual. In contrast, the cohesiveness of duricrust and underlying mottled zone or saprolite is significant, and this causes erosion to proceed abruptly.

5.3.1.4 SHep1 (Highly weathered bedrocks on erosional plain: iron oxide dominant)

The erosional plain landforms develop in the east and southeast part of Block G Tick Hill (figure 5.9). The landform is of very low relief and generally merges with colluvial plains or alluvial plains. In figure 5.9, the erosional plain is bounded by alluvial plain landform. A RGB de-correlation stretch image of the RLU shows likely dominance of kaolinite and iron oxide rich materials with a smaller patch of a different reflecting material within the plain (figure 5.9A). Individual mineral maps for kaolinite and iron oxides for the regolith-landform unit shown, confirm the abundance of high kaolinite and iron oxides (figure 5.9B and figure 5.9C). Kaolinite crystallinity map shows a strong abundance of the mineral in major part of the plain and correlates well with iron oxide content (figure 5.9C). The Mg-OH + carbonates map shows high abundance in the patch of the landform where the other two regolith minerals are lower or absent (figure 5.9D). The bounding landforms are low in all mineral maps shown.

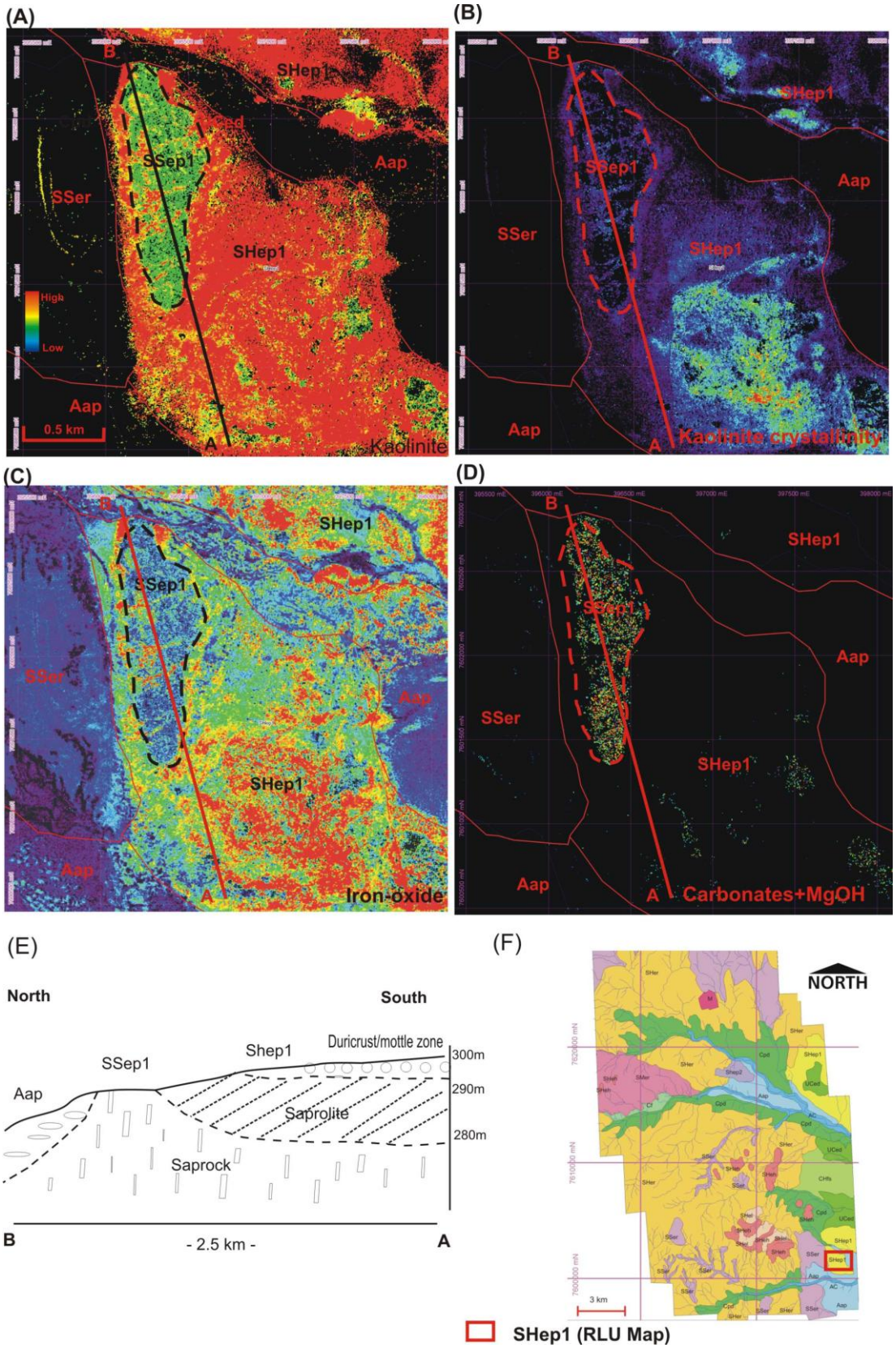

Figure 5.9: Mineral maps for the erosional plain landform unit. A) Kaolinite abundance map High abundance of kaolinite B) Kaolinite crystallinity map. C) Iron oxide map. D) Mg-OH+ carbonates map. E) Interpreted cross section A-B show in mineral map images. F). Regolith-map with location of regolith-landform.

Interpretation

The mineral maps for the erosional plain landform shown provide spatial information regarding the underlying regolith and variation in regolith across the plain. The landform is dominated by kaolinite and iron oxides as indicated by their respective maps, but their abundance could mean either colluvial ferruginous rich material or *in situ* material. The kaolinite crystallinity map points to the material being residual, and combined with its high iron content suggests that the material is ferruginous duricrust or mottled zone. Spatial variations in the iron oxide content suggest that laterally ferruginous material decreases outwards from the summit. Presence of kaolinite with moderate amounts of crystallinity suggests the presence of saprolite surrounding the ferruginous material. Moreover, the small patch towards the edge of the landform appears to be slightly weathered bedrock on the basis of basement rocks bearing Mg-OH+carbonates minerals. This patch could also be a pocket of calcrete ($CaCO_3$), but considering that previous studies have not reported much calcrete in the area (Anand et al., 2002a), the likelihood of the patch being basement saprock is preferred. Based on the mineral maps and their interpretation, a schematic section of the erosional plain is shown (figure 5.9E).

The above interpretation of the erosional plain regolith materials showcases the value of individual mineral maps. It would be difficult from air photos and traditional multispectral imagery to firstly interpret whether the plain had transported or residual regolith underlying it. Secondly, it would be difficult to recognize the true nature of the spectrally different patch within the plain. Interpretation of the regolith also allowed the explanation for presence of residual deep weathering profile with lateral variations in weathering degree and thickness of in situ weathered zones.

5.3.1.5 SHep2 (Highly weathered bedrocks on erosional plain: opal silica dominant)

This regolith-landform has a low relief but it is dominated by a very high reflectance signature as seen in the HyMap imagery through the CIR Image (RGB; R_{859}:R_{644}:R_{556}) (figure 5.10). From the entire Block G image, this regolith feature is striking as it is the large very high reflectance feature on the CIR image. The RGB de-correlation stretch image (figure 5.1) also reveals the unit clearly in magenta.

Individual mineral maps of kaolinite, Mg-OH and white mica show little to no presence over this particular regolith-landform, although iron oxide is present in moderate amounts but with patchy distribution. Field observations of this specific regolith type found a mix of siliceous lag and siliceous duricrust outcrop on low-relief landform (figure 5.10). Silcrete is a common regolith material occurring across Australia, and is considered to have origins in humid to arid climate (Taylor and Eggleton, 2001).

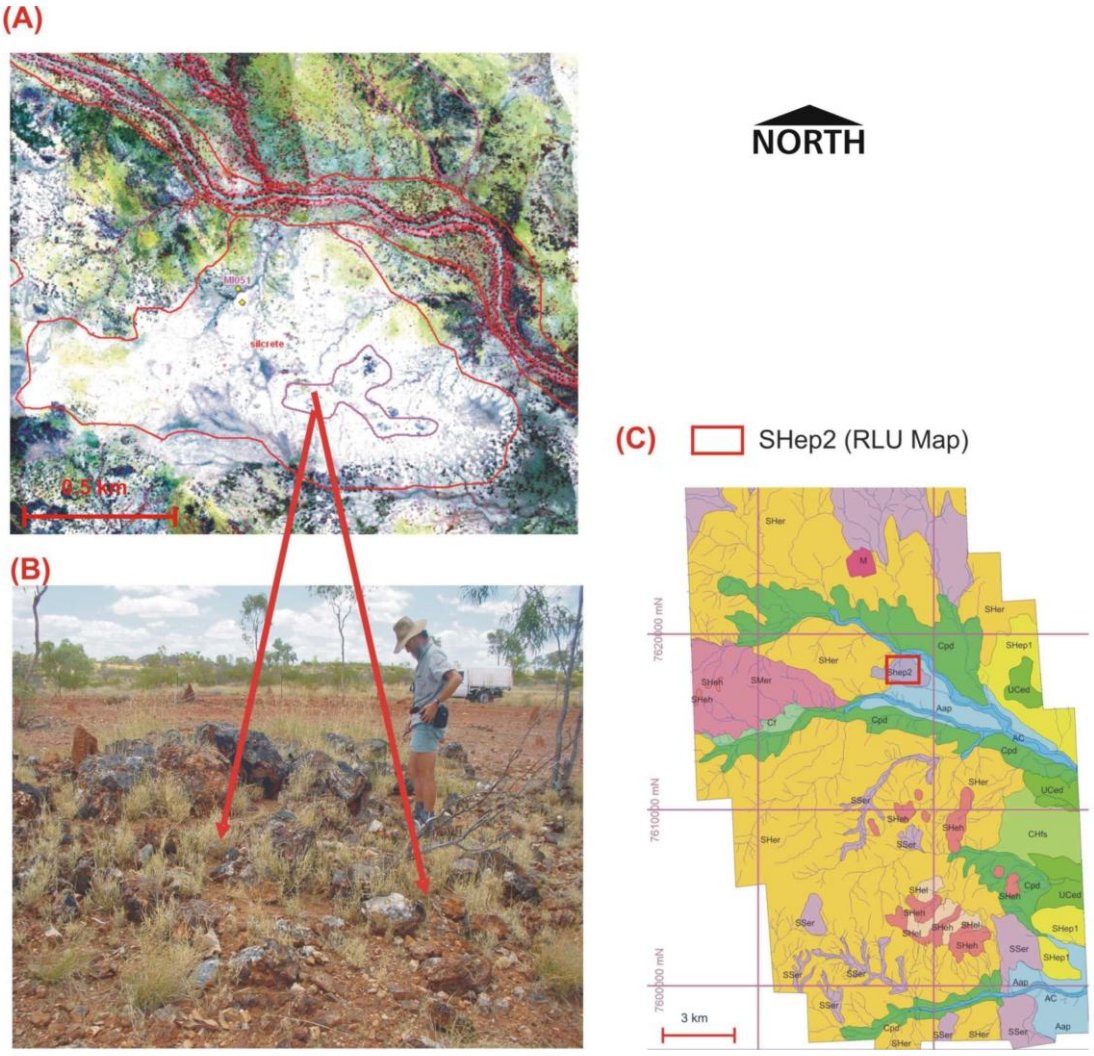

Figure 5.10: A. Quartz lag dominated by opaline silica at location mi051 and mi052 as seen obviously on HyMap (RGB; R_{859}:R_{644}:R_{556}) map. B. Siliceous outcrop and lag as seen in the field (*Image courtesy of Geological Survey of Queensland, 2007(Dr. Mal Jones in the background).*

Interpretation

The siliceous nature of the surface material is interpreted from the high reflectance in the CIR image. This interpretation is confirmed by field observations. Field description shows that this unit consists of extensive exposure of white and translucent siliceous outcrop composed of opaline silica (figure 5.10). The siliceous material appears as duricrust surface outcrops and as siliceous lags of varying sizes from boulder to pebble across the landform. Further, published geology map of the area shows the fresh rock to be dominated by Tertiary Formation which consists of mix of chalcedony, silisiclastic rocks and carbonate rocks (limestone). Although not classified as such, the surface outcrops are representative of silcretes. All the other regolith work in the region alludes to the presence of silicified bedrock and silcretes (Anand et al., 2002) and this outcrop is therefore very likely to be silcrete. The silcretes are likely to be related to the weathering product of the chalcedony and sandstone rich underlying rocks (Thiry and Milnes, 1991).

The silcretes on their outer surface have a black to purple ferruginous coating. This iron oxide coating shows up in the iron oxide mineral maps over this regolith-landform. Field samples of silcrete lag have been taken from location mi051 and mi052 around Mel Field Station (figure 5.10) and the field spectra of these samples show a typical spectrum of opal silica with the broad absorption around 2240nm depth. Those two samples were also used for validating the opal silica map product derived from the HyMap.

5.3.1.6 SMer (Moderately weathered bedrock on erosional rise)

This RLU is dominated by weathered bedrock exposures. The HyMap RGB de-correlation stretch image indicates this RLU to be bedrock exposure occupied mostly by weathered rock outcrops (green color on image, see figure. 5.1 HyMap de-correlation stretch). The ASTER RGB of iron oxide-Al-OH – Mg-OH (figure 5.2) also shows the unit to be dominated by weathered rock exposures. The degree of weathering of bedrock, however, is not clear or easily interpretable from the RGB combination images and an attempt is made to check whether individual mineral maps allow differentiation of weathering degree and if the weathering degree is linked to bedrock type and primary mineralogy.

The interpretation of four mineral maps (kaolinite, iron oxide, carbonate + Mg-OH abundance and kaolinite crystallinity) which will be discussed below can help identify and map the degree of weathering for this unit. The image of kaolinite abundance map shows that kaolinite is more dominant over the northeast section (labeled SHer) of the image and corresponds to higher amount of iron oxides (figure 5.11B and C). Kaolinite abundance is comparatively lesser to the south and southeast of the image although variations in abundance are present. Kaolinite crystallinity map shows that well ordered kaolin is abundant and restricted to the north area (SHer), and almost absent in the unit marked SMer. Within the SHer unit, kaolinite crystallinity is also absent in some parts as seen in dark areas. Carbonate and Mg-OH mineral map show high to moderate content within the southeast part of the image. Interestingly, the areas mapped as SHer and showing high to moderate kaolinite are geologically mapped as Cambrian Mt. Birnie beds and those with slightly higher carbonate + Mg-OH minerals (SMer) are mapped as Precambrian Saint Mungo Granite (Ryburn et al., 1988).

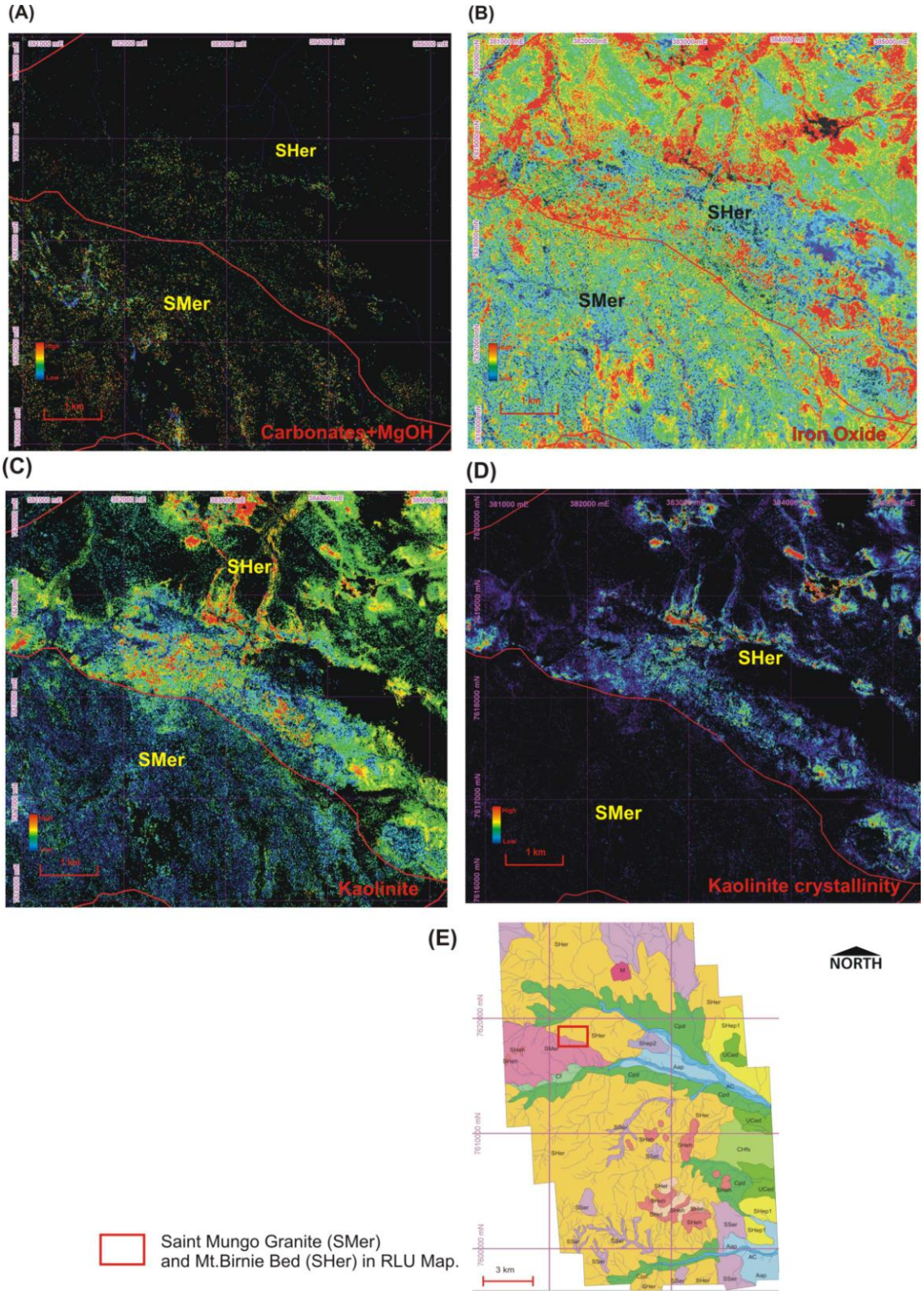

Figure 5.11 HyMap produced mineral maps for highly weathered (SHer) and moderately weathered rock (SMer) on erosional rise. A) Mineral map of carbonates+MgOH; B) Mineral map of iron oxide. C) Map of kaolinite abundance. SMer and SHer units shown share similar boundaries to that of Saint Mungo Granite (SMer area) and Mt.Birnie bed (SHer area). D). Location of the mineral maps shown.

Interpretation

The variation in the mineralogy, especially kaolinite, kaolinite crystallinity and Mg-OH contents of the regolith-landform, need to be interpreted in terms of lithology of the bedrock and its degree of weathering. Areas mapped as SHer and having a high to moderate kaolinite and iron oxide content are marked as Cambrian Mt. Birnie formation, which consists of massive ferruginous sandstone, conglomerates, mudstone and red shale (chapter 2). The weathering of Mt. Birnie beds results in the formation kaolinite and iron oxides, because the host lithology is suitable to the formation of these minerals. The mudstone and red shale provide the iron for iron oxide formation, while both lithologies provide the Al-Si for kaolinite. Further, the sediments, especially the red sandstones, due to their porous nature are relatively easily weathered as compared to the granite. The abundance of well ordered kaolinite within this unit suggests that it has residual deeply weathered profiles developed on it. The interpretation of its highly weathered residual nature is supplemented by the greater presence of iron oxides which together with the kaolinite abundance point to ferruginous duricrust or ferruginous soils occurring over some part of the unit. The areas within SHer that are devoid of well crystalline kaolinite are interpreted as colluvium deposits which would have poorly crystalline kaolinite. The poorly crystalline kaolinite bearing parts of SHer are mapped as recent deposits in the geology map, which augments the colluvial nature of the sediment. Therefore, the dark areas within SHer on the kaolinite crystallinity map can be mapped as colluvium on rises.

The Saint Mungo granite is a feldspar-hornblende-biotite granite that is weakly foliated to form gneiss and has also experienced amphibolite facies metamorphism (chapter 2). The hornblende in the granite is very likely to account for the high Mg-OH content seen in the image as compared to weathered the Mt Birnie Formation. Further, weathering of hornblende results in the formation of smectite (Mg-bearing) and goethite (Taylor and Eggleton, 2001). Weathering of feldspars results in the formation of smectite, and then kaolinite (Taylor and Eggleton, 2001). The presence of Mg-OH and lower level of kaolinite suggests the Saint Mungo granite is less weathered than the Mt Birnie formation and has not developed a highly weathered profile.

The reason for the two contrasting degrees of weathering are not clear, but the host rock type is likely to be a consideration. Sedimentary rocks, due to their porous nature are relatively easily chemically weathered as compared to crystalline igneous rocks. An alternative explanation for the difference in weathering degree could be resistance to erosion of specific rock types and their weathering products. It is possible that both the rock types had deeply weathered profiles on them, but the Mt Birnie Formation had a ferruginous cap in the form of a duricrust, which resisted erosion. Comparatively, the granite profile was devoid of a duricrust and was relatively easily eroded.

The above data highlights the fact that individual mineral maps allow the spatial differentiation of degree of weathering and also the host bedrock, a parameter which is difficult to map quantitatively nor effectively in the field or by air photos. However, the extent to which degree of weathering of bedrocks can be estimated will depend on the bedrock nature and mineralogy.

5.3.1.7 SSer (Slightly weathered bedrock on erosional rise)

The landform unit varies in elevation between 325m and 350m above sea level with the low relief (10 – 30 m) and is restricted to the upper drainage areas where dissection is high. The ASTER RGB image shows the mapped RLU as blue which suggests a high reflectance in Mg-OH minerals (figure 5.12A). The HyMap RGB de-correlation stretch of SSer unit image is represented in green and appears mostly composed of Mg-OH signature (figure 5.12B). The Mg-OH and carbonate mineral map derived from HyMap data shows a high abundance of the mineral assemblage along the particular regolith-landform as compared to the regolith mantling the adjoining higher relief landforms (figure 5.12C). The regolith mantling higher landforms appears to be composed of kaolinite and iron oxides as seen on the individual mineral maps. The ASTER RGB image also shows the mantling regolith-landform to be composed of iron oxide rich regolith as seen in red (figure 5.12A).

Interpretation

The RGB band combination images as well as individual mineral maps of the landform indicate the presence of Mg-OH rich regolith. As previously discussed, Mg-OH rich materials are indicative of fresh to slightly weathered primary rocks. The basement rocks in the region are mainly Proterozoic bedrock such as

amphibolites, gneiss, mafic and ultramafic rocks all of which have high abundance of Mg-OH and carbonate. The weathering of primary Mg-OH bearing minerals, such as hornblende and chlorite results in the formation of smectite and vermiculite in the saprock (Taylor and Eggleton, 2001). Therefore, this unit is indicative of slightly weathered to fresh rock. The unit is confined to the upper reaches of drainage which also supports the interpretation. Erosion is intense in this type of landform and marks the boundary of dissection into topographically elevated weathered regolith. The RLU mantling it – SHer – is dominated by iron oxide and is highly weathered residual soil or weathered rock.

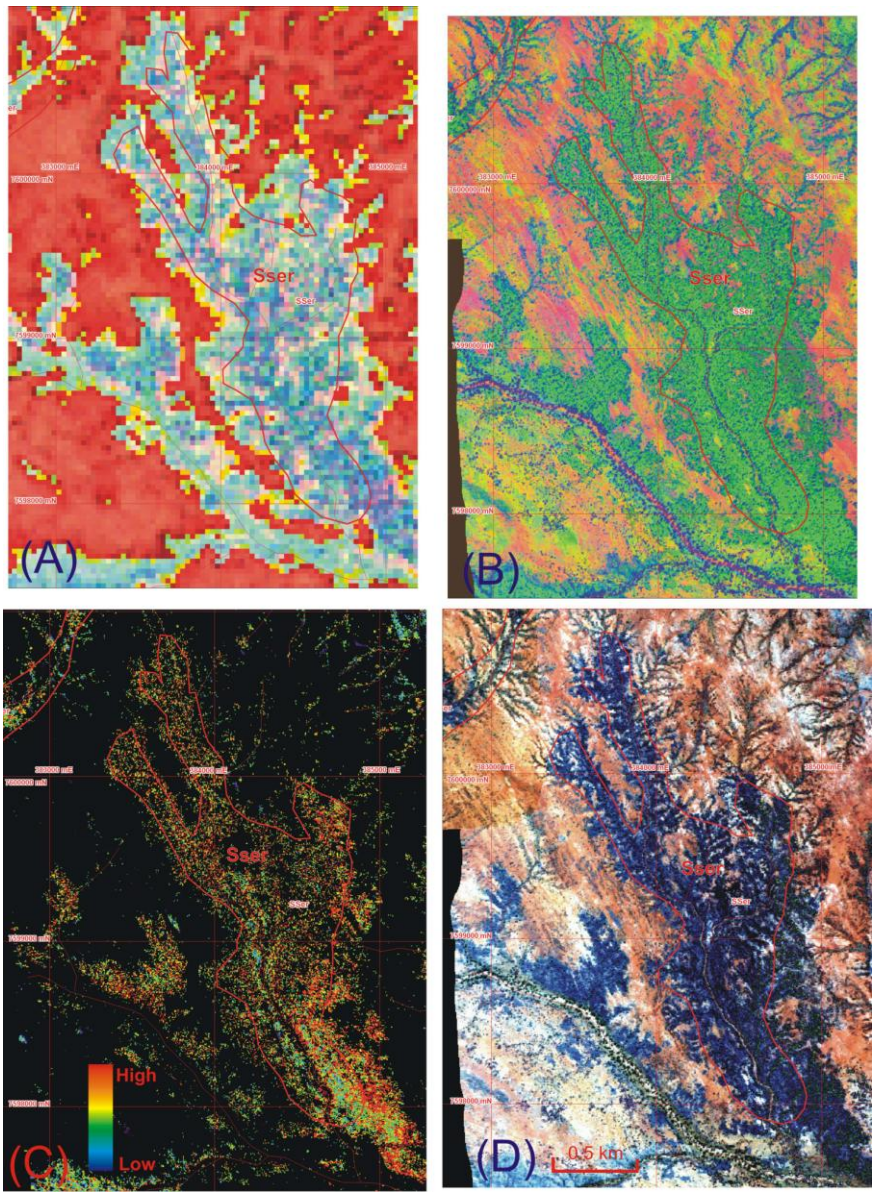

Figure 5.12: SSer regolith-landform unit images. A) ASTER RGB of FeOx-AlOH-MgOH; B) HyMap RGB of FeOx-AlOH-MgOH; C) HyMap MgOH image; D) HyMap true color composite.

5.3.2 Made land (M)

Most of the landforms described are products of natural processes of weathering, erosion and sedimentation. The landscape, however, also has man made features and these if large, have to be mapped. Trekelano Mine is one such man made feature. The mine is located within the middle of the Block G about 20km to the north of the TickHill Au mine. Copper-gold Trekelano project was owned by Cloncurry Metal Ltd and has been explored since 1970s until recently. (*http://www.cloncurrymetals.com.au/Trekelano.htm*). The mine site consists of a open pit mine, a tailings dam, waste pile and approach roads. The main mineralization is hosted by meta-sediments of the Corella Formation with adjoining meta-volcanics and younger intrusions. In terms of regolith-landforms, the mine site and its surroundings are disturbed due to human activity and therefore are classified as made land (figure 5.13).

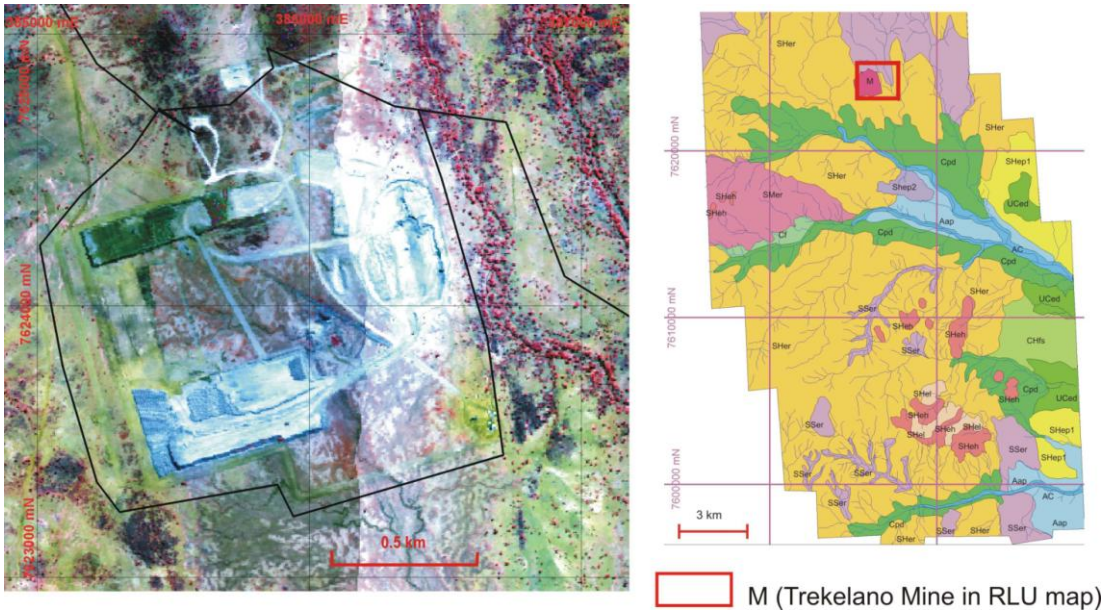

Figure 5.13: Trekelano Gold-Copper Mine, is categorized as M (made land) in RLU Map as seen through the HyMap CIR image.

5.3.3 Transported Regolith

Transported regolith in the study area is dominated by colluvium and alluvium deposits present on either depositional plains, depressions or alluvial plains and channels.

5.3.3.1 CHfs (Sheet flow deposit on sheet-flood fan)

RGB combination of HyMap true color ($R=R_{644}$,$G=R_{556}$,$B=R_{453}$), shows a typical sheet flow deposit on the surface. These colluvial sediment areas show a ripple or cascading texture in true color images, which is very typical of sheet flow processes. The landform is low relief (0-8 m) suggesting a fan or plain, but due to sheet flood nature as revealed by the surface texture and pattern, it is referred to as a fan. This depositional landform is adjoining a topographically higher erosional rise to the west (figure 5.14 A), and as described for the SHer unit, these rises are underlain by highly weathered regolith, namely in situ ferruginous soils or duricrusts. The kaolinite map shows a high abundance on the fan but the kaolinite crystallinity map shows kaolinite to be of high disorder, especially when compared to adjacent erosional areas (figure 5.14B). The sheet flow deposit, however, does show a moderate to low amount of kaolinite crystallinity, although some parts have negligible amounts. The iron oxide map shows the adjoining erosional areas to be abundant in iron oxides but iron is patchily distributed on the fan in the form of small north-west trending lobes (figure 5.14C).

Interpretation

The texture of the surface material in the images and presence of disordered kaolinite suggests the regolith material to have a transported origin. The adjoining erosional rises have comparatively well ordered kaolinite while the lower fan is poorly ordered with high iron oxide lobes aligned north-west which suggests sheet flow direction was perpendicular to the lobes. Unless the lobes are indicative of small ridges, it is difficult for iron oxide rich regolith to develop in situ with such morphology. It is more likely that the iron oxides are concentrated within minor depressions created by surface sheet flow, especially during high intensity rainfall events. The spatial relationship between the two regolith-landforms with the fan being topographically lower, implies the erosion of in situ regolith and deposition in lower landform as sheet wash deposits. This interpretation also provides confirmation that kaolinite tends to gradually become disordered on experiencing colluvial transport. The sheet flow deposit, however, does contain moderate amounts of well ordered kaolinite, which suggests that longer transport over tens of kilometers is necessarily to completely transform well ordered kaolinite to disordered kaolinite. Alternatively,

the moderate abundance of well ordered kaolinite in the sediment could be new kaolinite forming within the sediments due to weathering.

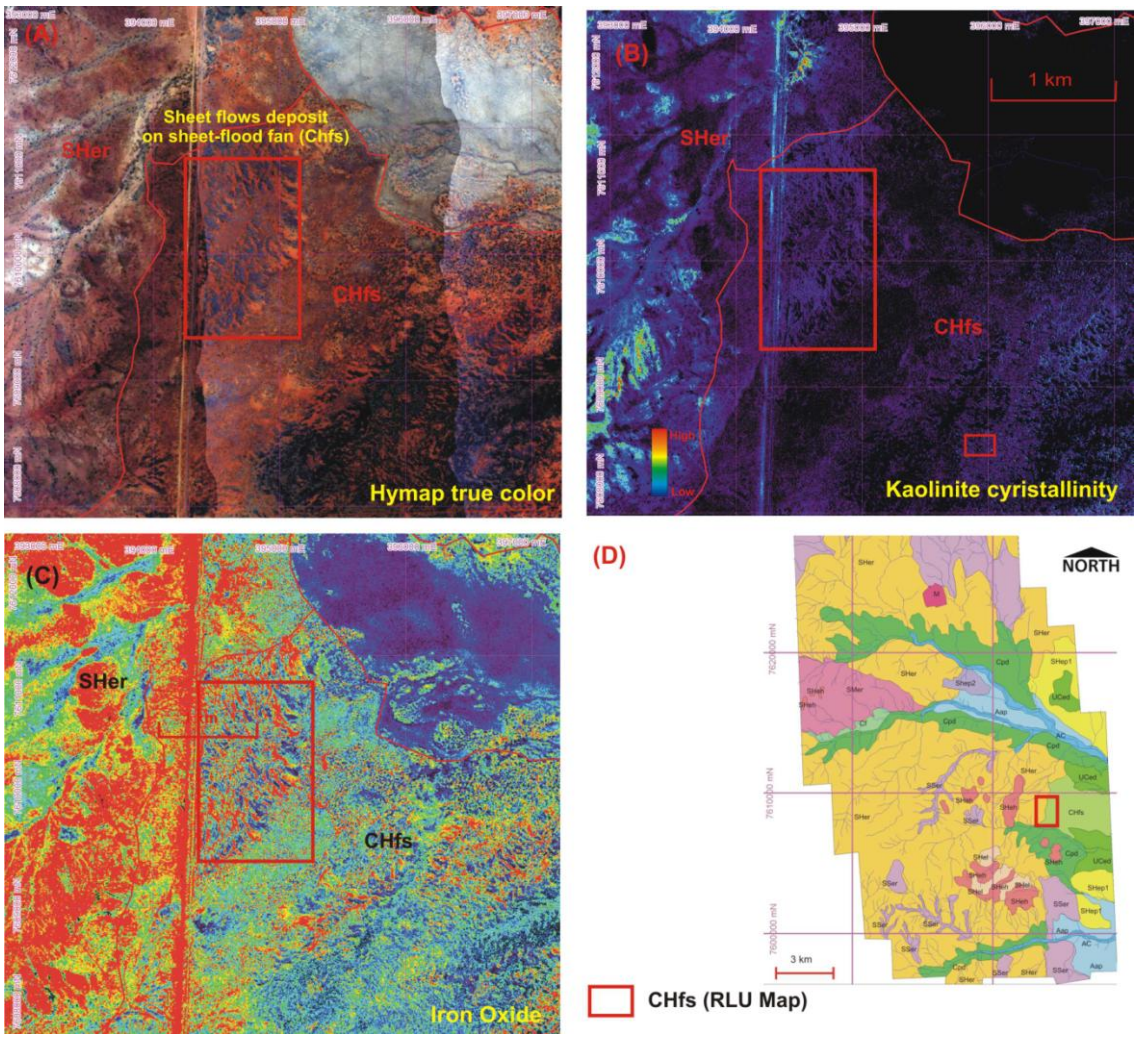

Figure 5.14: Colluvium on sheet flow fan (CHfs). The RLU is identified through RGB HyMap true color (A) and kaolinite disorder decreases slightly (blue-blue black image) (B), while the iron oxide decreases slightly compared to in situ weathering in SHer unit (C) as the materials are transported.

5.3.3.2 UCed (Clay; Unknown Origin on drainage depression)

This unit occurs as a very low relief, almost flat landform, resembling depressions. It appears to be a depression that receives sediment or water from surrounding colluvial and sheet flow fans and then becomes a source for drainage downstream. .

Individual mineral maps show that the landform is dominated by illite with little or no kaolinite, iron oxide nor Mg-OH minerals (figure 5.15). Therefore, it has

high white mica surface clay content. The presence of significant amount of clay was interpreted based on the presence of high illite content. In the HyMap true color image it occurs as grey to dark grey, uniformly textured landform

The unit appears to be a depression receiving fine sediment and water from upper erosional and depositional landforms. The unit is mapped as recent sediments on the geology map. The high white mica content suggests that either the clay is detrital or has formed *in situ*. It is difficult to pinpoint the origin of the clay. White mica does not appear to have strongly developed in the *in situ* regolith units described earlier and it is unlikely that it would be eroded and transported into depressions while kaolinite would not. If the clay was detrital, then kaolinite should be present in equal abundance. Therefore, a detrital origin for the clay in the depression appears less likely. Illites can form in saline ephemeral lakes (Meunier and Velde, 2004) or they could represent older deposit (Cenozoic).

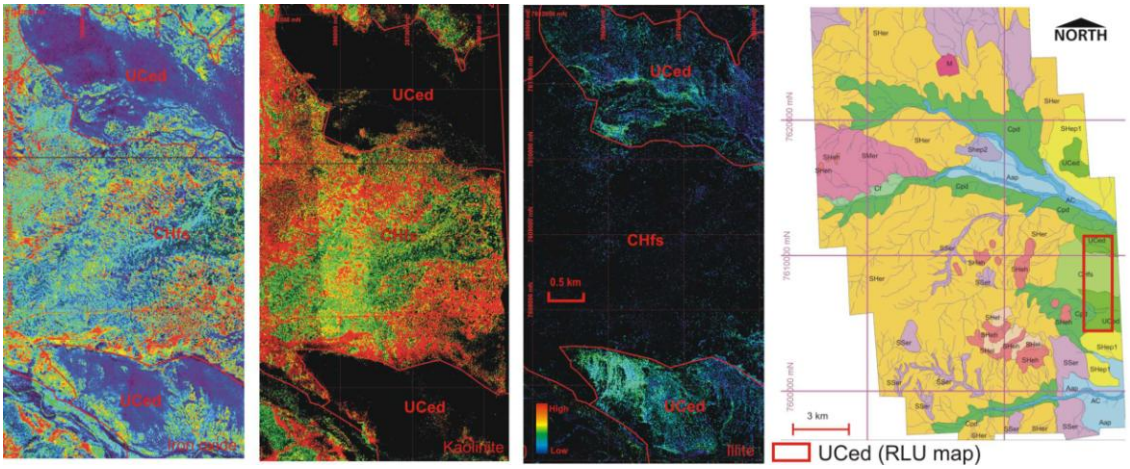

Figure 5.15: Maps for UCed (unknown clay origin in drainage depression). A) Iron oxide mineral map. B) Kaolinite mineral map. C) Illite mineral map. Right image shows regolith-landform map with image area outlined.

5.3.3.3 Cf (Colluvial sediments on fan)

This unit occupies small areas elongated as colluvial fan in an east-west direction. Low presence of kaolinite interpreted from the HyMap kaolinite image shows that this area is predominantly underlain by transported materials. In support of this argument, highly crystalline kaolinite are not present. Presence of some Some iron oxide are interpreted to mean that weathered materials developed on its surface.

5.3.3.4 Cpd (Colluvial sediments in depositional plain)

This typical landform unit has low relief. The low relief landform merges with the lower alluvial landforms. The mineral maps for the unit show high abundance of kaolinite and iron oxide.

Interpretation

This regolith landform covers areas close to the main river channel. Interpretation from the HyMap single mineral maps shows that these areas are mostly occupied by the colluvial sediments which have eroded from the higher highly weathered bedrock regions and have a high abundance of iron oxide and kaolinite. The difficulty in separating out different colluvial materials based on mineral maps occurs due to the inability of VNIR-SWIR sensing to detect textural differences of transported regolith. For example, quartz and its grain sizes are difficult to map, and much of transported regolith in the region is a combination of polymictic ferruginous gravels and quartz clasts (Anand et al., 2002).

5.3.3.5 Alluvial sediment on alluvial Plain (Aap) and Channel Deposit (ACa)

This unit generally consists of Cenozoic deposit mostly dominated by unconsolidated recent sediment composed of gravel, silt and mud (Rayburn et al., 1988). The development of drainage system is moderate to poor. The alluvial depositional landforms occur as natural levees, river bank deposit and flood plains. The different alluvial plain landforms can be recognized by a combination of topography, vegetation index and the landscape profile created from the digital elevation model. Generally, the vegetation is a good indicator of the alluvial channels and its pattern allows differentiation of alluvial landforms (figure 5.16).

The first and easily identified alluvial regolith-landform is the alluvial channel with channel deposits (ACa). This regolith-landform is likely to have coarse grained sediments typical of channels. This unit is a floodplain landform bearing finer overbank deposits (AOaf). The overbank deposits have less vegetation and consist of unconsolidated silt. The spectral characteristics suggest that the deposits are dominated by iron oxides and Al-OH bearing clays as seen by the colours in HyMap RGB stretch image. The difficulty with interpreting the different sediments

is that the grain size and texture are difficult to determine from spectral responses and this appears as a limitation to further characterization of the sediments.

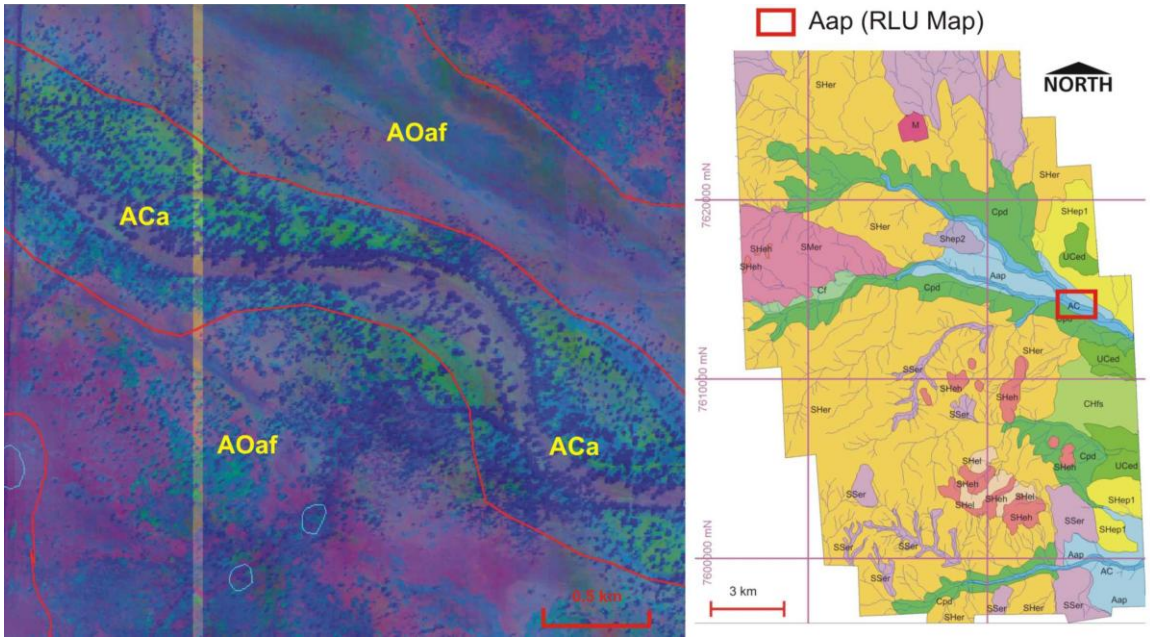

Figure 5.16: An alluvial landform for the area. The landform can be divided into alluvial channel with channel deposits (ACa), mantled by floodplains with overbank deposits (AOaf). High density of vegetation appears in blue developed along the river side (image taken from the HyMap RGB), pink-purple represent the exposed unconsolidated sediments likely rich in iron oxides and Al-OH bearing clays.

5.4 Discussion

5.4.1 The effectiveness of HyMap derived single mineral maps for mapping of regolith materials

Four main individual mineral maps – kaolinite, kaolinite crystallinity, iron oxides, Mg-OH + carbonates, and to a lesser extent silica and white mica maps, were used in combination to differentiate regolith materials and map regolith-landforms. For the area studied, a combination of the abundance for each mineral present can be used to define individual regolith-landform units, and subsequently map them. The combination of abundance of minerals acquired from mineral maps as used for identifying individual regolith materials is listed in table 5.1. Such mineral abundance combination allows the rapid mapping of regolith materials within a landscape and achieves one of the aims of the project.

Table 5.1: The abundance of minerals combined with the landform used to distinguish a regolith-landform unit.

No	RLU	Iron oxide	Kaolinite abundance	Kaolinite crystallinity	Mg-OH Carbonates	Opal Silica	Landform
1	SHel	moderate-high	high	High	none	none	mesas
2	SHeh	moderate	moderate-high	low-moderate	none-low	none	hills
3	SHer	high	moderate-high	low-moderate	low-high	none	erosional rises
4	SHep1	high	high	low-moderate	none-low	none	erosional plains
5	SHep2 (opal silica)	moderate	low	none-low	none	high	erosional plains
6	SMer	low-moderate	low-moderate	low	low-moderate	none	erosional rises
7	SSer	low	low	high	high-low	none	erosional rises
8	CHfs	low-high	low-high	low	low	none	erosional sheet-flood fan
9	UCed	low-moderate	none-low	none	none	none	drainage depression
10	Cf	moderate-high	none-low	none	none	none	erosional fan
11	Cpd	low-high	low-high	none-low	none-low	none	depositional plain
12	Aap	low-moderate	none-high	none	none	none	alluvial plain
13	AC	none	low	none	none	none	channel

However, the combinations proposed are not easily transferable across regions. The degree of weathering, bedrock and landforms all change in different regions, and the validity and value of individual mineral maps will too. Some areas are likely to have a greater abundance of white micas or smectites, which would complicate the use of mineral maps. Alternatively, the regolith development could be different with minimal preservation of weathering profiles and much of the area being covered by colluvium. For example, the validity of using kaolinite crystallinity for slightly to moderately weathered rocks (saprock and shallow saprolites) is unclear and needs to be tested.

From all 12 regolith landform units identified, iron oxide and kaolinite abundance is high in most areas of highly weathered regolith materials but not so in

less weathered units such as saprock. Kaolinite crystallinity is high on the mesa, hills and erosional rises.

Carbonates + Mg-OH single map is closely related to the basement exposures which contribute to define the degree of weathering. This can be seen on the moderately weathered materials (SMer) and slightly weathered materials (SSer). In addition, the high content of Mg-OH and carbonates on highly weathered materials on erosional rises (SHer unit) is interpreted to be areas with highly weathered bedrocks exposure.

Moreover, iron oxide abundance does not appear to be a good indicator of degree of weathering or distinguishing residual from transported regolith. Iron oxide abundance is a mere indicator of the presence of ferruginous materials, which in the region could be ferruginous soils, duricrusts of various morphology (nodular, vermiform, pisolitic) or mottled zones. Like kaolinite, it is present in both residual and transported regolith, although its pattern of occurrence can hold a clue to the type of regolith material (residual or transported), but requires further study.

Silica minerals, namely opal silica or opal CT, allow recognition of silica rich secondary rocks, mainly silcretes. In the region, silicified saprolite is common, and whether opal silica maps can be indicative of subtly silicified saprolite or not, needs further study.

5.4.2 Interpreting and Mapping Degree of Weathering

Hyperspectral remote sensing allowed the rapid mapping of spatial variation in regolith materials via a combination of four individual mineral maps (table 5.1). Importantly, the empirical evidence that kaolinite crystallinity or disorder is a good indicator of residual or *in situ* regolith, allowed the interpretation of deep weathering profiles under specific landforms. The regolith underlying mesas, hills and erosional plains showed presence of well ordered kaolinite, suggesting that they are underlain by deeply weathered “lateritic” profiles as described for the region by Anand et al., (2002). A high content of iron oxides with kaolinite suggests the presence of either ferruginous duricrusts or mottled zones, while in other landforms such as the erosional hills, only kaolinite was dominant, suggesting occurrence of saprolite with complete stripping of ferruginous zones. Such interpretations of the nature of the

regolith under different landforms would be difficult with the standard tool of airphotos.

The spatial variation in mineral content provides an important tool to map variation in weathering degree as well as the regolith material. The erosional rises within the landform unit showed variation from ferruginous units to saprolite to saprock based on the spatial variation of the abundance of iron oxides, kaolinite and Mg-OH minerals (figure 5.8). Furthermore, the spatial variations of individual minerals on the erosional rises (very flat landforms) highlight the presence of pockets of saprock within deeply weathered profiles. The rapid and accurate mapping of such pockets of saprock within highly weathered material would be difficult with air photos and broad band multispectral data alone.

5.4.3 Kaolinite Crystallinity – In situ vs Transported Regolith Separation

Information provided here and from other remote sensing studies (Cudahy et al., 2008), tend to confirm ground spectral studies (Pontual and Merry, 1996; Phang and Anand, 2000) which indicate kaolinite crystallinity could be a valued indicator to rapidly map insitu or residual regolith from transported regolith. In deeply weathered regions, such as Mt Isa and the Yilgarn Craton (Phang and Anand, 2000; Anand and Paine, 2002. Cudahy et al., 2008), well ordered kaolin appears to be a good indicator of underlying deeply weathered residual profiles, as observed in regolith-landforms like the mesas, hills and erosional plains. It is important to note that it is an indicator of highly weathered residual regolith and that residual regolith could develop and evolve in any bedrock ranging in age from Precambrian to Cenozoic (at least for the Mt. Isa region). Kaolinite crystallinity acts as a differentiator of recent surficial sediments from highly weathered residual regolith. This is observed for the sheet flow fan deposits which have lower kaolinite crystallinity as compared to the adjoining erosional rises, from where the fan received sediment.

The value of kaolinite crystallinity maps appear to be minimized in landforms underlain by slightly to moderately weathered regolith, as seen between the highly weathered Mt Birnie Formation and the adjoining, less weathered Saint Mungo Granite. The Saint Mungo granite is comparatively less weathered and kaolinite is comparatively minor, and therefore the kaolinite crystallinity as derived from hyperspectral data, does not appear to show up much and is not usable. It is possible that this could be a relative effect. For example, the very high kaolinite content and

high crystallinity in the adjacent deeply weathered regolith, reduces the kaolinite abundance within the less weathered granite, and as such is a processing problem. Further work is required to test the value of kaolinite crystallinity in saprock and saprolite exposures.

5.4.4. Regolith-Landform processes and evolution

The spatial distribution of regolith within different landforms and the interpretation of degree of weathering and nature of the regolith underlying those landforms allow inferences regarding landscape evolution of the area. However, to better explain regolith evolution of the area in terms of regolith material formation and geochemical mobility, detailed field observations of profiles and regolith are required, and therefore the analysis provided is simple and based on interpretation of regolith from mineral maps.

The presence of deeply weathered profiles capped by ferruginous materials ("lateritic" profiles) underlying mesas, plains and even hills, suggest the widespread presence of deep and highly weathered profiles in the region. Areas geologically mapped as Mesozoic sediments show the presence of deeply weathered profiles, which point to deep weathering occurring in the Cenozoic as proposed by other studies (Anand, et al., 2002). Presence of silcrete dominated landform also suggests deep weathering and chemical weathering conditions suitable for the movement of silica in solution. Anand et al., (2002) suggested that silicification of the regolith in the area is linked to the onset of arid conditions during the Late Miocene. Much of the ferruginous materials on the top of the profiles have well crystalline kaolin, suggesting residual profiles on bedrock. The presence of erosional landforms – mesas, rises, hills, erosional plains - underlain by highly weathered profiles indicate stripping of regolith from the landscape in the late Cenozoic. The stripping is more extensive in the north of the study area as no deep weathering profile remnants are preserved and mainly weathered basement (saprock) is exposed. Stripping would have to be initiated due to either base-level change or uplift and appears to have been started from the north of the area. Recent erosion is also eroding regolith as seen on the erosional rises, with bedrock exposures being exhumed due to dissection along upper reaches of drainages.

5.5 Summary

From the regolith-landform unit description and interpretation, together with the discussion, it can be concluded that integrated data of DEM, RGB images and mineral maps produced from ASTER and HyMap allow mapping of the regolith in the area. Individual mineral maps produced from HyMap aid the identification of regolith materials and its degree of weathering. Kaolinite and iron oxide abundance relates to the highly weathered nature of the materials, while Mg-OH + carbonates are indicative of slightly weathered to fresh nature of the basement rocks. Kaolinite crystallinity maps are useful indicators of spatial variation in regolith origin and are able to separate residual from transported regolith, especially when kaolinite is abundant in the materials being mapped.

Chapter 6

Summary and Recommendation

6.1 Summary

The main objective of this research was to produce mineral maps using multispectral ASTER and hyperspectral HyMap imagery and apply those maps to map regolith-landforms and study the regolith and its processes in the Tick Hill area, Mount Isa, Queensland. The minerals considered for mapping were those having diagnostic absorption features in the VNIR-SWIR wavelength range such as kaolinite, micas, iron oxides, smectites, carbonates and Mg-OH bearing minerals (chlorite, hornblende) and Si-OH minerals (opal).

Simple RGB band combinations, band ratios and Relative Band Depth (RBD) technique were used to process spectra from both sensors, and Spectral Indices method was only used to process HyMap data. In addition, most HyMap processing involved first making several masks– green vegetation, dry vegetation, atmospheric particles – and then applying these masks to individual minerals with specified thresholds, so as to minimize the spectral contributions from these materials to the desired mineral.

The mineral map products produced for ASTER are the Al-OH (kaolinite, white mica), Mg-OH (chlorite, carbonate, hornblende etc) and iron oxide. For HyMap, kaolinite, kaolinite crystallinity, white mica, iron oxides (hematite and goethite), opal silica (opal CT), and Al-smectite maps were produced.

The mineral map products were validated using regression analysis on ASD field spectra measurement of the rocks and regolith samples and same location pixel spectra for ASTER and HyMap data. XRD was used to confirm mineralogy with ASD and sensor data. The validation of the minerals maps indicated that most HyMap data produced mineral maps were effective in mapping the qualitative abundance and distribution of minerals. For ASTER, validation showed that iron oxides were not effectively mapped, while Al-OH and others were.

Simple band combination images of ASTER and HyMap in combination with DEM enabled the broad scale mapping of regolith-landform units. Individual mineral maps, especially those produced from ASTER data, mainly kaolinite, kaolinite crystallinity, iron oxides and Mg-OH + carbonates maps, were used to map regolith materials in detail. The minerals maps allowed the distinguishing of *in situ* from transported regolith via kaolinite crystallinity maps, differentiate the degree of weathering over similar landforms via Mg-OH and kaolinite crystallinity and interpret the presence of deep weathering profiles such as "lateritic" profiles underlying mesas, erosional plains and rises via a combination of iron oxide and kaolinite crystallinity maps. The individual mineral maps enhanced the interpretation of spatial distribution of regolith materials and thereby helped in understanding regolith processes on landforms. These interpretations would be difficult with broad band multispectral imagery and air photos.

6.2 Recommendation

Although the value of mineral maps in regolith material mapping has been shown in this research, much remains to be achieved. Following are some suggestions for future work.

- The production of white mica, smectite and silica maps where mixtures of these minerals occur on ground needs to be better validated. There appear to be absorption peak overlaps between Al-micas and Al-smectites, which could provide mixed results. Further, grain size effects need to be considered. This would also help via better validation methods such as pixel based validation.
- Field observations and confirmations of the regolith material maps produced need to be made so the true value of the maps can be realized.
- The value of kaolinite crystallinity in spatially distinguishing between *in situ* and transported regolith needs to be further tested in other regolith settings and possibly in detailed transect study.
- The observations and interpretations from the mineral maps need to be applied to other deeply weathered regions to test the value of the mineral maps.

REFERENCES

Stratigraphic Unit Database. Geoscience Australia http://dbforms.ga.gov.au/pls/www/geodx.strat_units.sch_full?wher=stratno=9132.

ENVI Online Tutorial. http://www.ittvis.com/ProductServices/ENVI/Tutorials.aspx

1983. Geology of The Dutchess - Urandangi Region. Geological Survey of Queensland, Queensland.

Abrams, M., Hook, S., 2000. Geologic Mapping with the MODIS ASTER (MASTER) Airborne Simulator at Cuprite, Nevada. http://asterweb.jpl.nasa.gov/bil_unpublished.asp.

Abrams, M., Hook, S., 2002. Imaging Spectroscopy in the thermal infrared. in Imaging Spectroscopy Application. Kluwer Academic Publishers, Nedherland.

Ambrose, G.J., Kruse, P.D., Putnam, P.E., 2001. Geology and hydrocarbon potential of the southern Georgina Basin, Australia. APPEA J, 41: 139-163.

Anand, R.R., Wildman, J.E., Varga, Z.S., Phang, C., 2001. Regolith evolution and geochemical dispersion in transported and residual regolith-Bronzewing gold deposit. Geochemistry: Exploration, Environment, Analysis, 1: 3.

Anand, R.R., Phang, C., Wilford, J., Wildman, J.E., Shu, L., Robertson, I.D.M., and Munday, T.J., 2002a. Regolith-landscape characteristics, evolution and regional synthesis of the Mt Isa Region,. 125, CRC-LEME, Perth.

Anand, R.R., Fraser, S.J., Jones, M.R., Shu, L., Munday, T.J., Phang, C., Robertson, I.M.D., Scoot, K.M., Vasconcelos, P., Wildman, J.E., Wilford, J., 2002b. Geochemical exploration in regolith dominated terrain, North Queensland CRC LEME, Perth.

Anand R.R., Pain, M.D., 2002c. Regolith geology of the Yilgarn Craton, Western Australia; implications for exploration. Australian Journal of Earth Sciences, 49(3): 162.

Anand, R.R., Phang, C., Wilford, J., 2003. Buckley River-Lady Loretta District, Queensland. CRC LEME, CSIRO Exploration and Mining, Geoscience Australia.

Berk, A., Bernstein, L.S., Robertson D.C., 1989. MODTRAN: a moderate resolution model for LOWTRANS7. In GL-TR-89-0122 (Hanscom Air Force,MA: Air Force Geophysics Laboratories): pp 28.

Bierwith, P., 2002. Evaluation of ASTER satellite data for geological applications: Consultancy report to Geoscience Australia (Unpublished).

Bierwirth, P., Huston, D., and Blewett, R., 2002. Hyperspectral Mapping of Mineral Assemblages Associated with Gold Mineralization in the Central Pilbara, Western Australia. Economic Geology, 97: 819-826.

Butt, C.R.M., 2005. Geochemical dispersion, process and exploration models. In "Regolith Expression of Australian Ore Systems. CRC LEME: 81-106.

Blake, D.H., Bultitude R.J., Donchak P.J.T., 1982. Dajarra Region (Qld) Maps. Geology Queensland Dajarra. Canberra: Australian Government Publishing Service, Canberra.

Blake, D.H., 1987. Geology of the Mount Isa Inlier and environs, Queensland and Nothern Territory. Bureau of Mineral Resources, Geology and Geophysics, Australia, Bulletin, 225.

Blake, D.H., Stuwart, A.J., 1992. Geology of the Mount Isa-Cloncurry Transect, 1:250,000 scale map. First edition. Australian Geological Survey Organisation 1v Map legend.

Broadman, J.W., 1988. Post-ATREM Polishing of AVIRIS Apparent Reflectance Data Using EFFORT: a lesson in Accuracy versus Precision. 1988 AVIRIS Geoscience Workshop, Jet Propulsion Laboratory, Padasena, CA.

Brown, A.J., Cudahy, T.J. and Walter, M.R., 2006. Hydrothermal alteration at the Panorama Formation, North Pole Dome, Pilbara Craton, Western Australia. Precambrian Research, 151(3-4): 211-223.

Clark, R.N., Gallagher, A.J., Swayze, G.A., 1990. Material Absorption Band Depth Mapping of Imaging Spectrometer Data Using a Complete Band Shape Least Squares Fit with Library Reference Spectra. Proceeding of the Second Airborne Visible/Infrared Imaging Spectrometer (AVIRIS) Workshop.JPL Publication(90-94): 176-186.

Clark, R.N., Gallgher A.J., Swayze, G.A., Gorelick, N., Kurse, F.A., 1991. Mapping with imaging spcetrometer data using the complete band shape least square algorithm simultaneously fit to multiple spectral features from multiple materials. Proceeding of the Second Airborne Visible/Infrared Imaging Spectrometer (AVIRIS) Workshop.JPL Publication, 91-28: pp 2-3.

Clark, R.N., 1999. Spectroscopy of Rocks and Minerals, and Principle of Spectroscopy. U.S. Geological Survey, New York.

Clark, R.N., Swayze, G.A., Livo, K.E., Kokaly, R.F., Sutley, S.J., Dalton, B., Mc.Doughal, R.R., Gent, C.A. 2003. Imaging Spectroscopy: Earth and Planetary Remote Sensing with the USGS Tectracorder and Expert Systems. *Journal of Geophysical Research.* http://speclab.cr.usgs.gov/PAPERS/tetracorder/

Conaghan, E.L., Hannan, K.W., Tolman, J., 2003. Mount Isa Cu and Pb-Zn-Ag Deposits, NW Queensland Australia. CRC LEME: 1-3.

Crowley, J.K., Brickey, D.W., Rowan, L.C., 1989. Airborne Imaging spectrometer data of the Ruby Mountains, Montana:mineral discrimination using relative absorption band-depth images. Remote Sensing of Environment, 29: 121-134.

Crowley, J.K., Williams, D.E., Hammarstrom, J.M., Piatak, M., Chou, I., and Mars, J.C., 2003. Spectral reflectance properties (0.4–2.5 µm) of secondary Fe-oxide, Fe-hydroxide, and Fe-sulphate-hydrate minerals associated with sulphide-bearing mine wastes Geochemistry: Exploration, Environment, Analysis, 3(3): 219-228.

Cowley, J.K., Swayze, G.A, 1995. Mapping minerals, amorphous materials, environmental materials, vegetation, water, ice, and other materials: the USGS Tricorder Algorithm. In: Summaries of the Fifth Annual JPL Airborne Earth Science Workshop, JPL Publication (95-1): 39-40.

Cudahy, T.J., Ramanaidou, E.R., 1997. Measurement of the hematite:goethite ratio using field visiblel and near-infrared reflectance spectrometry in channel iron deposits, Western Australia. Australian Journal of Earth Sciences, 44: 411-420.

Cudahy, T., E.P., 2002. Geophysical and Remote Sensing Methods for Regolith Exploration. CRC- LEME open file report 144: 13-21.

Cudahy, T., Caccetta, M., Cornelius, A., Hewson, R., Wells, M., Skwarnecki, M., Halley, S., Hausknecht, P., Mason, P., and Quigley, M. 2005. Regolith, geology and alteration mineral maps from new generation airborne and satellite remote sensing technologies: results of research carried out as MERIWA Project No. M370, East Perth, W.A.

Cudahy, T., Jones, M., Thomas, M., Laukamp, C., Caccetta, M., Hewson, R., Rodger, A., Verrall, M., 2008. Next Generation Mineral Mapping: Queensland Airborne HyMap and Satellite ASTER Surveys 2006-2008, CSIRO Exploration & Mining Report P2007/364.

Cudahy, T., Jones, M., Thomas, M., Cocks, P., Agustin, F., Cacetta, M., Hewson, R.D., Verrall, M., and Rodger, A., 2009. Mapping soil surface mineralogy at Tick Hill, Northwest Queensland, using airborne hyperspectral imagery. Chapter 17, Digital Soil Mapping, Published by Elsevier Press, 19 pages (in press).

Dauth, C., 1997. Airborne Magnetic, Radiometric and Satellite Imagery for Regolith Mapping in the Yilgarn Craton of Western Australia. Exploration Geophysics, 28: 199-203.

Dehaan R.L., Taylor, G., 2006. Mapping indicators of soil salinity using HyMap hyperspectral imagery. . International Journal of Geoinformatics, 2(1): 61-78.

Di Tommaso, I., Rubinstein, N., 2007. Hydrothermal alteration mapping using ASTER data in the Infiernillo porphyry deposit, Argentina. Ore Geology Reviews, 32(1-2): 275-290.

Ducart, D.F., Crosta, A.P., Souza Filho, C.R., 2006. Alteration Mineralogy at the Cerro La Mina Epithermal Prospect, Patagonia, Argentina: Field Mapping, Short-Wave Infrared Spectroscopy, and ASTER Images. Economic Geology, 101(5): 981-996.

Duke, E.F., 1994. Near Infrared spectra of muscovite, Tschermak substitution, and metamorphic reaction progress: Implications for remote sensing. GEOLOGY, 22: 621-624.

Dulong, F.T., Jackson, J.C., 1997. X-Ray Powder Diffraction. U.S Geological Survey.

Drury, S., Hunt, 1988. Remote sensing of laterized Archean Greenstone Terrain: Marshall Pool Area, Northeastern Yilgarn Block, WA. Photogrammetric Engineering and Remote Sensing, 4(12): 1717-1725.

Drury, S., 2001. Image Interpretation in Geology. Blackwell Science.

Eggleton, R.A., 2001. The Regolith Glossary: Surficial Geology, Soils and Landscapes. CRC LEME.

Eriksson, K.A., Taylor, S.R., Korsch, R.J., 1991. Geochemistry of 1.8-1.67 Ga mudstone and siltstone from the Mount Isa Inlier, Queensland, Australia: Provenance and tectonic implications. Geochemica et Cosmochimia Acta, 56: 899-909.

Fujisada, H., 1994. Overview of ASTER instrument on EOS-AM1 platform. Proceeding of the SPIE(2268): 14-36.

Gad, S. and Kusky, T., 2007. ASTER spectral ratioing for lithological mapping in the Arabian-Nubian shield, the Neoproterozoic Wadi Kid area, Sinai, Egypt. Gondwana Research, 11(3): 326-335.

Gozzard, J.R., 2006. Image Processing of ASTER Multispectral Data. In: I.a. Resources (Editor). Geological Survey of Western Australia.

Gupta, R.P., 2003. Remote Sensing Geology. Springer.

Green, A.A, Berman, M., Switzer, P., and Craig M.D., 1988. A Transform for Ordering Multispectral Data in terms of Image Quality with Implications for Noise Removal. IEEE Transaction on Geoscience and Remote Sensing, 26(1): pp 65-74.

Hewson, R.D., Cudahy, T.J., Huntington, J.F., 2001. Geologic and alteration mapping at Mt.Fitton, South Australia, using ASTER satellite-borne data. International Geoscience and Remote Sensing Symposium 1: 724-726.

Hewson, R.D., Cudahy, T.J., Mizuhiko, S., Ueda, K. and Mauger, A.J., 2005. Seamless geological map generation using ASTER in the Broken Hill-Curnamona province of Australia. Remote Sensing of Environment, 99(1-2): 159-172.

Hewson, R.D., Cudahy, T.J., Drake-Brockman, J., Meyers, J., Hashemi, A., 2006. Mapping geology associated with manganese mineralisation using spectral sensing techniques at Woodie Woodie, East Pilbara. Exploration Geophysics, 37(389-400).

Holcombe R.J., Oliver N.H.S., Hill E.J., Pearson, P.J., 1993. Reply to Discussion Tectono-metamorphic evolution of the Mary Kathleen Fold Belt, northwest Queensland. Tectonophysics, 191(3/4): 213-215.

Howard 1967. Drainage Analysis in Geologic Interpretation: A Summation. American Association of Petroleum Geologists Bulletin. 51: 2246–2259.

Hunt, G.R., 1977. Spectral signature of particulate minerals in the visible and near infrared. Geophysics, 42(3): 501-513.

Iwasaki A., Fujisada, H., 2005. ASTER Geometric Performance. IEEE Transaction on Geoscience and Remote Sensing, 43(12).

Jackson, J.A., 1997. Glossary of Geology, Fourth Edition. Amer Geological Institute, 769 pp.

Jennings, J.N. and Mabbutt, J.A. 1977. Physiographyic outlines and regions. In: Australia – A geography (ed. D.N. Jeans). Sydney University Press.

Kalinowski, A., Oliver, S., 2004. ASTER Mineral Index Processing Manual, Remote Sensing Applications. Geoscience Australia.

Lau, I.C., 2004. Regolith-landform and mineralogical mapping of the White Dam Prospect, eastern Olary Domain, South Australia, using integrated remote sensing and spectral techniques, The University of Adelaide, Adelaide, Australia.

Lewis, M., 2002. Mapping Arid Vegetation Associations with HyMap Imagery. IEEE Xplore.

Mars, J.C., and Rowan, L.C, 2006. Regional mapping of phyllic- and argillic-altered rocks in the Zagros magmatic arc, Iran, using Advanced Spaceborne Thermal Emission and Refl ection Radiometer (ASTER) data and logical operator algorithms. Geosphere, 2: 161-186.

Marshall, L.J., Oliver, N.H.S., 2008. Constraints on hydrothermal fluid pathways within Mary Kathleen Group stratigraphy of the Cloncurry iron-oxide–copper–gold District, Australia. Precambrian Research, 163(1-2): 151-158.

Mason, P., 2002. MMTG A-List Software Manual. 920 C, CSIRO Exploration and Mining Confidential Report 920C. CSIRO Exploration and Mining, Mineral and Environmental Sensing Group, Information Systems Team., Sydney, Australia.

Mauger, A., 2003. Comparison of various remote sensing and spectral radiometer instruments. MESA, 29(26-29).

Meunier, A., Velde, B., 2004. Illite: Origin, Evolution and Metamorphism. Springer.

Moore, M., and Reynolds, R.C., 1989. X-Ray Diffraction and the Identification and Analysis of Clay Minerals. Oxford University Press, New York.

Nahon, D., 1986. Evolution of iron crusts in tropical landscapes. In: S.H.C.a.D.P. Dethier (Editor), Rates of Chemical Weathering of Rocks and Minerals. London Academic Press pp. 169–191.

Nahon, D., Tardy, Y., 1992. The ferruginous laterites. In: Butt, C.R.M. & Zeegers, H. (eds) Regolith Exploration Geochemistry in Tropical and Subtropical Terrains. Elsevier Science Publishers.

Ninomiya, Y., 2002. Mapping Quartz, Carbonate Minerals, and Mafic-ultramafic Rocks using Remotely Sensed Multispectral Thermal Infrared ASTER Data. Society of Photo-Optical Instrumentation Engineers. Bellingham, Washington.

Ninomiya, Y., Fu, B. and Cudahy, T.J., 2005. Detecting lithology with Advanced Spaceborne Thermal Emission and Reflection Radiometer (ASTER) multispectral thermal infrared "radiance-at-sensor" data. Remote Sensing of Environment, 99(1-2): 127-139.

Oliver, S., and van der Wielen, S., 2006. Mineral mapping with ASTER. AusGeo News, 82: 3p.

Oliver, N.H.S., Butera, K.M., Rubenach, M.J., Marshall, L.J., Cleverley, J.S., Mark, G., Tullemans, F., Esser, D., 2008. The protracted hydrothermal evolution of the Mount Isa Eastern Succession: A review and tectonic implications. Precambrian Research, 163(1-2): 108-130.

Ollier, C., Pain, C., 1996. Regolith, soils and landforms. John Wiley, Chichester, New York, 316 p. pp.

Ong, C., Cudahy T., Caccetta M., and Hick, P., 2001.Quantifying dust loading on magroves using Hyperspectral techniques. IEEE Xplore.

Pain, C., Chan, R., Craig, M., Gibson, D., Ursem, P., and Wilford, J., 2000a. RTMAP Regolith Database Field Book and User Guide. CRC LEME Open File Report 138.

Pain, C.F., Craig, M.A., Gibson D.L., and Wilford J.R., 2000b. Regolith-landform mapping: an Australian approach. In (ed. P.T. Bobrowsky) Geoenvironmental Mapping: Methods, Theory and Practice. Taylor and Francis 29-56.

Pontual, S., and Merry, N., 1996. An exploratory strategy to aid the differentiation of residual from transported kaolinites using field-based spectral analysis. Restricted report, Ausspec International, Melbourne: 122p.

Phang, C., Anand, R.R., 2000. Distinguishing transported and residual regolith material in Yandal Greenstone Belt: Regolith, Geology and Mineralisation (eds.Philips, N and Anand, R). AIG Bulletin, 32: 125-134.

Phang, C., 2004. Tringadee Zinc Anomaly, NE Queensland. CRD LEME , CSIRO Exploration and Mining.

Rowan, L.C. and Mars, J.C., 2003. Lithologic mapping in the Mountain Pass, California area using Advanced Spaceborne Thermal Emission and Reflection Radiometer (ASTER) data. Remote Sensing of Environment, 84(3): 350-366.

Rowan, L.C., Simpson, C.J., Mars, J.C, 2004. Hyperspectral analysis of the ultramafic complex andadjacent lithologies at Mordor, NT, Australia. Remote Sensing of Environment, 91: 419-431.

Rowan, L.C., Schmidt, R.G., and Mars, J.C., 2006. Distribution of hydrothermally altered rocks in the Reko Diq, Pakistan mineralized area based on spectral analysis of ASTER data. Remote Sensing of Environment, 104(1): 74-87.

Ryburn, R.J., Wilson, I.H., Grimes K.G., and Hill R.M., 1988. Geological Map Commentary, Queensland 1:100 000. Queensland, Bureau of Mineral Resources Australia.

Sabins, F.F., 1987. Remote Sensing: Principles and Interpretation. Freeman, New York, 449 p. pp.

Santos, M.D.C., Varajão, A.F.D.C. and Yvon, J., 2006. Geochemistry of a sedimentary lateritic kaolin deposit in Quadrilátero Ferrífero, Brazil. Journal of Geochemical Exploration, 88(1-3): 318-320.

Smith, A.M.S. How to convert ASTER radiance values to reflectance. An online guide. http://www.cnrhome.uidaho.edu/default.aspx?pid=85984.

Smith, D.K., 1992. Nomenclature of the forms of Crystalline and Non-Crystalline Silica. The Pennslyvania State University.

Swayze, G.A., Smith, K.S., Clark, R.N., Sutley, S.J., Pearson, R.M., Vance, J.S., Hageman, P.L., Briggs, P.H., Meier, A.L., Singleton, M.J., and Roth, S., 2000. Using Imaging Spectroscopy to Map Acidic Mine Waste. Environment Science Technology, 34(47-54).

Tapley, I.J., Gozzard, J.R, 1992. Regolith-landform mapping in the Lawlers District. Report 1: Aerial photographic interpretation and Landsatt Thematic Mapper processing for mapping regolith-landforms, CSIRO Australia Division of Exploration and Mining, Perth. Report 239R CSIRO/AMIRA Project P243.

Taylor, G., Eggleton, R.A., 2001. Regolith Geology and Geomorphology. John Wiley, New York, 375 p., pp.

Thiry, M., Milnes, A.R., 1991. Pedogenic and groundwater silcretes at Stuart Creek opal field, South Australia. Journal of Sedimentary Petrology, 61(1): 111-127.

Twidale, C.R. 1996. Geomorphology of the Leichhardt-Gilbert Area of north-west

Queensland. Land Research Series No. 16, CSIRO, Melbourne. 56 pp.

Van der Meer, F., de Jong, S.M., 2001. Imaging Spectroscopy: Basic Principles and Prospective Applications. Kluwer Academic Publishers.

Van der Meer, F., de Jong, S.M., 2002. Imaging Spectrometry: Basic Principles and Prospective Applications (Remote Sensing and Digital Image Processing). Springer.

Van Ruitenbeek, F.J.A., Debba, P., van der Meer, F.D., Cudahy, T., van der Meijde, M., Hale, M., 2006. Mapping white micas and their absorption wavelengths using hyperspectral band ratios. Remote Sensing of Environment, 102(3-4): 211-222.

Vaughan, R.G., Clvin, W.M., 2005. Mapping Weathering and Alteration Minerals in the Comstock and Geiger Grade Areas Using Visible to Thermal Infrared Airborne Remote Sensing Data, Comstock Field Trip Guide. Geological Society of Nevada Symposium 2005.Reno, NV.

Watts, D.R., Harris, N.B.W. and Nasa Gleen Soars Working Group, 2005. Mapping Granite and Gneiss in Domes along the North Himalayan Antiform with ASTER SWIR band ratios. Geological Society of America Bulletin, 117(7-8): 879-886.

Wilford, J.R., 2003. Selwyn District, Queensland. CRD LEME. Geoscience Australia.

Won, M., Below, R., 1999. Cambrian Radiolaria from Goergina Basin, Queensland, Australia. Mircopaleontology, 45(4): 325.

APPENDIX 1:

Rock samples photo and field description from Block G Tick Hill NW Queensland.

(*images courtesy of CSIRO Exploration & Mining, Bentley WA Australia*) (Cudahy et.al., 2008).

Figure 1: Sample no.MI039

Massive yellow-buff dolomite/limestone (PLkc); brecciated; chert and Fe discontinuous layers.

Figure 2: Sample no.MI041

Dolerite ridge, Feldspar and amphibole layering. Some Cu carbonates.

Figure 3: Sample no.MI042

Thick bedded buff-yellow limestone/dolomite associated with small Cu mines. S 86/294, quartz veins, Cu carbonates, epidote, pink albite

Figure 4: Sample no.MI043

Devoncourt Limestone, finely laminated (1-5 cm) buff limestone with bedding parallel foliation defined white mica.

Figure 5: Sample no.MI044

Saddle between mesas, white-pink felsic intrusive. Feldspar-quartz graphic intergrowth, lineation 60/260 defined by quartz. Minor zones 10cm wide of hematite and albite.

Figure 6: Sample no.MI045

Top of mesa, above angular unconformity. Ferruginous and clay-rich flat-lying sediments. Pebbly sandstones, quartz cobbles, fine sandstone. Ripple marks and X-bedding. Ripple marks have 2.5 cm spaced.

Figure 7: MI046

Side of mesa slope, 1 mm laminated amphibolitic gneiss, with feldspar and black amphibole fine grained <1 mm. Biotite?

Figure 8: Sample no.MI047

Felsic gneiss in road cutting next to water tank. Foliated, weathered, white rock with increased schistosity compared to the felsic gneiss at MI044. S1 52/235.

Figure 9: Sample no.MI048
Amphibolite gneiss with strong foliation defined by feldspar and dark minerals 1-3 mm in size. Epidote and pink albite alteration in places.

Figure 10: Sample no.MI049
Felsic gneiss at top of hill. Overprinting pink albite, epidote and quartz in veins/fractures

Figure 11: Sample no.MI050
Gneiss, white and black lineated 1mm

Figure 12: Sample no.MI051
Abundant opaline silica in alluvium/colluvium, grey, white, red, yellow silica and a spongy light brown cracking clay soil. No calcrete.

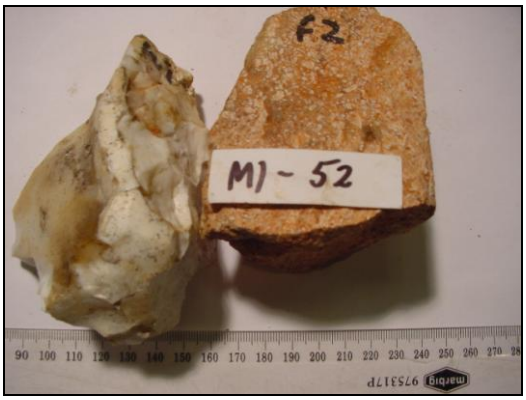

Figure 13: Sample no.MI052
Extensive exposure of white and translucent opaline silica.

Figure 14: Sample no.MI053
Light yellow shale, foliated, kaolinised

Figure 15: Sample no.MI054
Cambrian sediments. Cherts, sandstones, pebbly sandstones. Goethite-rich

APPENDIX 2:

X-Ray Diffraction for Analysis of Clay Minerals

Basic procedure

The five samples that showed potential to bear clay minerals based on their bulk XRD (mi046f2, mi047f1, mi047f2, mi053f1, mi053f1) were prepared for clay separate XRD analysis. The procedure was:

- Take 30 g of samples and grind in mortar and pestle with alcohol.
- Use filter and mesh to separate the fine and coarse fraction.
- Place the powder into beaker mix with Calgon 0.6% {contain of $(NaPO_3)n$ Na_2O 50% and NaOH 10%).
- The clay solution is ultrasonically dispersed for 15 minutes.
- Sample is kept aside and allowed to settle overnight, and the top 2 cm of the solution are pipetted out.
- The sample is sucked through a ceramic tile which allows the water to be drained and an oriented clay sample to form on top of the clay tile.
- The oriented clay sample was subjected to different saturation and reaction tests to identify the clay mineral.
- The identification of single clay minerals was done by different treatments and the treatments and clay identification table is provided below (Dulong&Jackson, 1997).

Mineral / Treatment	As collected	Mg-sat	Glycol	300 ˚C	550 ˚C
Kaolinite	7.2 Å	7.2 Å	7.2 Å	7.2 Å	gone
Halloysite	10 Å	10 Å	10 Å	7 Å	gone
Illite	10 Å	10 Å	10 Å	10 Å	10 Å
Na-smectite	12.5 Å	15 Å	17 Å	10 Å	10 Å
Ca-smectite	15 Å	15 Å	17 Å	10 Å	10 Å
Mg-vermiculite	~14 Å	14.4 Å	~14.4 Å	10 Å	10 Å
Chlorite	14.2 Å	14.2 Å	14.2 Å	14.2 Å	14.2 Å

Here is the detail description of the method used to separate the different clay minerals:

1. **Decantation Method (air dried – untreated)**

   Samples are measured in the air dried state (AD).

2. **Etylene Glycol**

   Ethylene glycol was reacted with the sample and sample allowed to dry.

3. **Mg-Saturation**

   On the oriented clay separates, few drops of .1 Magnesium chloride ($MgCl_2$) was placed and solution sucked through the plate.

4. **Heating 300ºC**

   Separated clay samples were heated in a furnace at 300^0C for 1 hour. If smectites are present, they collapse to 10 Å.

5. **Heating 550 ºC**

   The clay separate samples were heated in a furnace at 550^0C for 1 hour This method allows identification of chlorite as heating to this temperature collapses the 14.2 Å peak to 10 Å.

Tick Hill Clay Sample Description using XRD

The description below are the minerals identified and summarized from the three treatments (air dried, etylen glycol, Mg-saturated and heating in 300 degree).

1. **mi046f2**

   The clay minerals in this sample are kaolinite which has a stable peak at 7.18 Å (001) and 3.557 Å (002), and Na-smectite showed a peak at 12.57 Å (air dried) which expanded to 18 Å (glycol).

2. **mi047f1**

   Kaolinite (7.08 Å) standing overlay with the clinochlore (chlorite) and it expands a bit to 7.19 Å under Mg-saturated treatment. Illite-muscovite peak occurs at 10.03 Å (air dried treatment) and hardly moves on treatments. Another interesting pattern is the occurrence for chlorite which is only slightly changed from 14.07 Å (air dried), 14.18 (Mg-saturated), and 14.09 Å under heating 300ºC (see the table). Smectite (Na-smectite, shows the peak (001) at 12.59 Å (air dried) and expands to 18.0 Å (glycol). Under Mg-saturation this mineral

collapsed to 15.9 Å and on heating at 300ºC it shifted slightly to 12.43 Å. As the peak does not collapse to 10 Å on heating, we can conclude that this pattern is not purely Na-smectite but interstratified clay, very likely to be chlorite-smectite (Reynolds &.Moore, 1989).

3. mi047f2

Illite-muscovite peaks remain stable at 10.02 Å (001), 5.01 Å (002) and 3.33 Å(003). The mixed layer clay (*refer to mi047f1*) is between Na-smectite and chlorite and shows a peak at 12.64 Å (air dried), 18.2 Å`(glycol) and collapses to 12.4 Å when heated to 300º C.

4. mi053f1

Kaolinite peaks remain unchanged under three treatments at 7.1 Å (001) and 3.5 Å (002). Illite-muscovite peak remains unchanged at 10.1 Å (001).

5. mi054f1

Sample contains only kaolinite with peaks remaining stable on treatment 7.16 Å (001) and 3.56 Å (002).

The table below shows the clay contents of samples analyzed by XRD (Agustin, 2007):

No. Sample	Kaolinite	Na-smectite	Illite-Muscovite	Chlorite
Mi046f2	✓	✓	-	-
Mi047f1	✓	✓	✓	✓
Ni047f2	-	✓	-	✓
Mi053f1	✓	-	✓	-
Mi054f1	✓	-	-	-

APPENDIX 3: XRD measurement of Block G, Tick Hill NW Queensland

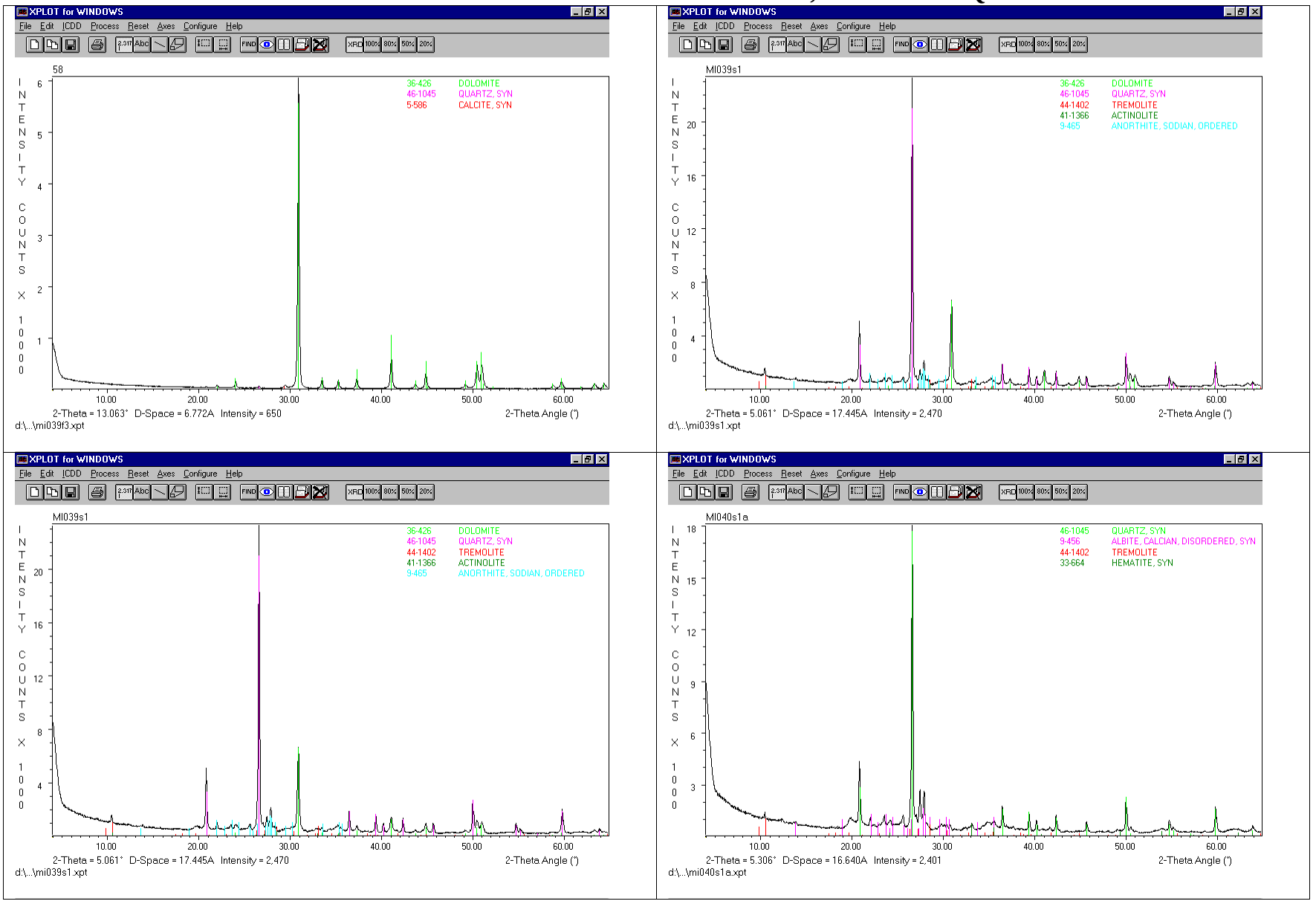

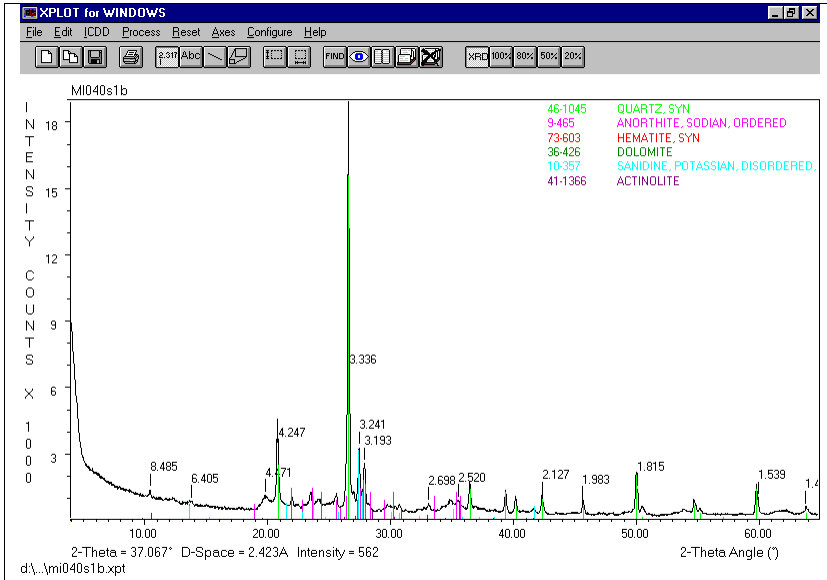
XPLOT for WINDOWS
File Edit ICDD Process Reset Axes Configure Help
MI040s1b
INTENSITY COUNTS X 1000
46-1045 QUARTZ, SYN
9-465 ANORTHITE, SODIAN, ORDERED
73-603 HEMATITE, SYN
36-426 DOLOMITE
10-357 SANIDINE, POTASSIAN, DISORDERED,
41-1366 ACTINOLITE
8.485
6.405
4.271
4.247
3.336
3.241
3.193
2.698
2.520
2.127
1.983
1.815
1.539
2-Theta = 37.067° D-Space = 2.423A Intensity = 562
2-Theta Angle (°)
d:\...\mi040s1b.xpt

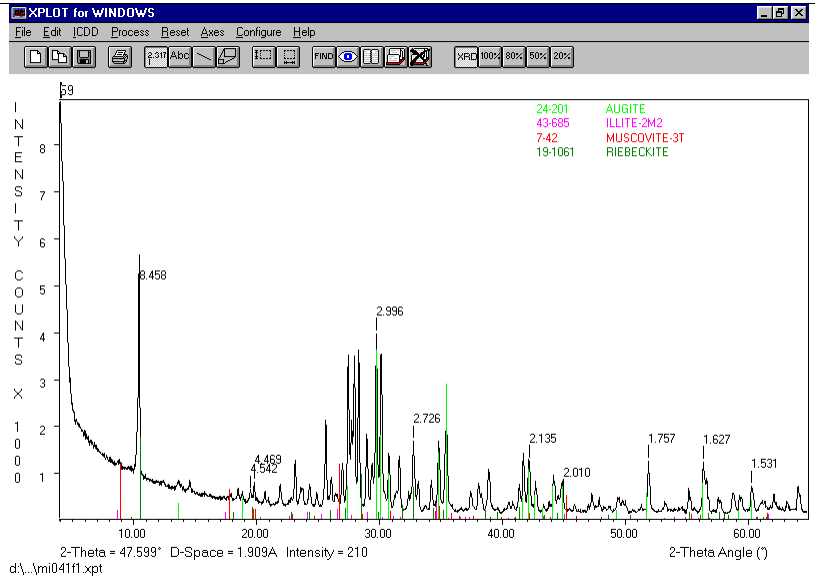
XPLOT for WINDOWS
File Edit ICDD Process Reset Axes Configure Help
59
INTENSITY COUNTS X 1000
24-201 AUGITE
43-685 ILLITE-2M2
7-42 MUSCOVITE-3T
19-1061 RIEBECKITE
8.458
4.469
4.542
2.996
2.726
2.135
2.010
1.757
1.627
1.531
2-Theta = 47.599° D-Space = 1.909A Intensity = 210
2-Theta Angle (°)
d:\...\mi041f1.xpt

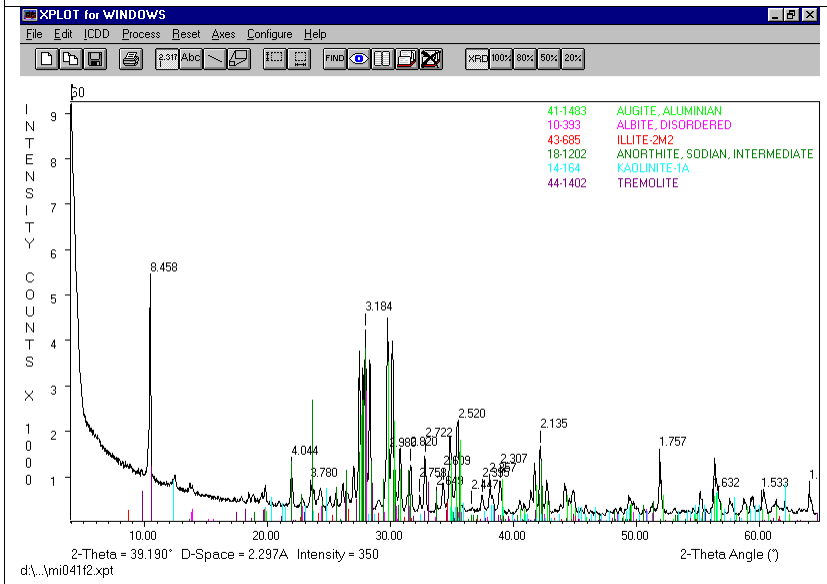
XPLOT for WINDOWS
File Edit ICDD Process Reset Axes Configure Help
60
INTENSITY COUNTS X 1000
41-1483 AUGITE, ALUMINIAN
10-393 ALBITE, DISORDERED
43-685 ILLITE-2M2
18-1202 ANORTHITE, SODIAN, INTERMEDIATE
14-164 KAOLINITE-1A
44-1402 TREMOLITE
8.458
4.044
3.780
3.184
2.520
2.135
1.757
1.533
2-Theta = 39.190° D-Space = 2.297A Intensity = 350
2-Theta Angle (°)
d:\...\mi041f2.xpt

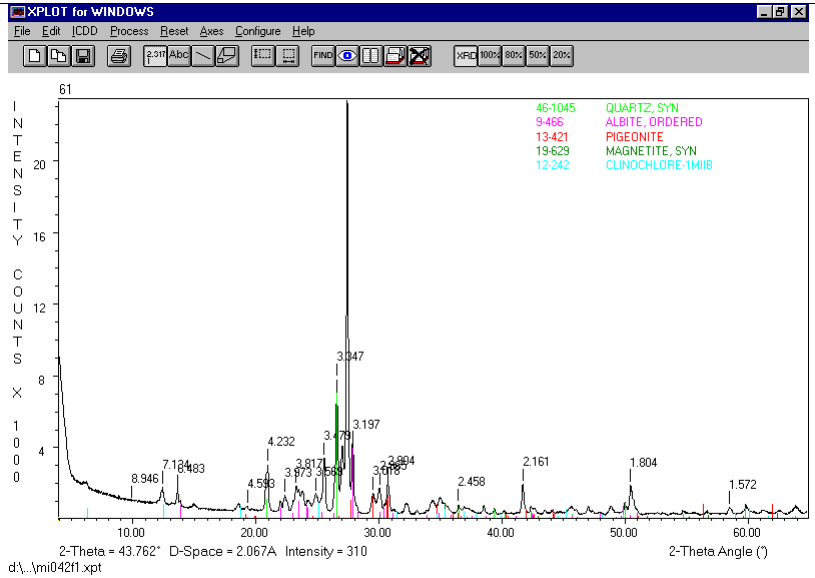
XPLOT for WINDOWS
File Edit ICDD Process Reset Axes Configure Help
61
INTENSITY COUNTS X 1000
46-1045 QUARTZ, SYN
9-466 ALBITE, ORDERED
13-421 PIGEONITE
19-629 MAGNETITE, SYN
12-242 CLINOCHLORE-1MIIB
8.946
7.184
4.593
4.232
3.817
3.479
3.247
3.197
2.458
2.161
1.804
1.572
2-Theta = 43.762° D-Space = 2.067A Intensity = 310
2-Theta Angle (°)
d:\...\mi042f1.xpt

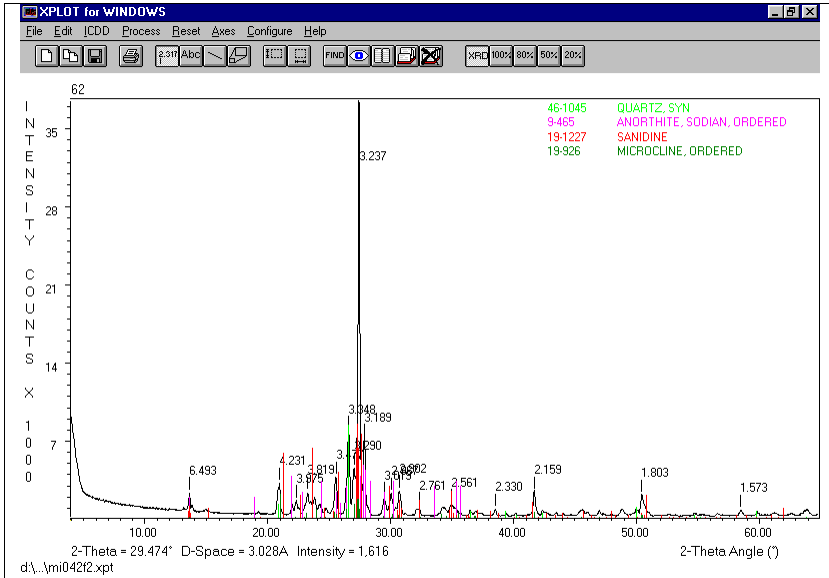
XPLOT for WINDOWS
File Edit ICDD Process Reset Axes Configure Help
62
46-1045 QUARTZ, SYN
9-465 ANORTHITE, SODIAN, ORDERED
19-1227 SANIDINE
19-926 MICROCLINE, ORDERED
INTENSITY COUNTS X 1000
3.237
3.348
3.189
6.493
4.231
2.761
2.561
2.330
2.159
1.803
1.573
10.00 20.00 30.00 40.00 50.00 60.00
2-Theta = 29.474° D-Space = 3.028A Intensity = 1,616
2-Theta Angle (°)
d:\...\mi042f2.xpt

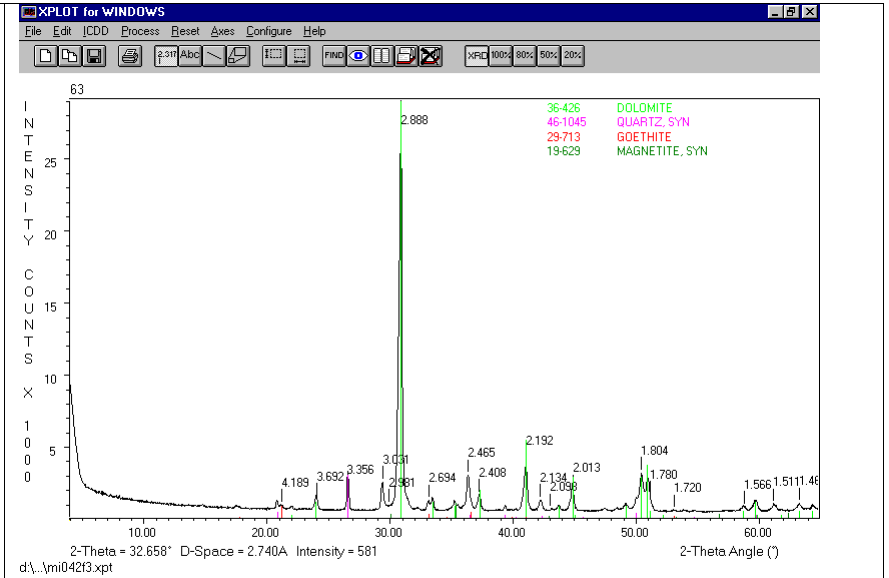
XPLOT for WINDOWS
File Edit ICDD Process Reset Axes Configure Help
63
36-426 DOLOMITE
46-1045 QUARTZ, SYN
29-713 GOETHITE
19-629 MAGNETITE, SYN
INTENSITY COUNTS X 1000
2.888
4.189
3.692
3.356
3.031
2.981
2.694
2.465
2.408
2.192
2.134
2.098
2.013
1.804
1.780
1.720
1.566
10.00 20.00 30.00 40.00 50.00 60.00
2-Theta = 32.658° D-Space = 2.740A Intensity = 581
2-Theta Angle (°)
d:\...\mi042f3.xpt

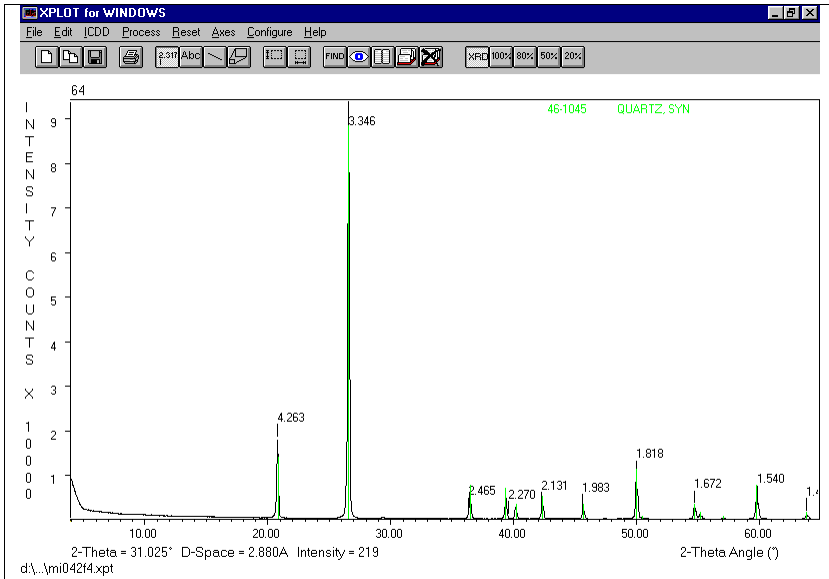
XPLOT for WINDOWS
File Edit ICDD Process Reset Axes Configure Help
64
46-1045 QUARTZ, SYN
INTENSITY COUNTS X 10000
3.346
4.263
2.465
2.270
2.131
1.983
1.818
1.672
1.540
10.00 20.00 30.00 40.00 50.00 60.00
2-Theta = 31.025° D-Space = 2.880A Intensity = 219
2-Theta Angle (°)
d:\...\mi042f4.xpt

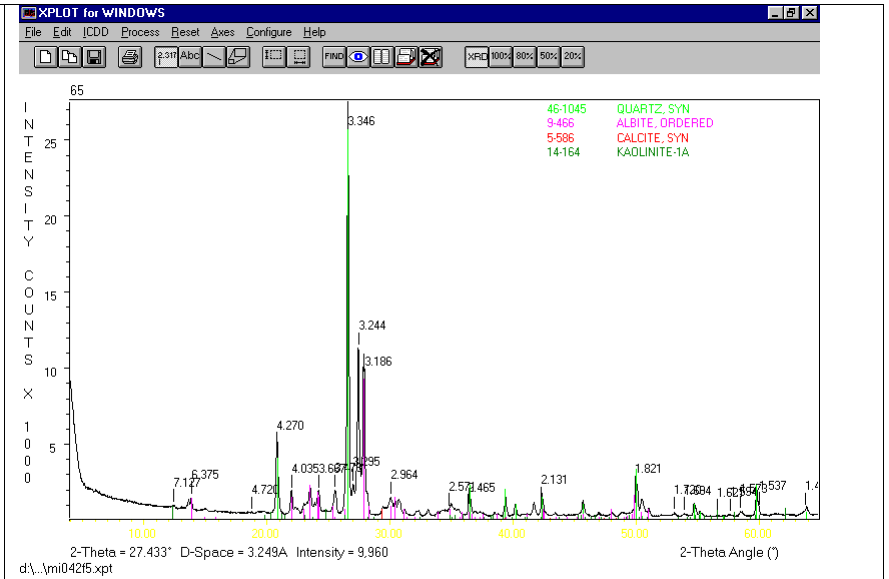
XPLOT for WINDOWS
File Edit ICDD Process Reset Axes Configure Help
65
46-1045 QUARTZ, SYN
9-466 ALBITE, ORDERED
5-586 CALCITE, SYN
14-164 KAOLINITE-1A
INTENSITY COUNTS X 1000
3.346
3.244
3.186
4.270
7.127
6.375
4.720
4.035
3.687
2.964
2.571
2.465
2.131
1.821
1.537
10.00 20.00 30.00 40.00 50.00 60.00
2-Theta = 27.433° D-Space = 3.249A Intensity = 9,960
2-Theta Angle (°)
d:\...\mi042f5.xpt

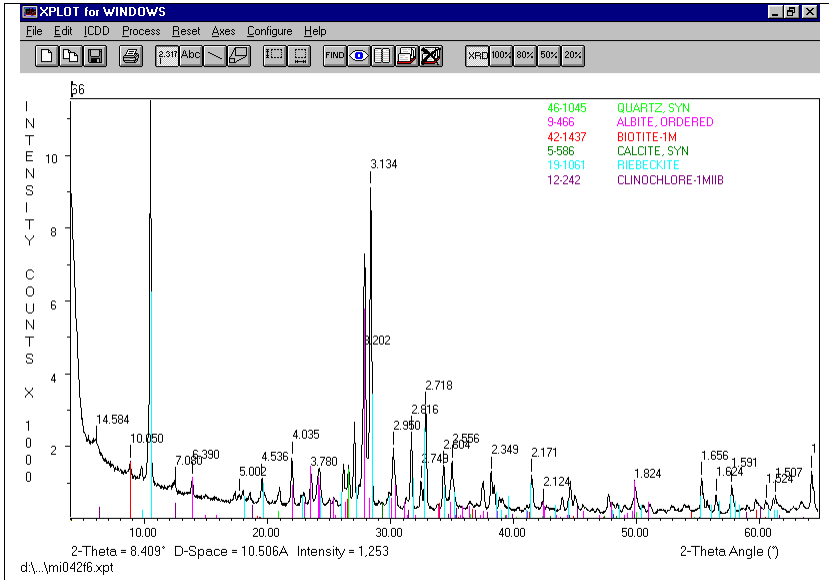
XPLOT for WINDOWS
File Edit ICDD Process Reset Axes Configure Help
f6
INTENSITY COUNTS X 1000
46-1045 QUARTZ, SYN
9-466 ALBITE, ORDERED
42-1437 BIOTITE-1M
5-586 CALCITE, SYN
19-1061 RIEBECKITE
12-242 CLINOCHLORE-1MIIB
3.134
3.202
14.584
10.050
7.080
6.390
5.002
4.536
4.035
3.780
2.950
2.816
2.718
2.556
2.349
2.171
2.124
1.824
1.656
1.624
1.591
1.524
1.507
2-Theta = 8.409° D-Space = 10.506A Intensity = 1,253
2-Theta Angle (°)
d:\...\mi042f6.xpt

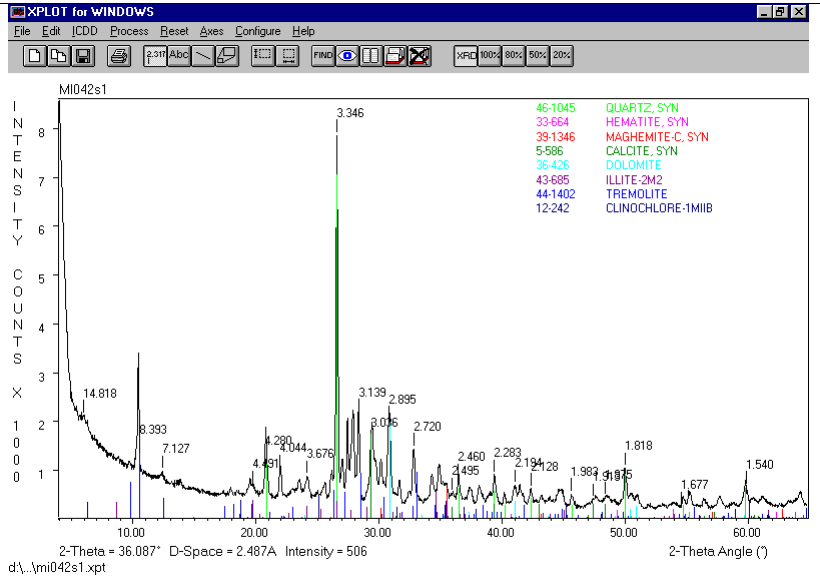
XPLOT for WINDOWS
File Edit ICDD Process Reset Axes Configure Help
MI042s1
INTENSITY COUNTS X 1000
46-1045 QUARTZ, SYN
33-664 HEMATITE, SYN
39-1346 MAGHEMITE-C, SYN
5-586 CALCITE, SYN
36-426 DOLOMITE
43-685 ILLITE-2M2
44-1402 TREMOLITE
12-242 CLINOCHLORE-1MIIB
3.346
14.818
8.393
7.127
4.491
4.280
4.044
3.676
3.139
3.036
2.895
2.720
2.460
2.495
2.283
2.194
2.128
1.983
1.818
1.677
1.540
2-Theta = 36.087° D-Space = 2.487A Intensity = 506
2-Theta Angle (°)
d:\...\mi042s1.xpt

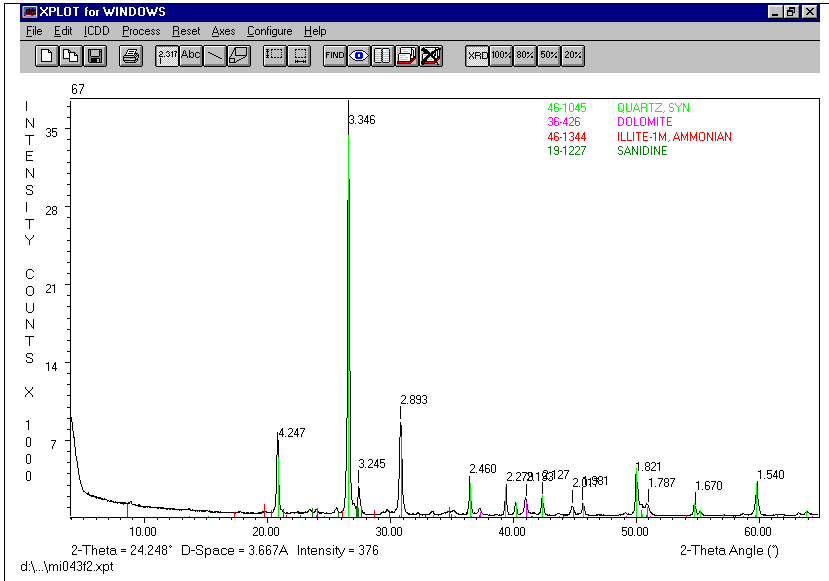
XPLOT for WINDOWS
File Edit ICDD Process Reset Axes Configure Help
f7
INTENSITY COUNTS X 1000
46-1045 QUARTZ, SYN
36-426 DOLOMITE
46-1344 ILLITE-1M, AMMONIAN
19-1227 SANIDINE
3.346
4.247
3.245
2.893
2.460
2.279
2.127
1.821
1.787
1.670
1.540
2-Theta = 24.248° D-Space = 3.667A Intensity = 376
2-Theta Angle (°)
d:\...\mi043f2.xpt

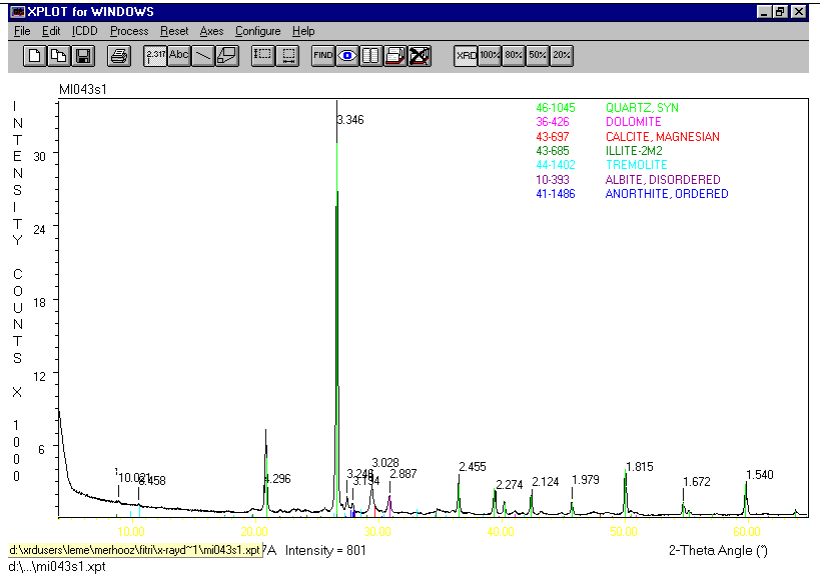
XPLOT for WINDOWS
File Edit ICDD Process Reset Axes Configure Help
MI043s1
INTENSITY COUNTS X 1000
46-1045 QUARTZ, SYN
36-426 DOLOMITE
43-697 CALCITE, MAGNESIAN
43-685 ILLITE-2M2
44-1402 TREMOLITE
10-393 ALBITE, DISORDERED
41-1486 ANORTHITE, ORDERED
3.346
10.081
8.458
4.296
3.248
3.184
3.028
2.887
2.455
2.274
2.124
1.979
1.815
1.672
1.540
d:\xrdusers\leme\merhooz\litri\x-rayd~1\mi043s1.xpt
A Intensity = 801
2-Theta Angle (°)
d:\...\mi043s1.xpt

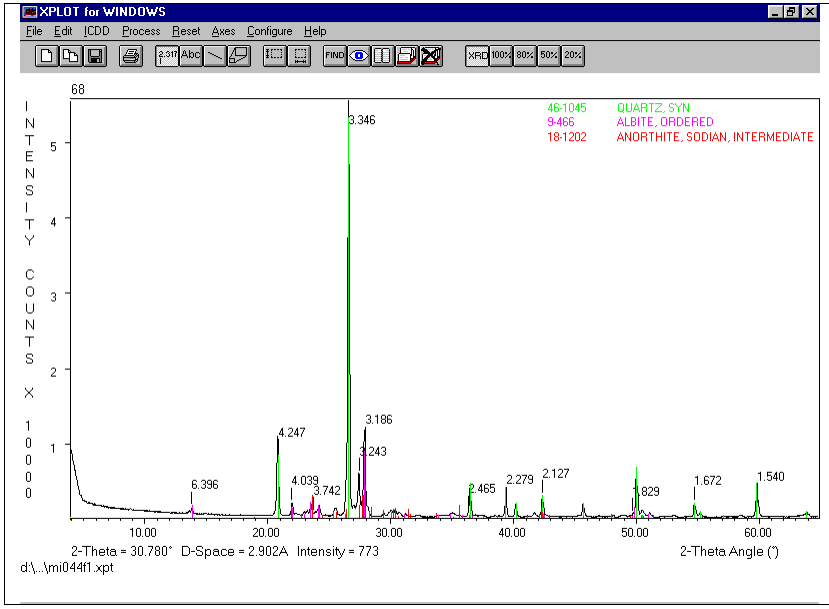
XPLOT for WINDOWS
File Edit ICDD Process Reset Axes Configure Help
68
46-1045 QUARTZ, SYN
9-466 ALBITE, ORDERED
18-1202 ANORTHITE, SODIAN, INTERMEDIATE
INTENSITY COUNTS X 10000
3.346
4.247
3.186
3.243
6.396
4.039
3.742
2.465
2.279
2.127
1.829
1.672
1.540
10.00 20.00 30.00 40.00 50.00 60.00
2-Theta = 30.780° D-Space = 2.902A Intensity = 773
2-Theta Angle (°)
d:\...\mi044f1.xpt

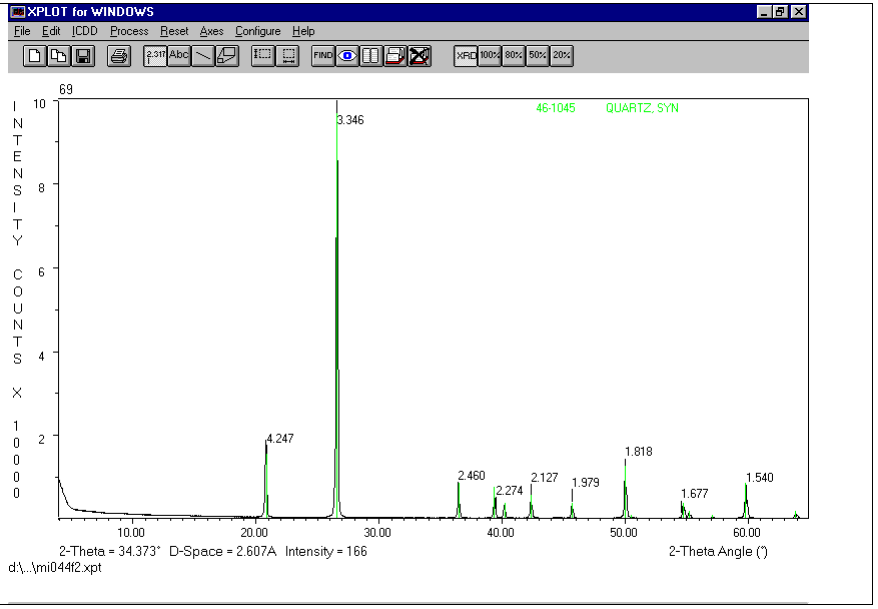
XPLOT for WINDOWS
File Edit ICDD Process Reset Axes Configure Help
69
46-1045 QUARTZ, SYN
INTENSITY COUNTS X 10000
3.346
4.247
2.460
2.274
2.127
1.979
1.818
1.677
1.540
10.00 20.00 30.00 40.00 50.00 60.00
2-Theta = 34.373° D-Space = 2.607A Intensity = 166
2-Theta Angle (°)
d:\...\mi044f2.xpt

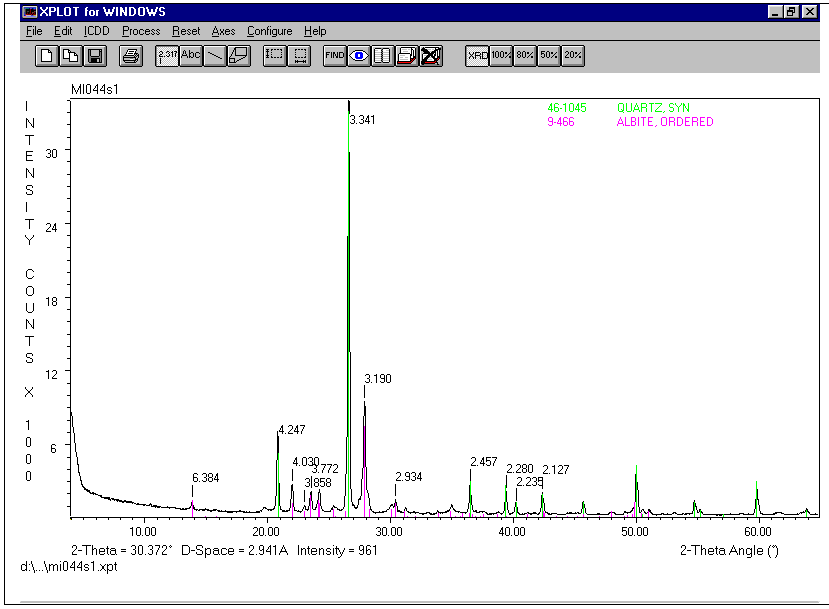
XPLOT for WINDOWS
File Edit ICDD Process Reset Axes Configure Help
MI044s1
46-1045 QUARTZ, SYN
9-466 ALBITE, ORDERED
INTENSITY COUNTS X 1000
3.341
3.190
4.247
6.384
4.039
3.772
3.858
2.934
2.457
2.280
2.239
2.127
10.00 20.00 30.00 40.00 50.00 60.00
2-Theta = 30.372° D-Space = 2.941A Intensity = 961
2-Theta Angle (°)
d:\...\mi044s1.xpt

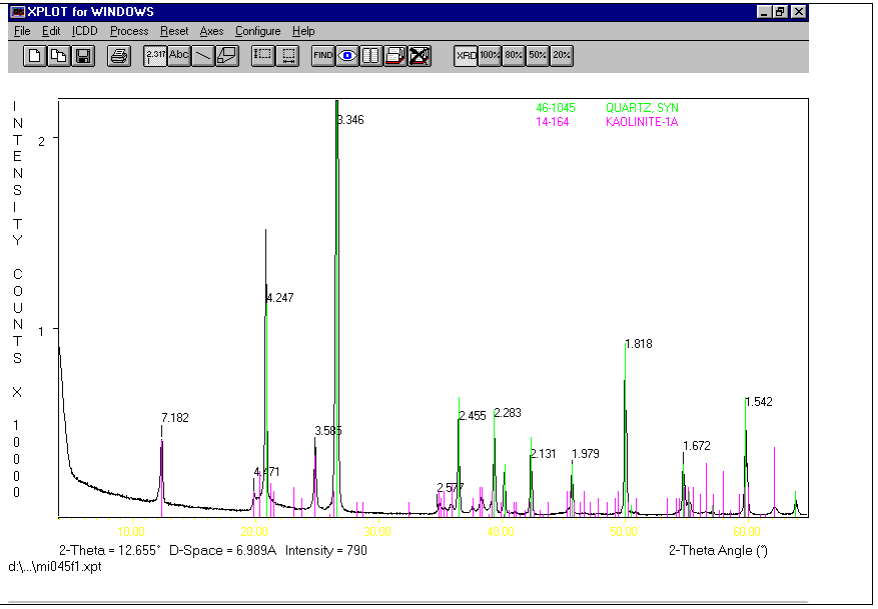
XPLOT for WINDOWS
File Edit ICDD Process Reset Axes Configure Help
46-1045 QUARTZ, SYN
14-164 KAOLINITE-1A
INTENSITY COUNTS X 10000
3.346
4.247
7.182
3.585
4.471
2.577
2.455
2.283
2.131
1.979
1.818
1.672
1.542
10.00 20.00 30.00 40.00 50.00 60.00
2-Theta = 12.655° D-Space = 6.989A Intensity = 790
2-Theta Angle (°)
d:\...\mi045f1.xpt

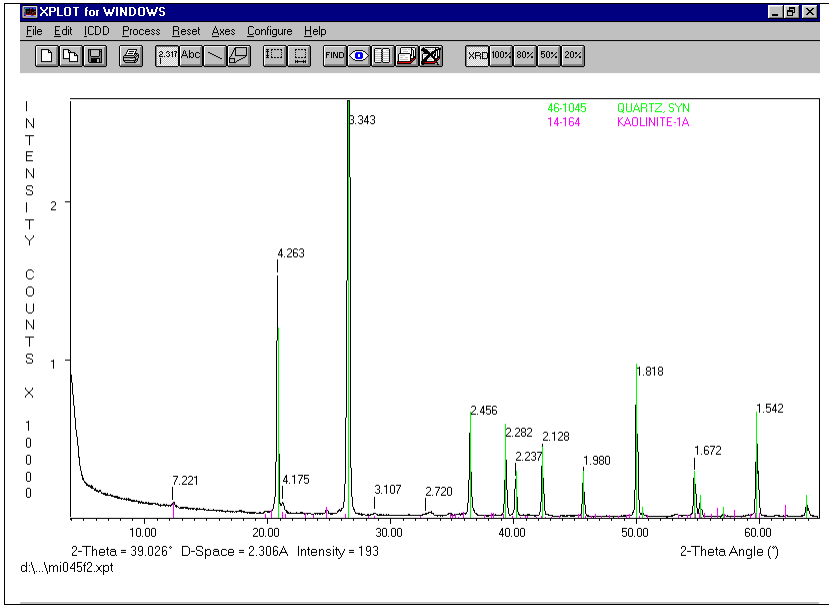
XPLOT for WINDOWS
File Edit ICDD Process Reset Axes Configure Help
INTENSITY COUNTS X 10000
46-1045 QUARTZ, SYN
14-164 KAOLINITE-1A
3.343
4.263
7.221
4.175
3.107
2.720
2.456
2.282
2.237
2.128
1.980
1.818
1.672
1.542
10.00 20.00 30.00 40.00 50.00 60.00
2-Theta = 39.026° D-Space = 2.306A Intensity = 193
2-Theta Angle (°)
d:\...\mi045f2.xpt

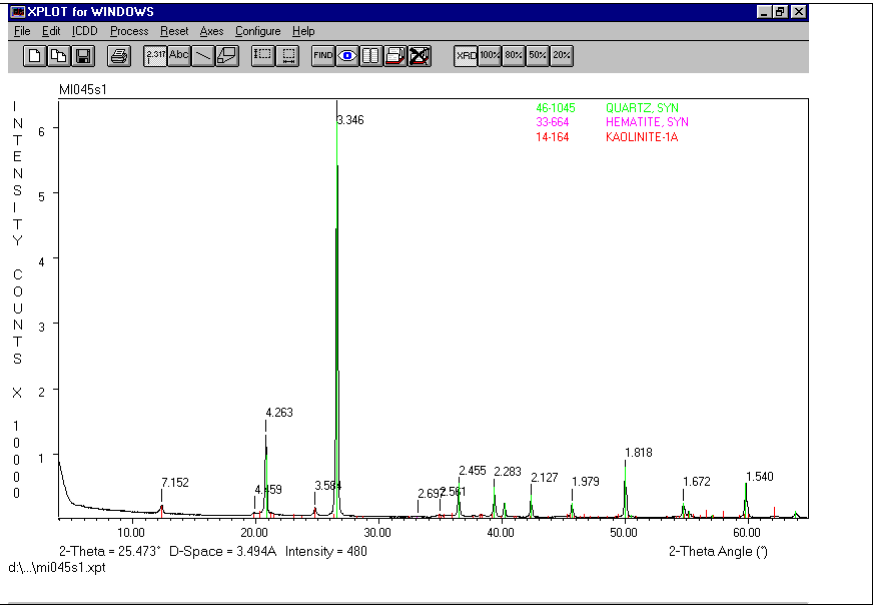
XPLOT for WINDOWS
File Edit ICDD Process Reset Axes Configure Help
MI045s1
INTENSITY COUNTS X 10000
46-1045 QUARTZ, SYN
33-664 HEMATITE, SYN
14-164 KAOLINITE-1A
3.346
4.263
7.152
4.459
3.584
2.692
2.561
2.455
2.283
2.127
1.979
1.818
1.672
1.540
10.00 20.00 30.00 40.00 50.00 60.00
2-Theta = 25.473° D-Space = 3.494A Intensity = 480
2-Theta Angle (°)
d:\...\mi045s1.xpt

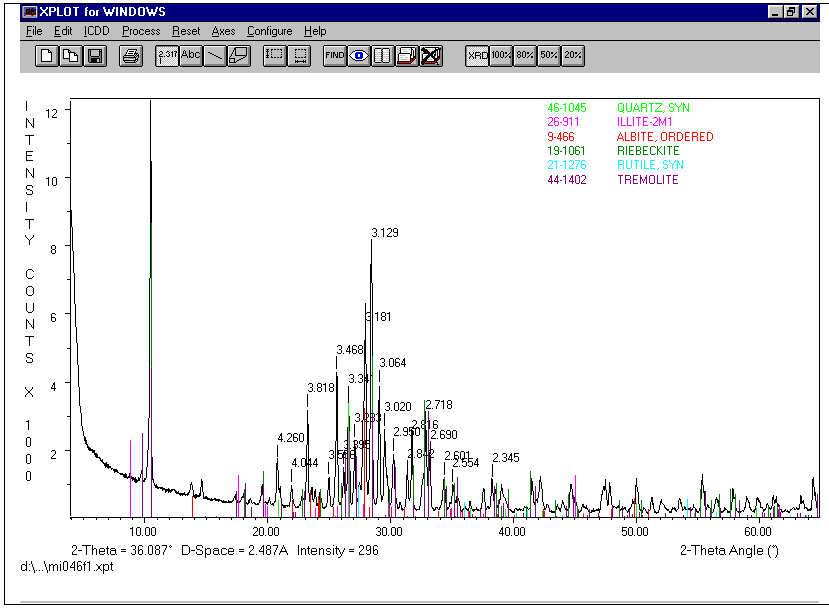
XPLOT for WINDOWS
File Edit ICDD Process Reset Axes Configure Help
INTENSITY COUNTS X 10000
46-1045 QUARTZ, SYN
26-911 ILLITE-2M1
9-466 ALBITE, ORDERED
19-1061 RIEBECKITE
21-1276 RUTILE, SYN
44-1402 TREMOLITE
3.129
3.181
3.468
3.064
3.818
3.020
2.718
4.260
4.044
2.816
2.690
2.601
2.954
2.345
10.00 20.00 30.00 40.00 50.00 60.00
2-Theta = 36.087° D-Space = 2.487A Intensity = 296
2-Theta Angle (°)
d:\...\mi046f1.xpt

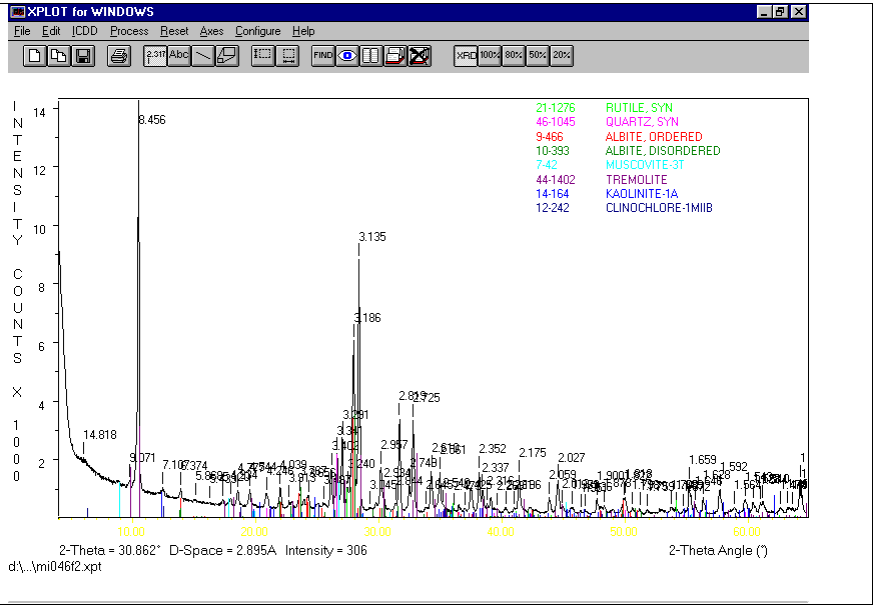
XPLOT for WINDOWS
File Edit ICDD Process Reset Axes Configure Help
INTENSITY COUNTS X 10000
21-1276 RUTILE, SYN
46-1045 QUARTZ, SYN
9-466 ALBITE, ORDERED
10-393 ALBITE, DISORDERED
7-42 MUSCOVITE-3T
44-1402 TREMOLITE
14-164 KAOLINITE-1A
12-242 CLINOCHLORE-1MIIB
8.456
3.135
3.186
14.818
9.071
7.106
2.957
2.352
2.175
2.027
1.659
1.592
10.00 20.00 30.00 40.00 50.00 60.00
2-Theta = 30.862° D-Space = 2.895A Intensity = 306
2-Theta Angle (°)
d:\...\mi046f2.xpt

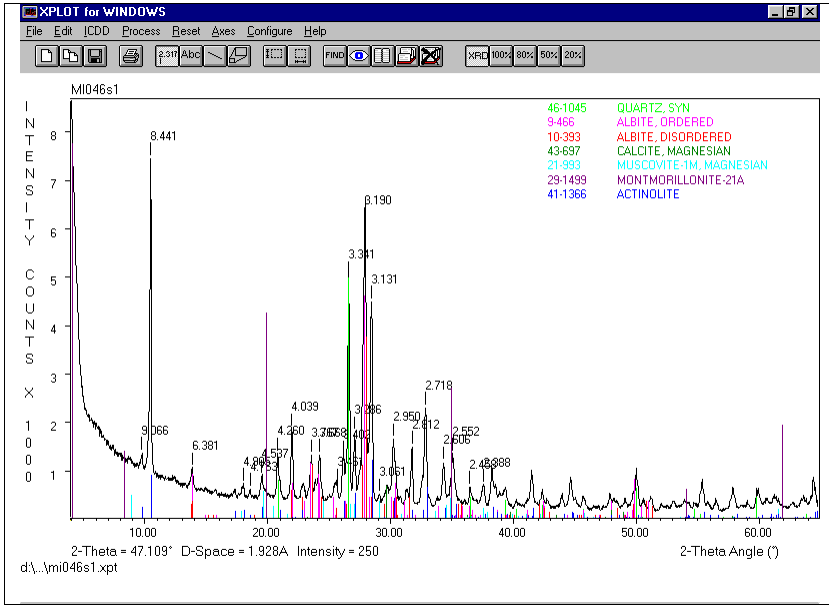
XPLOT for WINDOWS
File Edit ICDD Process Reset Axes Configure Help
MI046s1
INTENSITY COUNTS X 1000
46-1045 QUARTZ, SYN
9-466 ALBITE, ORDERED
10-393 ALBITE, DISORDERED
43-697 CALCITE, MAGNESIAN
21-993 MUSCOVITE-1M; MAGNESIAN
29-1499 MONTMORILLONITE-21A
41-1366 ACTINOLITE
8.441
9.066
6.381
8.190
3.341
3.131
4.039
4.260
2.718
2.950
2.612
2.552
2.605
3.061
2-Theta = 47.109° D-Space = 1.928A Intensity = 250
2-Theta Angle (°)
d:\...\mi046s1.xpt

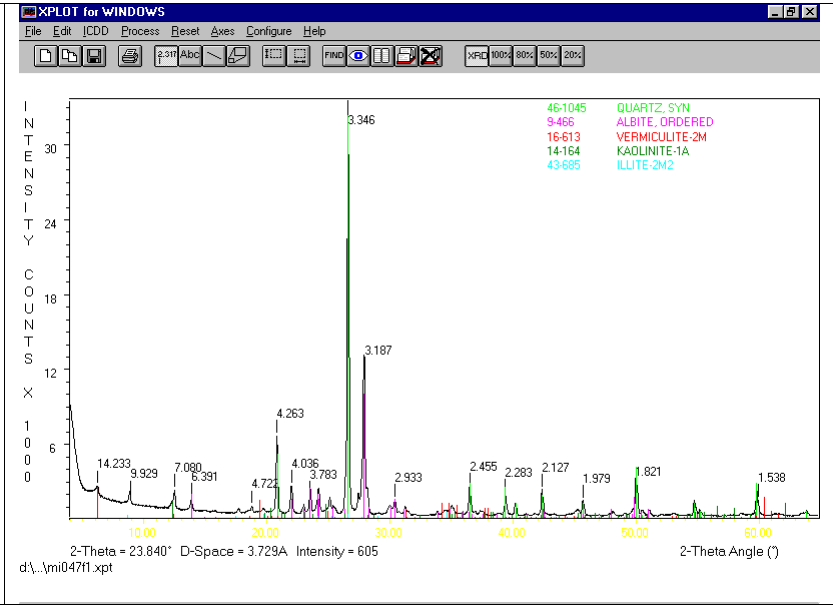
XPLOT for WINDOWS
File Edit ICDD Process Reset Axes Configure Help
INTENSITY COUNTS X 1000
46-1045 QUARTZ, SYN
9-466 ALBITE, ORDERED
16-613 VERMICULITE-2M
14-164 KAOLINITE-1A
43-685 ILLITE-2M2
3.346
3.187
4.263
14.233
9.929
7.080
6.391
4.722
4.036
3.783
2.933
2.455
2.283
2.127
1.979
1.821
1.538
2-Theta = 23.840° D-Space = 3.729A Intensity = 605
2-Theta Angle (°)
d:\...\mi047f1.xpt

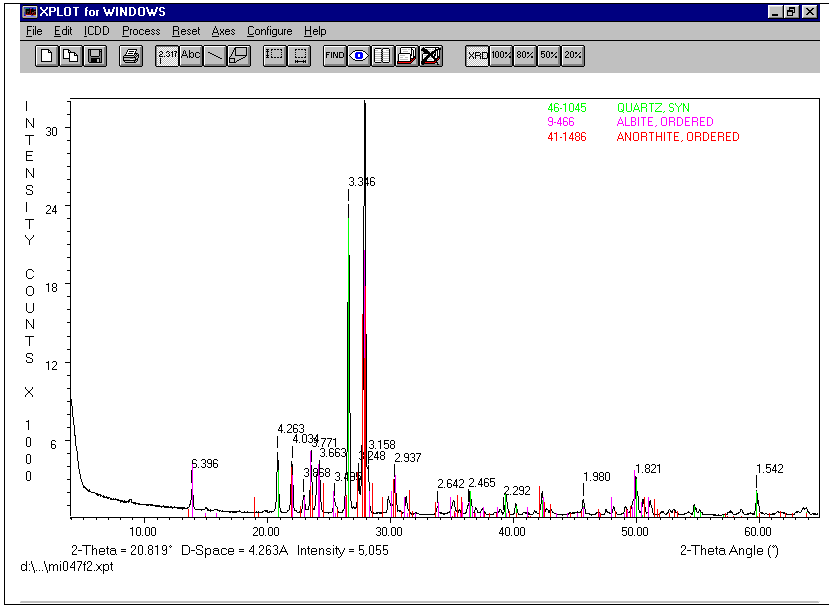
XPLOT for WINDOWS
File Edit ICDD Process Reset Axes Configure Help
INTENSITY COUNTS X 1000
46-1045 QUARTZ, SYN
9-466 ALBITE, ORDERED
41-1486 ANORTHITE, ORDERED
3.346
4.263
4.039
3.771
3.663
3.158
3.248
2.937
6.396
2.642
2.465
2.292
1.980
1.821
1.542
2-Theta = 20.819° D-Space = 4.263A Intensity = 5,055
2-Theta Angle (°)
d:\...\mi047f2.xpt

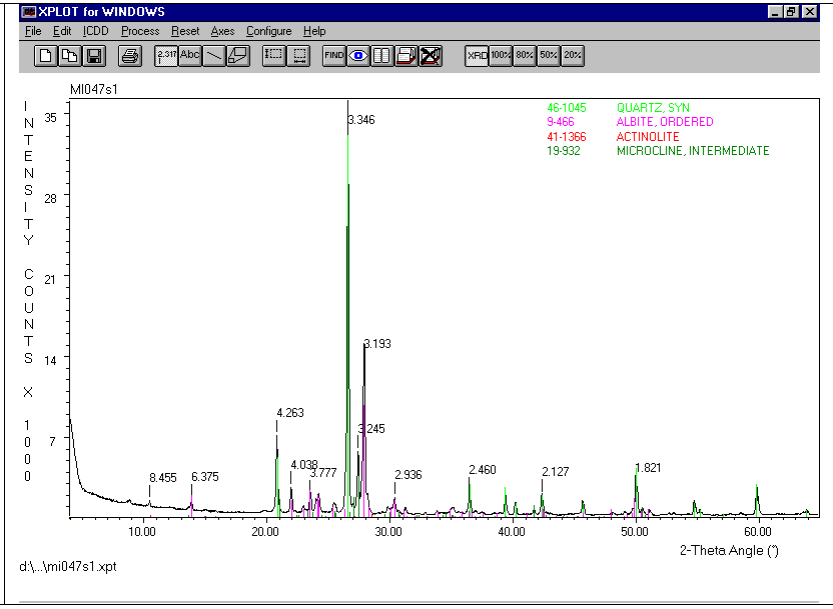
XPLOT for WINDOWS
File Edit ICDD Process Reset Axes Configure Help
MI047s1
INTENSITY COUNTS X 1000
46-1045 QUARTZ, SYN
9-466 ALBITE, ORDERED
41-1366 ACTINOLITE
19-932 MICROCLINE, INTERMEDIATE
3.346
3.193
4.263
3.245
4.038
3.777
8.455
6.375
2.936
2.460
2.127
1.821
2-Theta Angle (°)
d:\...\mi047s1.xpt

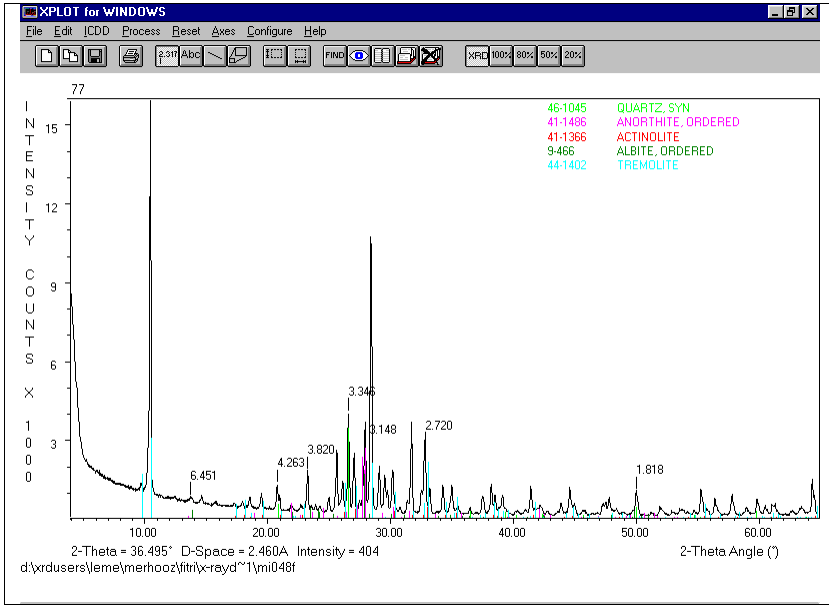
XPLOT for WINDOWS
File Edit ICDD Process Reset Axes Configure Help
77
INTENSITY COUNTS X 1000
46-1045 QUARTZ, SYN
41-1486 ANORTHITE, ORDERED
41-1366 ACTINOLITE
9-466 ALBITE, ORDERED
44-1402 TREMOLITE
6.451
4.263
3.820
3.346
3.148
2.720
1.818
2-Theta = 36.495° D-Space = 2.460A Intensity = 404
2-Theta Angle (°)
d:\xrdusers\leme\merhooz\fitri\x-rayd~1\mi048f

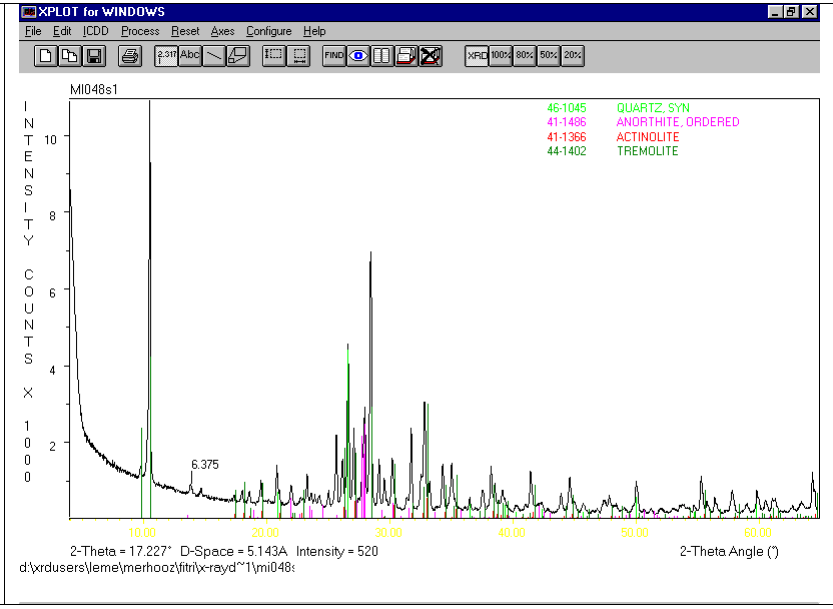
XPLOT for WINDOWS
File Edit ICDD Process Reset Axes Configure Help
MI048s1
INTENSITY COUNTS X 1000
46-1045 QUARTZ, SYN
41-1486 ANORTHITE, ORDERED
41-1366 ACTINOLITE
44-1402 TREMOLITE
6.375
2-Theta = 17.227° D-Space = 5.143A Intensity = 520
2-Theta Angle (°)
d:\xrdusers\leme\merhooz\fitri\x-rayd~1\mi048

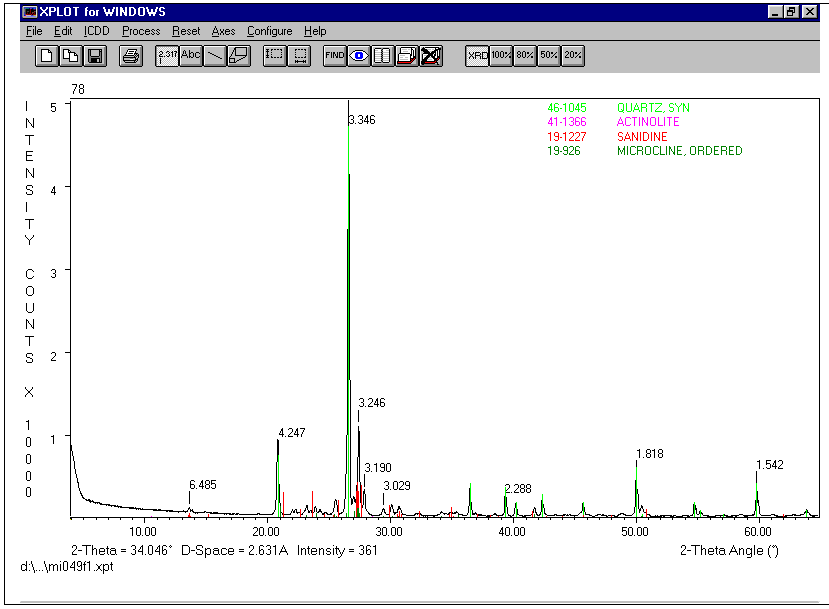
XPLOT for WINDOWS
File Edit ICDD Process Reset Axes Configure Help
78
INTENSITY COUNTS X 10000
46-1045 QUARTZ, SYN
41-1366 ACTINOLITE
19-1227 SANIDINE
19-926 MICROCLINE, ORDERED
6.485
4.247
3.346
3.246
3.190
3.029
2.288
1.818
1.542
2-Theta = 34.046° D-Space = 2.631A Intensity = 361
2-Theta Angle (°)
d:\...\mi049f1.xpt

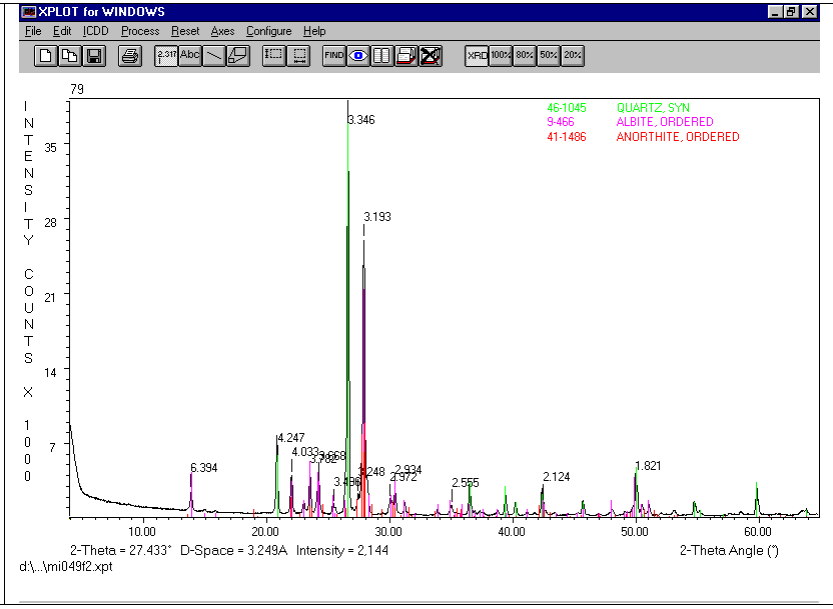
XPLOT for WINDOWS
File Edit ICDD Process Reset Axes Configure Help
79
INTENSITY COUNTS X 10000
46-1045 QUARTZ, SYN
9-466 ALBITE, ORDERED
41-1486 ANORTHITE, ORDERED
6.394
4.247
4.033
3.668
3.346
3.193
3.248
2.972
2.934
2.555
2.124
1.821
2-Theta = 27.433° D-Space = 3.249A Intensity = 2,144
2-Theta Angle (°)
d:\...\mi049f2.xpt

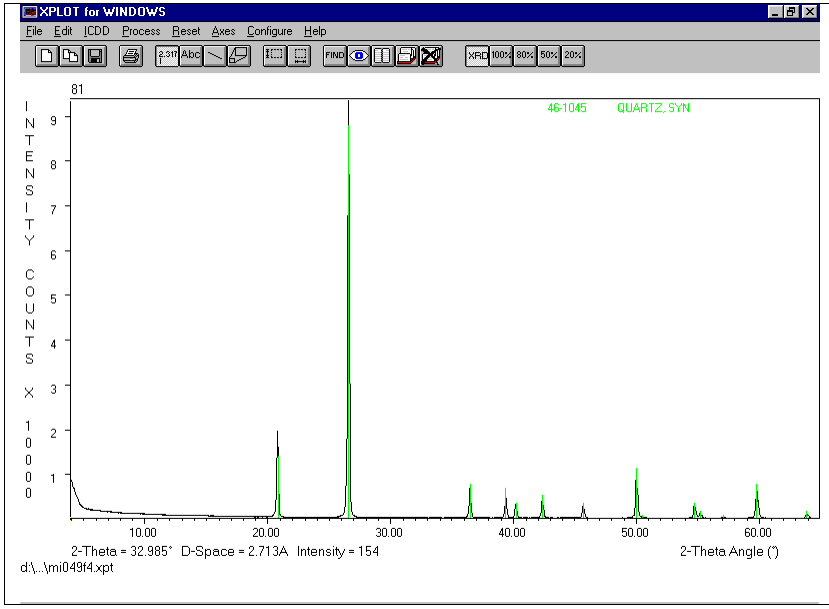
XPLOT for WINDOWS
File Edit ICDD Process Reset Axes Configure Help
81
46-1045 QUARTZ, SYN
INTENSITY COUNTS X 10000
2-Theta = 32.985° D-Space = 2.713A Intensity = 154
2-Theta Angle (°)
d:\...\mi049f4.xpt

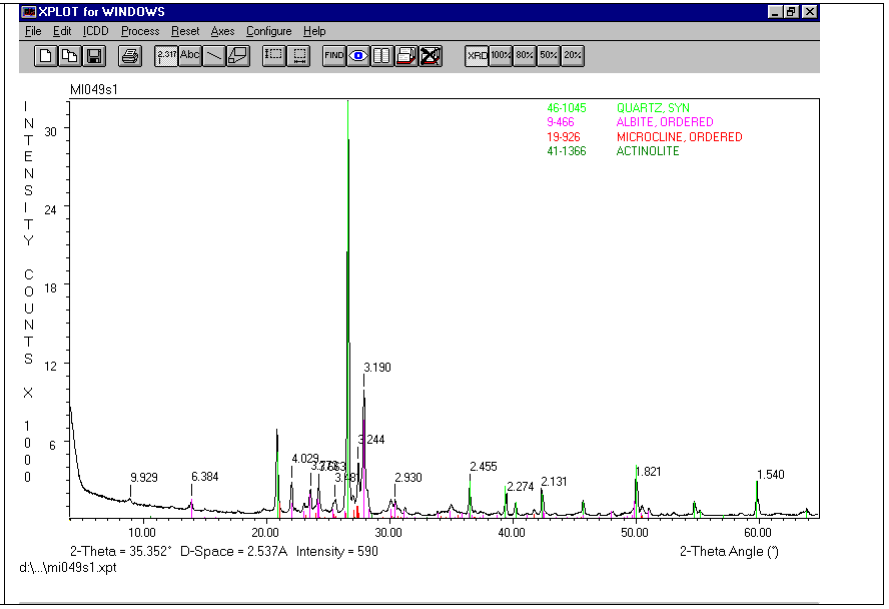
XPLOT for WINDOWS
File Edit ICDD Process Reset Axes Configure Help
MI049s1
46-1045 QUARTZ, SYN
9-466 ALBITE, ORDERED
19-926 MICROCLINE, ORDERED
41-1366 ACTINOLITE
3.190
3.244
4.029
9.929
6.384
2.930
2.455
2.274
2.131
1.821
1.540
INTENSITY COUNTS X 1000
2-Theta = 35.352° D-Space = 2.537A Intensity = 590
2-Theta Angle (°)
d:\...\mi049s1.xpt

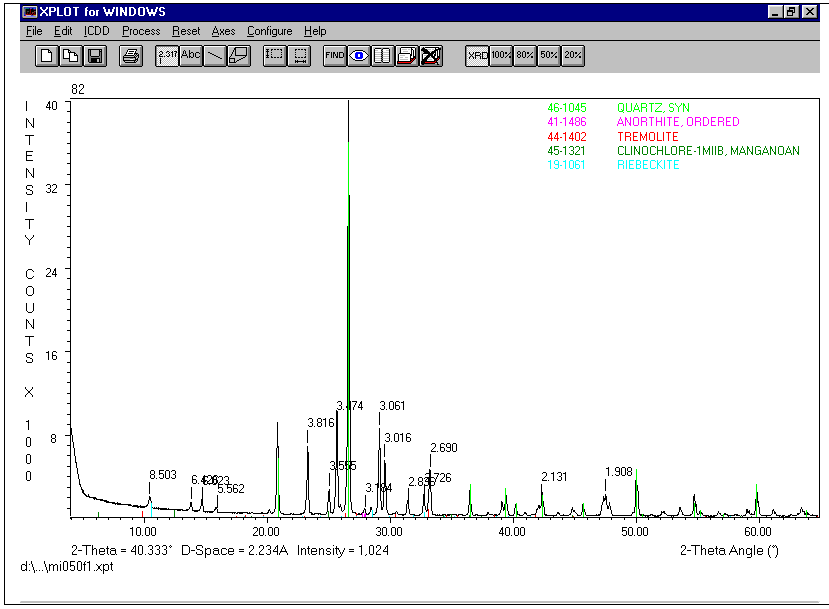
XPLOT for WINDOWS
File Edit ICDD Process Reset Axes Configure Help
82
46-1045 QUARTZ, SYN
41-1486 ANORTHITE, ORDERED
44-1402 TREMOLITE
45-1321 CLINOCHLORE-1MIIB, MANGANOAN
19-1061 RIEBECKITE
3.474
3.061
3.816
3.016
2.690
3.555
3.194
2.726
8.503
5.562
2.131
1.908
INTENSITY COUNTS X 1000
2-Theta = 40.333° D-Space = 2.234A Intensity = 1,024
2-Theta Angle (°)
d:\...\mi050f1.xpt

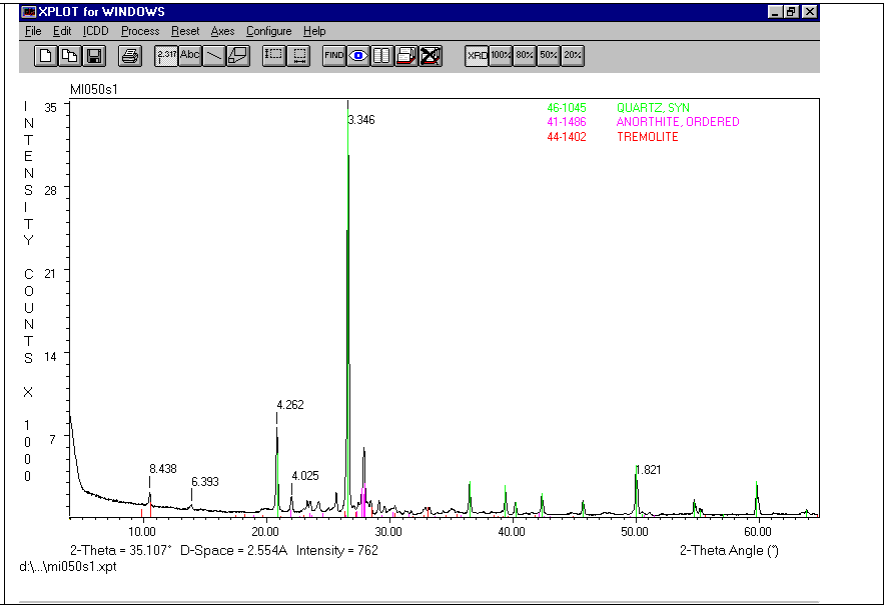
XPLOT for WINDOWS
File Edit ICDD Process Reset Axes Configure Help
MI050s1
46-1045 QUARTZ, SYN
41-1486 ANORTHITE, ORDERED
44-1402 TREMOLITE
3.346
4.262
8.438
6.393
4.025
1.821
INTENSITY COUNTS X 1000
2-Theta = 35.107° D-Space = 2.554A Intensity = 762
2-Theta Angle (°)
d:\...\mi050s1.xpt

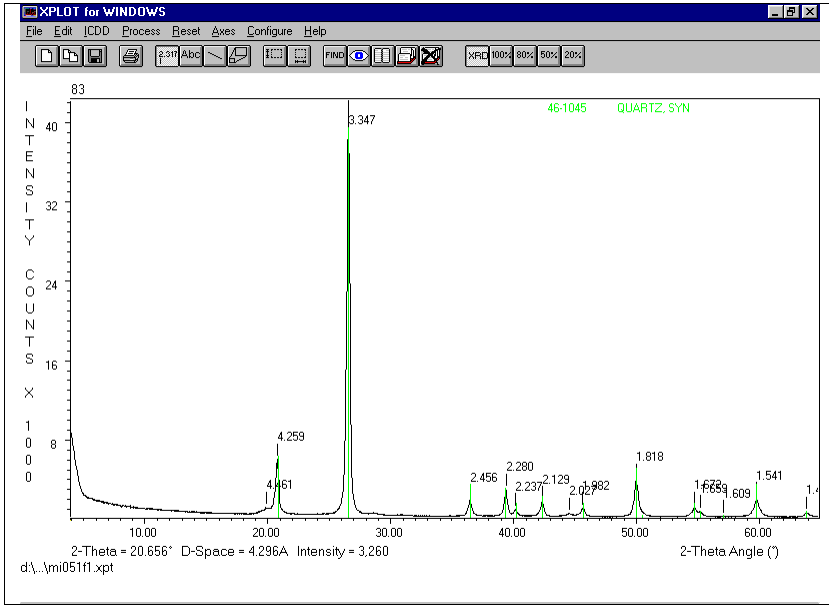
XPLOT for WINDOWS
File Edit ICDD Process Reset Axes Configure Help
83
46-1045 QUARTZ, SYN
INTENSITY COUNTS X 1000
3.347
4.259
4.461
2.456
2.280
2.237
2.129
2.027
1.982
1.818
1.678
1.659
1.609
1.541
10.00 20.00 30.00 40.00 50.00 60.00
2-Theta = 20.656° D-Space = 4.296A Intensity = 3,260
2-Theta Angle (°)
d:\...\mi051f1.xpt

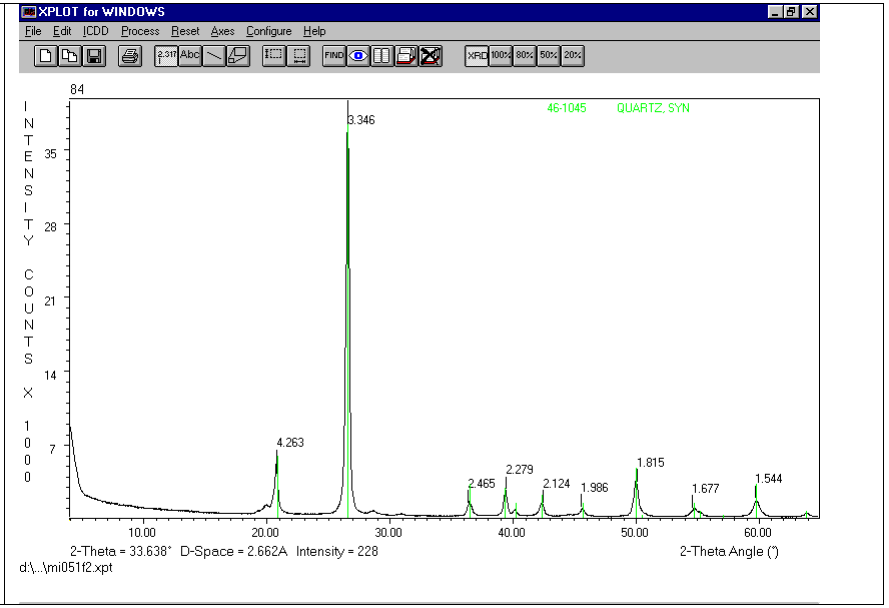
XPLOT for WINDOWS
File Edit ICDD Process Reset Axes Configure Help
84
46-1045 QUARTZ, SYN
INTENSITY COUNTS X 1000
3.346
4.263
2.465
2.279
2.124
1.986
1.815
1.677
1.544
10.00 20.00 30.00 40.00 50.00 60.00
2-Theta = 33.638° D-Space = 2.662A Intensity = 228
2-Theta Angle (°)
d:\...\mi051f2.xpt

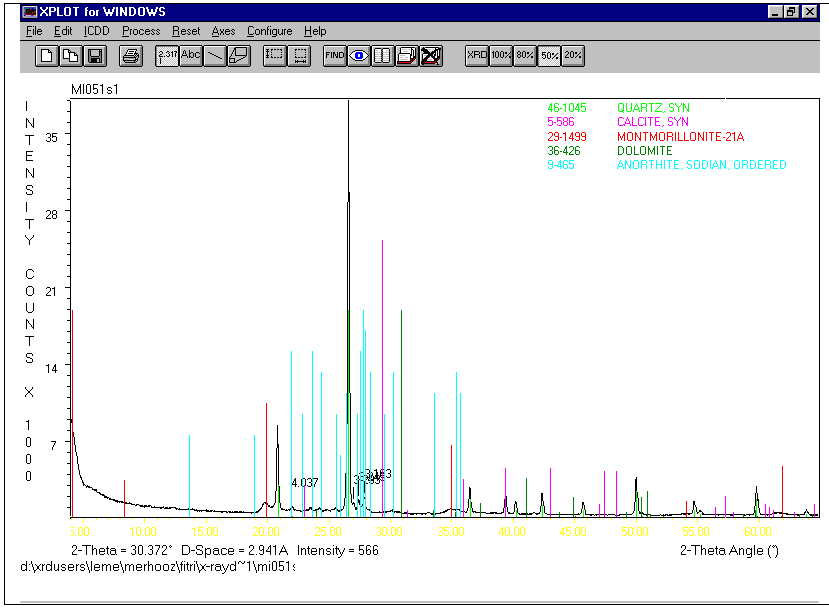
XPLOT for WINDOWS
File Edit ICDD Process Reset Axes Configure Help
MI051s1
46-1045 QUARTZ, SYN
5-586 CALCITE, SYN
29-1499 MONTMORILLONITE-21A
36-426 DOLOMITE
9-465 ANORTHITE, SODIAN, ORDERED
INTENSITY COUNTS X 1000
4.037
3.183
10.00 15.00 20.00 25.00 30.00 35.00 40.00 45.00 50.00 55.00 60.00
2-Theta = 30.372° D-Space = 2.941A Intensity = 566
2-Theta Angle (°)
d:\xrdusers\leme\merhooz\fitri\x-rayd~1\mi051

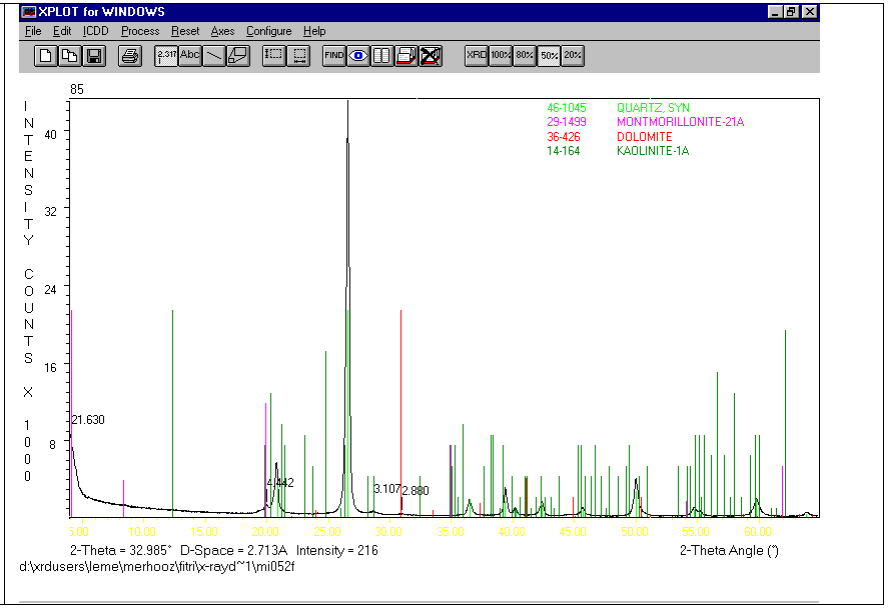
XPLOT for WINDOWS
File Edit ICDD Process Reset Axes Configure Help
85
46-1045 QUARTZ, SYN
29-1499 MONTMORILLONITE-21A
36-426 DOLOMITE
14-164 KAOLINITE-1A
INTENSITY COUNTS X 1000
21.630
4.442
3.107
2.880
10.00 15.00 20.00 25.00 30.00 35.00 40.00 45.00 50.00 55.00 60.00
2-Theta = 32.985° D-Space = 2.713A Intensity = 216
2-Theta Angle (°)
d:\xrdusers\leme\merhooz\fitri\x-rayd~1\mi052f

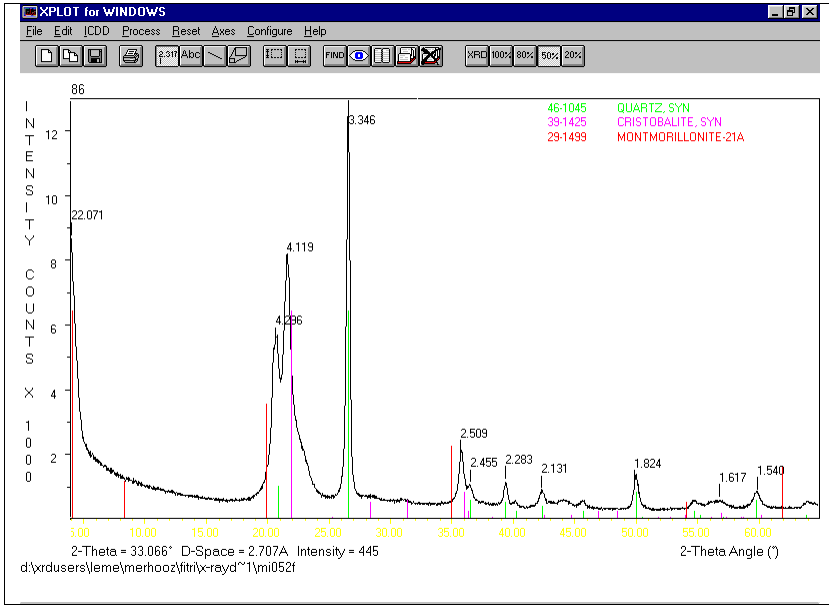
XPLOT for WINDOWS
File Edit ICDD Process Reset Axes Configure Help
86
INTENSITY COUNTS X 1000
46-1045 QUARTZ, SYN
39-1425 CRISTOBALITE, SYN
29-1499 MONTMORILLONITE-21A
22.071
4.119
4.296
3.346
2.509
2.455
2.283
2.131
1.824
1.617
1.540
2-Theta = 33.066° D-Space = 2.707A Intensity = 445
2-Theta Angle (°)
d:\xrdusers\leme\merhooz\fitri\x-rayd~1\mi052f

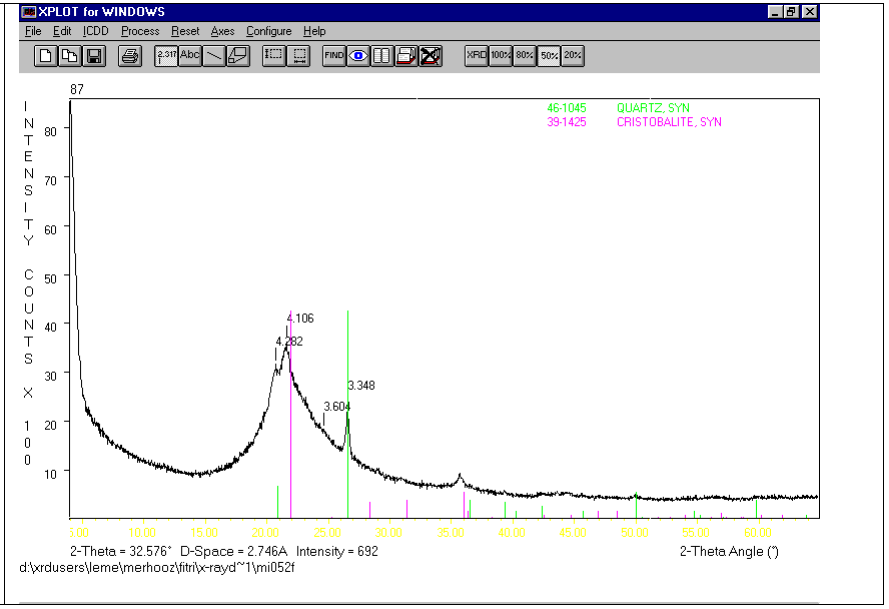
XPLOT for WINDOWS
File Edit ICDD Process Reset Axes Configure Help
87
INTENSITY COUNTS X 1000
46-1045 QUARTZ, SYN
39-1425 CRISTOBALITE, SYN
4.106
4.282
3.348
3.604
2-Theta = 32.576° D-Space = 2.746A Intensity = 692
2-Theta Angle (°)
d:\xrdusers\leme\merhooz\fitri\x-rayd~1\mi052f

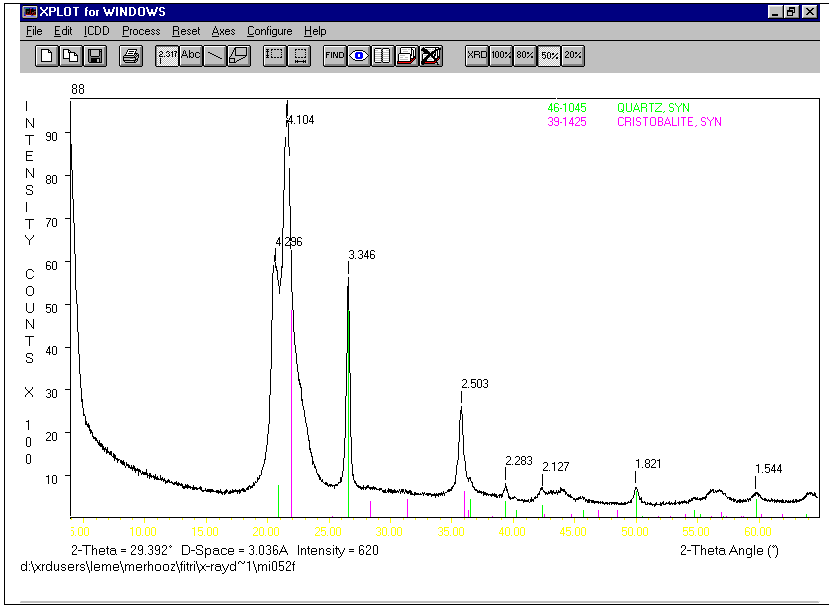
XPLOT for WINDOWS
File Edit ICDD Process Reset Axes Configure Help
88
INTENSITY COUNTS X 1000
46-1045 QUARTZ, SYN
39-1425 CRISTOBALITE, SYN
4.104
4.296
3.346
2.503
2.283
2.127
1.821
1.544
2-Theta = 29.392° D-Space = 3.036A Intensity = 620
2-Theta Angle (°)
d:\xrdusers\leme\merhooz\fitri\x-rayd~1\mi052f

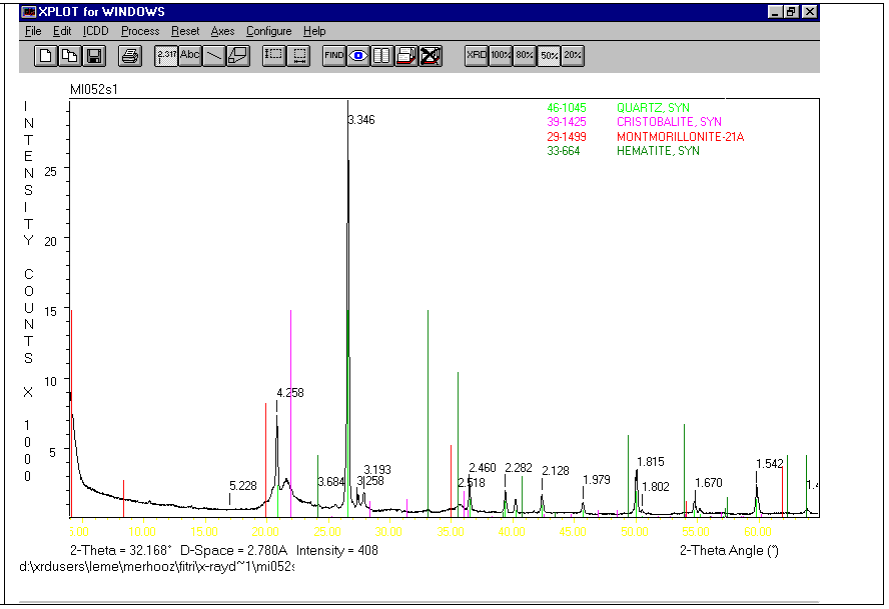
XPLOT for WINDOWS
File Edit ICDD Process Reset Axes Configure Help
MI052s1
INTENSITY COUNTS X 1000
46-1045 QUARTZ, SYN
39-1425 CRISTOBALITE, SYN
29-1499 MONTMORILLONITE-21A
33-664 HEMATITE, SYN
3.346
4.258
5.228
3.684
3.193
3.258
2.460
2.518
2.282
2.128
1.979
1.815
1.802
1.670
1.542
2-Theta = 32.168° D-Space = 2.780A Intensity = 408
2-Theta Angle (°)


XPLOT for WINDOWS
File Edit ICDD Process Reset Axes Configure Help
89
INTENSITY COUNTS X 10000
46-1045 QUARTZ, SYN
7-25 MUSCOVITE-1M, SYN
29-1499 MONTMORILLONITE-21A
3.336
4.280
10.021
7.174
5.048
4.471
3.593
2.996
2.465
2.279
2.139
1.824
1.498
2-Theta = 28.657° D-Space = 3.112A Intensity = 342
2-Theta Angle (°)
d:\xrdusers\leme\merhooz\fitri\x-rayd~1\mi053f

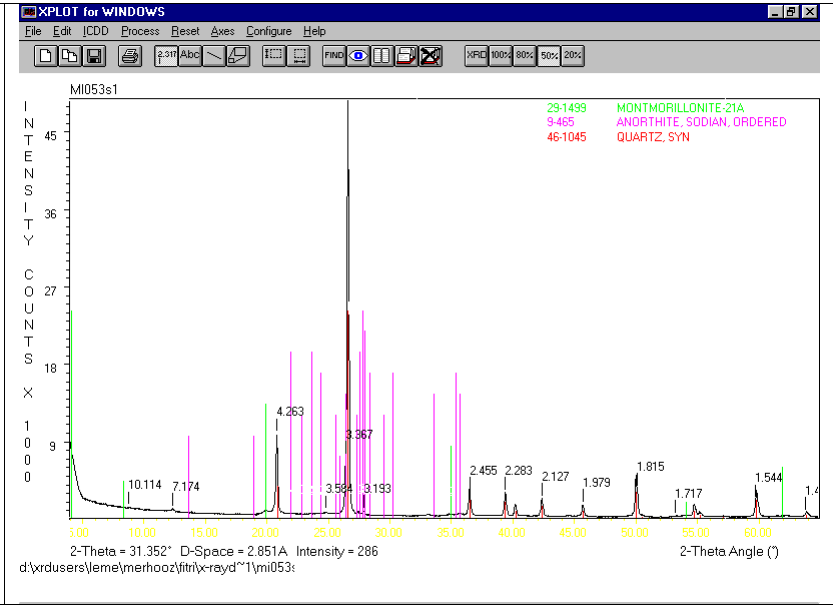
XPLOT for WINDOWS
File Edit ICDD Process Reset Axes Configure Help
MI053s1
INTENSITY COUNTS X 10000
29-1499 MONTMORILLONITE-21A
9-465 ANORTHITE, SODIAN, ORDERED
46-1045 QUARTZ, SYN
4.263
3.367
10.114
7.174
3.194
3.193
2.455
2.283
2.127
1.979
1.815
1.717
1.544
2-Theta = 31.352° D-Space = 2.851A Intensity = 286
2-Theta Angle (°)
d:\xrdusers\leme\merhooz\fitri\x-rayd~1\mi053

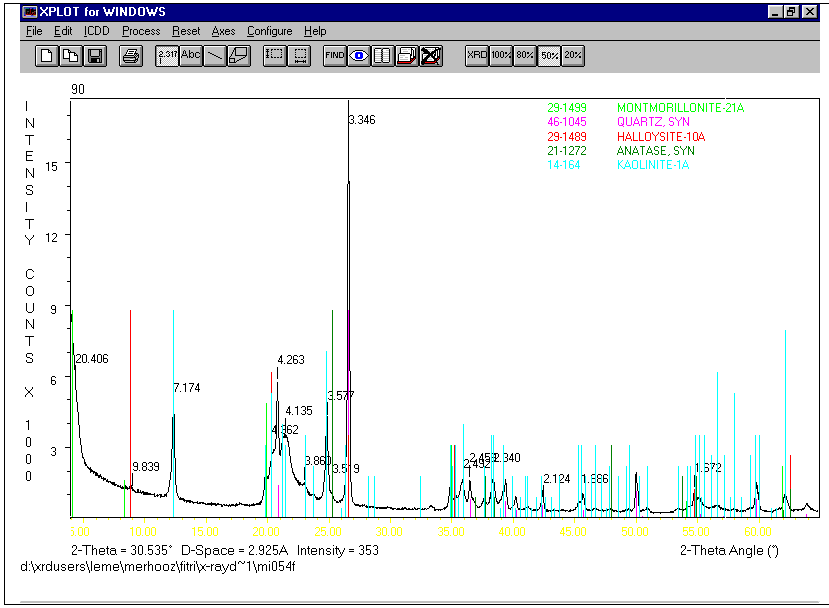
XPLOT for WINDOWS
File Edit ICDD Process Reset Axes Configure Help
90
INTENSITY COUNTS X 10000
29-1499 MONTMORILLONITE-21A
46-1045 QUARTZ, SYN
29-1489 HALLOYSITE-10A
21-1272 ANATASE, SYN
14-164 KAOLINITE-1A
3.346
20.406
7.174
4.263
4.135
4.362
3.577
3.867
9.839
2.452
2.340
2.124
1.586
1.372
2-Theta = 30.535° D-Space = 2.925A Intensity = 353
2-Theta Angle (°)
d:\xrdusers\leme\merhooz\fitri\x-rayd~1\mi054f

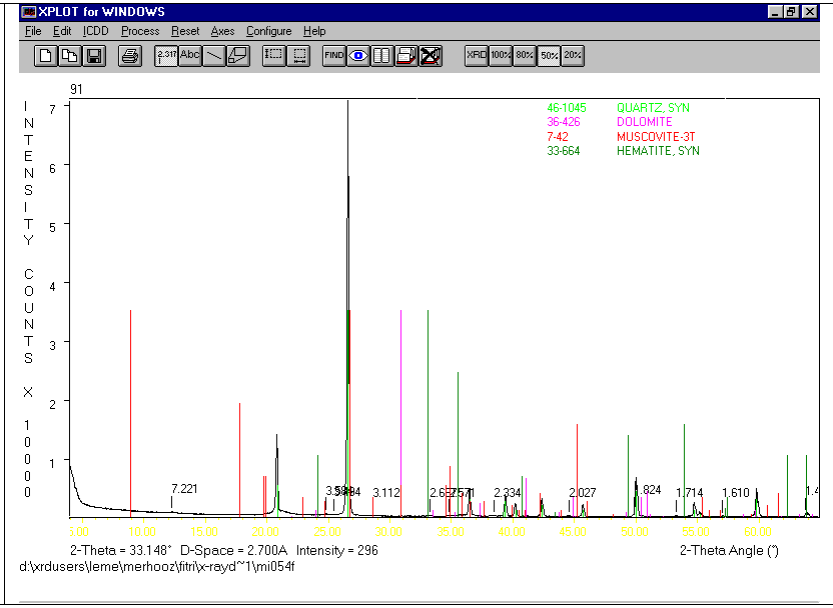
XPLOT for WINDOWS
File Edit ICDD Process Reset Axes Configure Help
91
INTENSITY COUNTS X 10000
46-1045 QUARTZ, SYN
36-426 DOLOMITE
7-42 MUSCOVITE-3T
33-664 HEMATITE, SYN
7.221
3.112
2.334
2.027
1.824
1.714
1.610
2-Theta = 33.148° D-Space = 2.700A Intensity = 296
2-Theta Angle (°)
d:\xrdusers\leme\merhooz\fitri\x-rayd~1\mi054f

APPENDIX 4:

ASD spectra field measurement and mineral interpretation of Block G Tick Hill NW Queensland

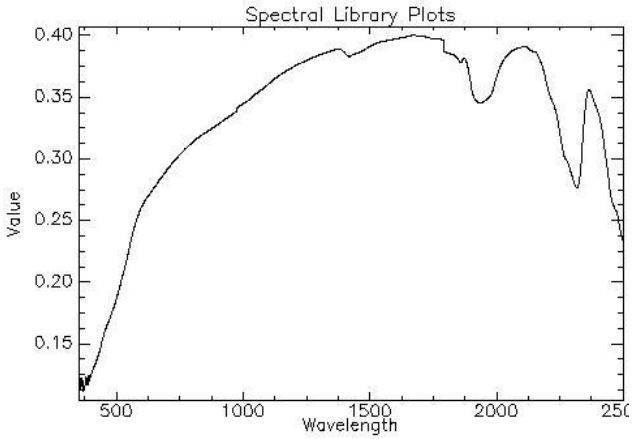

Mi039f1 (dolomite)

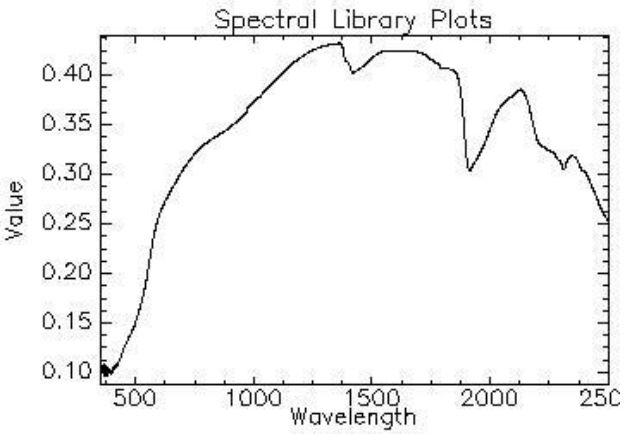

Mi039f2 (dolomite ?)

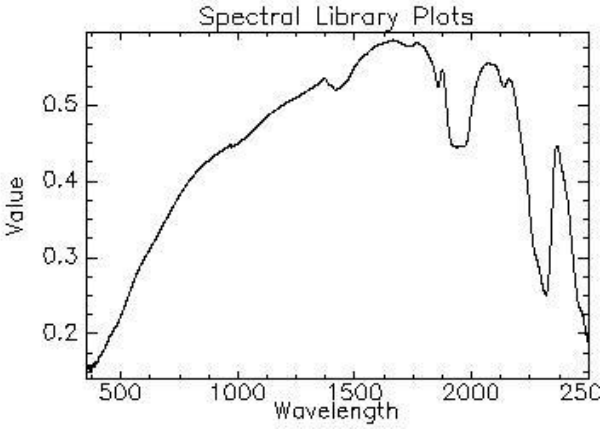

Mi039f3 (dolomite)

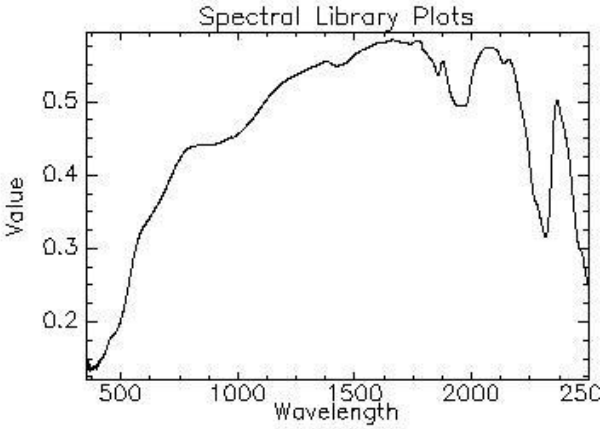

Mi039f4 (dolomite)

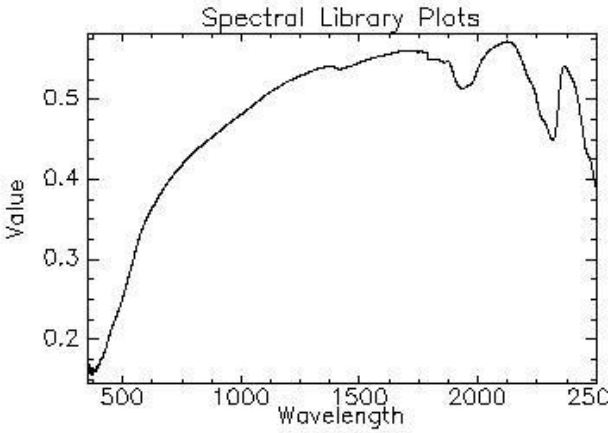

Mi039w1 (dolomite)

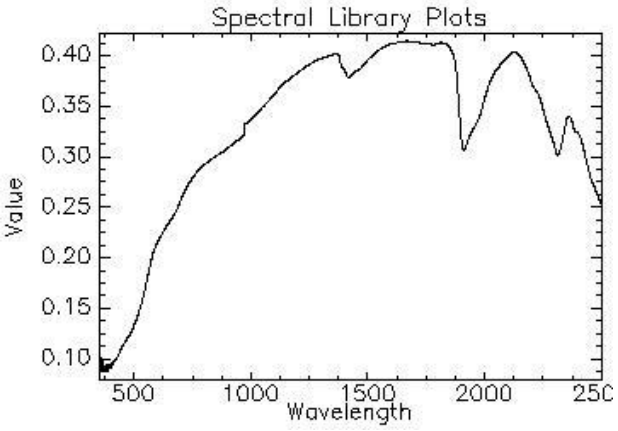

Mi039w2 (dolomite)

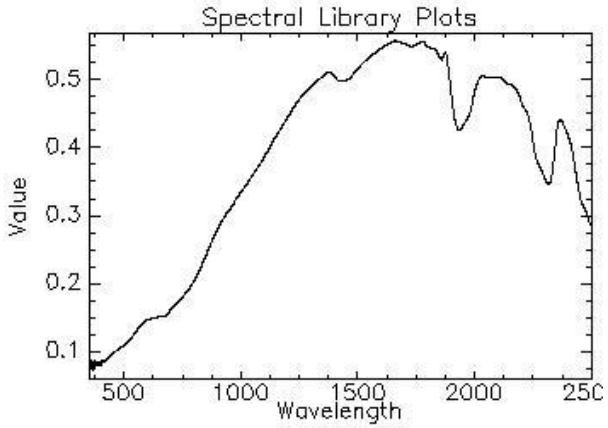

Mi039w3 (dolomite)

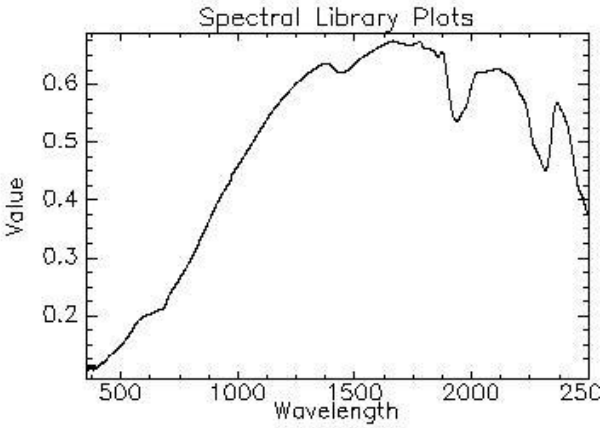

Mi039w4 (dolomite)

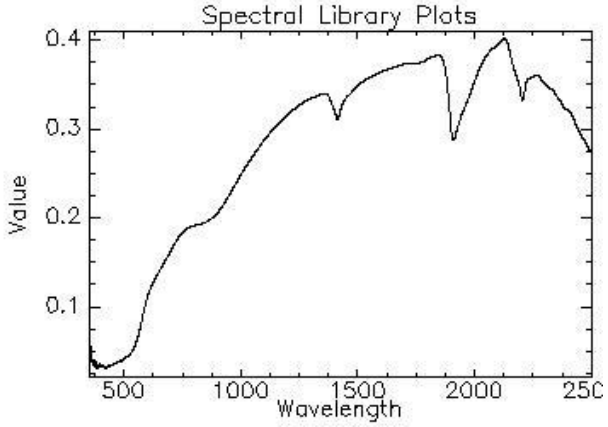

Mi040s1 (montmorillonite)

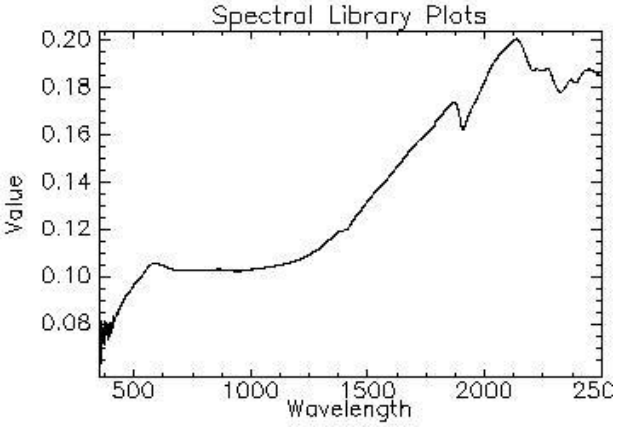

Mi041f1 (siderite?, hornblende?, small hematite)

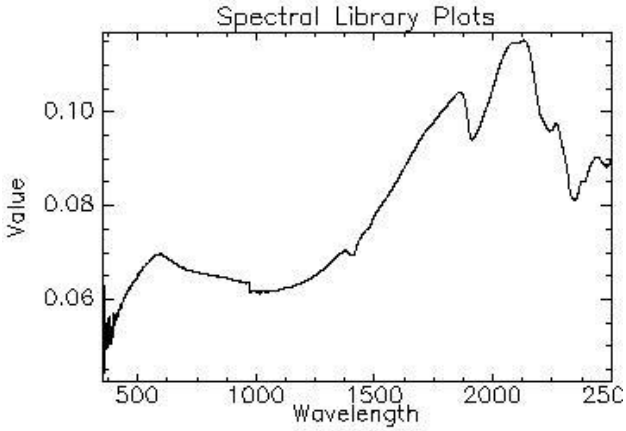

Mi041f2 (siderite, dolomite)

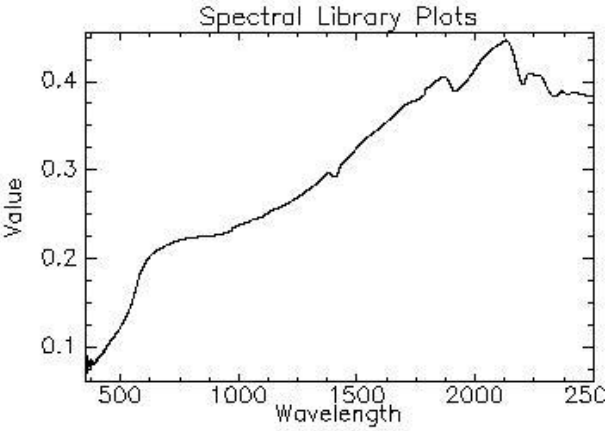

Mi041w1 (siderite, montmorillonite(small)

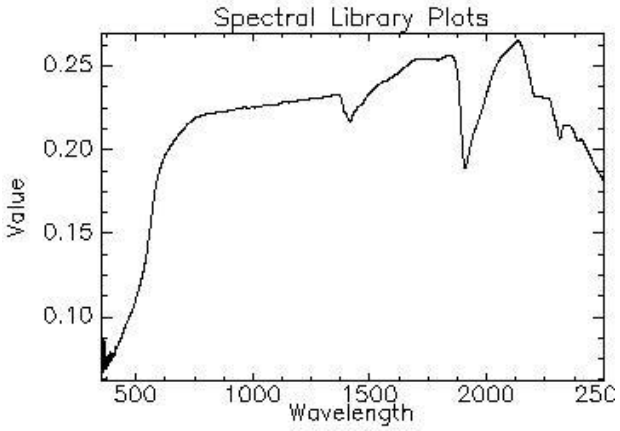

Mi041w2 (siderite_small?)

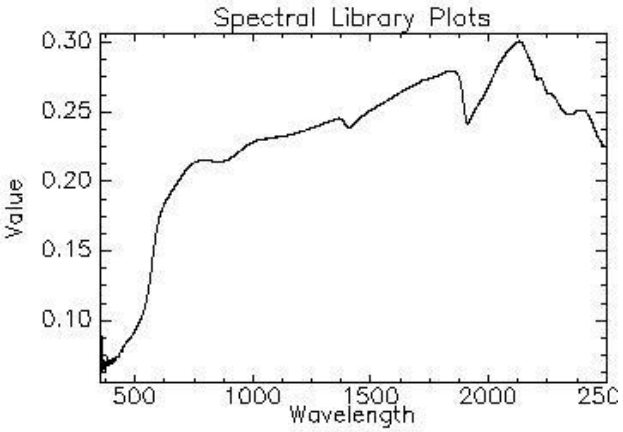

Mi042f1 (dolomite?)

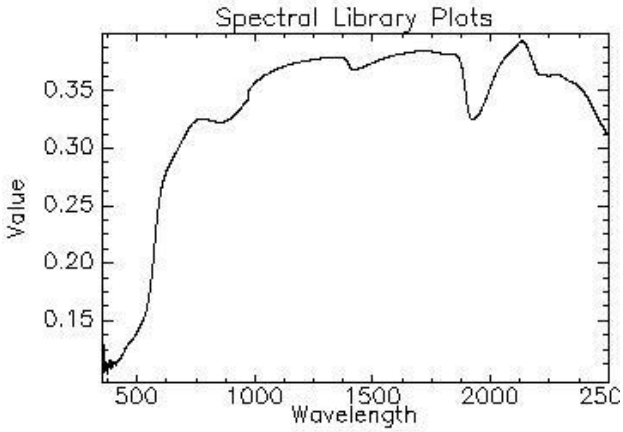

Mi042f2 (hematite,goethite, dolomite?)

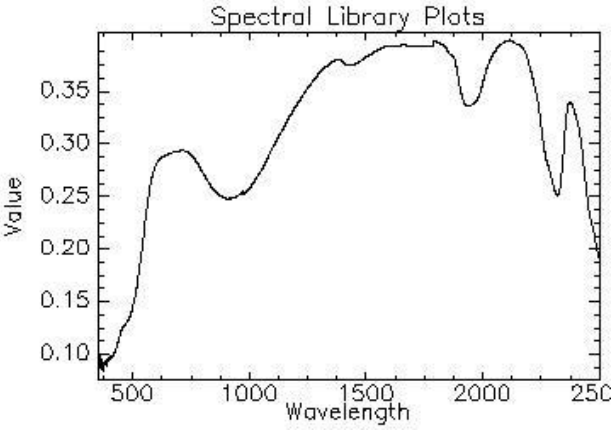

Mi042f3 (goethite, dolomite)

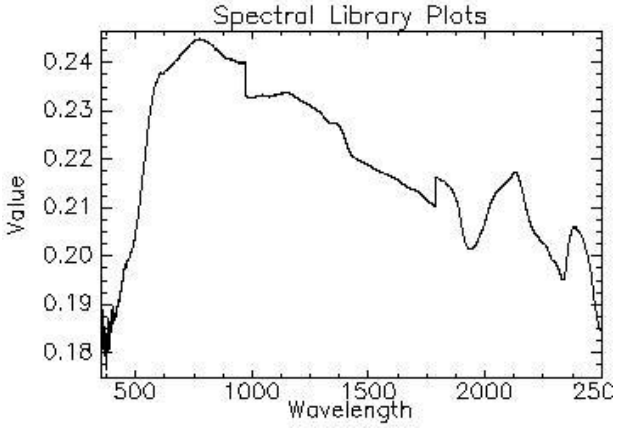

Mi042f4 (siderite?)

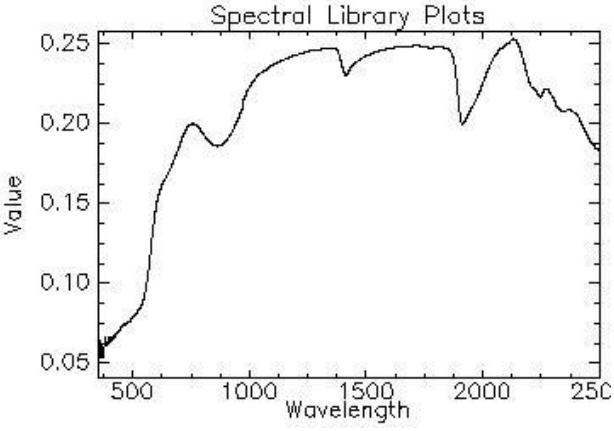

Mi042f5 (hematite, montmorillonite?)

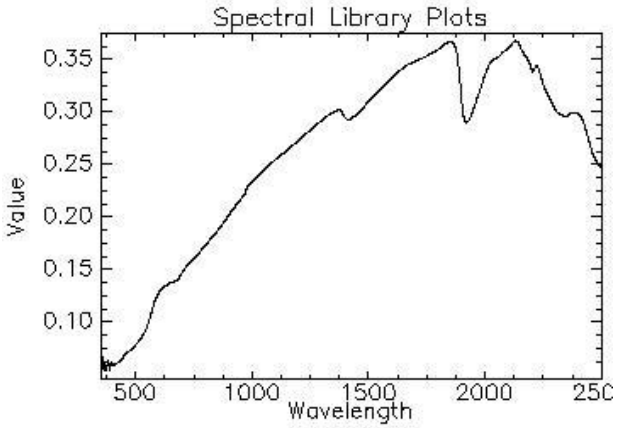

Mi042w1 (muscovite?)

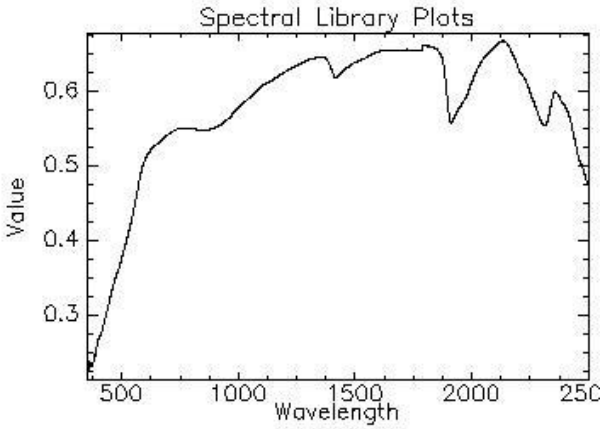

Mi042w2 (hematite, dolomite?)

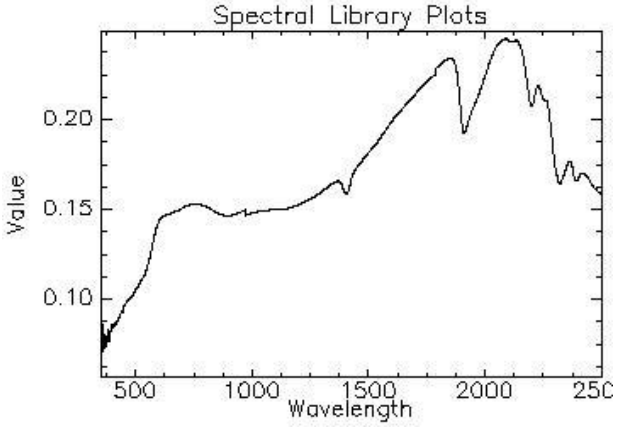

Mi042w3 (goethite?, dolomite?)

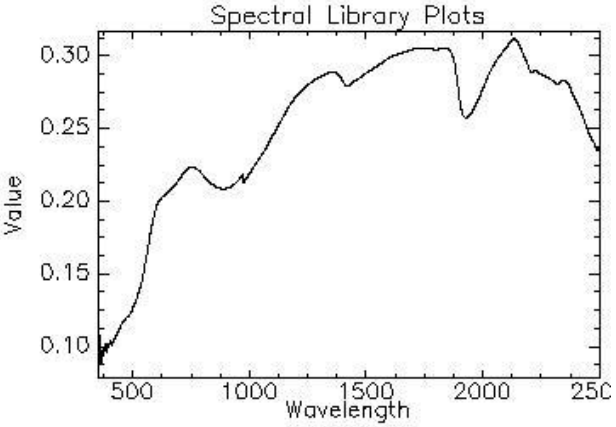

Mi042w4 (hematite)

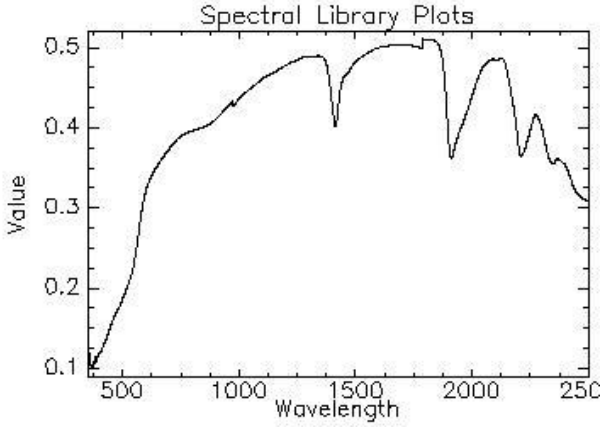

Mi042w5 (illite-muscovite)

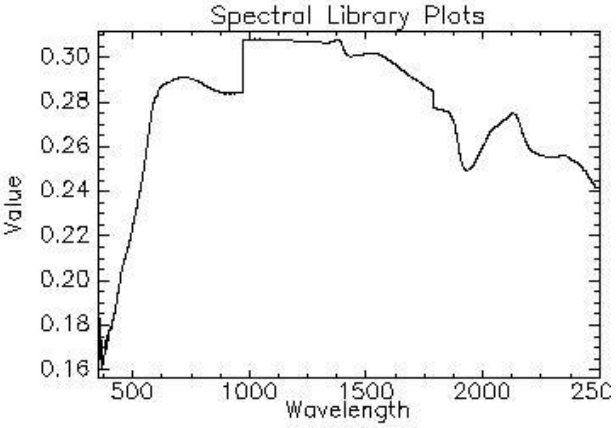

Mi042w6 (montmorillonite?)

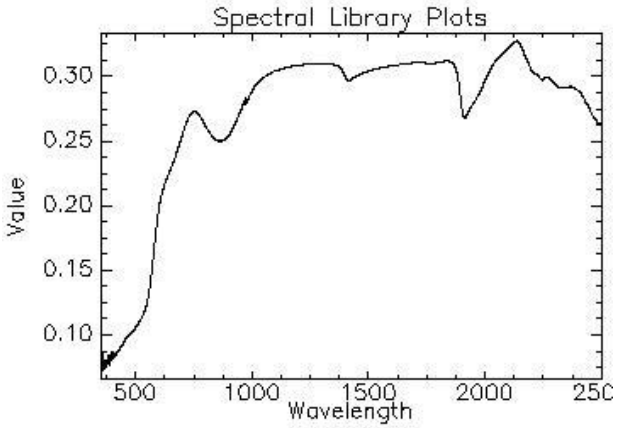

Mi042w7 (hematite)

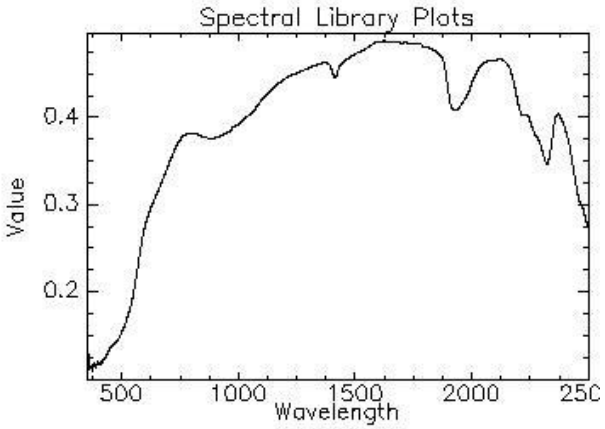

Mi043f1 (hematite, dolomite)

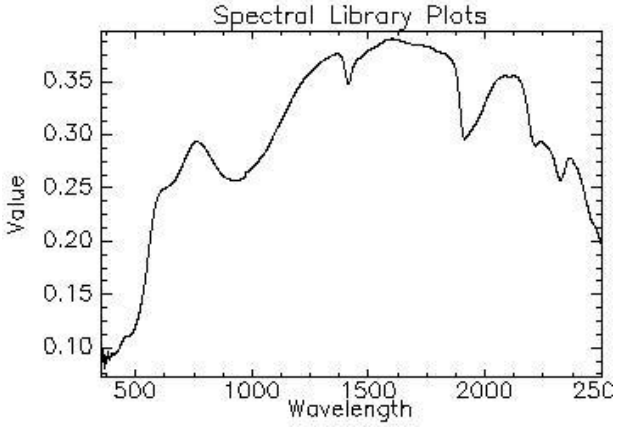

Mi043f2 (goethite, illite)

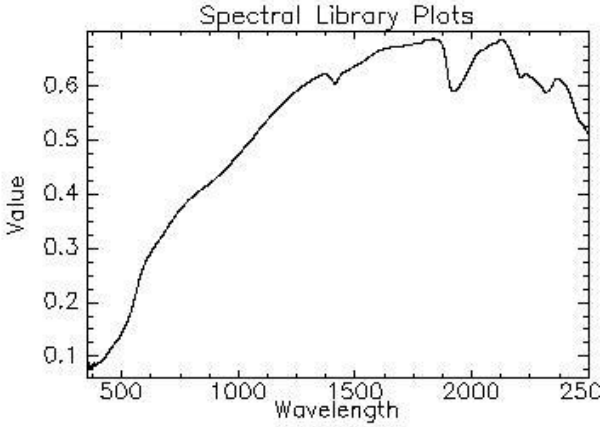

Mi043w1 (dolomite?)

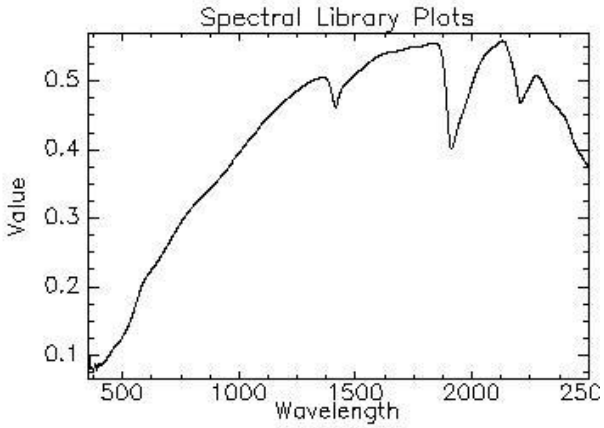

Mi043w2 (montmorillonite)

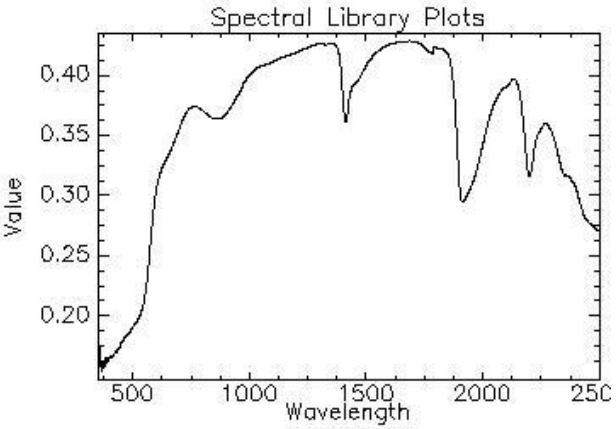

Mi044f1(hematite, montmorillonite)

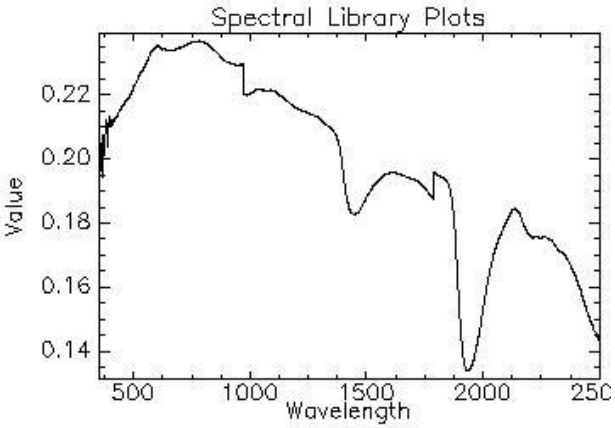

Mi044f2 (Hydrothermal?)

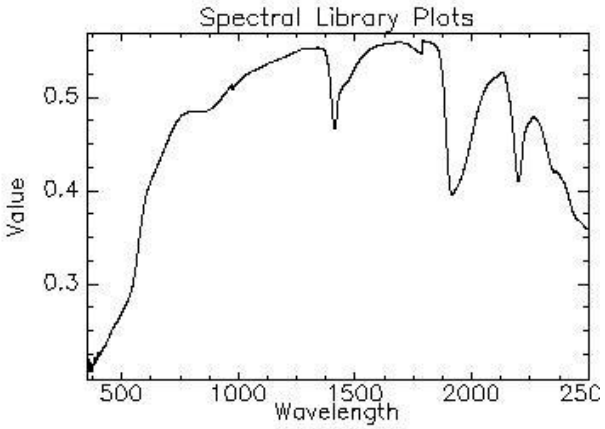

Mi044f3 (hematite, montmorillonite)

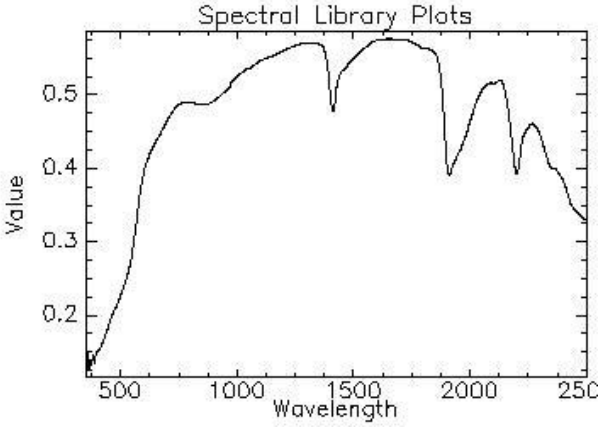

Mi044w1 (hematite, illite-muscovite)

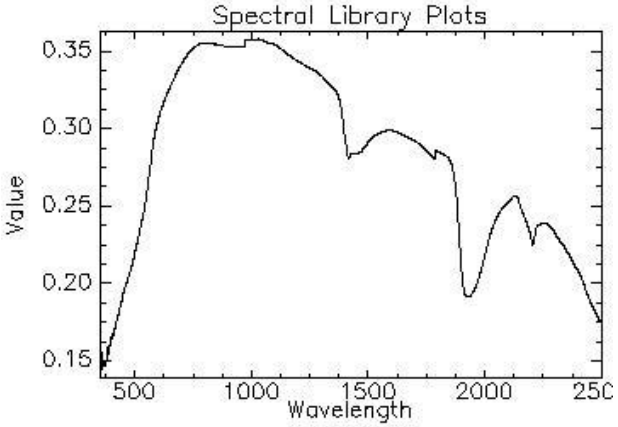

Mi044w2 (montmorillonite)

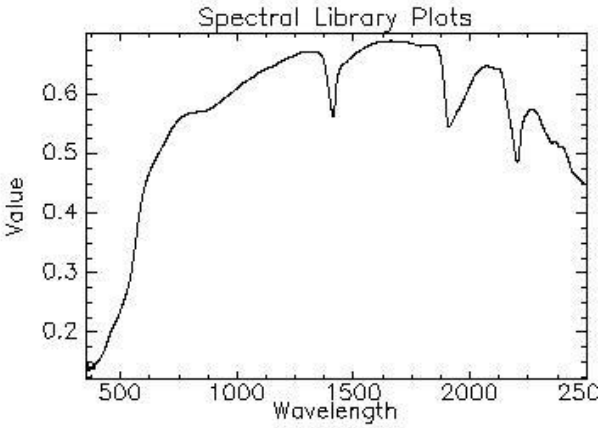

Mi044w3 (illite-muscovite)

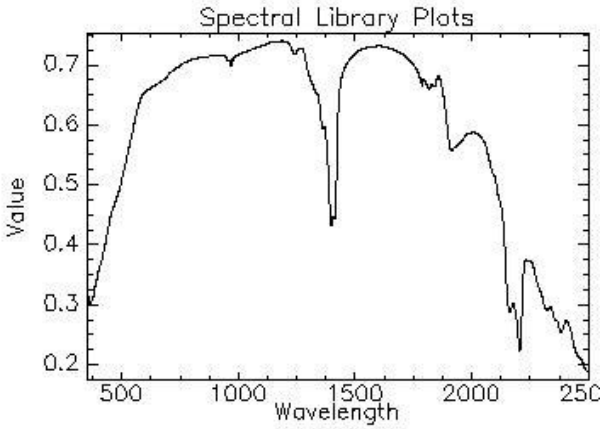

Mi045f1 (kaolinite)

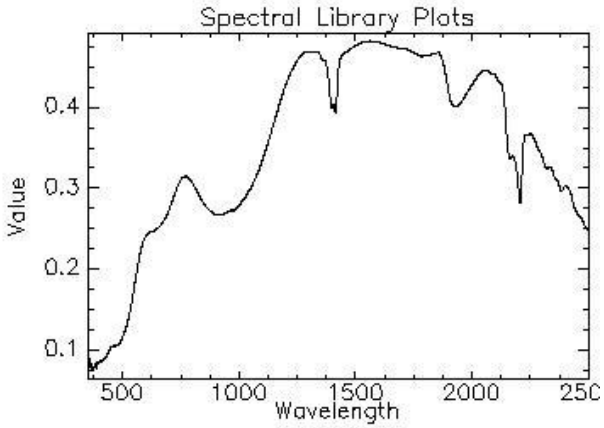

Mi045f2 (goethite, kaolinite)

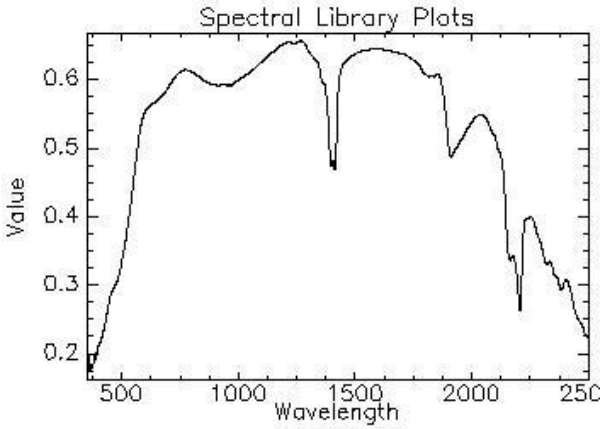

Mi045f3 (goethite, kaolinite)

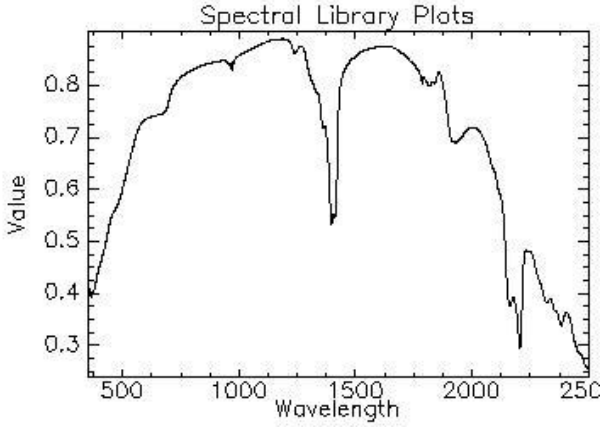

Mi045w1 (kaolinite)

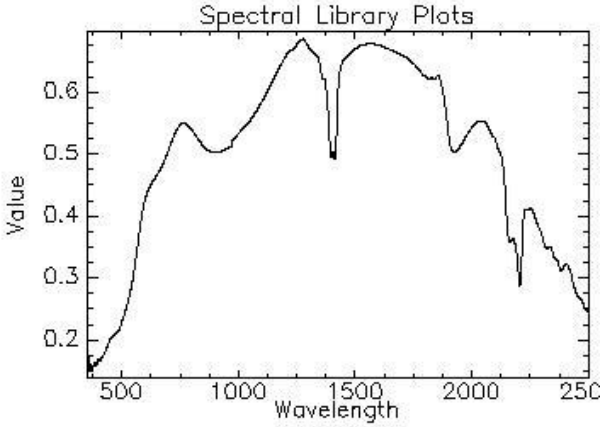

Mi045w2 (goethite, kaolinite)

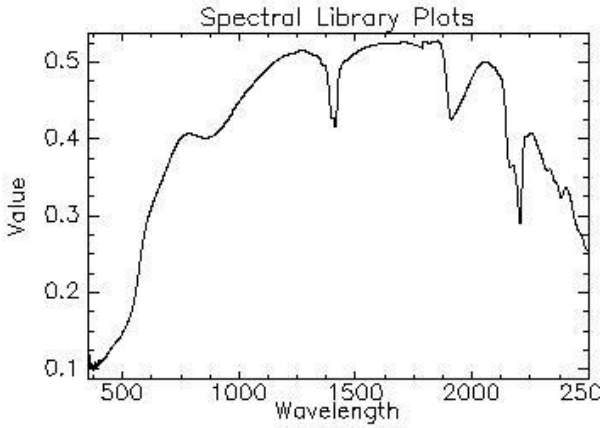

Mi045w3 (hematite, kaolinite)

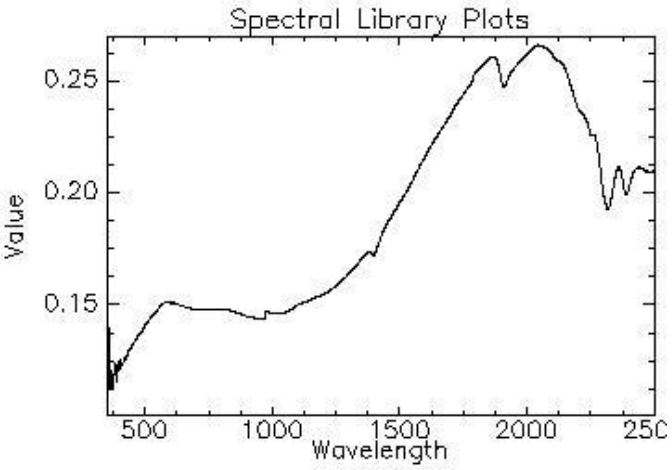

Mi046f1 (dolomite, Mg clay?)

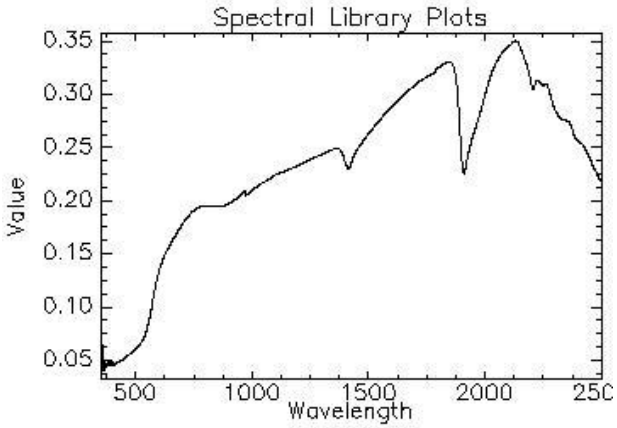

Mi046f2 (illite, smectite)

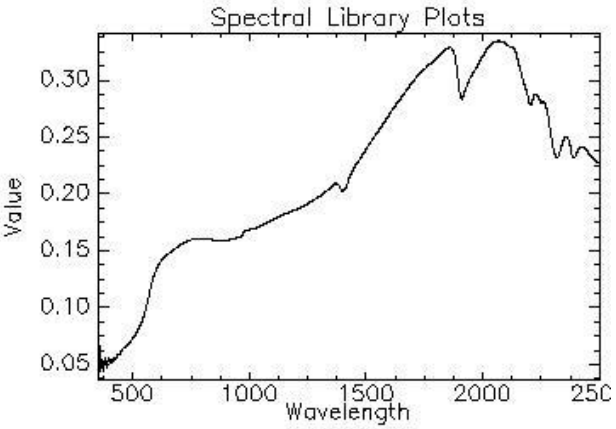

Mi046w1 (montmorillonite, hornblende?)

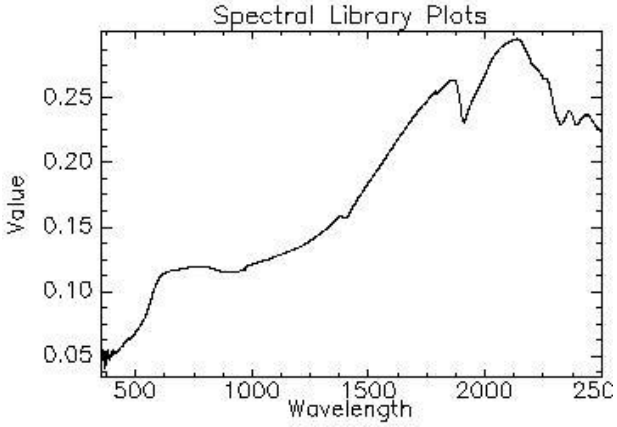

Mi046w2 (hornblende)

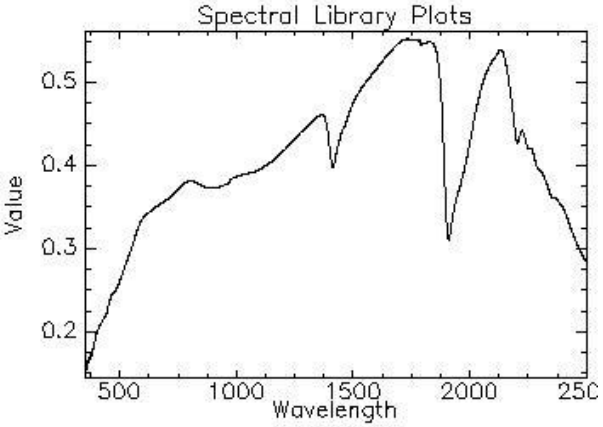

Mi047f1 (goethite, illite, smectite)

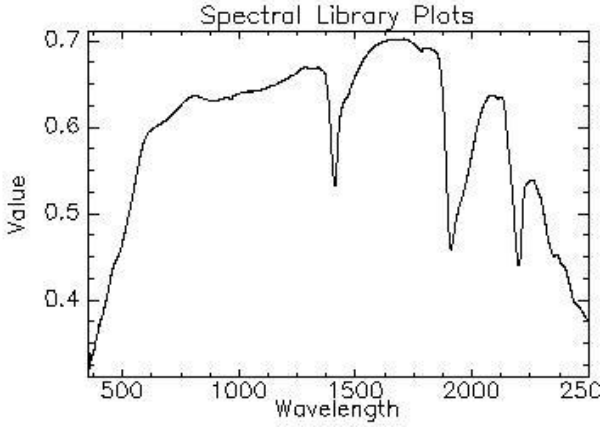

Mi047f2 (goethite, illite-muscovite)

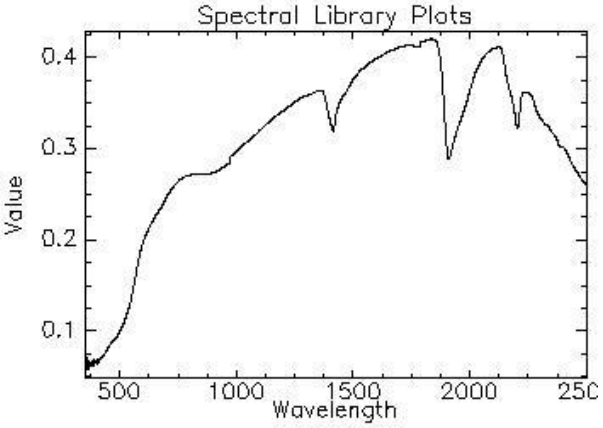

Mi047s1 (goethite, montmorillonite)

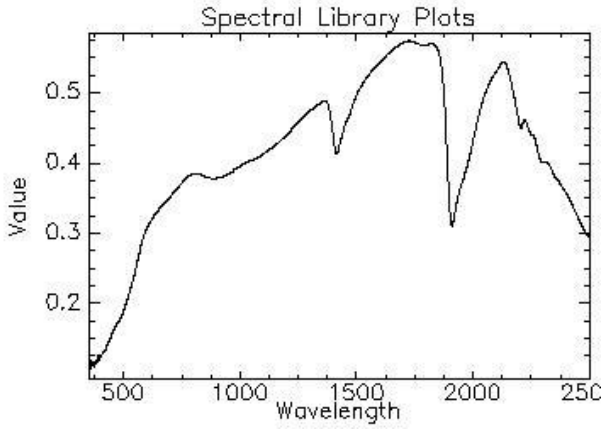

Mi047w1 (hematite, montmorillonite)

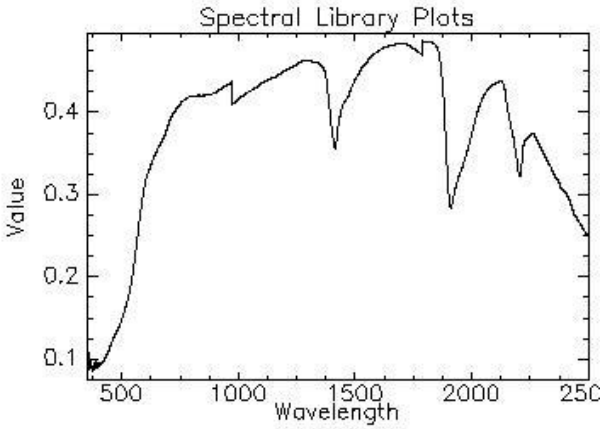

Mi047w2(hematite, montmorillonite)

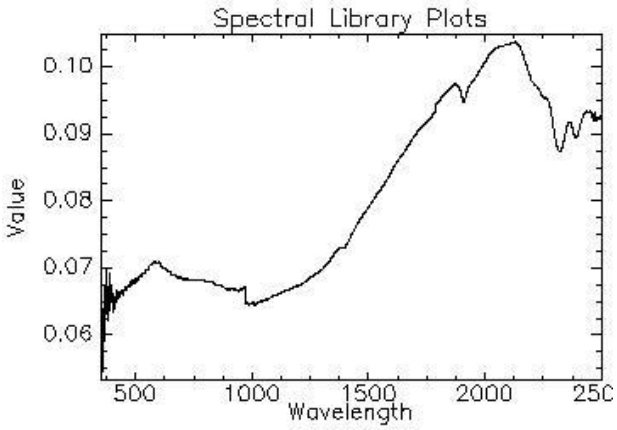

Mi048f1 (siderite?)

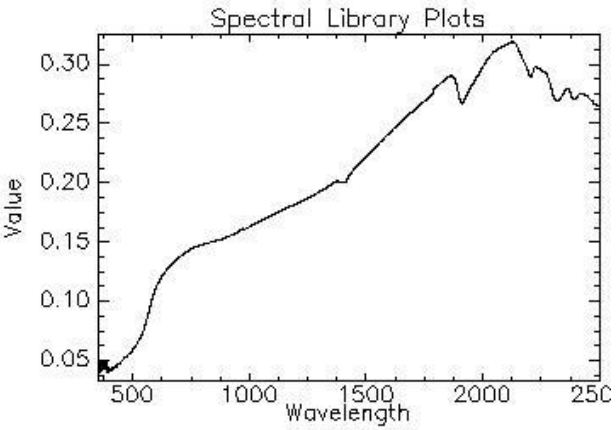

Mi048s1 (hornblende?)

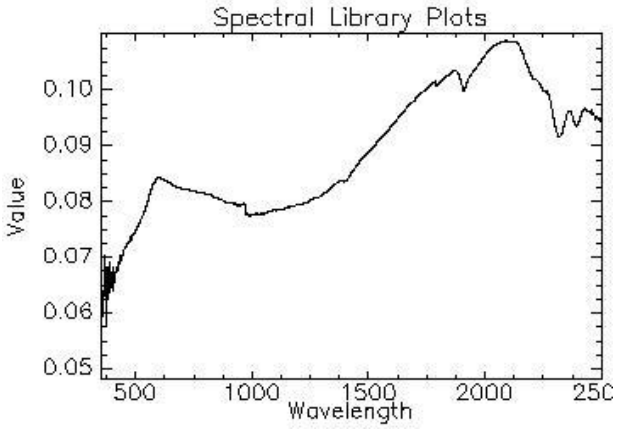

Mi048w1(hornblende)

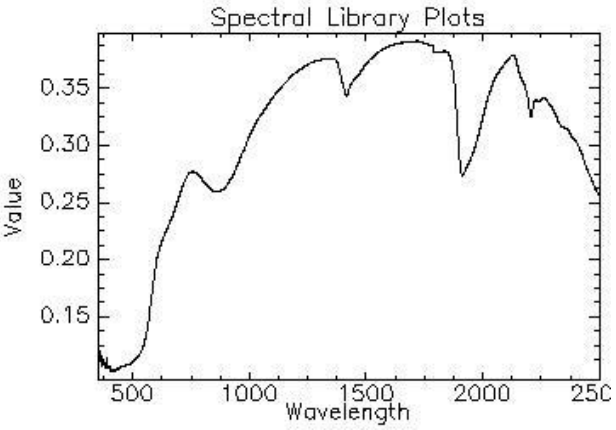

Mi049f1(hematite, montmorillonite)

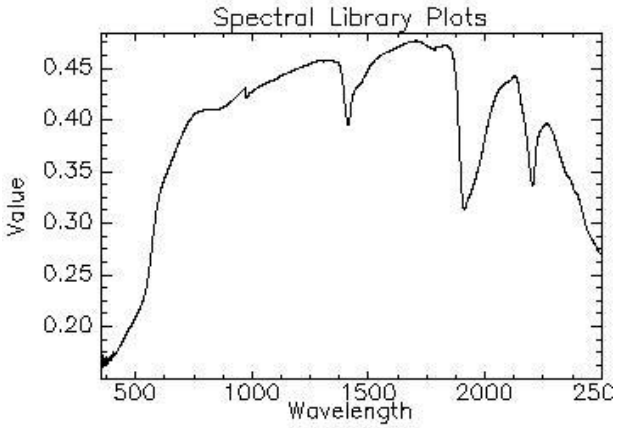

Mi049f2(montmorillonite)

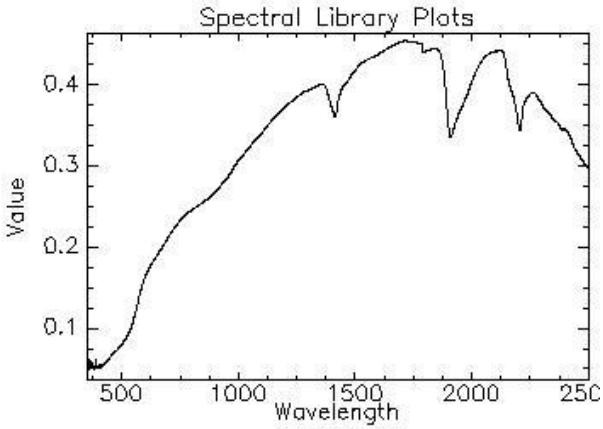

Mi049s1(montmorillonite)

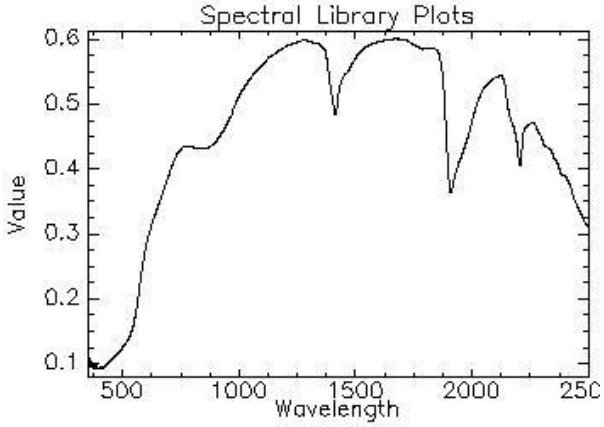

Mi049w1(hematite, montmorillonite)

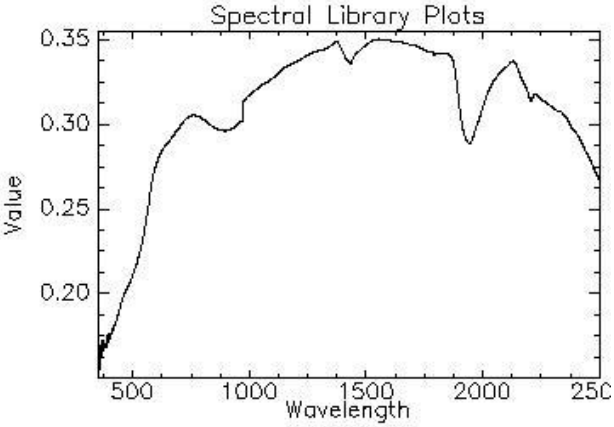

Mi049w2 (goethite, montmorillonite)

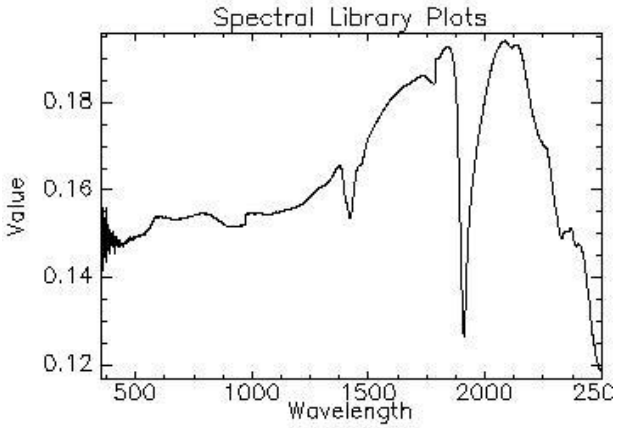

Mi050f1 (montmorillonite?)

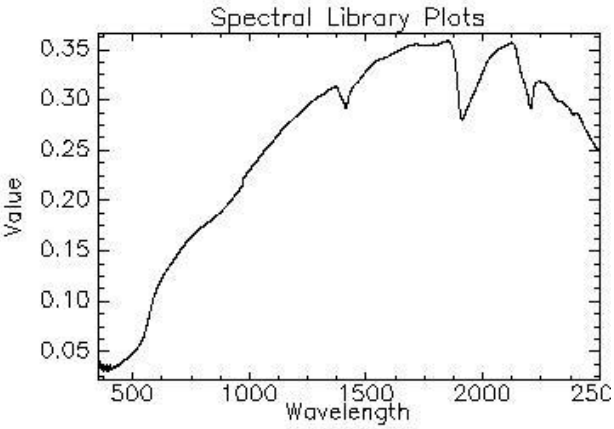

Mi050s1 (montmorillonite)

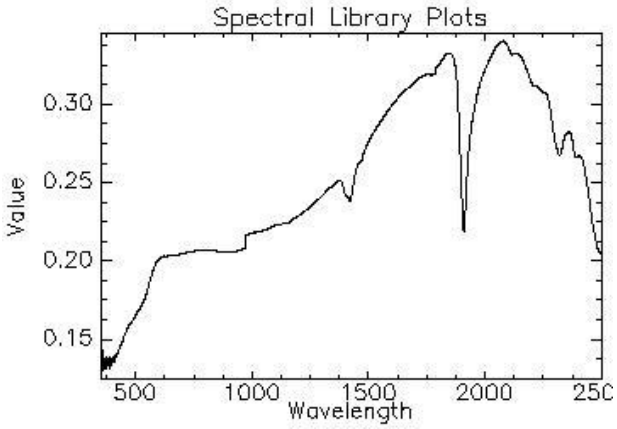

Mi050w1(goethite, illite-muscovite)

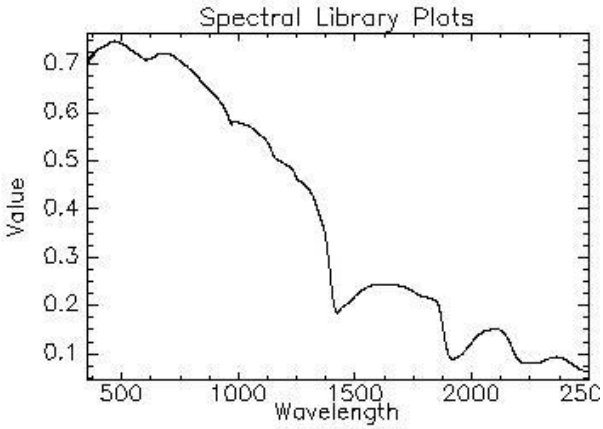

Mi051f1(opal silica)

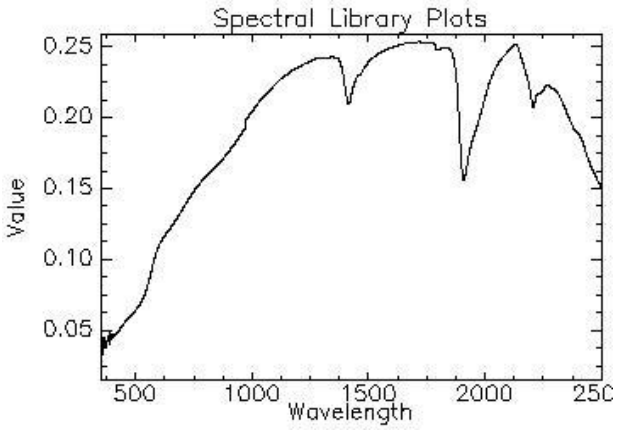

Mi051s1(montmorillonite)

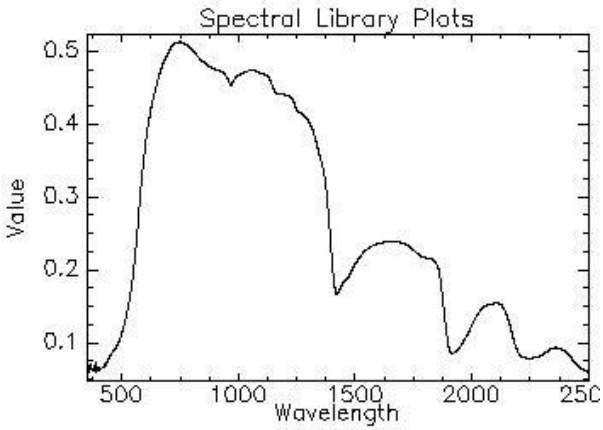

Mi051w1(opal silica)

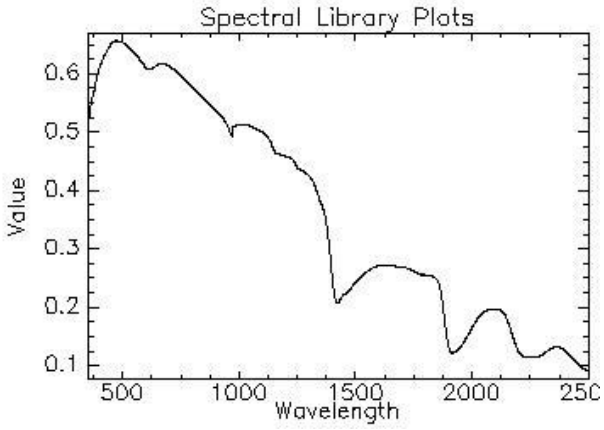

Mi052f1 (opal silica)

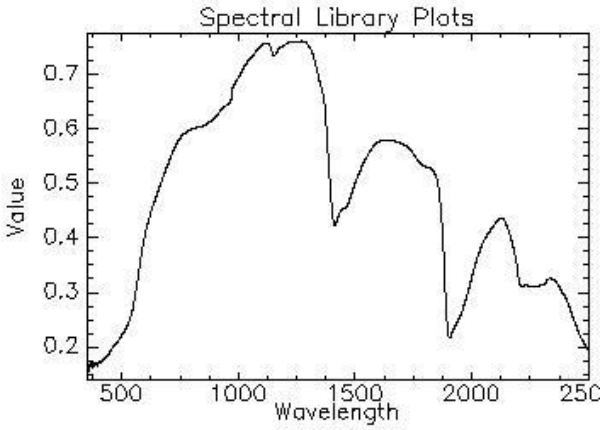

Mi052f2 (hematite, opal silica)

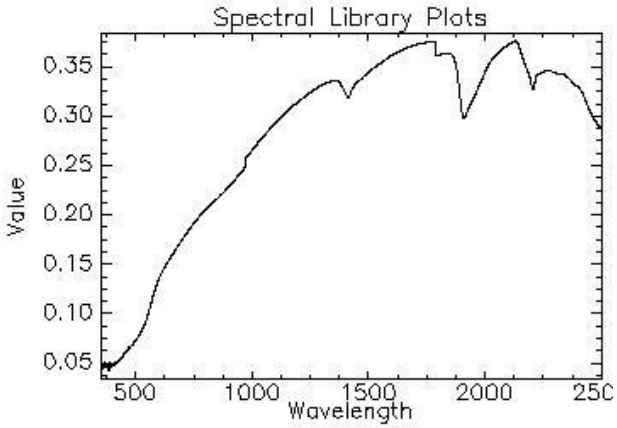

Mi052s1 (montmorillonite?)

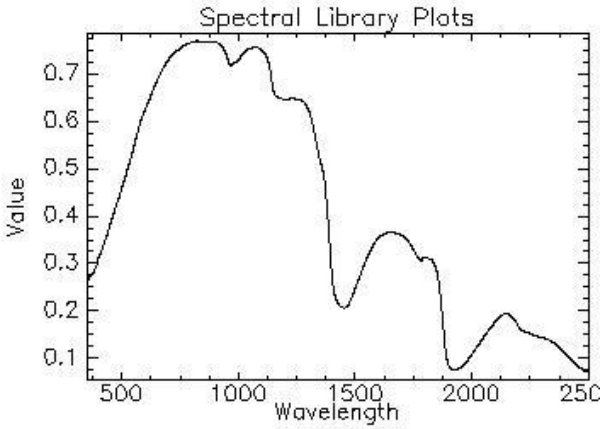

Mi052w1(goethite, opal silica)

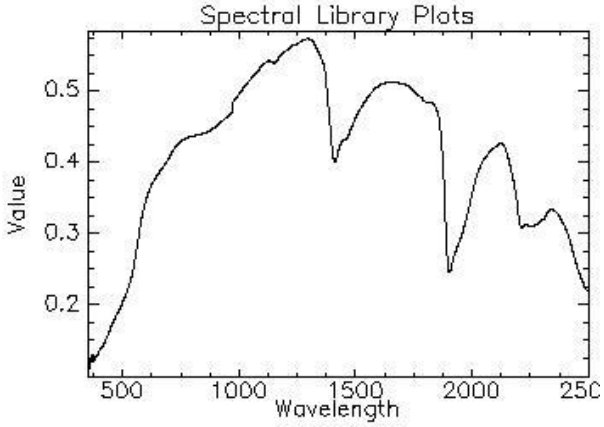

Mi052w2(opal silica?)

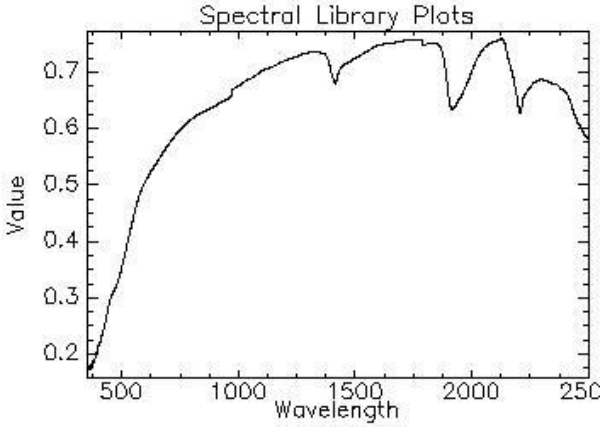

Mi053f1(montmorillonite)

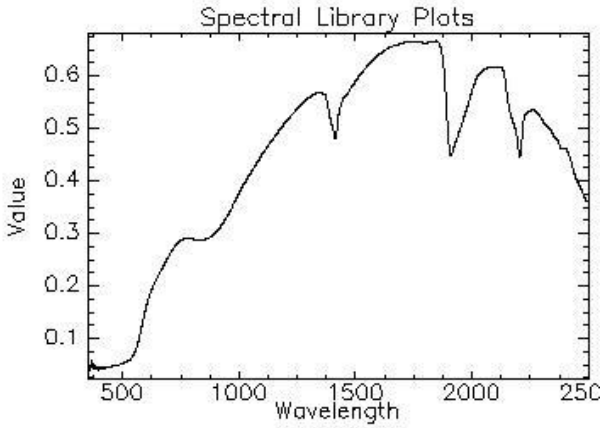

Mi053w1(hematite, montmorillonite)

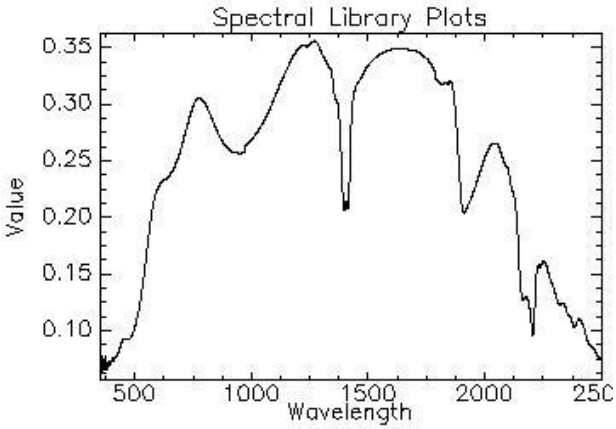

Mi054f1(goethite, kaolinite)

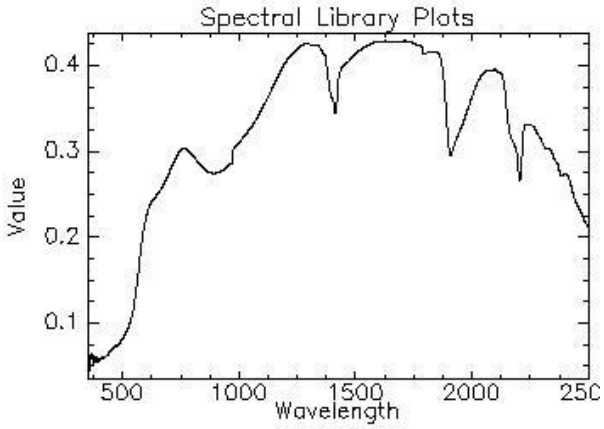

Mi054f2(goethite, kaolinite)

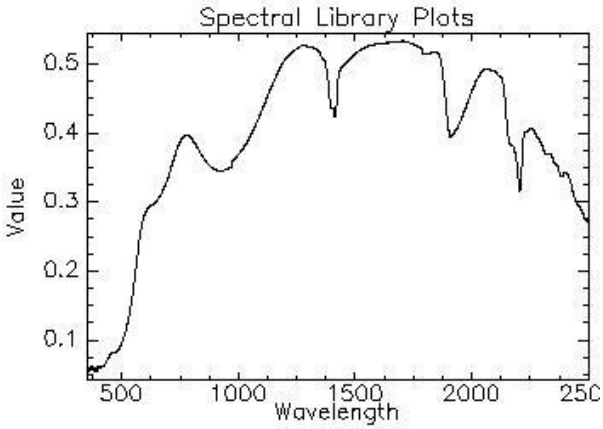

Mi054f3(hematite, kaolinite)

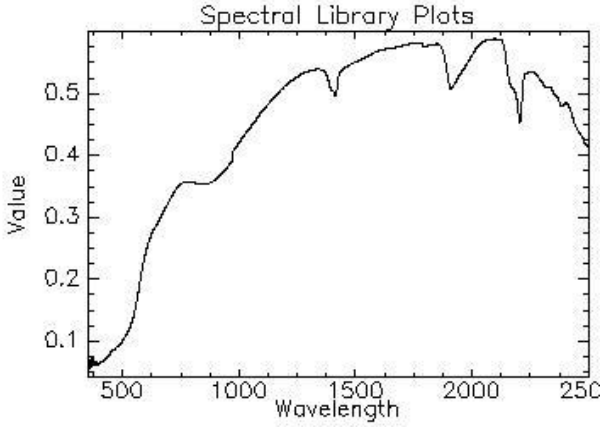

Mi054s1(hematite, kaolinite)

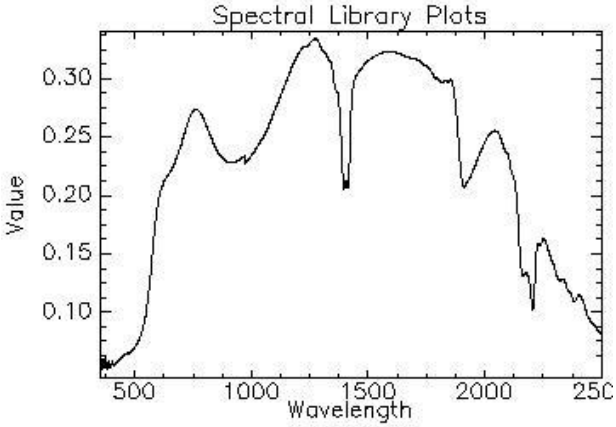

Mi054w1(goethite, kaolinite)

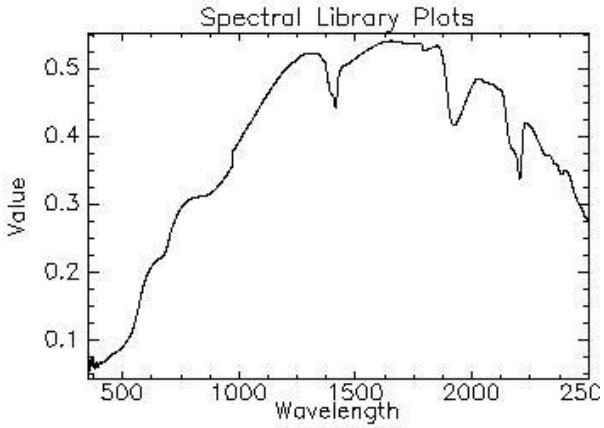

Mi054w2(hematite, kaolinite)

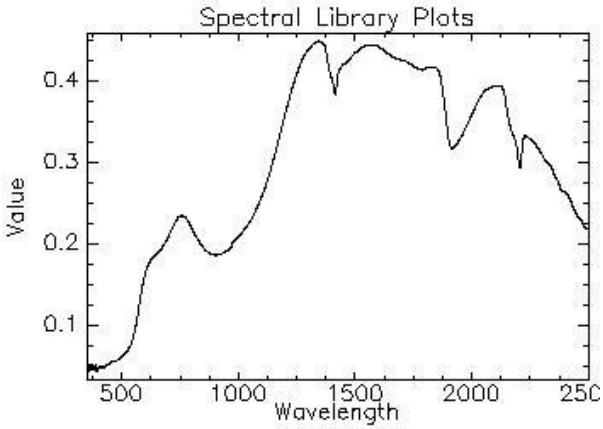

Mi054w3(goethite, kaolinite)

APPENDIX 5: Tick Hill Samples ASD and XRD Interpretation

No.	Sample	East	North	Bulk XRD	ASD Field spectra measurement	XRD clay separation
1	mi039f1	376084	7635471	-	Dolomite	-
2	mi039f2	376084	7635471	Quartz, calcite(magnesian), dolomite	Dolomite	-
3	mi039f3	376084	7635471	Dolomite, quartz(small)	Dolomite	-
4	mi039f4	376084	7635471	-	dolomite	-
5	Mi039s1	376084	7635471	Quartz, dolomite, anorthite, actonolite, tremolite	-	-
6	mi039w1	376084	7635471	-	Dolomite	-
7	mi039w2	376084	7635471	-	Dolomite	-
8	mi039w3	376084	7635471	-	Dolomite	-
9	mi039w4	376084	7635471	-	Dolomite	-
10	mi040s1a	375852	7635727	Quartz, albite, tremolite, hematite(small)	Montmorillonite	-
11	mi040s1b	375852	7635727	Quartz, anorthite, hematite, dolomite, sanidine, actinolite	-	-
12	mi041f1	379871	7634837	Augite, illite, muscovite, riebeckite	Hornblende? siderite?	-
13	mi041f2	379871	7634837	-	Siderite, dolomite?	-
14	mi041w1	379871	7634837	-	Siderite,montmorillonite (small)	-
15	mi041w2	379871	7634837	-	Siderite (small)	-
16	mi042f1	379825	7635046	Quartz,albite, pigeonite, magnetite, clinochlore	Dolomite?	-
17	mi042f2	379825	7635046	Quartz, anorthite, sanidine, microcline	Hematite, goethite, dolomite?	-
18	mi042f3	379825	7635046	Dolomite, quartz, goethite, magnetite(small)	Goethite, dolomite	-
19	mi042f4	379825	7635046	Quartz	Siderite?	-
20	mi042f5	379825	7635046	Quartz, albite, calcite, kaolinite	Hematite, montmorillonite?	-
21	mi042f6	379825	7635046	Quartz,albite,biotite,calcite,riebeckite,clinochlore	-	-
22	mi042w1	379825	7635046	-	Illite/Muscovite?	-

23	mi042w2	379825	7635046	-	Hematite, dolomite?	-
24	mi042w3	379825	7635046	-	Goethite?, dolomite?	-
25	mi042w4	379825	7635046	-	Hematite	-
26	mi042w5	379825	7635046	-	Illite-muscovite	-
27	mio42w6	379825	7635046	-	Montmorillonite?	-
28	mi042w7	379825	7635046	-	Hematite	-
29	mi042s1	379825	7635046	Quartz,hematite, calcite,dolomite,illite,tremolite,clinochlore	-	-
30	mi043f1	393489	7603430	-	Hematite, dolomite	-
31	mi043f2	393489	7603430	Quartz,dolomite,illite,sanidine	Goethite, illite	-
32	mi043s1	393489	7603430	Quartz,dolomite,calcite(small),illite,tremolite,albite,anorthite	-	-
33	mi043w1	393489	7603430	-	Dolomite?	-
34	mi043w2	393489	7603430	-	Montmorillonite	-
35	mi044f1	389235	7605477	Quartz,albite,anorthite	Hematite, montmorillonite	-
36	mi044f2	389235	7605477	Quartz	?	-
37	mi044s1	389235	7605477	Quartz,albite	-	-
38	mi044f3	389235	7605477	-	Hematite, montmorillonite	-
39	mi044w1	389235	7605477	-	Hematite, illite-muscovite	-
40	mi044w2	389235	7605477	-	Montmorillonite	-
41	mi044w3	389235	7605477	-	Illite-muscovite	-
42	mi045f1	389265	7605527	Quartz, kaolinite	Kaolinite	-
43	mi045f2	389265	7605527	Quartz, kaolinite	Goethite, kaolinite	-
44	mi045s1	389265	7605527	Quartz, hematite, kaolinite	-	-
45	mi045f3	389265	7605527	-	Goethite, kaolinite	-
46	mi045w1	389265	7605527	-	Kaolinite	-
47	mi045w2	389265	7605527	-	Goethite, kaolinite	-
48	mi045w3	389265	7605527	-	Hematite, kaolinite	-

49	mi046f1	389203	7605516	Quartz, illite, albite, riebeckite, rutile, tremolite	Dolomite, magnesium clay?	-
50	mi046f2	389203	7605516	Rutile,quartz,albite,muscovite,tremolite,kaolinite,clinochlore	Illite-muscovite	Kaolinite, Montmorillonite
51	mi046s1	389203	7605516	Quartz,albite,calcite,muscovite,montmorillonite,actinolite	-	-
52	mi046w1	389203	7605516	-	Montmorillonite, hornblende?	-
53	mi046w2	389203	7605516	-	Hornblende	-
54	mi047f1	389075	7605543	Quartz,albite,vermiculite, kaolinite,illite	Goethite, illite-muscovite	Kaolinite, montmorillonite, illite/muscovite, chlorite
55	mi047f2	389075	7605543	Quartz,albite,anorthite	Goethite, illite-muscovite	Montmorillonite, chlorite
56	mi047s1	389075	7605543	Quartz,albite,actonolite,microcline	Goethite, montmorillonite	-
57	mi047w1	389075	7605543	-	Hematite, montmorillonite	-
58	mi047w2	389075	7605543	-	Hematite, montmorillonite	-
59	mi048f1	388891	7604667	Quartz,anorthite,actinolite.albite,tremolite	Siderite?	-
60	mi048s1	388891	7604667	Quartz,anorthite,actinolite,tremolite	Hornblende	-
61	mi048w1	388891	7604667	-	Hornblende	-
62	mi049f1	388804	7604748	Quartz,actinolite, sanidine, microcline	Hematite, montmorillonite	-
63	mi049f2	388804	7604748	Quartz,albite,anorthite	Montmorillonite	-
64	mi049f4	388804	7604748	Quartz	-	-
65	mi049s1	388804	7604748	Quartz,albite,mircocline,actinolite	Montmorillonite	-
66	mi049w1	388804	7604748	-	Hematite, montmorillonite	-
67	mi049w2	388804	7604748	-	Goethite, montmorillonite	-
68	mi050f1	388743	7605098	Quartz,anorthite,tremolite,clinochlore, riebeckite	Montmorillonite?	-
69	mi050s1	388743	7605098	Quartz,anorthite,tremolite	Montmorillonite	-
70	mi050w1	388743	7605098	-	Goethite, illite-muscovite	-

71	mi051f1	387899	7618366	Quartz	Opal silica (opal CT)	-
72	mi051f2	387899	7618366	Quartz	-	-
73	mi051s1	387899	7618366	Quartz, calcite, montmorillonite,dolomite, anorthite	Montmorillonite	-
74	mi051w1	387899	7618366	-	Opal silica (opalCT)	-
75	mi052f1	387928	7618274	Quartz,montmorilonite,dolomite?kaolinite?	Opal silica (opalCT)	-
76	mi052f1b	387928	7618274	Quartz, crystobalite, montmorilonite	-	-
77	mi052f2	387928	7618274	Quartz, crystobalite	Hematite, opal silica (opalCT)	-
78	Mi052f3	387928	7618274	Quartz, crystobalite	-	-
79	mi052s1	387928	7618274	Quartz, crystobalite, montmorilonite,hematite?	Montmorillonite ?	-
80	mi052w1	387928	7618274	-	Goethite, opal silica (opalCT)	-
81	mi052w2	387928	7618274	-	Opal silica ? opalCT	-
82	mi053f1	392708	7617594	Quartz,muscovite,montmorillonite	Montmorillonite	Kaolinite, illite/muscovite
83	mi053w1	392708	7617594	-	Hematite, montmorillonite	-
84	mi053s1	392708	7617594	Montmorillonite, anorthite, quartz	-	-
85	mi054f1	393492	7623270	Montmorillonite, quartz,halloysite, anatase, kaolinite	Goethite, kaolinite	Kaolinite
86	mi054f2	393492	7623270	Quartz, dolomite,muscovite, hematite	Goethite,kaolinite	-
87	mi054f3	393492	7623270	-	Hematite, kaolinite	-
88	mi054s1	393492	7623270	-	Hematite, kaolinite	-
89	mi054w1	393492	7623270	-	Goethite, kaolinite	-
90	mi054w2	393492	7623270	-	Hematite, kaolinite	-
91	mi054w3	393492	7623270	-	Goethite, kaolinite	-

APPENDIX 6:
ASTER MINERAL MAPPING PRODUCTS

No	ASTER Product Name	Base algorithm	Mask (filters)	Color chart	Accuracy/Description
1	ASTER true color 321	RGB (band3:band2:band1)	No	RGB color	Moderate : vegetation is well lining in red false color
2	ASTER 643	RGB (band6:band4:band3)	no	RGB color	Good to moderate: the image is well highlighted the bedrocks
3	ASTER kaolinite map	Band7/band5	Al-OH (b5+b7)/b6 Al-mica (b5/b6) Vegetation mask	Rainbow Red: high Blue: low	Moderate; application mask make better of this product
4	ASTER white mica & Al-smectite map (sericite-muscovite-illite-smectite)	(Band5+band7/band6)	Vegetation mask	Rainbow Red: high Blue: low	Low
5	ASTER iron oxide map	Band2/band1 Band 4/band3	Vegetation mask Vegetation mask	Rainbow Red: high Blue: low	Low
6	ASTER Mg-OH carbonates map	(Band 6+band8/band7)	Vegetation mask	Rainbow Red: high Blue: low	Moderate; mixing with other Al-OH mineral due to lack of band width

APPENDIX 7:
HyMap MINERAL MAPPING PRODUCTS

No	HyMap Product Name	Base algorithm	Mask (filters)	Color chart	Accuracy/Description
1	**HyMap natural color (true color)**	RBG (b_{14}:b_8:b_1) or (R_{644}:R_{556}:R_{453})	no	RGB color	Moderate: problem with mosaicing, lining on strips boundary occur.
2	**HyMap false color (CIR)**	RGB (b_{29}:b_{14}:b_8) or (R_{859}:R_{644}:R_{556})	no	RGB color	Moderate: mosaicing is not properly perform
3	**HyMap De-correlation stretch**	RGB (b_{116}:b_{109}:b_{29}) or (R_{2333}:R_{2212}:R_{859})	no	RGB color	Good; highlighted the bedrocks, vegetation and weathered materials
4	**HyMap kaolinite abundance**	Kaolinite_2200D (b_{104}+b_{111})/(b_{109}) (R_{2122}+R_{2193})/(R_{2158}) including validation	Kaolinite 2160D (R_{2122}+R_{2193})/(R_{2158}) Composite mask	Rainbow Red: high Blue: low	Moderate; highlighted kaolinite major depth at 2200D
5	**HyMap kaolinite crystallinity**	Kaolinite 2160D (R_{2122}+R_{2193})/(R_{2158})	HyMap kaolinite abundance; mask min.1.96	Rainbow Red: high Blue: low	Moderate; highlight kaolinite 2160D
6	**HyMap Al smectite content**	Normalized depth 4th order polynomial between 2120 to 2245 nm (MMTG A-List) **OR** (b_{106}+b_{112})/(b_{109}+b_{106}) (R_{2158}+R_{2264})/(R_{2212}+R_{2158}) for validation	white mica 2350D mask max. 1.035 kaolinite 2160D mask max 1.98 composite mask	Rainbow Red: high Blue: low	Low; mix with kaolinite 2200D and in red(high) complicated with mica 2350D

7	**HyMap, white mica content (muscovite, illite,possibly smectite,kaolinite)**	Normalized depth 4th order polynomial between 2120 to 2245 nm (MMTG A-list) **OR** $(b_{106}+b_{113})/(b_{108}+b_{109})$ $(R_{2158}+R_{2281})/(R_{2193}+R_{2212})$ for validation	Composite mask $(R_{2318}+R_{2295}+R_{2369})/(R_{2333}+R_{2350}+R_{2366})$ For 2350D --- threshold >1.035 $(R_{2138}+R_{2190})/ (R_{2156}+R_{2179})$ For 2200D --- threshold <1.005	Rainbow Red: high Blue: low	Moderate : highlighted the white mica absorption at 2200D and 2350D
8	**HyMap iron oxide abundance**	Normalized depth fitted 2nd order polynomial between 776 and 1074nm -900nm (MMTG A-List) **OR** $(b_{23}+b_{43})/(b_{29}+b_{35})$ $(R_{774}+R_{1058})/(R_{859}+R_{937})$ for validation	Composite mask	Rainbow Red: high Blue: low	Moderate ; mix with vegetation a bit
9	**HyMap MgOH carbonates abundance**	$(b_{112}+b_{117})/(b_{115}+b_{116})$ $(R_{2264}+R_{2349})/(R_{2316}+R_{2333})$ (including validation)	Composite mask HyMap kaolinite abundance; mask max.1.005	Rainbow Red: high Blue: low	Moderate-Low Blue (low); mix with 2200D and 2350D white mica Red (high); typical carbonates at 2300-2400nm
10	**HyMap opal silica abundance**	Normalized depth 4th order polynomial between 2140nm and 2365nm (MMTG A-List) **OR** $(b_{104}+b_{117})/(b_{110}+b_{111})$ $(R_{2122}+R_{2349})/(R_{2229}+R_{2247})$ for validation	Al-OH absorption;mask min.1 Mg-OH $(b_{112}+b_{117})/(b_{115}+b_{116})$ mask max. 1.1035 HyMap white mica content; mask max. 0.015	Rainbow Red: high Blue: low	Moderate: opal silica mix with Al-OH absorption at 2200D.